Mathematical Models for Facilitated Diffusion and the Brownian Ratchet

Christine Louise Lind Cole

A dissertation submitted in partial fulfillment
of the requirements for the degree of

Doctor of Philosophy

University of Washington

2011

Program Authorized to Offer Degree:
Applied Mathematics

University of Washington
Graduate School

This is to certify that I have examined this copy of a doctoral dissertation by

Christine Louise Lind Cole

and have found that it is complete and satisfactory in all respects,
and that any and all revisions required by the final
examining committee have been made.

Chair of the Supervisory Committee:

Hong Qian

Reading Committee:

Bernard Deconinck

Eric Shea-Brown

Hong Qian

Date: 8/31/2011

In presenting this dissertation in partial fulfillment of the requirements for the doctoral degree at the University of Washington, I agree that the Library shall make its copies freely available for inspection. I further agree that extensive copying of the dissertation is allowable only for scholarly purposes, consistent with "fair use" as prescribed in the U.S. Copyright Law. Requests for copying or reproduction of this dissertation may be referred to ProQuest Information and Learning, 300 North Zeeb Road, Ann Arbor, MI 48106-1346, 1-800-521-0600, to whom the author has granted "the right to reproduce and sell (a) copies of the manuscript in microform and/or (b) printed copies of the manuscript made from microform."

Signature 

Date 8/31/2011

University of Washington

Abstract

Mathematical Models for Facilitated Diffusion and the Brownian Ratchet

Christine Louise Lind Cole

Chair of the Supervisory Committee:
Professor Hong Qian
Applied Mathematics

In this dissertation, mathematical models for two biophysically related topics are investigated: facilitated diffusion and the Brownian ratchet. Both phenomena exhibit counterintuitive behavior: in the case of facilitated diffusion, transport of a fast-moving ligand (e.g. oxygen) is enhanced through reversible association with a slow-moving macromolecule (e.g. hemoglobin); in the case of the Brownian ratchet, a diffusing particle with random fluctuations among several internal states can yield directed motion against an external force.

In Part I, a chemical kinetic model for facilitated transport of a ligand mediated by a carrier molecule is developed. This is an alternative formulation of the problem that has been extensively studied using partial differential equations, by J.D. Murray and J. Wyman, among many others. The chemical kinetic model illuminates the *open, driven* nature of the system: a fixed gradient in the ligand drives the transport, and the presence of the carrier molecule introduces a "parallel pathway" guaranteeing an enhanced rate of transport for the ligand. A general model for N ligands is also presented. Analytical results from the models are compared to previous experimental measurements and theoretical results from Wyman-Murray facilitated diffusion of oxygen and carbon monoxide in muscle.

In Part II, a continuous diffusion formalism Brownian ratchet model is introduced as an alternative formulation of the model proposed by C.S. Peskin, G.M. Odell, and G. Oster to describe the actin polymerization driven stochastic movement of the bacteria *Listeria monocytogenes*. It is shown that an attractive force between the polymer and the bacterium has the

same effect as an increased resistant force on the bacterium. The growth of a bundle consisting of N identical polymer filaments is also considered. The bundle grows as a single leading filament with similar velocity to that of single polymer in the absence of a load, but the bundle can oppose N times the external force under the stalling condition. Relationships are obtained for the velocity of the bacterium movement and its apparent diffusivity as functions of the resistant force and the number of filaments in the bundle. The theoretical study provides new insights for statistical data analysis in future experiments.

TABLE OF CONTENTS

LIST OF FIGURES

LIST OF TABLES

ACKNOWLEDGMENTS

It is a pleasure to express my appreciation to Professor Hong Qian, whose guidance and expert advice made this work possible.

My sincere gratitude also goes to Professors Bernard Deconinck and Eric Shea-Brown for their helpful comments and careful reading of this dissertation.

I would also like to acknowledge the support of the graduate students, faculty, and staff of the Department of Applied Mathematics. Special thanks go to two members of my cohort, Katie Oliveras and Kirsten Fagnan, for their friendship and collaboration, both during and after graduate school.

I am indebted to the Department of Applied Mathematics for providing me with many different teaching opportunities, and to the students who I had the pleasure of serving, either as an instructor or a teaching assistant, for affirming my love of teaching.

DEDICATION

To my parents, Bruce and Barbara Lind, and my husband, Doug Cole, for their encouragement, patience, and understanding.

Chapter 1

INTRODUCTION

The common biophysical theme of this dissertation is *active diffusion*. Typically, when one thinks of diffusion, one might think of gradient driven models for a chemical spreading through a solution from high concentration regions to low concentration regions or heat spreading through a metal rod. From another perspective, that of "white noise" driven models, one imagines a passive object moving according to random interactions with its environment. In the canonical examples, a piece of pollen in a bathtub moves according to Brownian motion due to bombardment by the water molecules, and a drunk moves through a city according to a random walk by picking a direction at random at each street intersection. All of these examples describe the same physical phenomenon, but one group focuses on the distribution of a large population of individuals while the other focuses on the individuals themselves. The type of mathematics used in each case reflects these differences in the scale. If the motion is spatially continuous, diffusion or stochastic differential equations are used, while if the motion is spatially discrete, chemical master equations or the Gillespie algorithm are used. In each of these scenarios, the transport can be considered to be *passive*, meaning that it simply follows a gradient or "goes with the flow." In this work, we will consider two different situations in which the transport is actually *active*, rather than passive. The two biophysical systems we will study at length are facilitated diffusion and the Brownian ratchet model for molecular motor transport. Both of these systems are examples where the power of (random) diffusion is harnessed to produce directed motion, or transport, of some substance, which can occur against the direction of the gradient; this is the sense in which we mean that the transport is *active*.

In this dissertation, we present mathematical models for two biophysical phenomena: facilitated diffusion and the Brownian ratchet. In both cases, counterintuitive behavior is observed. In the case of facilitated diffusion, transport of a fast-moving ligand is enhanced through reversible binding with a slow-moving protein molecule, and in the case of the Brownian ratchet,

a fluctuating barrier under an external force can undergo directed motion against that force as the result of an interaction with a polymer or polymer bundle. While these phenomena have already been fertile grounds for mathematical modeling, we have approached them from a different angle in order to obtain new insights. In the case of facilitated diffusion, our approach is to study a system of coupled ordinary differential equations rather than using the typical partial differential equation model. By doing so, we gain insight into the source of the facilitation effect. For the Brownian ratchet, we use a continuous diffusion formalism approach rather than a spatially discrete model. This method allows us to naturally extend the basic model to make predictions about more complicated systems. The common mathematical modeling theme across both topics is to build upon simple models from which we can obtain analytical results that can be compared with experimental results.

This dissertation is split into two parts. In each part, we have included a chapter introducing the motivating biophysical phenomenon, as well as previous mathematical models in order to put our work in context. Next, the basic models and results are introduced, followed by extensions to the simple models. In the case of facilitated diffusion, we compare several of our analytical results with sets of experimental data from the literature. In the case of the Brownian ratchet, we present our analytical results as predictions that can be compared with experimental results in the future. In Appendices A, C, and D, we include mathematical details that would interrupt the flow of the exposition. In Appendix B, we detail simulation techniques for both models. Below, we outline in more detail what can be found in each chapter.

1.1 Part I: Facilitated Diffusion

In Chapter 2, we introduce the concept of facilitated diffusion in the context of our motivating system: oxygen transport mediated by hemoglobin or myoglobin. We also discuss existing mathematical models, and the experimental results with which we will compare our analytical results. Chapter 3 mainly consists of work that we have published in Ref. [7]. In this chapter, a simple chemical kinetic model is developed which describes the behavior of small ligands that can bind reversibly with large carrier molecules with slower intrinsic rates of transport. Under certain conditions, which we describe, the presence of the slower carriers in fact enhances the transport of the ligand. This is the chemical version of Wyman-Murray's facilitated diffusion,

meaning that our model assumes that the transport is between spatially discrete compartments, rather than spatially continuous transport, or diffusion, as in the work of Wyman and Murray. The simple model illuminates the *driven* nature of the enhancement of the transport by the carrier molecules: we show that the facilitated transport depends crucially on a "grand canonical" setting in which the free ligand concentrations are kept constant in the presence of the facilitating protein, in contrast to a canonical setting with constant *total* ligand concentrations. Results from the simple model are compared to previous experimental and theoretical results for Wyman-Murray facilitated diffusion of oxygen and carbon monoxide in muscle. A relation is established between the association-dissociation rates and the down-stream ligand concentration, or back pressure, required for the facilitation effect to occur. Sections 3.6 and 3.7 contain previously unpublished material, consisting of a discussion of the single ligand model from the point of view of an energy-driven phenomenon, and the connection between facilitated diffusion and partially reflected Brownian motion which could be pursued in future work, respectively.

In Chapter 4, we extend our model to the case of N diffusing ligands, specifically investigating the solution to the 2-ligand model with special attention to the scenario of oxygen and carbon monoxide as competing ligands. This particular case is pertinent to carbon monoxide poisoning in the human body.

1.2 Part II: Brownian Ratchet

In Chapter 5, we introduce molecular motors, including polymerization against a force, and review the existing mathematical models used to describe them. We conclude this chapter with a novel extension of the standard coupled states diffusion model that illuminates the uncertainty in how a molecular motor operates in the absence of a measurement force. Next, in Chapter 6, we introduce the continuous diffusion formalism for our Brownian ratchet model. Finally, in Chapter 7, we present extensions to the basic model which we have published in Ref. [8] which were motivated by actin polymerization driven stochastic movement of the bacteria *Listeria monocytogenes*. Experimental results suggested a dynamic association between the growing actin filaments and the propelled bacteria. Based on the continuous diffusion formalism for the Brownian ratchet (BR), we introduce such an attractive interaction into the one-dimensional BR model and show that its effect is equivalent to an external resistant force on the bacterium.

Such a force significantly reduces the Brownian motion of a driven bacterium, and accentuates the stepping due to polymerization. We then consider the growth, with and without a barrier, of a filamentous bundle consisting of N identical filaments. It is shown that the bundle grows with a similar rate as a single filament in the absence of a load, but can oppose N times the external force under the stalling condition. A set of relationships describing the velocity of the bacterium movement (V_z) and its apparent diffusivity (D_z) as functions of the resistant force (F) and the number of filaments in a bundle (N) are obtained. The theoretical study suggests methods for data analysis in future experiments with applied external resistant force.

1.3 Appendices

In Appendix A, we summarize the King-Altman-Hill (KAH) method and show in detail how it can be applied to the single ligand model for facilitated transport from Chapter 3, then present the results from the KAH method for the two ligand model from Chapter 4. Appendix B contains simulation algorithms both for the partially reflected Brownian motion system mentioned in Chapter 3 and for the polymer-barrier systems of Chapters 6 and 7. In Appendix C, we show how the time dependent gap distribution from in Chapter 6 can be obtained using the "New Method" of Fokas. Finally, in Appendix D, we include a brief discussion of the center of friction of two random walkers.

Part I

MATHEMATICAL MODELS FOR FACILITATED DIFFUSION

Chapter 2

INTRODUCTION TO FACILITATED DIFFUSION

In this chapter, we give an overview of the rich history of Wyman-Murray facilitated diffusion, including important experimental results in Section 2.1 as well as mathematical models in 2.2. The interested reader should note that Wittenberg provides an excellent history of the experimental methods and mathematical models used to study facilitated diffusion up to 1970 in Ref. [87]. Here, we will merely highlight the results that we will later draw upon for comparison with our model.

We begin with a brief description of our motivating biophysical system. The role of hemoglobin in enhancing oxygen transport was postulated as early as 1932 by Roughton [70]. Experiments were designed and executed to measure the facilitation of oxygen transport through cells due to the presence of hemoglobin and myoglobin during the 1960's and early 1970's by Wittenberg, Hemmingsen, and Scholander, to name a few [86, 87, 26, 73]. Mathematical models based on reaction-diffusion equations were proposed, and approximate solutions were studied analytically by Murray, Wyman, Rubinow & Dembo, and numerically by Kreuzer & Hoofd [49, 88, 72, 37]. The theory behind this type of facilitated diffusion suggests that under certain conditions the flux of a small ligand, such as oxygen, diffusing in an aqueous solution can be enhanced by the presence of a large protein, such as hemoglobin, to which the ligand binds reversibly and rapidly. However, since the diffusion coefficient of the protein-ligand complex is orders of magnitude smaller than that of the free ligand, the phenomenon described above seems counterintuitive. To illustrate the counterintuitive nature of the problem, Wyman [88] asked "How could a fly hope to increase his rate of progress by alighting on the back of a tortoise?" It turns out, conceptually, that if a large gradient in the free ligand concentration is maintained, then the resulting phenomenological Fick's flux of the *total* ligand is significantly greater when the carrier molecule is present in the system, even when the carrier molecule moves very slowly. This theory is now one of the established mechanisms by which oxygen and

carbon monoxide are transported in muscle respiration, with the role of the facilitating carrier protein being played by hemoglobin and/or myoglobin [52, 50, 21], and has also inspired the model for the phosphocreatine shuttle [44].

2.1 Experimental Results

Although the rich history of experiments designed to investigate the role of hemoglobin and myoglobin in oxygen transport began as early as 1932, we will compare our model with data from experiments done by Mochizuki and Forster in 1962, and Wittenberg in 1966, found in Refs. [46] and [86] respectively. We will begin by describing Wittenberg's experiments since it is his work that motivated our modeling efforts.

2.1.1 Wittenberg, 1966

The seminal results of Wittenberg were published in 1966 in an article titled "The molecular mechanism of hemoglobin-facilitated oxygen diffusion," [86]. In this article, Wittenberg demonstrated experimentally what Wyman and others already believed: that the facilitation of the oxygen flux was due to random transport of oxygen bound hemoglobin. Wittenberg presented figures showing data for several different carrier molecules that either did or did not enhance the transport of oxygen. Wittenberg also presented data for systems with carbon monoxide as the diffusing ligand, as well as data for oxygen and carbon monoxide present in the same system with myoglobin as the carrier molecule. In particular, we will compare our model with the data from Figures 1, 5, 9, and 10 of Ref. [86], which have been reproduced in Figures 2.1-2.4. Since we will make use of several of Wittenberg's data sets, it is important to describe the conditions under which he performed his experiments.

Wittenberg's experiments utilized a water-tight diffusion chamber which was submerged in a bath of water that was held at $20.3 \pm 0.5^{\circ}\ C$. The chamber consisted of two compartments separated by a milipore filter which had been soaked in a solution of carrier molecules. The milipore filters had an exposed area of 11.5 cm^2, and were typically $150 \pm 10\ \mu m$ thick, with the exception of some specially prepared filters that were used to determine that the facilitated flux is inversely proportional to the diffusion path length. The pore size was $0.45 \pm 0.02\ \mu m$ and the porosity was 79%, indicating that the volume filled with fluid is 79% of the total volume of

the filter. Both compartments of the chamber were held at a total pressure of 1 atm during the experiments. Gases that had been equilibrated with the bath temperature were streamed into each chamber. The left chamber, whose volume was not specified, had gas mixtures of varying proportions of oxygen, carbon monoxide, and nitrogen streamed in at a rate of $40mL/min$ that were vented to atmosphere in order to maintain a particular partial pressure of oxygen at the left end of the milipore filter, corresponding to the "up-stream" end of the system. The right chamber, whose volume was 30 mL, had a wet helium stream at a rate of $60mL/min$ directed at the right end surface of the milipore filter to ensure "rapid dilution of the diffusing gases" in order to maintain an oxygen partial pressure of zero at the right hand side of the milipore filter, or "down-stream" end of the system. The stream exiting the right chamber passed through drierite to dry it out before passing through a sampling valve, where 10 mL portions of the outflowing gas could be sent to a gas chromatograph for analysis. Note for future reference that Wittenberg's ligand fluxes were reported in $\mu L/min$ at pressure 760 $mm\ Hg$ and temperature $0^\circ\ C$. Oxygen, nitrogen, and carbon monoxide partial pressures were reported in $mm\ Hg$. Hemoglobin and myoglobin concentrations were reported in $milimole/L\ (heme)$.[1]

We now briefly describe the four main results for the oxygen-hemoglobin and carbon monoxide-hemoglobin and -myoglobin systems that we would like to compare with our theory. Note that each result will be discussed in more detail in the following chapters. Wittenberg's first result of interest, reproduced in Figure 2.1, shows the oxygen flux as a function of oxygen partial pressure at the up-stream end of the system. Wittenberg demonstrated that the total oxygen flux in the presence of hemoglobin (closed circles) was greater than that in the absence of hemoglobin (open circles), approximately by a constant value for the range of partial pressures shown. Next, we will compare our theoretical results with Wittenberg's results shown in Figure 2.2 concerning the relationship between the facilitated oxygen flux and the hemoglobin concentration. In this figure, we see that the facilitation effect reaches a peak near 6 $milimoles/L\ (heme)$ and is approximately the same for both hemoglobin (closed circles) and myoglobin (open circles). Wittenberg's next result of interest was that neither hemoglobin or myoglobin facilitated the

[1]The distinction here is that while hemoglobin has four "heme groups," or binding sites for the ligands, myoglobin only has one heme group, or binding site. Wittenberg's method of reporting the concentrations as $milimole/L\ (heme)$ allows a direct comparison between the two different carriers despite the different number of heme groups.

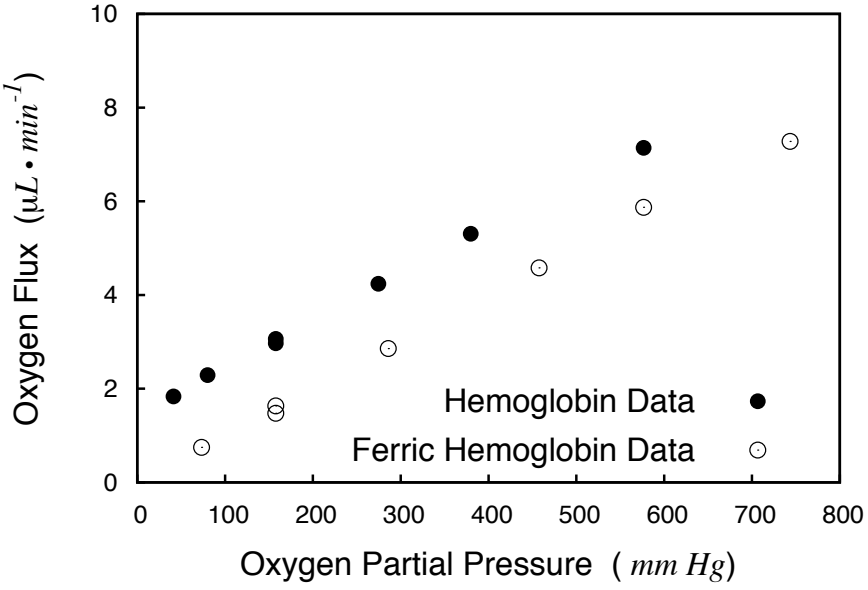

Figure 2.1: **Wittenberg's Figure 1**.
For comparison with our theory, recreated from the data found in Ref. [86].

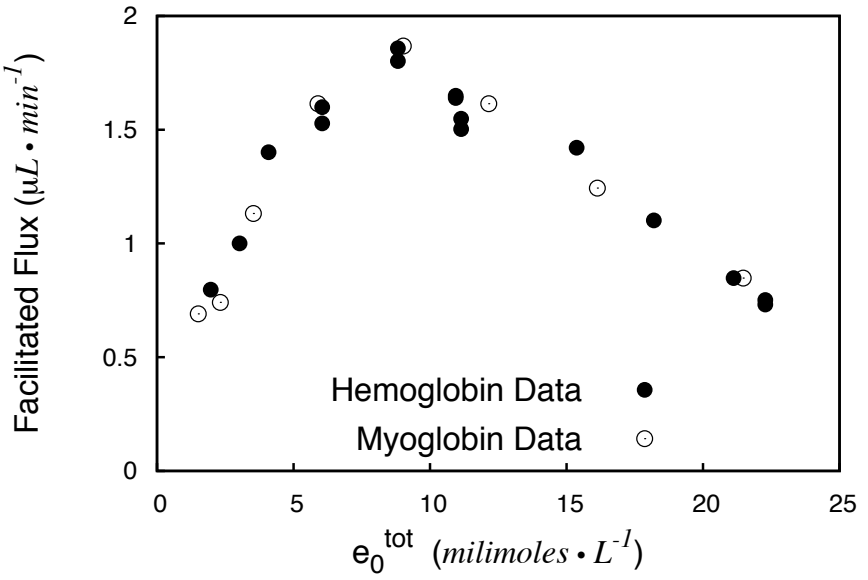

Figure 2.2: **Wittenberg's Figure 5**.
For comparison with our theory, recreated from the data found in Ref. [86].

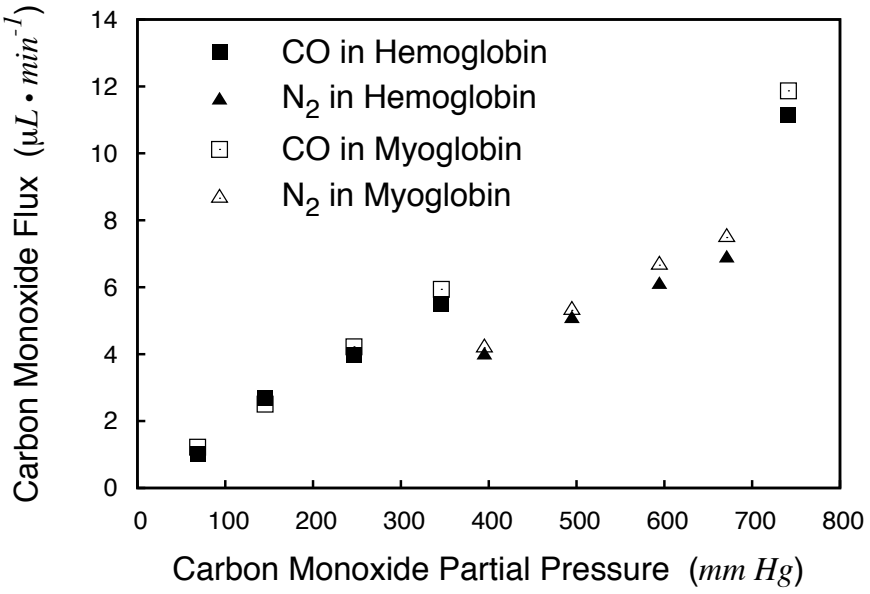

Figure 2.3: **Wittenberg's Figure 9**.
For comparison with our theory, recreated from the data found in Ref. [86].

flux of carbon monoxide, which is shown in Figure 2.3. This is especially interesting because it is in direct conflict with the results found by Mochizuki and Forster that are described in the next section. Finally, in Chapter 4, we will compare the results from our 2-ligand model with Wittenberg's data on the simultaneous diffusion of oxygen and carbon monoxide through a solution of myoglobin, shown in Figure 2.4. In this figure, we see that adding a small quantity of carbon monoxide decreases the facilitation effect of myoglobin on oxygen transport.

2.1.2 Mochizuki & Forster, 1962

In 1962, prior to Wittenberg's experiments, Mochizuki and Forster (MF) published the results of experiments that they performed studying the effect of hemoglobin on a mixture of carbon monoxide and oxygen as the diffusing ligands in a short article in *Science*: Ref. [46]. Their main result was that not only was carbon monoxide transport enhanced by the presence of hemoglobin, but that the carbon monoxide flux was in fact further enhanced by presence of gradient-free oxygen at both ends of the system. Their results were summarized in Figure 2 of

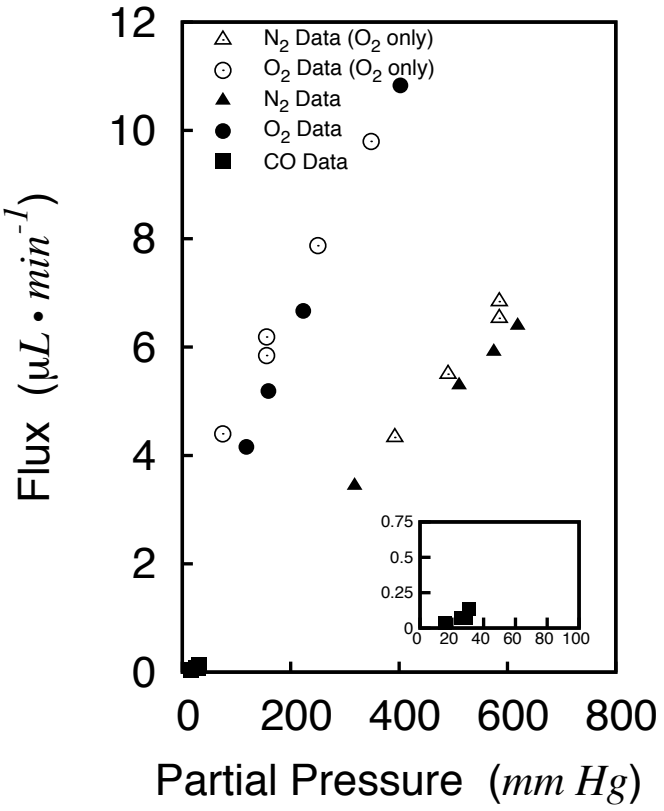

Figure 2.4: **Wittenberg's Figure 10**.
For comparison with our theory, recreated from the data found in Ref. [86].

Ref. [46], which we have reproduced in Figure 2.5.

The experimental setup of MF was very similar to that of Wittenberg, however, there were some major differences in their experimental methods. First, although MF reported that the carbon monoxide fluxes they measured were in a steady state, they also reported that the down-stream concentration of carbon monoxide increased over the course of the experiment, suggesting that a true steady state may not have been achieved. Furthermore, MF study a lower range of partial pressures, or concentrations, of carbon monoxide than Wittenberg.[2] MF also use a different system of units for reporting their results. Note that their ligand partial pressures were reported in units of $\%\ atm$ and their fluxes were reported in units of mm^3/min.

In Chapters 3 and 4, we will show that both MF and Wittenberg's results can be explained using our mathematical model, and that there is in fact no contradiction between their seemingly conflicting reports on the facilitation, or lack thereof, of carbon monoxide by hemoglobin.

2.2 Mathematical Models

The mathematical models describing facilitated diffusion primarily fall under the category of steady-state reaction-diffusion partial differential equation models where the ligands, carrier molecules, and ligand-carrier complexes diffuse according to Fick's law, and the reactions refer to the association and dissociation of the ligand-carrier complexes. In 1965-6, several authors independently published reaction-diffusion models for facilitated diffusion [89, 40, 88], however, it is mainly the work of Wyman and the subsequent work of Murray, that we will focus on in this section. We will also describe contributions from Kreuzer & Hoofd, as well as Rubinow and his co-authors. Finally, we will discuss the similarities and differences between our work, and work done in the 1980's by Ebel, which we only discovered after doing most of our analysis.

2.2.1 Wyman, Murray, et. al., 1966-1977

In his 1966 article, titled "Facilitated diffusion and the possible role of myoglobin as a transport mechanism," Wyman put forth a model for facilitated diffusion in terms of translational diffusion

[2] For the data shown in Figure 2 of Ref. [46], the maximum carbon monoxide partial pressure is less than 2 $\%\ atm = 15.2\ mm\ Hg$, compared to a maximum value of approximately 750 $mm\ Hg$ from Figure 9 or approximately 20 $mm\ Hg$ in Figure 10 of Ref. [86]. (See Section 4.2.1 for a more detailed discussion of Wittenberg's Figure 10.)

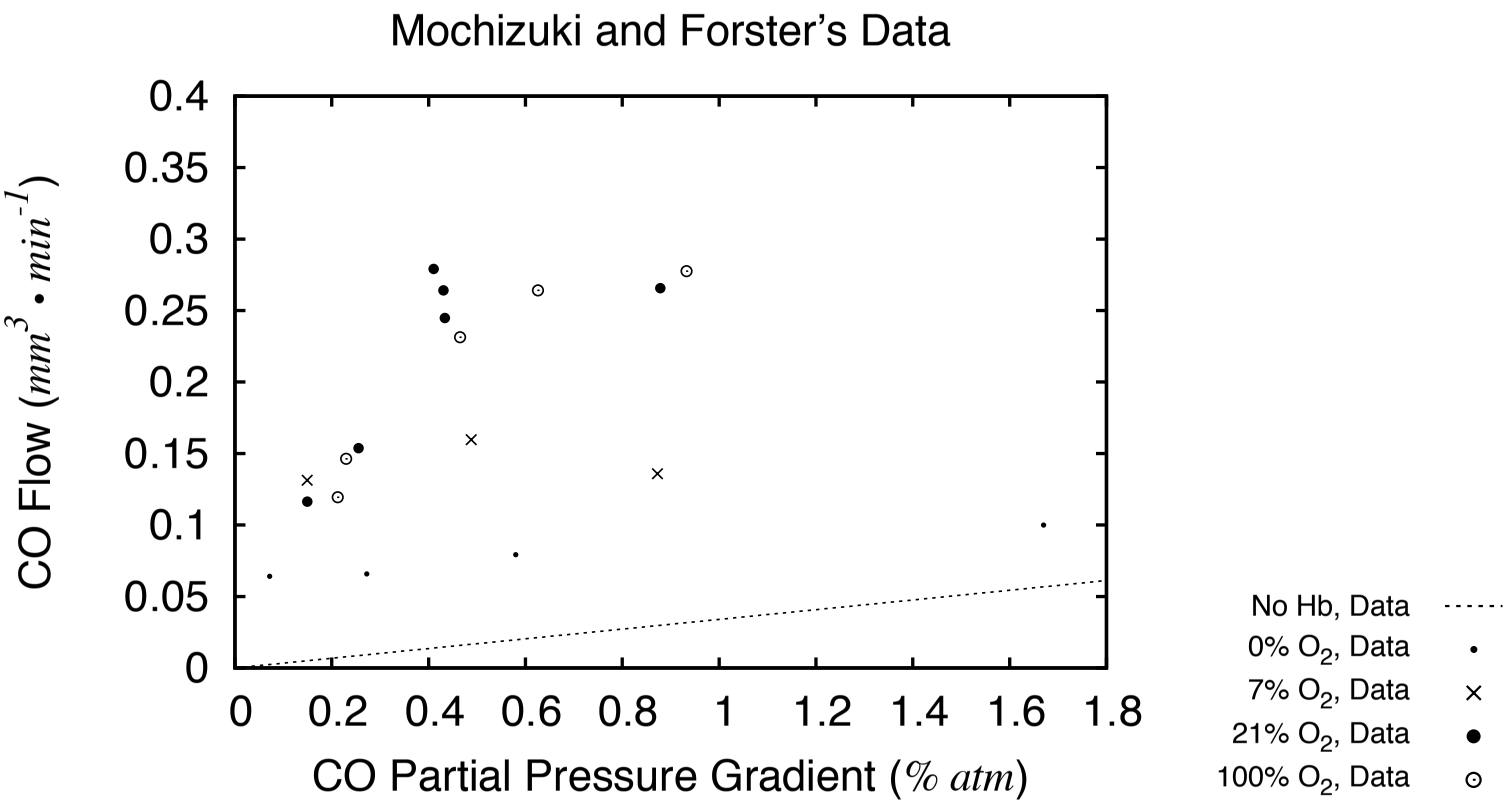

Figure 2.5: **Mochizuki & Forster's Experimental Results.**
For comparison with our theoretical results, recreated from data found in Figure 2 of Ref. [46].

of the carrier molecule [88], which he notes is essentially equivalent to models put forth by other researchers, but the key difference is that his model does not assume that the ligand and carrier molecule are in equilibrium throughout the solution. Wyman's model is as follows. Consider a system in which oxygen and carrier molecules are present and diffuse in the x direction. Let $c(x,t)$ represent the concentration of free oxygen, c_p represent the (constant) concentration of the carrier molecule, m represent the number of sites on the carrier that can bind oxygen, and $Y(x,t)$ represent the fractional saturation of the carrier molecule with the ligand. Then the quantity $mc_pY(x,t)$ is the concentration of the bound oxygen in the system. Oxygen and the carrier molecule also combine reversibly according to the reaction

$$O_2 + Hb \xrightarrow{\rho} HbO_2, \tag{2.1}$$

where ρ represents the rate of the reaction, and will be defined later. Note that Wyman writes (2.1) using hemoglobin as the carrier, and oxygen as the ligand, but any choice of ligand and carrier that combine reversibly could be used. The change in concentration of the bound and free oxygen at any point x at time t, respectively, is due to translational diffusion and the chemical reaction from (2.1):

$$\frac{\partial(mc_pY(x,t))}{\partial t} = D_p\frac{\partial^2(mc_pY(x,t))}{\partial x^2} + \rho, \tag{2.2}$$

$$\frac{\partial c(x,t)}{\partial t} = D_c\frac{\partial^2 c(x,t)}{\partial x^2} - \rho, \tag{2.3}$$

where D_p, D_p are the diffusion coefficients of bound and free oxygen, respectively. We know that in the steady state,

$$\frac{\partial(mc_pY(x))}{\partial t} = \frac{\partial c(x)}{\partial t} = 0, \tag{2.4}$$

so we can sum (2.2) and (2.3) to obtain

$$\frac{d}{dx}\left(D_p\frac{d(mc_pY(x))}{dx} + D_c\frac{dc(x)}{dx}\right) = 0. \tag{2.5}$$

Upon integration, Wyman obtains

$$D_p\frac{d(mc_pY(x))}{dx} + D_c\frac{dc(x)}{dx} = -F, \tag{2.6}$$

where the constant F is the total flux of free and bound oxygen in the system. Next, Wyman goes on to define ρ, the chemical reaction term, as

$$\rho = k'mc_p\left(1-Y\right)c - kmc_pY, \tag{2.7}$$

where k' is the association rate and k is the dissociation rate for the oxygen-hemoglobin complex. By integrating (2.6) once more, and rearranging terms, we obtain

$$D_p m c_p Y(x) = -Fx - D_c c(x) + B, \tag{2.8}$$

where B is an integration constant. Then, combining (2.3), (2.4), (2.7), and (2.8), Wyman obtains a second order nonlinear, non-homogeneous ODE for the steady state concentration of the free oxygen which can be written as:

$$D_c \frac{d^2c}{dx^2} = \rho = k' m c_p c(x) + \left(\frac{k'c(x)+k}{D_p}\right)\left(D_c c(x) + Fx - B\right), \tag{2.9a}$$

$$\frac{d^2c}{dx^2} = \alpha + \beta c(x) + \gamma x + \delta x c(x) + \epsilon \left(c(x)\right)^2, \tag{2.9b}$$

where α, β, γ, δ, ϵ are simply constants in terms of the parameters seen in (2.9a) which we will not refer to later, rather they are used in (2.9b) to emphasize the form of the differential equation.[3] Wyman does not go on to solve (2.9) analytically, rather he performs some calculations which show that in the case of oxygen in the presence of hemoglobin or myoglobin, the facilitated diffusion is mainly due to translational diffusion of the carrier molecules. Wyman also rules out rotational diffusion of the carrier molecules as a significant contribution to the facilitation effect. He then goes on to mention that a numerical solution to (2.9) could be obtained using experimental values for the physical parameters mentioned. In Ref. [37], Kreuzer and Hoofd obtain such a numerical solution, which we will briefly discuss in Section 2.2.2.

In his 1971 paper titled, "On the molecular mechanism of facilitated oxygen diffusion by haemoglobin and myoglobin," Murray builds upon the foundation of Wyman's model by adding appropriate boundary conditions, and solving the second order nonlinear, non-homogeneous ODE using singular perturbation methods [49]. In particular, Murray studies a one-dimensional system, along which the ligand, carrier, and ligand-carrier complexes diffuse in the x direction, with boundaries at $x = 0$ and $x = \ell$. This leads to boundary conditions

$$c(0) = c_0, \qquad Y(0) = Y_0, \qquad c(\ell) = c_\ell, \qquad Y(\ell) = Y_\ell. \tag{2.10}$$

---

[3] Note that in Ref. [88], (2.9a) appears as

$$D_c \frac{d^2c}{dx^2} = \rho = k' m c_p c(x) - \left(\frac{k'c(x)+k}{D_p}\right)\left(D_c c(x) + Fx - B\right),$$

which is easily seen to be a typo or sign error upon combining (2.7) with (2.8).

Murray applies the conditions shown in (2.10) to Wyman's (2.8) to obtain an expression for the total oxygen flux, F:

$$F = \frac{1}{\ell}\left(D_c\left(c_0 - c_\ell\right) + D_p m c_p\left(Y_0 - Y_\ell\right)\right), \tag{2.11}$$

immediately showing that the oxygen flux is inversely proportional to the diffusion path length, which was one of Wittenberg's experimental results. Murray further states that Y_0 and Y_ℓ cannot be directly assigned values, but can be found as functions of c_0 and c_ℓ, which is where the difficulties in this model lie. Murray derives the analogous equation to Wyman's (2.9) by solving for $Y(x)$ in (2.11) using the chemical reaction rate ρ, as Wyman did. In terms of Murray's boundary conditions, and the expression for F given in (2.11),

$$Y(x) = Y_0 + \frac{1}{mc_pD_p}\left(\frac{x}{\ell}\left(D_c(c_\ell - c_0) + mc_pD_p(Y_\ell - Y_0)\right) - D_c(c - c_0)\right). \tag{2.12}$$

Murray's version of the second order nonlinear, non-homogeneous ODE shown in (2.9) is in turn given by

$$\begin{aligned} D_c\frac{d^2c}{dx^2} = &-\left(D_cc_0 + Y_0mc_pD_p\right)\frac{k}{D_p} + \left(\frac{kD_c}{D_p} - k'mc_p\left(Y_0 - 1 + \frac{D_cc_0}{D_pmc_p}\right)\right)c(x) \\ &+ \frac{k}{D_p}\left(D_c(c_0 - c_\ell) + D_pmc_p(Y_0 - Y_\ell)\right)\frac{x}{l} \\ &+ \frac{k'}{D_p}\left(D_c(c_0 - c_\ell) + D_pmc_p(Y_0 - Y_\ell)\right)\frac{x}{l}c(x) + \frac{k'D_c}{D_p}\left(c(x)\right)^2, \end{aligned} \tag{2.13a}$$

$$\frac{d^2c_1}{dx_1^2} = (\alpha + \gamma x_1) + (\beta + \delta x_1)c_1(x_1) + \lambda\left(c_1(x_1)\right)^2, \tag{2.13b}$$

where (2.13b) is the dimensionless form of (2.13a).[4] Much of Murray's analysis is devoted to a singular perturbation method for defining Y_0 and Y_ℓ in terms of the other parameters in the system. After finding expressions for Y_0 and Y_ℓ that hold under the condition that rapid changes in the concentration are unlikely to take place anywhere in the system, i.e. chemical equilibrium, which is motivated by the singular perturbation method and the values of the physical parameters for oxygen, hemoglobin, and myoglobin, Murray finds the following

[4]The non-dimensionalization was done by defining dimensionless variables $c_1 = c/c_0$ and $x_1 = x/\ell$, and multiplying both sides of (2.13a) by the factor $\ell^2/(c_0D_c)$. The terms $\alpha, \gamma, \beta, \delta, \lambda$ are constants that can be expressed in terms of the system parameters by carrying out the non-dimensionalization algebra.

expressions for the oxygen flux in the system:

$$F = F_d + F_f, \tag{2.14a}$$

$$F_d = \frac{D_c}{\ell}\left(c_0 - c_\ell\right), \tag{2.14b}$$

$$F_f = \frac{m c_p D_p k k' \left(c_0 - c_\ell\right)}{\ell\left(k' c_0 + k\right)\left(k' c_\ell + k\right)}, \tag{2.14c}$$

where k' and k are the association and dissociation rate constants for the oxygen-hemoglobin reaction. It is this set of equations, which appear in (24) of Ref. [49], that we will use to compare with the theoretical results of our model in Chapter 3. Note that Murray also states that c_ℓ cannot be prescribed precisely either, so he goes on to define the following expression for c_ℓ in terms of the other parameters in the system:

$$c_\ell = \frac{k c_0 (1 - s)}{c_0 s k' + k(1 + s)}, \tag{2.15}$$

where s represents the gradient in the saturation of the carrier molecule, determined experimentally by Wittenberg to be $s = 0.85$ for hemoglobin and $s = 0.45$ for myoglobin with oxygen as the ligand [49].

We have reproduced Murray's theoretical results for the oxygen flux through hemoglobin and myoglobin as a function of oxygen partial pressure at $x = 0$ which are shown in Figures 2.6 and 2.7. Note that the results from Murray's model have units $mol/(cm^2\ s)$ and mol/cm^3 for the fluxes and concentrations, respectively. In order to compare his results with Wittenberg's experimental data, Murray uses the following conversion factors, with no explanation of how they were derived or calculated:

$$100\ mm\ Hg\ pO_2 = 1.56 \times 10^{-7}\ \frac{mol}{cm^3}\ O_2, \tag{2.16}$$

$$1\ \text{Wittenberg Unit} = 0.85 \times 10^{-10}\ \frac{mol}{cm^2\ s}. \tag{2.17}$$

Fortunately, other researchers are more explicit in how their conversions were carried out, as we will soon see.

In a subsequent paper, titled "Facilitated diffusion: the case of carbon monoxide," Murray and Wyman apply the model to the special case of carbon monoxide, and explain why carbon monoxide is not facilitation by hemoglobin or myoglobin [52]. Their argument is as follows. For

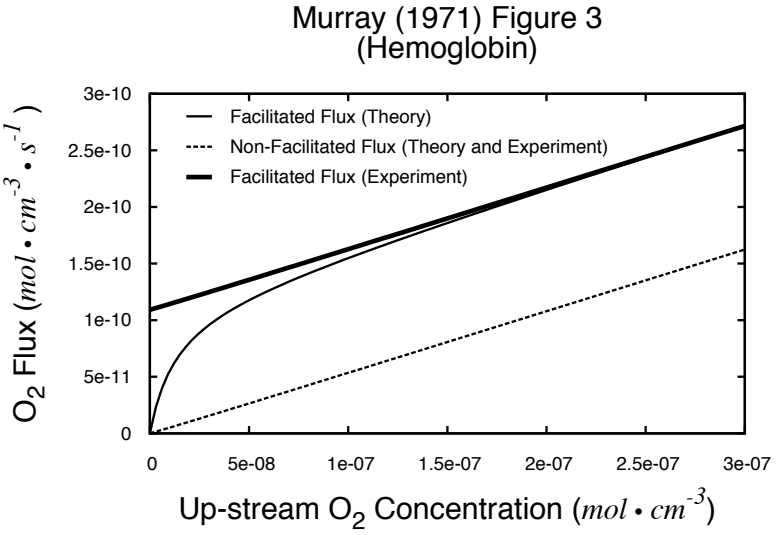

Figure 2.6: **Murray's Figure 3.**
Results for oxygen flux *vs* oxygen concentration at $x = 0$ in the presence of hemoglobin, after [49]. Plotted using (2.14) and (2.15) with the parameter values shown in Table 2.1.

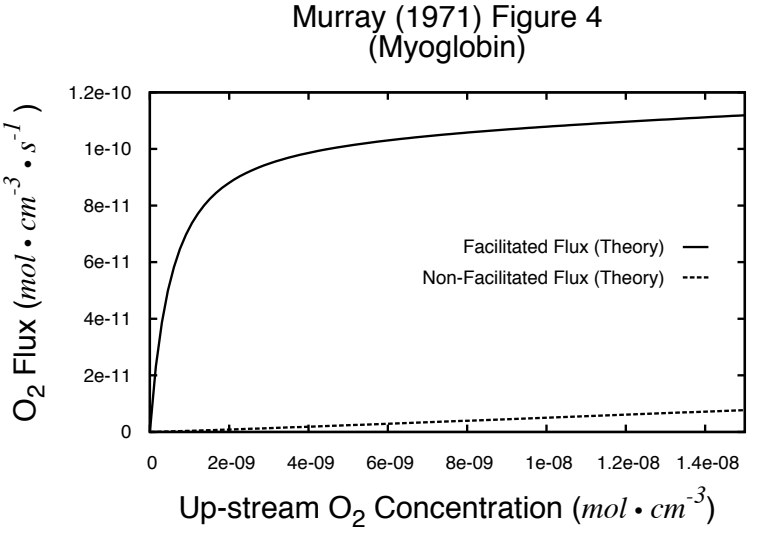

Figure 2.7: **Murray's Figure 4.**
Results for oxygen flux *vs* oxygen concentration at $x = 0$ in the presence of myoglobin, after [49]. Plotted using (2.14) and (2.15) with the parameter values shown in Table 2.1.

Table 2.1: **Murray's Parameter Values from Table 1 of [49] and Table 1 of [52].**

Parameter	Hemoglobin	Myoglobin
mc_p	$1.2 \times 10^{-5}\ mol \cdot cm^{-3}$	
D_p	$2.45 \times 10^{-7}\ cm^2 \cdot s^{-1}$	$4.35 \times 10^{-7}\ cm^2 \cdot s^{-1}$
m	4	1
ℓ	$2.2 \times 10^{-2}\ cm$	
Oxygen Values		
D_c	$1.2 \times 10^{-5}\ cm^2 \cdot s^{-1}$	
k	$40\ s^{-1}$	$11\ s^{-1}$
k'	$2.85 \times 10^{9}\ cm^3 \cdot mol^{-1} \cdot s^{-1}$	$14 \times 10^{9}\ cm^3 \cdot mol^{-1} \cdot s^{-1}$
Carbon Monoxide Values		
D_c	$9 \times 10^{-4}\ cm^2 \cdot s^{-1}$	
k	$8 \times 10^{-3}\ s^{-1}$	$1.7 \times 10^{-2}\ s^{-1}$
k'	$2 \times 10^{8}\ cm^3 \cdot mol^{-1} \cdot s^{-1}$	$5 \times 10^{8}\ cm^3 \cdot mol^{-1} \cdot s^{-1}$

oxygen in a solution of either hemoglobin or myoglobin, each of the constants in (2.13b) are of the same order. However, for carbon monoxide, α and γ are less than β, δ and λ by a factor $O(10^3)$, primarily due to the relatively smaller dissociation constant k. This leads to a singular perturbation problem of a different character, leading Murray and Wyman to conclude that for the case of carbon monoxide, $Y_0 = Y_\ell = 1$, i.e. the carrier molecule is completely saturated by the ligand throughout the system, so that the total flux of carbon monoxide is due to simple diffusion alone. Wyman and Murray conclude that for a system in which the carrier molecule is completely saturated, facilitation cannot occur. This conclusion seems to conflict with MF's experimental results that were mentioned in the previous section. We will discuss this issue further in Section 3.4.3.

In the next section, we will briefly discuss the theoretical results of Kreuzer and Hoofd [37], who use the same one-dimensional diffusion model to study facilitated diffusion, but use different boundary conditions. In 1973, Mitchell and Murray published a paper titled "Facilitated diffusion: the problem of boundary conditions," in which they prove that the two different methods produce the same results up to the first order solutions, which they claim is sufficient for the experimental measurement techniques for most biological situations [45].

A few years later, in 1977, Britton and Murray published an article titled "The effect of carbon monoxide on haem-facilitated oxygen diffusion," in which they extended their basic model to a situation including two ligands that can bind reversibly with the carrier molecule [5]. They were primarily concerned with the steady state scenario where oxygen is facilitated by hemoglobin in the presence of a small amount of carbon monoxide, a situation which is analogous to Wittenberg's Figure 10. They were interested in this scenario because they wanted to use this model as a starting point for a study of carbon monoxide poisoning in man, which was subsequently published by Britton in Ref. [4]. Since we will compare our model with their results in Chapter 4, we will summarize their model and results here. Let c_1, c_2, c_3 represent the concentrations of free oxygen, free carbon monoxide and unbound hemoglobin, respectively, and let c_4, c_5 represent the concentrations of oxygen-bound and carbon-monoxide-bound hemoglobin, respectively. The association-dissociation reactions between the ligands and hemoglobin

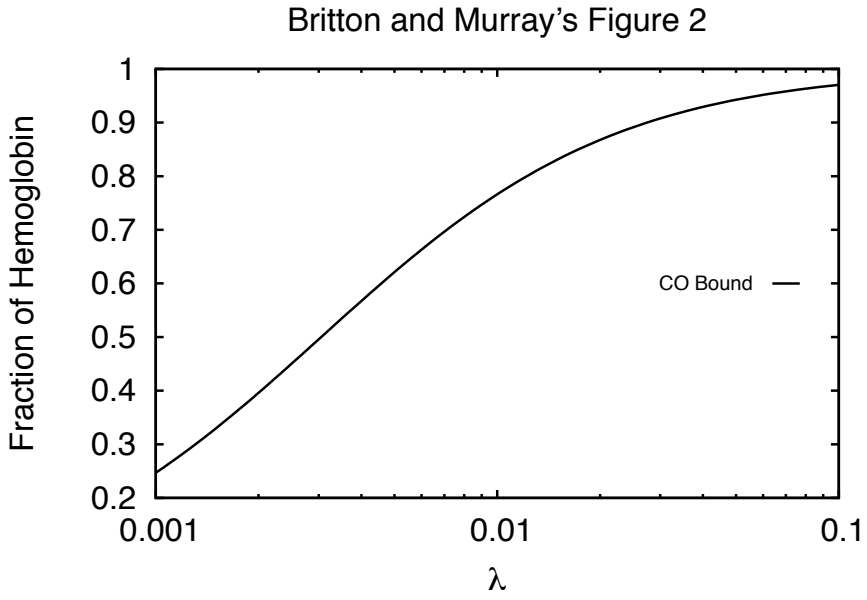

Figure 2.8: **Britton & Murray's Figure 2.**
Plotted using (2.25) and (2.26) with parameter values from Table 4.1, after Ref. [5].

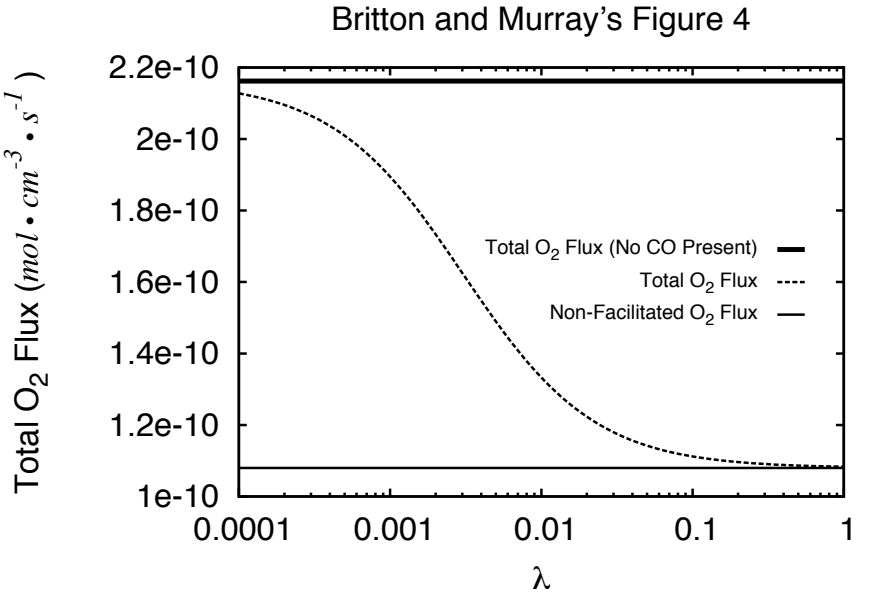

Figure 2.9: **Britton & Murray's Figure 4.**
Plotted using (2.25) and (2.26) with parameter values from Table 4.1, after Ref. [5].

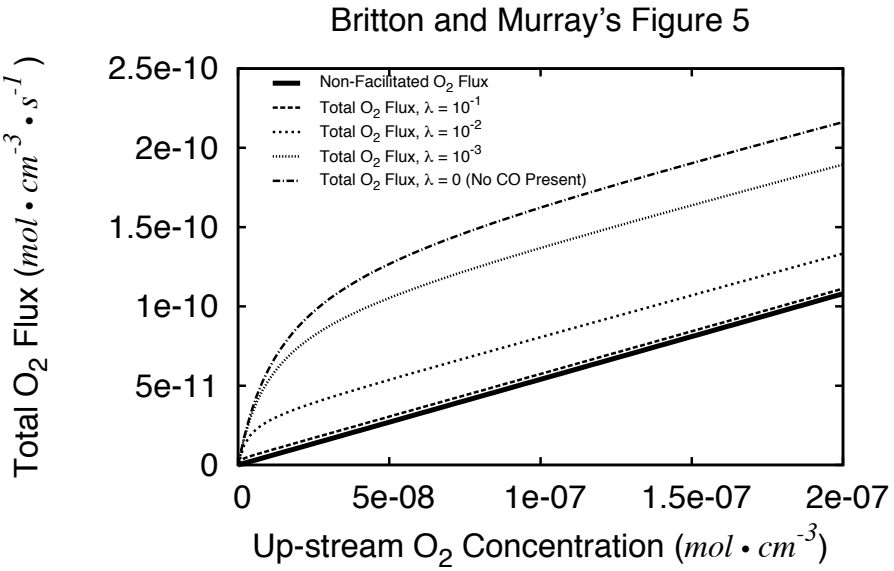

Figure 2.10: **Britton & Murray's Figure 5.**
Plotted using (2.25) and (2.26) with parameter values from Table 4.1, after Ref. [5].

are given by

$$Hb + O_2 \underset{k_{-1}}{\overset{k_1}{\rightleftharpoons}} HbO_2, \qquad Hb + CO \underset{k_{-2}}{\overset{k_2}{\rightleftharpoons}} HbCO. \tag{2.18}$$

Then the concentrations of the ligands, carriers, and complexes change according to

$$\frac{\partial c_i}{\partial t} = -\rho_i + D_i \frac{\partial^2 c_i}{\partial x^2}, \qquad i = 1, 2, \ldots, 5, \tag{2.19}$$

where the D_i are the diffusion coefficients for the species, and the ρ_i are given by

$$\rho_1 = k_1 c_1 c_3 - k_{-1} c_4, \quad \rho_2 = k_2 c_2 c_3 - k_{-2} c_5, \quad \rho_3 = \rho_1 + \rho_2, \quad \rho_4 = -\rho_1, \quad \rho_5 = -\rho_2, \tag{2.20}$$

and are due to the law of mass action and (2.18). Note that Britton and Murray assume that the free and bound carrier molecules diffuse at the same rate, i.e. $D_3 = D_4 = D_5 = D$. Britton and Murray solve the equations in (2.19) subject to the boundary conditions that the free ligand concentrations are fixed at $x = 0$ an $x = \ell$ and that since the carrier molecules cannot leave the system, their derivatives vanish at $x = 0$ and $x = \ell$:

$$\frac{dc_3}{dx} = \frac{dc_4}{dx} = \frac{dc_5}{dx}, \qquad \text{for } x = 0, \quad x = \ell. \tag{2.21}$$

Then they state that due to the results of [45], they can use the boundary conditions

$$c_i = c_i(0) \quad \text{at } x = 0, \qquad c_i = c_i(\ell) \quad \text{at } x = \ell, \tag{2.22}$$

instead, and determine the values for $c_i(0), c_i(\ell)$ for $i = 3, 4, 5$ later, as Murray did in his previous work. They do however use (2.21) along with (2.19) and (2.20) to show that the total carrier concentration is conserved:

$$c_3 + c_4 + c_5 = c_t. \tag{2.23}$$

Britton and Murry define $\gamma_1 = c_1(0)$ and $\gamma_2 = c_2(0) = \lambda\gamma_1$, where λ represents the ratio of carbon monoxide to oxygen at the up-stream end of the system, and state that they know from Wittenberg's experiments that $c_1(\ell) \approx c_1(0) \times 10^{-2}$.[5] They follow a similar non-dimensionalization and singular perturbation procedure to that used previously in Refs. [49, 52, 45] and conclude from their analysis that the concentration of the carbon-monoxide-bound hemoglobin, c_5 is constant, as in Wyman and Murray's previous work on carbon monoxide. Thus, in essence, they fix the quantities $c_1(0), c_2(0), c_1(\ell)$ and assert that $c_5(0) = c_5(\ell)$.[6] For the total oxygen flux, Britton and Murray find

$$F_{O_2} = \left[D_1\left(c_1(0) - c_1(\ell)\right) + D\left(c_4(0) - c_4(\ell)\right)\right]/\ell, \tag{2.24}$$

where the first component corresponds to the flux of the free oxygen, which we can readily calculate, and the second component corresponds to the flux of the bound oxygen, which we can determine from Britton and Murray's singular perturbation results. Britton and Murray find that

$$c_5 = c_t \frac{k_2\gamma_2/k_{-2}}{1 + 1 + k_1\gamma_1/k_{-1} + k_2\gamma_2/k_{-2}} \qquad (constant), \tag{2.25a}$$

$$c_4(x) = c_t \frac{k_1 c_1(x)\left(1 - c_5\right)}{k_1 c_1(x) + k_{-1}}, \tag{2.25b}$$

$$c_3(x) = c_t \frac{k_{-1}\left(1 - c_5\right)}{k_1 c_1(x) + k_{-1}}, \tag{2.25c}$$

[5] Despite a careful reading of Ref. [87], we cannot find where this fact is mentioned. Perhaps this fact was actually communicated in personal correspondence between the authors.

[6] In contrast, in our extended model, we fix the concentrations of the free ligands at each end of the system and solve for the concentration of the free and bound carrier molecules. We will discuss this point further in Section 4.2.2.

so we can re-write (2.24) as a function of λ and γ_1 as

$$F_{O_2} = \frac{D_1\gamma_1}{\ell}\left(1-10^{-2}\right) + \frac{Dc_t k_1\gamma_1}{\ell}\left(\frac{1}{k_1\gamma_1+k_{-1}} - \frac{10^{-2}}{k_1\gamma_1 10^{-2}+k_{-1}}\right)\left(\frac{1+k_1\gamma_1/k_{-1}}{1+1+k_1\gamma_1/k_{-1}+k_2\lambda\gamma_1/k_{-2}}\right). \quad (2.26)$$

We have reproduced Britton and Murray's theoretical results in Figures 2.8-2.10. [7] Their main result is that even an extremely small amount of carbon monoxide present at the up-stream end of the system can appreciably reduce the facilitation of oxygen diffusion by hemoglobin.

2.2.2 Kreuzer & Hoofd, 1970-1976

In their 1970 article titled "Facilitated diffusion of oxygen in the presence of hemoglobin," Kreuzer and Hoofd (KH) responded to Wyman's call for a numerical solution of (2.9) [37]. Their model was slightly different from those we have discussed so far. First, they explicitly included both the free and bound carrier molecules, rather than modeling the fractional saturation of the carrier as Wyman and Murray did. However, the more significant difference was in the boundary conditions that they employed. Rather than prescribing values for the the ligand-carrier complex at the boundary of the system, they imposed the biophysically relevant condition that the carrier molecules cannot escape from the system, either in free or bound form, i.e. $\frac{dY}{dx} = 0$ at $x = 0$ and $x = \ell$, in the notation of Murray. In turn, this implies that $D_c\frac{dc}{dx} = -F$ at $x = 0$ and $x = \ell$, as can be seen from (2.6). Kreuzer and Hoofd then went on to numerically solve the equivalent of (2.9) according to these boundary conditions.

KH compared their numerical results with Wittenberg's experimental data from Figures 1 and 5 of Ref. [86]. Their model results in comparison to the oxygen flux as a function of the up-stream concentration, or partial pressure, of oxygen agreed extremely well with Wittenberg's data, as did Murray's results from Ref. [49]. Their model also yielded suitable agreement with Wittenberg's data for the facilitated flux as a function of the carrier molecule concentration, when using empirical relationships derived from experimental data for the hemoglobin diffusion

[7] Note that when we attempt to re-create Britton and Murray's Figures 4 and 5 using their parameter values, we noticed that our results differed from theirs by approximately a factor of two. We believe that there was a systematic error in their figures, since our version agrees with results previously published by Murray using the same set of parameter values.

coefficient as a function of the total hemoglobin concentration in the system, which was not done by Murray. This detail will be considered in the context of our model in Section 3.4.2.

In 1976, Kreuzer and Hoofd published an article titled, "Facilitated diffusion of CO and oxygen in the presence or hemoglobin or myoglobin," Ref. [38], in which they studied the transport of carbon monoxide mediated by either hemoglobin or myoglobin, both in the presence and absence of oxygen. Using a typical reaction-diffusion model for facilitated diffusion of carbon monoxide and oxygen in the presence of a carrier molecule, they assumed a form for the concentration profiles that includes the sum of an equilibrium profile and two exponential terms that decay according to the distance from the up- and down-stream ends of the system. They defined a weighted derivative and determined an approximate equation for the total carbon monoxide flux that did not hold up for small diffusion path lengths, which they then modified to reflect the correct behavior in the limits: $\ell \to 0$, $p \to 0$, $\ell \to \infty$, and $p \to \infty$, where ℓ is the diffusion path length and p is the weighted derivative, as defined in (15) of KH's paper.

There are two results from this paper that we are particularly interested in. First, KH's results indicated that myoglobin and hemoglobin do facilitate the diffusion of carbon monoxide, in direct contrast to Wyman and Murray's results from Ref. [52] and apparently Wittenberg's experimental results from Figures 9 and 10 of Ref. [86]. KH mentioned that both Wittenberg and Murray considered cases where the carbon monoxide partial pressure was high, $\approx 100\ mm\ Hg$, for which KH's model predicted that the carbon monoxide flux is only augmented by a few percent, and furthermore that the physiological carbon monoxide pressures are significantly lower: in a range where the facilitation effect is more pronounced. We will discuss this result further in Section 3.4.3.

Next, KH compared their results with the experimental data of Mochizuki and Forster which we discussed in Section 2.1.2. This will be important to us because it gives some hints for the parameter values that may apply to MF's experimental conditions. KH's results were in fair agreement, except for the 7% O_2 data set, for which they stated they had no explanation. We will perform a similar comparison to MF's data in Section 4.2.3.

2.2.3 Rubinow, Dembo, & Nedelman, 1977-1981

A few years after Wyman and Murray's initial series of articles on facilitated diffusion, in 1977, Rubinow and Dembo (RD) published an article titled "The facilitated diffusion of oxygen by hemoglobin and myoglobin," in which they extended the singular perturbation solution of equation (2.9), with the focus on the so-called "paradox of Wittenberg," [72]. The paradox to which they refer is the fact that the data in Wittenberg's Figure 5 of Ref. [86] seem to coincide for the facilitated flux of oxygen as a function of the carrier molecule concentration for both hemoglobin and myoglobin. This should be a surprising fact, since hemoglobin has four oxygen-binding sites while myoglobin only has one such site, and their association-dissociation rates, as well as the diffusion coefficients, are also different. RD's conclusion is that the data appear to coincide for two reasons. First, the faster diffusion coefficient of myoglobin, relative to hemoglobin, is largely offset by the slower dissociation constant for oxygen-myoglobin complex, relative to the oxygen-hemoglobin complex. RD also believe that the oxygen flux for high myoglobin concentrations was underestimated by Wittenberg due to the autoxidation of the myoglobin during the course of the experiments. We will discuss RD's alternative formulation of Wyman's (2.9), but we are mainly indebted to their explicit discussion of their comparison with Wittenberg's experimental results, which will be the main focus of this section.

RD's mathematical model is very similar to Wyman and Murray's models, with the main difference in the formulation having to do with the boundary conditions, as in the model of Kreuzer and Hoofd mentioned earlier. It is instructive to show how they derive their equivalent of equation (2.9). First, let $c(x,t)$, $h(x,t)$, $y(x,t)$ denote the concentrations of the free ligand, free heme concentration, and bound heme-ligand complex, respectively. Then the rates of changes of the concentrations are given by

$$\frac{\partial c}{\partial t} = D\frac{\partial^2 c}{\partial x^2} - k_+ ch + k_- y, \tag{2.27a}$$

$$\frac{\partial h}{\partial t} = D_p\frac{\partial^2 h}{\partial x^2} - k_+ ch + k_- y, \tag{2.27b}$$

$$\frac{\partial y}{\partial t} = D_p\frac{\partial^2 y}{\partial x^2} + k_+ ch - k_- y, \tag{2.27c}$$

where D and D_p are the diffusion coefficients for the free ligand and both free and bound carrier molecules, respectively, and k_+ and k_- are the association and dissociation constants,

respectively. As is usual, RD solve for the steady state of these PDEs. The steady-state concentrations $c(x), h(x), y(x)$ satisfy the following boundary conditions:

$$h'(x=0) = h'(x=\ell) = 0, \tag{2.28a}$$

$$y'(x=0) = y'(x=\ell) = 0, \tag{2.28b}$$

$$c(x=0) = c_0, \quad c(x=\ell) = c_\ell, \quad Dc'(x=0) = Dc'(x=\ell) = -j, \tag{2.28c}$$

and the condition that the total concentration of the carrier molecules that are originally present in the system is h_0. In the steady state, if we take the sum of (2.27b) and (2.27c), we obtain

$$0 = D_p \frac{d^2}{dx^2}(h+y), \quad \text{or,} \quad h(x) + y(x) = Ax + B, \tag{2.29}$$

where $A = 0$ and $B = h_0$ are integration constants which were determined using (2.28a) and (2.28b), i.e. since the carrier molecule cannot escape the system, the total bound and free carrier concentration remains constant at the initial level that the carrier was present in the system. Furthermore, if we take the sum of (2.27a) and (2.27c), in the steady state,

$$0 = \frac{d^2}{dx^2}(Dc + D_p y), \quad \text{or,} \quad Dc(x) + D_p y(x) = Hx + K, \tag{2.30}$$

where, $H = -j$ and $K = Dc_0 + D_p y_0$ are constants of integration determined using (2.28a) and (2.28c), and y_0 denotes the value of $y(x=0)$, which is not prescribed. Furthermore, we can solve for the oxygen flux, j using (2.29) and (2.28c):

$$j = \frac{1}{\ell}\left[D(c_0 - c_\ell) + D_p(y_0 - y_\ell)\right], \tag{2.31}$$

where again, y_ℓ denotes the value of $y(x=\ell)$ and is not prescribed. Then, from (2.27a), (2.29), and (2.30), we have

$$D\frac{d^2c}{dx^2} = k_+ h_0 c + \frac{1}{D_p}(k_+ c + k_-)\left(Dc - (Dc_0 + D_p y_0) + jx\right), \tag{2.32}$$

where j is as in (2.31). We can see that this is equivalent to Murray's formulation, but the flux dependence on the gradient in the bound carrier molecule arises from (2.28c) and is not initially prescribed. As in Murray's work, RD found a solution using a singular perturbation technique, but incorporated more terms in the expansion. For certain regimes of the parameter values,

which RD stated are in satisfactory agreement with the observations of the oxygen-hemoglobin system, RD's results simplify to

$$j = j_N + j_F, \tag{2.33a}$$

$$j_N = \frac{D}{\ell}\left(c_0 - c_\ell\right), \tag{2.33b}$$

$$j_F = \frac{h_0 D_p K\left(c_0 - c_\ell\right)}{\ell\left(c_0 + K\right)\left(c_\ell + K\right)}, \tag{2.33c}$$

where $K = \frac{k_-}{k_+}$, which agrees exactly with Murray's results. Under different parameter regimes, RD include more terms in j_F which they assert are necessary to adequately describe the oxygen-myoglobin system.

Now we will discuss the illuminating example of how RD compare their results with Wittenberg's experimental results. We will base our method of comparison closely on theirs, which is why it is included here.

Rubinow & Dembo's Comparison with Wittenberg's Results

The theoretical results for RD's model share the same units as Murray's results: $mol/(cm^2\ s)$ and mol/cm^3 for fluxes and concentrations respectively. However, RD plotted their theoretical results in terms of Wittenberg's original units. Fortunately, RD offered more guidelines on how to convert to Wittenberg's units, but some aspect of their unit conversion was still obscured.

RD stated that they used Henry's law to convert their concentrations to partial pressures:

$$c_0 = \sigma p_0, \qquad c_l = \sigma p_l, \tag{2.34}$$

where σ is the solubility constant of oxygen. RD cites "Sendroy et al." for the value at $20°\ C$:

$$\sigma = 1.8{\times}10^{-3}\frac{mM}{torr}\times\frac{m\ mol}{L}\times\frac{mol}{10^3 m\ mol}\times\frac{L}{10^3 mL}\times\frac{mL}{cm^3}\times\frac{torr}{mm\ Hg} = 1.8{\times}10^{-9}\frac{mol}{cm^3\times mm\ Hg}. \tag{2.35}$$

RD also suggested that there is something more subtle in the flux unit conversion, first by calling j the *oxygen current density*. They stated that the total current of oxygen, J, is given by

$$J = \rho A j = \rho A(j_N + j_F) = J_N + J_F, \tag{2.36}$$

where $\rho = 0.79$ is the porosity and $A = 11.5\ cm^2$ is the cross-sectional area of the milipore filter.

Now we can perform a dimensional analysis to make sure that the units for J_N due to (2.34) and (2.36) match those used by RD:

$$\begin{aligned} J_N &= \frac{\rho A D \sigma (p_0 - p_l)}{l}, \\ &\sim \frac{(cm^2)\left(\frac{cm^2}{s}\right)\left(\frac{mol}{cm^3 \times mm\ Hg}\right)(mm\ Hg)}{cm} \sim \frac{mol}{s}. \end{aligned} \tag{2.37}$$

All that remains is to determine how to convert from mol/s to mL/min. The time-unit conversion is trivial, so we must focus on how to convert from mol to mL of a gas. RD did not say anything about how the final unit conversion was carried out in Ref. [72]. However, in Ref. [53], Nedelman & Rubinow offered a hint when they assumed a molar volume of $24.04 \frac{L}{mol}$ for carbon monoxide at $20^\circ\ C$. This inspired us to use the ideal gas law to find the appropriate molar volume for oxygen for these experiments. Since Wittenberg reported fluxes in μL at $760\ mm\ Hg$, $0^\circ\ C$, we can use the ideal gas law to calculate the molar volume conversion factor:

$$\begin{aligned} \frac{V}{n} &= \frac{RT}{P}, \\ &= \frac{\left(8.314472 \frac{N \times m}{K \times mol}\right)(273\ K)}{(760\ mm\ Hg)\left(\frac{N/m^2}{7.5006 \times 10^{-3} mm\ Hg}\right)}, \\ &= 2.241 \times 10^{-2} \frac{m^3}{mol} \times \frac{10^6 cm^3}{m^3} \times \frac{mL}{cm^3} \times \frac{L}{10^3 mL}, \\ &= 22.41 \frac{L}{mol}. \end{aligned} \tag{2.38}$$

Now we can calculate the overall conversion factor:

$$1 \frac{mol}{s} = 1 \frac{mol}{s} \times \frac{22.41\ L}{mol} \times \frac{10^6\ \mu L}{L} \times \frac{60\ s}{min} \approx 1.344 \times 10^9 \frac{\mu L}{min}. \tag{2.39}$$

The final piece of the puzzle for converting RD's flux units into Wittenberg's flux units can now be put into place. For example, at $p_0 = 100\ mm\ Hg$ and $p_l = 0\ mm\ Hg$, RD's flux values

should be:

$$\begin{aligned} J_N &= \frac{\rho A D \sigma (p_0 - p_l)}{l}, \\ &\approx \frac{(0.79)(11.5\ cm^2)\left(10^{-5}\frac{cm^2}{s}\right)\left(1.8\times 10^{-9}\frac{mol}{cm^3\times mm\ Hg}\right)(100\ mm\ Hg)}{2.45\times 10^{-2} cm}, \\ &\approx 6.67\times 10^{-10}\frac{mol}{s}\times\frac{22.41\ L}{mol}\times\frac{10^6\ \mu L}{L}\times\frac{60\ s}{min}, \\ &\approx .897\frac{\mu L}{min}. \end{aligned} \tag{2.40}$$

This is not the case in their figure, where $J_N(100\ mm\ Hg) > 1\ \mu L/min$, so something must still be missing. We suspect that part of the inconsistency comes from using $D \approx 10^{-5}$ in the above calculation, while RD probably used $D(h_0)$ from Riveros-Moreno & Wittenberg's experimental results from Ref. [68]. In any case, this unit conversion gets us in the ballpark at least, and is the convention that we will adopt for our calculations. In addition, RD used their formulas for J_F and Riveros-Moreno's curves for $D(h_0)$ and $D_p(h_0)$ to generate a comparison to Wittenberg's Figure 10. Their curves had the correct qualitative behavior, but did not match very well quantitatively.

In 1981, Nedelman and Rubinow published an article titled "Facilitated diffusion of oxygen and carbon monoxide in the large affinity regime," in which they studied only the facilitated component of the oxygen or carbon monoxide flux, and in particular focused on the case where the facilitation effect is relatively small, as in the case of carbon monoxide and hemoglobin or myoglobin [53]. Although they did not present a two-ligand model, we will follow their technique for comparing the results of their model to Mochizuki and Forster's experimental data set for 0 % O_2 in Section 4.2.3.

2.2.4 Ebel, 1985

After the submission of Ref. [7] for publication, we discovered an article by Ebel from 1985, titled "Carrier facilitated diffusion," which contains, among other things, models that are extremely similar to the models we put forth in Chapters 3 and 4 [13]. In particular, Ebel's "single jump" models for thin membranes are nearly identical to our independently derived models. We eventually decided not to pursue the publication of our N ligand model due to these similarities,

but we believe that there is still merit in presenting our results in this dissertation, particularly the comparison between our model and Mochizuki and Forster's experimental results.

The "single jump," in Ebel's language, refers to the limiting case of the reaction-diffusion models where the membrane is so thin that the diffusion of the carriers from one end to the other can be described as a single jump. In other words, the membrane is so thin that a stationary state is reached instantaneously in the interior of the membrane so that spatial inhomogeneities can be ignored. In particular, all fluxes are determined by reactions that occur at the interfaces, jumps between the interfaces, and parameters of the system describing these events.

The main differences between our model and Ebel's model can be summarized as follows. Ebel does not allow for the transport of the free ligand through the membrane, i.e. the *only* transport of the ligand is via the carrier molecule pathway, which is both qualitatively and quantitatively different from the case that we are interested in. Also, Ebel always assumes that the diffusion of the carriers is unbiased. We do not initially make this assumption, but we do focus on the unbiased diffusion case after we have found solutions to the general model. Ebel allows for differing association-dissociation kinetics at the two ends of the system, as well as for different transport rates for the free and bound carriers. We also include these possibilities in our general single ligand model in Chapter 3. However, for our N ligand model in Chapter 4, we assume that the kinetics are the same at each end of the system, and the free and bound carriers have the same transport rates in order to simplify the algebra. These cases could easily be added if necessary, but we concluded that the gain in generality would be more than offset by the tediousness of the algebra required to write out the solutions, especially since it is not necessary for our system of interest. In addition, Ebel studies cases where the diffusion rates are greater than the association-dissociation rates, as well as the opposite case. We did not study the rapid diffusion case, because it was not relevant to our motivating system. We could of course look at this case in more detail as well. Finally, Ebel does not present a general N ligand model in Ref. [13].

As we mentioned previously, Ebel's single jump models do not account for the transport of the free ligand from the up-stream to down-stream ends of the system. However, the transport of the free carriers and the bound carrier-ligand complexes are modeled using the same set of law of mass action ODEs that can be found in our model in equations (3.3) and (4.2), up to

notational differences, as well as the minor differences mentioned in the previous paragraph. Therefore, the resulting equations for the facilitated fluxes will also be the same. However, in our model the total flux of the ligand will be the sum of the facilitated flux and the flux due to Fickian diffusion of the free ligand.

Although the mathematics is essentially identical for the concentrations of the carrier and carrier-ligand complexes, the interpretation of the results from our model in the context of facilitated diffusion of oxygen and/or carbon monoxide in hemoglobin or myoglobin is of a different character than the systems in which Ebel is interested. Ebel is mainly concerned with membrane transport systems in which the carrier molecules diffuse more rapidly than the ligands, or the ligands cannot diffuse freely at all, which is exactly the opposite of the facilitated diffusion systems that motivated our study of the problem. Therefore, our interpretations focus on a different regime, leading to the insight that it is precisely the "grand-canonical," or "open" character of the ligand-carrier system which leads to a non-equilibrium steady state under which the facilitated diffusion of oxygen by hemoglobin or myoglobin is guaranteed to occur, as discussed in Section 3.5, which is not present in Ebel's work.

We will conclude our comments on Ebel's work by mentioning the author's list of four observable phenomena that can be seen in both models:

1. **Saturation:** The facilitated flux "saturates," or approaches a maximum value with increasing concentration gradients.

2. **Competitive Inhibition:** The presence of a second ligand can reduce the magnitude of the facilitated flux for the first ligand.

3. **Counter-Transport:** Under certain conditions, the presence of a second ligand can induce a flux of the first ligand that is either against the concentration gradient, or exists in the absence of a concentration gradient.

4. **Competitive Acceleration:** The presence of a second ligand can actually increase the flux of the first ligand under certain conditions. (This is also known as "co-transport" or "sym-transport.")

Chapter 3

FACILITATED TRANSPORT OF A SINGLE LIGAND

Solutions to the reaction-diffusion models provide a good match with the experimental results, but previous mathematical models were missing a simple but profound insight into the mechanism of the facilitation. We propose a simple chemical kinetic model for the facilitated transport of a ligand by a carrier molecule to which the ligand binds reversibly. The simple kinetic model provides all of the key results for Wyman-Murray facilitated diffusion. Our model shows that the facilitation by the carrier molecule is guaranteed, as long as a free ligand gradient is kept constant, due to the cell being an open chemical system [65] with respect to the ligand.[1]

The key physico-chemical notion in this facilitated transport is that free ligand concentrations, at both the up-stream and down-stream ends of the system, are kept constant. Thus the transport is driven by a fixed chemical potential. Because of this, the presence of the carrier molecules, even though their transport rate is slow, creates additional, "parallel pathways" for transport. In the language of electrical circuitry: adding an resistor in parallel, even a very large one, always increases the overall conductance.

3.1 A Simple Chemical Kinetic Model Revealing All Complexities

The simple chemical kinetic model describes a one dimensional system in which both ligand and a carrier molecules are present in solution. A schematic diagram of the system being modeled can be seen in Figure 3.1. The positive direction of transport is from left to right, meaning that the concentration of the ligand at the left-hand "up-stream" end of the system is larger than the concentration at the right-hand "down-stream" end. The ligands are free to pass through the barriers at either end of the system, but the carrier molecules are not. Ligand

[1]This chapter, through Section 3.5, is a postprint version of an article published as:
Simple Chemical Model for Facilitated Transport with an Application to Wyman-Murray Facilitated Diffusion, Christine Lind Cole and Hong Qian, *Acta Physico-Chimica Sinica*, Volume 26, Issue 11, ©2010.
Reproduced with permission from the Editorial office of Acta Physico-Chimica Sinica.

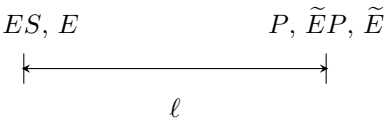

Figure 3.1: **Model Diagram.**
Schematic diagram for the one dimensional facilitated transition system. S and P represent the free ligand at the left-hand "up-stream" end of the system and the right-hand "down-stream" end of the system respectively. Similarly, E and $\widetilde{E}$ represent the carrier molecules while ES and $\widetilde{E}P$ represent the ligand-carrier complexes.

molecules, carrier molecules, and ligand-carrier complexes each move through the solution by simple gradient driven diffusion. Furthermore, the ligands bind reversibly with the carrier molecules. It will be shown that the presence of the carrier molecules will enhance the total ligand transport.

The ligand-macromolecule system is a natural setting for modeling facilitated transitions. We will now use the *compartmental representation* for the transport and identify the ligand at the up-stream end of the system and down-stream end of the system as S and P respectively, as in the enzymatic reaction terminology. The transport reactions are assumed to be first-order, parallel to Fick's law for diffusion. Thus, we are effectively considering a simple biochemical kinetic model based on standard [18] reversible Michaelis-Menten enzyme kinetics! Our model describes a system in which there are two conformational states of the enzyme, E and $\widetilde{E}$, representing the carrier molecule before and after a "conformational change." The enzyme-substrate, ES, and enzyme-product, $\widetilde{E}P$, complexes represent the ligand bound to the carrier molecule before and after the conformational change. The conformational change represents the compartmentalized transport from the up-stream end to the down-stream end of the system. The substrate can also convert to the product directly without the enzyme, corresponding to the ligand moving from one end of the system to the other in the diffusion formalism. Let ℓ denote the distance between the two ends of the system.

The chemical kinetic model can be summarized by the following set of reversible reactions:

$$S \underset{k_{-1}}{\overset{k_{+1}}{\rightleftharpoons}} P, \quad E + S \underset{k_{-2}}{\overset{k_{+2}}{\rightleftharpoons}} ES, \quad \widetilde{E} + P \underset{k_{-3}}{\overset{k_{+3}}{\rightleftharpoons}} \widetilde{E}P,$$
$$ES \underset{k_{-4}}{\overset{k_{+4}}{\rightleftharpoons}} \widetilde{E}P, \quad E \underset{k_{-5}}{\overset{k_{+5}}{\rightleftharpoons}} \widetilde{E}. \tag{3.1}$$

The equilibrium energy balance loop law, or detailed balance, also requires that

$$\frac{k_{+4}}{k_{-4}} \times \frac{k_{-3}}{k_{+3}} \times \frac{k_{-5}}{k_{+5}} \times \frac{k_{+2}}{k_{-2}} = \frac{k_{+1}}{k_{-1}}. \tag{3.2}$$

Let $c_S, c_P, c_E, c_{\widetilde{E}}, c_{ES}$, and $c_{\widetilde{E}P}$ denote the concentrations of the reactants. Then by the law of mass action, the concentrations of the reactants are governed by the set of six ordinary differential equations with initial conditions shown in (3.3):

$$\frac{dc_S}{dt} = k_{-1}c_P + k_{-2}c_{ES} - (k_{+2}c_E + k_{+1})\, c_S, \qquad c_S(0) = s_0, \tag{3.3a}$$
$$\frac{dc_P}{dt} = k_{-3}c_{\widetilde{E}P} + k_{+1}c_S - \left(k_{+3}c_{\widetilde{E}} + k_{-1}\right) c_P, \qquad c_P(0) = p_0, \tag{3.3b}$$
$$\frac{dc_{ES}}{dt} = k_{+2}c_E c_S + k_{-4}c_{\widetilde{E}P} - (k_{-2} + k_{+4})\, c_{ES}, \qquad c_{ES}(0) = 0, \tag{3.3c}$$
$$\frac{dc_{\widetilde{E}P}}{dt} = k_{+4}c_{ES} + k_{+3}c_P c_{\widetilde{E}} - (k_{-4} + k_{-3})\, c_{\widetilde{E}P}, \qquad c_{\widetilde{E}P}(0) = 0, \tag{3.3d}$$
$$\frac{dc_E}{dt} = k_{-2}c_{ES} + k_{-5}c_{\widetilde{E}} - (k_{+2}c_S + k_{+5})\, c_E, \qquad c_E(0) = e_0, \tag{3.3e}$$
$$\frac{dc_{\widetilde{E}}}{dt} = k_{+5}c_E + k_{-3}c_{\widetilde{E}P} - (k_{+3}c_P + k_{-5})\, c_{\widetilde{E}}, \qquad c_{\widetilde{E}}(0) = \widetilde{e}_0. \tag{3.3f}$$

Note that this set of initial conditions assumes that the system is initially composed of only free substrates, enzymes, and products. The initial conditions are not essential to our analysis since we are mainly concerned with the unique steady state of the system, but they can be used for numerical computations. The sum of equations (3.3c) through (3.3f) is zero, so the total amount of enzyme in the system is conserved,

$$c_E + c_{\widetilde{E}} + c_{ES} + c_{\widetilde{E}P} = e_0 + \widetilde{e}_0 = e_0^{tot}, \tag{3.4}$$

as we expect because the enzymes (i.e., carrier molecules) cannot leave the biophysical system.

The equations as shown in (3.3) also have a conservation for the total ligand concentration: the sum of equations (3.3a) through (3.3d) is also zero. This is the standard set-up for reactions in a closed chemical system. We discover that the kinetics of the system can be significantly

different depending on whether the system is closed with respect to S and P, meaning that the total ligand concentrations in each compartment are held constant, or open, meaning that the free ligand concentrations in each compartment are held constant. In Gibbs' statistical mechanics, these are known as canonical and grand canonical ensembles, respectively [29].

Our goal is to study facilitated transport, so we will be interested in the rate enhancement of the conversion of the substrate to the product due to the presence of the carrier molecule in the steady state. We use the King-Altman-Hill method [34, 30] to solve for the steady-state concentrations of the different forms of the enzyme:

$$c_E = \frac{e_0^{tot} D_0}{\sum_{i=0}^{3} D_i}, \quad c_{\widetilde{E}} = \frac{e_0^{tot} D_1}{\sum_{i=0}^{3} D_i}, \quad c_{ES} = \frac{e_0^{tot} D_2}{\sum_{i=0}^{3} D_i}, \quad c_{\widetilde{E}P} = \frac{e_0^{tot} D_3}{\sum_{i=0}^{3} D_i}, \tag{3.5}$$

where the expressions for the D_i are given by:

$$D_0 = k_{-5}k_{+4}k_{-3} + k_{-2}k_{-5}k_{-3} + k_{-2}k_{-5}k_{-4} + k_{-2}k_{-4}k_{+3}c_P, \tag{3.6a}$$

$$D_1 = k_{-2}k_{+5}k_{-4} + k_{-2}k_{+5}k_{-3} + k_{+5}k_{+4}k_{-3} + k_{+2}k_{+4}k_{-3}c_S, \tag{3.6b}$$

$$D_2 = k_{+2}k_{-5}k_{-3}c_S + k_{+2}k_{-5}k_{-4}c_S + k_{+2}k_{-4}k_{+3}c_S c_P + k_{+5}k_{-4}k_{+3}c_P, \tag{3.6c}$$

$$D_3 = k_{+2}k_{-5}k_{+4}c_S + k_{+2}k_{+4}k_{+3}c_S c_P + k_{+5}k_{+4}k_{+3}c_P + k_{-2}k_{+5}k_{+3}c_P. \tag{3.6d}$$

Note that the steady-state enzyme concentrations are functions of the free ligand concentrations, c_S, c_P, which are assumed to be constant in the grand canonical setting, as well as in the King-Altman-Hill method [58].[2]

3.2 Canonical Scenario: Constant Total Ligand Concentrations

In the canonical scenario, the total ligand concentration in each compartment is held constant so that

$$c_S^{tot} = c_{ES} + c_S = s_0, \quad c_P^{tot} = c_{\widetilde{E}P} + c_P = p_0. \tag{3.7}$$

Then we can use the results given above by noting that, in the steady state, the concentrations of the free ligands, c_S and c_P, can be found using (3.5) along with (3.3a) and (3.3b).

[2] A summary of the King-Altman-Hill Method can be found in Appendix A.

From (3.5) we know that the steady-state concentrations of the free enzymes, c_E and $c_{\widetilde{E}}$, satisfy

$$\frac{c_{ES}}{c_E} = K_2 c_S \frac{1+\frac{k_{+3}k_{-4}k_{+5}c_P}{k_{+2}c_S(k_{-3}k_{-5}+k_{-4}k_{-5}+k_{+3}k_{-4}c_P)}}{1+\frac{k_{-3}k_{+4}k_{-5}}{k_{-2}(k_{-3}k_{-5}+k_{-4}k_{-5}+k_{+3}k_{-4}c_P)}}, \tag{3.8}$$

$$\frac{c_{\widetilde{E}P}}{c_{\widetilde{E}}} = K_3 c_P \frac{1+\frac{k_{+2}k_{+4}k_{-5}c_S}{k_{+3}c_P(k_{-2}k_{+5}+k_{+4}k_{+5}+k_{+2}k_{+4}c_S)}}{1+\frac{k_{-2}k_{-4}k_{+5}}{k_{-3}(k_{-2}k_{+5}+k_{+4}k_{+5}+k_{+2}k_{+4}c_S)}}. \tag{3.9}$$

where $K_2 = \frac{k_{+2}}{k_{-2}}$ and $K_3 = \frac{k_{+3}}{k_{-3}}$ for notational convenience. For the rest of this section, we will assume that $k_{\pm 2}, k_{\pm 3} \gg k_{\pm 4}, k_{\pm 5}$, which is appropriate for studying facilitated transport since the association-dissociation reaction rates should be fast compared to the transport reaction rates. Thus we have

$$\frac{c_{ES}}{c_E} = K_2 c_S, \qquad \frac{c_{\widetilde{E}P}}{c_{\widetilde{E}}} = K_3 c_P. \tag{3.10}$$

Furthermore, by setting (3.3c) and (3.3e) equal to zero and equating like terms, we know that in the steady state

$$k_{+4}c_{ES} + k_{+5}c_E = k_{-4}c_{\widetilde{E}P} + k_{-5}c_{\widetilde{E}}. \tag{3.11}$$

Equations (3.4), (3.7), (3.10), and (3.11) give a system of six simultaneous algebraic equations, with six unknowns, $c_S, c_P, c_{ES}, c_{\widetilde{E}P}, c_E, c_{\widetilde{E}}$, representing the steady-state concentrations of the reactants. The six simultaneous equations can be combined to yield two implicit equations containing only the free enzyme steady-state concentrations, c_E, $c_{\widetilde{E}}$, the total concentrations of the enzyme, substrate, and product, e_0^{tot}, s_0, p_0, and the reaction rate constants:

$$\frac{K_2 s_0 c_E}{1+K_2 c_E} + c_E = e_0^{tot} - c_{\widetilde{E}} - \frac{K_3 p_0 c_{\widetilde{E}}}{1+K_3 c_{\widetilde{E}}}, \tag{3.12}$$

$$\frac{k_{+4}K_2 s_0 c_E}{1+K_2 c_E} + k_{+5}c_E = \frac{k_{-4}K_3 p_0 c_{\widetilde{E}}}{1+K_3 c_{\widetilde{E}}} + k_{-5}c_{\widetilde{E}}. \tag{3.13}$$

The curves described by equations (3.12) and (3.13) have exactly one intersection in the $c_E/c_{\widetilde{E}}$ plane corresponding to a unique steady state, which can be seen by the following argument. Equation (3.13) represents a monotonically increasing curve in the $c_E/c_{\widetilde{E}}$ plane which passes through the origin, while equation (3.12) gives a monotonically decreasing curve in the $c_E/c_{\widetilde{E}}$ plane. There will be only one point of intersection of the two curves in the (biophysically relevant) positive quadrant. Since the steady-state concentrations of the other species,

$c_S, c_P, c_{ES}, c_{\widetilde{E}P}$, can each be expressed only in terms of c_E, $c_{\widetilde{E}}$, and other known constants, there is exactly one steady state for our system of ODEs. In this type of Michaelis-Menten kinetics, the unique steady state is globally attractive and asymptotically stable [51].

Recall that since we are interested in the enhancement of the reaction rate for creating the product, we will examine the steady-state net reaction velocity,

$$v = K_+ c_S^{tot} - K_- c_P^{tot} = K_+ s_0 - K_- p_0, \tag{3.14}$$

where K_+ and K_- are the apparent forward and backward rates of $S \cup ES \underset{K_-}{\overset{K_+}{\rightleftharpoons}} P \cup \widetilde{E}P$. The apparent rates are given by

$$K_+ c_S^{tot} = \frac{k_{+1} + k_{+4} K_2 c_E}{1 + K_2 c_E} c_S^{tot}, \qquad K_- c_P^{tot} = \frac{k_{-1} + k_{-4} K_3 c_{\widetilde{E}}}{1 + K_3 c_{\widetilde{E}}} c_P^{tot}. \tag{3.15}$$

Note that

$$\begin{aligned} \min(k_{+1}, k_{+4}) \leq K_+ \leq \max(k_{+1}, k_{+4}), \\ \min(k_{-1}, k_{-4}) \leq K_- \leq \max(k_{-1}, k_{-4}), \end{aligned} \tag{3.16}$$

so if $k_{+4} < k_{+1}$, then the apparent forward rate has to be less than k_{+1}. Similarly, if $k_{-4} < k_{-1}$, then the apparent backward rate is less than k_{-1}. Therefore, we can see that for the canonical scenario, there can be no enhancement of the transport due to the presence of the enzyme if the $ES \rightleftharpoons \widetilde{E}P$ reaction is much slower than the direct conversion of $S \rightleftharpoons P$. In the diffusion formalism it is known that the diffusion coefficients of hemoglobin and myoglobin are approximately two orders of magnitude smaller than the diffusion coefficient of oxygen and carbon monoxide, so $k_{\pm 4} \ll k_{\pm 1}$. Therefore, not only will there be no facilitated transport of oxygen in a closed system of this type, but the apparent forward rate will actually be significantly slower than if no carrier molecules were present. This is the situation one intuitively considers. Since we know that the ligand is free to flow across the barriers in biophysically relevant systems and, more importantly, that the concentrations of the ligands at the barriers are maintained, we will see how the results from the mathematical model are different in the grand canonical scenario.

3.3 Grand Canonical Scenario: Constant Free Ligand Concentrations

In the grand canonical scenario, the free ligand concentration is held constant in each compartment. Therefore, with the presence of the enzyme, the total amount of the ligand in both the free and bound forms in either compartment, c_S^{tot} and c_P^{tot}, can vary. This is the essence of the problem of facilitated diffusion. In this case, since

$$c_S(t) = s_0, \qquad c_P(t) = p_0, \tag{3.17}$$

we can use the results from the King-Altman-Hill method in (3.5) directly. Again, we are interested in the steady-state reaction velocity:

$$v = (k_{+1}c_S - k_{-1}c_P) + \left(k_{-3}c_{\widetilde{E}P} - k_{+3}c_{\widetilde{E}}c_P\right) = v_N + v_F, \tag{3.18}$$

where v_N and v_F denote the non-facilitated and facilitated steady-state reaction velocities respectively. Note that the non-facilitated reaction velocity is the component that is due to direct conversion of the substrate to the product, and the facilitated reaction velocity is the component that is due to the presence of the enzyme in the system. Using (3.2) and (3.5), we obtain

$$v_N = k_{+1}s_0 - k_{-1}p_0, \tag{3.19a}$$

$$v_F = \frac{k_{+4}k_{-5}K_2e_0^{tot}\left(k_{+1}s_0 - k_{-1}p_0\right)}{k_{+1}\Omega}, \tag{3.19b}$$

$$v = \left(1 + \frac{k_{+4}k_{-5}K_2e_0^{tot}}{k_{+1}\Omega}\right)\left(k_{+1}s_0 - k_{-1}p_0\right), \tag{3.19c}$$

where $K_2 = \frac{k_{+2}}{k_{-2}}$, $K_3 = \frac{k_{+3}}{k_{-3}}$ as in Section 3.2, and

$$\begin{aligned}\Omega \;=\; & (k_{-5} + k_{+5}) + (k_{-4} + k_{+4})\,K_2K_3s_0p_0 + (k_{+4} + k_{-5})\,K_2s_0 \\ & + (k_{-4} + k_{+5})\,K_3p_0 + (k_{-5} + k_{+5})\left(\frac{k_{-4}}{k_{-3}} + \frac{k_{+4}}{k_{-2}}\right) \\ & + (k_{-4} + k_{+4})\left(\frac{k_{-5}}{k_{-3}}K_2s_0 + \frac{k_{+5}}{k_{-2}}K_3p_0\right).\end{aligned} \tag{3.20}$$

Since all of the rate constants and steady-state concentrations are positive quantities, the presence of the enzyme increases the production of P *for any values of the rate constants.* In other

words, for the grand canonical scenario, facilitation is guaranteed as long as the enzyme is present in the system initially.

In the special case where $k_{\pm 4} = k_{\pm 5}$ and $k_{\pm 2} = k_{\pm 3}$, which is the original system of interest for facilitated diffusion, v_F simplifies to

$$v_F = \frac{k_{-4}k_{+4}K_2 e_0^{tot}\,(k_{+1}s_0 - k_{-1}p_0)}{k_{-1}(k_{+4}+k_{-4})\left[(1+K_2s_0)(1+K_2p_0) + \frac{k_{-4}(1+K_2s_0)+k_{+4}(1+K_2p_0)}{k_{-2}}\right]}. \tag{3.21}$$

Note that if we assume that $k_{\pm 2} \gg k_{\pm 4}$, as in Section 3.2, v_F can be compared with equation 24 of Ref. [49] and equation 11 of Ref. [72].

The conclusion from the above two sections is that if the system is in the canonical scenario, and $k_{+4} \ll k_{+1}$, $k_{-4} \ll k_{-1}$, then there will be no facilitated transport due to the presence of the protein since the transport mediated by $ES \rightleftharpoons \widetilde{E}P$ is slow. However, if the system is in the grand canonical scenario, then regardless of whether $k_{\pm 4}$ are large or small, there is an additional transport via $ES \rightleftharpoons \widetilde{E}P$. In this case, facilitated transport occurs.

3.4 Comparison with Wittenberg's Experimental Results

In this section, we will compare the theoretical results from our model with three of Wittenberg's key experiments. In Section 3.4.1, we will study the facilitation effect of hemoglobin on oxygen as a function of the oxygen partial pressure at the up-stream end of the system. Next, in section 3.4.2, we will examine the effect of increasing the total concentration of the carrier molecules present in the system. Section 3.4.3 concerns the effect of hemoglobin and myoglobin on the transport of carbon monoxide. In each case, the results from our model suitably reproduce the experimental results. Finally, in Section 3.4.4, we derive a relation between the down-stream ligand concentration, or down-stream partial pressure, and the association-dissociation rates.

We now explain how to compare the theoretical results with the experimental data of Wittenberg [86]. We shall determine how the quantities in our model relate to the ligand partial pressures and fluxes reported by Wittenberg. First, we can see that the oxygen and carbon monoxide partial pressures can be equated to our model's free ligand concentrations using Henry's Law:

$$s_0 = \sigma P P_0, \qquad p_0 = \sigma P P_\ell, \tag{3.22}$$

where PP_0, PP_ℓ denote the ligand partial pressures at the up-stream and down-stream ends of the system, and σ is the solubility constant of the ligand being studied. According to Ref. [72] and Ref. [53] respectively, the values of σ for Wittenberg's experimental conditions are:

$$\sigma_{O_2} = 1.8 \times 10^{-9} mol \cdot cm^{-3} \cdot mm\ Hg^{-1}, \qquad \sigma_{CO} = 1.08 \times 10^{-9} mol \cdot cm^{-3} \cdot mm\ Hg^{-1}. \quad (3.23)$$

Next, we must convert our steady-state reaction velocity, v, which has units of *ligand concentration per time*, into a quantity with units *moles of ligand diffusing per time*, which we will call the *total ligand flux*, using a scaling factor γ, which is described as follows. In order to do this, a conversion factor of a "volume element" will be required. Note that in the comparison between Wittenberg's experiments and Wyman-Murray's diffusion theory, a "cross-section area element" was needed. From Wittenberg's experiments, we know the cross-sectional area of the milipore filter, $A = 11.5\ cm^2$, as well as the (dimensionless) porosity of the filter, $\rho = 0.79$, so the effective cross-sectional area across which the ligands can diffuse is ρA. A one-dimensional diffusion process and a two-compartment kinetics transport model can be related by the distance across which the ligands and enzymes diffuse, ℓ. Therefore, we choose our "volume factor" to be the effective volume: $V_{eff} = \rho A \ell$. In order to convert the total ligand flux, J, to Wittenberg's units of $\mu L \cdot min^{-1}$, we also need to use a conversion factor determined using the ideal gas law for Wittenberg's experimental conditions of 760 $mm\ Hg$, $0°C$ for the flux values: $\alpha = 1.344 \times 10^9 \mu L \cdot s \cdot min^{-1} \cdot mol^{-1}$. Thus our scaling factor is given by $\gamma = \alpha \rho A \ell$.

Finally, we must determine which values to use for the rate constants in our model. The association-dissociation rate constants for oxygen and carbon monoxide combining with hemoglobin and myoglobin are known [86], and can be used directly in our model. The relationship between our transport rate constants and the diffusion of the ligands and enzymes follows from the above mentioned scaling factor. First, we will assume that the diffusion of the ligand, ligand-carrier complex, and carrier is unbiased so that $k_{+1} = k_{-1}$ and $k_{+4} = k_{-4}$. Then our

equation for the total ligand flux, J, in Wittenberg's units of $\mu L \cdot min^{-1}$ becomes:

$$J = \gamma\left(v_N + v_F\right) = J_N + J_F, \tag{3.24a}$$

$$J_N = \gamma k_{+1}\left(s_0 - p_0\right), \tag{3.24b}$$

$$J_F = \frac{\gamma k_{+4} K_2 e_0^{tot}\left(s_0 - p_0\right)}{2\left[(1 + K_2 s_0)(1 + K_2 p_0) + \frac{k_{+4}}{k_{-2}}\left(2 + K_2\left(s_0 + p_0\right)\right)\right]}. \tag{3.24c}$$

As in the case of the steady-state reaction velocity, the subscript N denotes the non-facilitated component of the total flux and the subscript F denotes the facilitated component of the total flux. Therefore, we will refer to J_N and J_F as the non-facilitated and facilitated fluxes respectively. We can see that our theory predicts that the facilitated flux approaches a constant value as the partial pressure at the up-stream end of the system increases, as expected from Wittenberg's experiments:

$$J_{F_\infty} = \lim_{s_0 \to \infty} J_F = \frac{\gamma k_{+4} e_0^{tot}}{2\left[(1 + K_2 p_0) + \frac{k_{+4}}{k_{-2}}\right]}. \tag{3.25}$$

This implies that the total ligand flux approaches a line with slope γk_{+1} as a function of s_0. Therefore, we can match the slope of a line fitting Wittenberg's experimental data points for non-facilitated fluxes with our theoretical curves to determine a value for k_{+1}. Once we have determined a value for k_{+1}, we can set the value for k_{+4} using the idea that the ratio of the transport rates should be the same as the ratio of the diffusion coefficients:

$$\frac{k_{+4}}{k_{+1}} = \frac{D_{carrier}}{D_{ligand}} = \beta, \tag{3.26}$$

where the $D_{carrier}$ is the diffusion coefficient of the carrier molecule, either hemoglobin or myoglobin, and D_{ligand} is the diffusion coefficient of the ligand, either oxygen or carbon monoxide.

Now that we have a method for comparing our theoretical predictions with Wittenberg's experimental data, we can proceed.

3.4.1 Facilitation of Oxygen by Hemoglobin as a Function of Oxygen Partial Pressure

Figure 3.2 shows a comparison of our theoretical results with Wittenberg's experimental data using *Human Hemoglobin A* [86]. In this experiment, Wittenberg measured the flux of oxygen through a solution of ferric hemoglobin, to which oxygen does not bind, corresponding to the

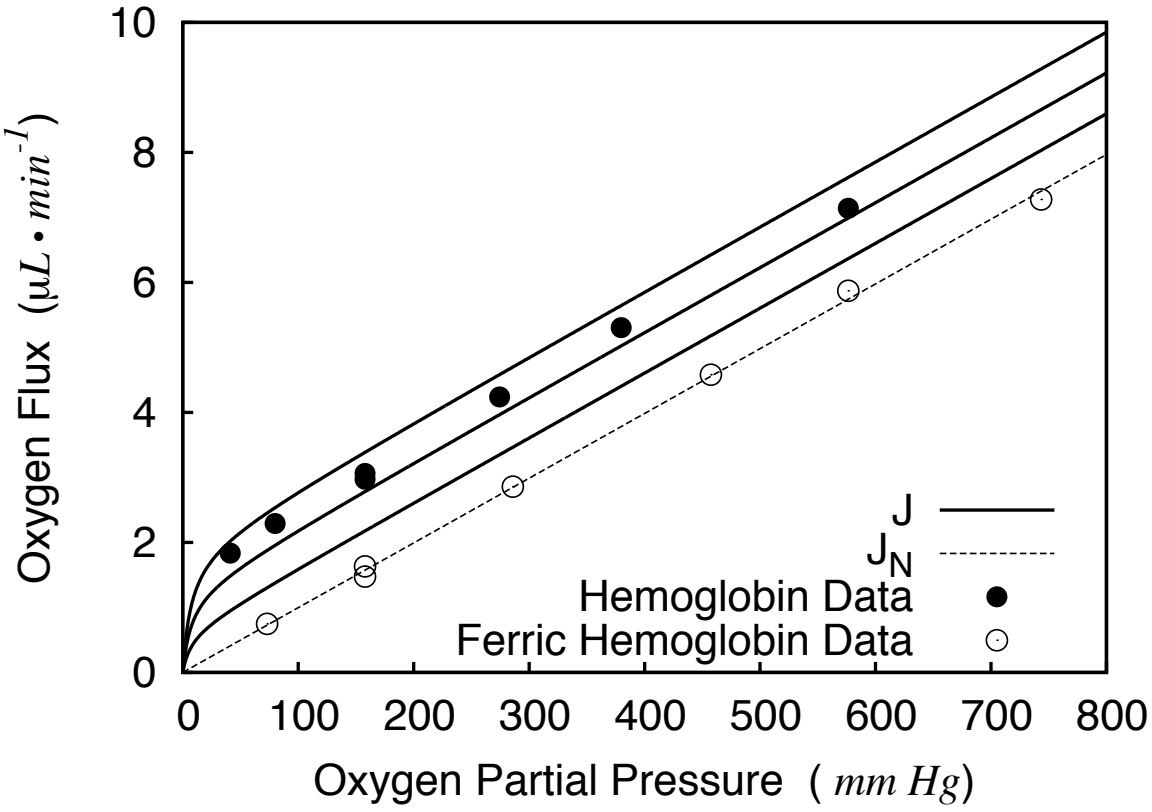

Figure 3.2: **Oxygen Flux *vs* Partial Pressure for Hemoglobin.**
Theoretical results from our model are compared with Wittenberg's experimental data [86]. The open circles show the flux of oxygen through ferric hemoglobin, which does not react with oxygen. The solid circles show the flux of oxygen through *Human Hemoglobin A*. The dashed line represents the non-facilitated oxygen flux, J_N, plotted using (3.24b). The solid curves, representing the total oxygen flux in the presence of hemoglobin, J, were plotted using (3.24a) with $k_{+4} = \beta\, k_{+1},\ 2\beta\, k_{+1},\ 3\beta\, k_{+1}$ in increasing order from top to bottom, as discussed in section 3.4.1. The value of $k_{+1} = 0.0206\ s^{-1}$ was calculated using the experimental data as described in section 3.4. Other parameter values were, from Ref. [86]: $k_{+2} = 3 \times 10^9\ cm^3 \cdot s^{-1} \cdot mol^{-1}$, $k_{-2} = 40\ s^{-1}$, $e_0^{tot} = 1.12 \times 10^{-5}\ mol \cdot cm^{-3}$, $p_0 = 0\ mol \cdot cm^{-3}$, $\rho = 0.79$, $A = 11.5\ cm^2$, from Ref. [87]: $\ell = 2.2 \times 10^{-2}\ cm$, and from Ref. [49]: $D_{Hb} = 2.45 \times 10^{-7}\ cm^2 \cdot s^{-1}$, $D_{O_2} = 1.2 \times 10^{-5}\ cm^2 \cdot s^{-1}$.

open circles, and through a solution of hemoglobin, corresponding to the closed circles. The dashed line represents the non-facilitated flux, which is plotted using (3.24b) by fitting k_{+1} to the ferric hemoglobin data as described above. In order to take the range of values for the diffusion coefficients of oxygen and hemoglobin reported in the literature into account, Murray's values [49] were used to calculate the value of $\beta = \frac{D_{Hb}}{D_{O_2}}$, and three solid curves were generated using (3.24a) and the relationships $k_{+4} = \beta\ k_{+1},\ 2\beta\ k_{+1},\ 3\beta\ k_{+1}$, increasing from the lowest to the highest solid curve. The parameter values used to calculate the total and non-facilitated fluxes are reported in the caption of Figure 3.2.

Wittenberg reports that the total ligand flux, corresponding to the solid curves, exceeds the non-facilitated flux, corresponding to the dashed curve, by a constant amount for partial pressures at the up-stream end of the system exceeding approximately 20 $mm\ Hg$. Our model clearly reproduces that result, as we expect from (3.25).

3.4.2 Facilitation of Oxygen by Hemoglobin and Myoglobin as a Function of Total Carrier Concentration

Next we can compare our model with Wittenberg's experimental results concerning the facilitated flux as a function of total carrier concentration, as shown in Figure 3.3. Wittenberg's experimental data for hemoglobin and myoglobin are shown as solid and open circles respectively. The three curves in the main graphs were generated using (3.24c) with $PP_0 = 750\ mm\ Hg$ and the same parameters as in Figure 3.2, except that the values of $D_{Hb},\ D_{Mb}$ were calculated using the method described below.

Wittenberg reported that the facilitated flux is proportional to the total carrier concentration for dilute solutions, and decreases at higher concentrations. In our model, the facilitated flux, J_F, is linear in the total concentration of the enzyme, e_0^{tot}, which means that our model cannot reproduce Wittenberg's results without incorporating additional information. This is easily done by allowing the enzyme transport rate, k_{+4}, to depend on the total carrier concentration. Riveros-Moreno and Wittenberg found that the diffusion coefficients for hemoglobin and myoglobin are constant for concentrations less than approximately 6 $milimoles \cdot Liter^{-1}\ (Heme)$ and decrease for higher concentrations [68]. We can fit their data for the diffusion coefficients,

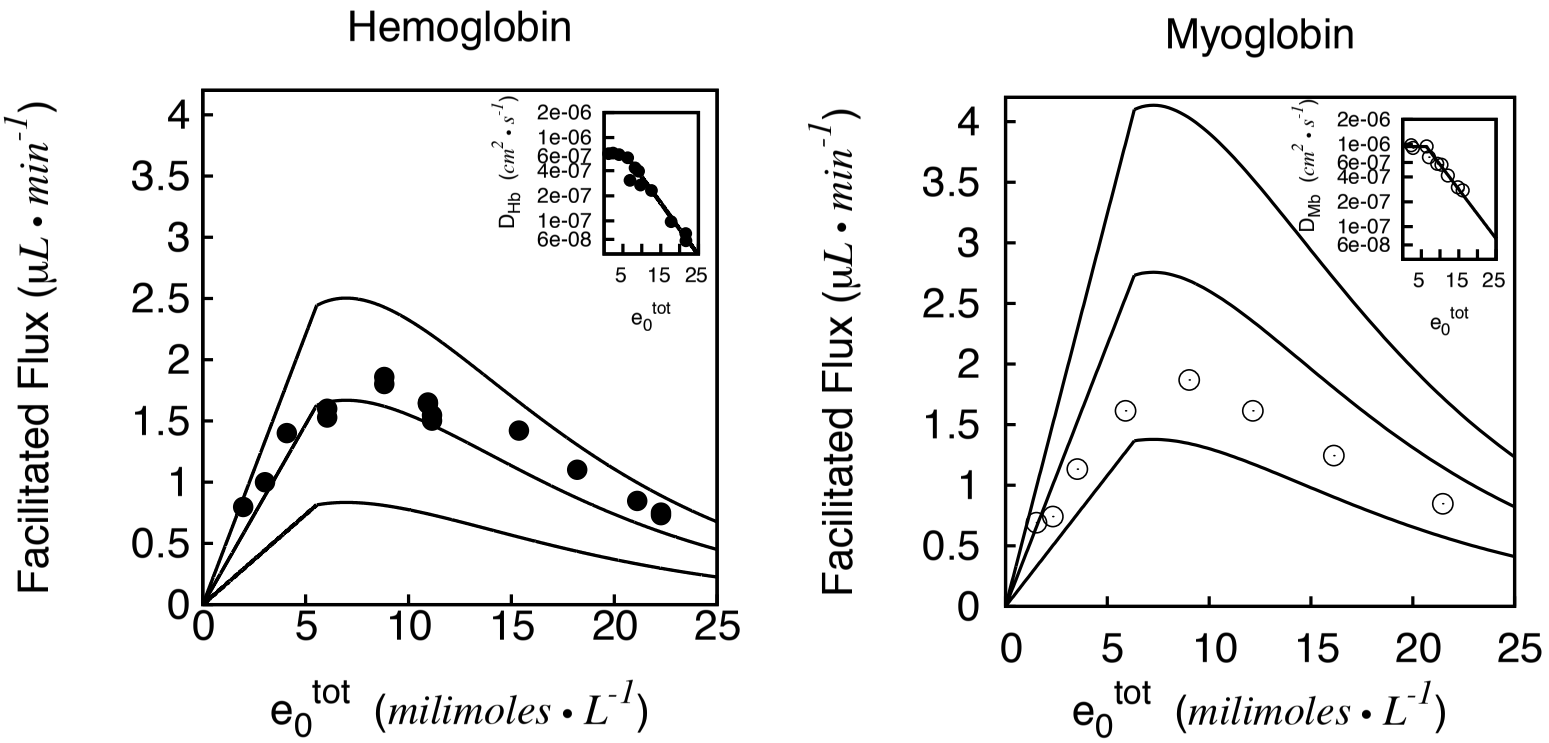

Figure 3.3: **Facilitated Oxygen Flux *vs* Total Heme Concentration.**
Theoretical results from our model are compared with Wittenberg's experimental data [86]. In each plot, the solid circles represent hemoglobin data and the open circles represent myoglobin data. The solid curves, representing the facilitated oxygen flux, J_F, in the presence of hemoglobin or myoglobin, were generated using (3.24c) with $k_{+4} = \beta\ k_{+1},\ 2\beta\ k_{+1},\ 3\beta\ k_{+1}$, where the values for D_{Hb}, D_{Mb} depend on e_0^{tot} according to the relationships shown in the inset plots, as described in section 3.4.2. The partial oxygen pressure at the up-stream end of the system is assumed to be $PP_0 = 750\ mm\ Hg$, and all of the other parameter values are the same as in Figure 3.2, with the exception that for myoglobin, $k_{+2} = 14 \times 10^9\ cm^3 \cdot mol^{-1} \cdot s^{-1}$ and $k_{-2} = 11\ s^{-1}$ as in Ref. [86].
Inset Plots: Self-Diffusion Coefficient *vs* Total Heme Concentration.
The experimental data points were reproduced from Ref. [68]. Curves were fit to the data as described in section 3.4.2.

shown in the inset graphs in Figure 3.3, to determine an empirical relationship between the diffusion coefficients and the total carrier concentration. When we allow k_{+4} to vary with increasing e_0^{tot} according to these relationships, we see that our model qualitatively agrees with the experimental results. Therefore we can conclude that the facilitated flux reaches a maximum value due to crowding of the carrier molecules at higher concentrations.

3.4.3 Carbon Monoxide Facilitation by Hemoglobin and Myoglobin

Finally, we would like to compare theoretical results from our model with Wittenberg's experimental results concerning carbon monoxide facilitation by hemoglobin and myoglobin, which can be seen in Figures 3.4 and 3.5. Wittenberg's data for carbon monoxide and nitrogen fluxes are shown as squares and triangles that are solid for solutions containing hemoglobin and open for solutions containing myoglobin. Wittenberg reports that the ratio of non-facilitated flux of carbon monoxide to the total flux of nitrogen, which is non-facilitated since nitrogen does not react with the carriers, was measured as

$$\frac{J_N \text{ Carbon Monoxide}}{J_N \text{ Nitrogen}} = 1.50. \tag{3.27}$$

The non-facilitated flux is the dashed line through the carbon monoxide data which was plotted using (3.24b) and the value of k_{+1} calculated by matching the slope of the dashed line fit through the nitrogen flux data, multiplied by the conversion factor in (3.27). Note that we chose to perform only one fit using both sets of nitrogen data since they seem to coincide. The solid curves in Figure 3.4 represent the total carbon monoxide flux using (3.24a) and various values for the diffusion coefficients as described in the caption, assuming that there is no back pressure in the experimental setup: $PP_\ell = 0\ mm\ Hg$. The solid curves in Figure 3.5 are generated in the same way, except we assume that there is a small back pressure of $PP_\ell = 1\ mm\ Hg$.

Wittenberg reports that neither hemoglobin or myoglobin enhances the transport of carbon monoxide. Total flux curves plotted for various parameter values, assuming that the back pressure is zero, can be seen in Figure 3.4. If we use the values from Murray and Wyman [52] then we see no enhancement, which is shown by the solid curves that coincide with the carbon monoxide data in Figure 3.4. However, other authors report values for the diffusion coefficients under which our model predicts a facilitated carbon monoxide flux of as much as 2.5 $\mu L \cdot min^{-1}$

for hemoglobin and 1.8 $\mu L \cdot min^{-1}$ for myoglobin. One notable feature shared by all of the total flux curves in Figure 3.4 is that the facilitated carbon monoxide flux approaches its maximum value quite rapidly compared to the results for oxygen and hemoglobin, shown in Figure 3.2. Upon investigation, we find that the facilitated carbon monoxide flux will be nearly abolished if there is a back pressure as small as $PP_\ell = 1\ mm\ Hg$ at the down-stream end of the system, *regardless of which parameter values are used*, as can be seen in Figure 3.5. We suspect that Wittenberg's experimental apparatus may not have been capable of keeping the partial pressure at the down-stream end of the system low enough to be able to see any facilitation effect, which is in agreement with the conclusions of Ref. [52].

Mochizuki and Forster, using a slightly different setup from that of Wittenberg, were able to measure a facilitation of carbon monoxide by hemoglobin [46]. Although Mochizuki and Forster's methods differed from Wittenberg's methods, we can use the same parameters and criteria that Nedelman and Rubinow used to compare their reaction-diffusion model [53] with the experimental data. From Figure 2 in Ref. [46], we measure Mochizuki and Forster's facilitated flux to be $J_{F_{exp}} \approx 0.053\ \mu L \cdot min^{-1}$, and our model predicts that $J_{F_\infty} \approx 0.050\ \mu L \cdot min^{-1}$, an excellent agreement.[3]

These results lead to the observation that the enhancement can be abolished by either taking k_{-2} to be small enough so that the second term in the denominator of J_F becomes dominant, or by setting p_0 large enough. This suggests that if the dissociation rate is too slow, then the ligand cannot escape the carrier molecule fast enough in order to enhance the transport. In other words, the dissociation reaction is rate limiting. Furthermore, if the facilitated flux approaches the maximum value rapidly, even small back pressures in the system will abolish the facilitation effect.

---

[3]Parameters used: $k_{+2} = 6.75 \times 10^8\ cm^3 \cdot mol^{-1} \cdot s^{-1}$, $k_{-2} = 0.05\ s^{-1}$, $e_0^{tot} = 6.65 \times 10^{-6}\ mol \cdot cm^{-3}$, $s_0 = 4.1 \times 10^{-6}\ mol \cdot cm^{-3}$, $p_0 = \frac{s_0}{2}$, $D_{CO} = 1.64 \times 10^{-5}\ cm^2 \cdot s^{-1}$, $D_{Hb} = 6.28 \times 10^{-7}\ cm^2 \cdot s^{-1}$, $\ell = 2.45 \times 10^{-2}\ cm$, $A_{eff} = 5.53\ cm^2$, $\alpha = 1.526 \times 10^9\ \mu L \cdot min^{-1}$, k_{+1} as in Figure 3.5.

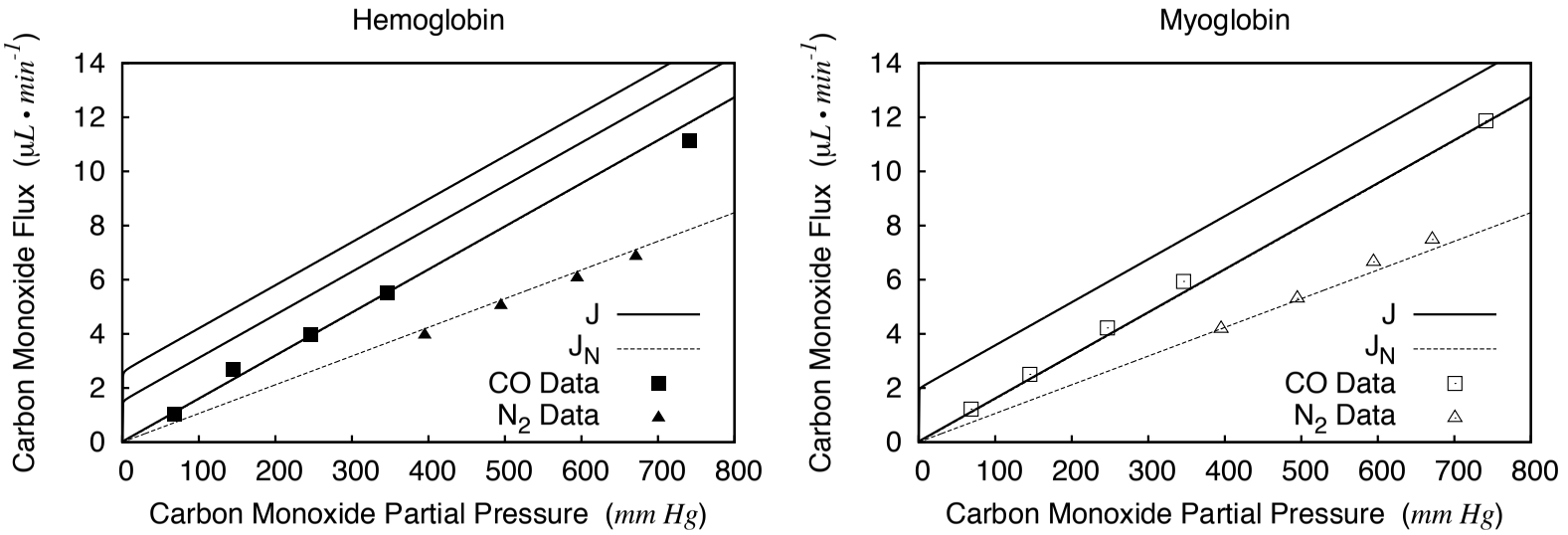

Figure 3.4: **Carbon Monoxide Flux *vs* Partial Pressure.**
Theoretical results from our model are compared with Wittenberg's experimental data [86]. The triangles correspond to nitrogen fluxes through hemoglobin (solid) and myoglobin (open), while the rectangles correspond to carbon monoxide fluxes through hemoglobin and myoglobin. In both plots, the lower dashed line fits both sets of nitrogen data, and represents the non-facilitated nitrogen flux since nitrogen does not react with hemoglobin or myoglobin. The upper dashed line represents the non-facilitated flux carbon monoxide flux, J_N. Each of the solid curves represents the total carbon monoxide flux, J, using (3.24a) with parameter values from different authors as described below. The value for the carbon monoxide transport rate, $k_{+1} = 0.0548\ s^{-1}$, was calculated as described in section 3.4.3. In this figure, we assume that $PP_\ell = 0\ mm\ Hg$.

Hemoglobin Parameters:
From Ref. [86]: $e_0^{tot} = 11 \times 10^{-6}\ mol \cdot cm^{-3}$, from Ref. [53]: $k_{+2} = 6.75 \times 10^8\ cm^3 \cdot mol^{-1} \cdot s^{-1}$, $k_{-2} = 0.05\ s^{-1}$, top solid curve, from Ref [53]: $D_{Hb} = 6.4 \times 10^{-7}\ cm^2 \cdot s^{-1}$, $D_{CO} = 1.98 \times 10^{-5}\ cm^2 \cdot s^{-1}$, middle solid curve, from Ref. [4]: $D_{Hb} = 2.45 \times 10^{-7}\ cm^2 \cdot s^{-1}$, $D_{CO} = 1.3 \times 10^{-5}\ cm^2 \cdot s^{-1}$, bottom solid curve, from Ref. [52]: $D_{Hb} = 2.5 \times 10^{-7}\ cm^2 \cdot s^{-1}$, $D_{CO} = 9 \times 10^{-4}\ cm^2 \cdot s^{-1}$.

Myoglobin Parameters:
From Ref. [86]: $e_0^{tot} = 8.1 \times 10^{-6}\ mol \cdot cm^{-3}$, $k_{+2} = 0.5 \times 10^9\ cm^3 \cdot mol^{-1} \cdot s^{-1}$, $k_{-2} = 0.017\ s^{-1}$, top solid curve, from Ref. [38]: $D_{Mb} = 3.1 \times 10^{-7}\ cm^2 \cdot s^{-1}$, $D_{CO} = 0.93 \times 10^{-5}\ cm^2 \cdot s^{-1}$, bottom solid curve, from Ref. [52]: $D_{Mb} = 4.4 \times 10^{-7}\ cm^2 \cdot s^{-1}$, $D_{CO} = 9 \times 10^{-4}\ cm^2 \cdot s^{-1}$.

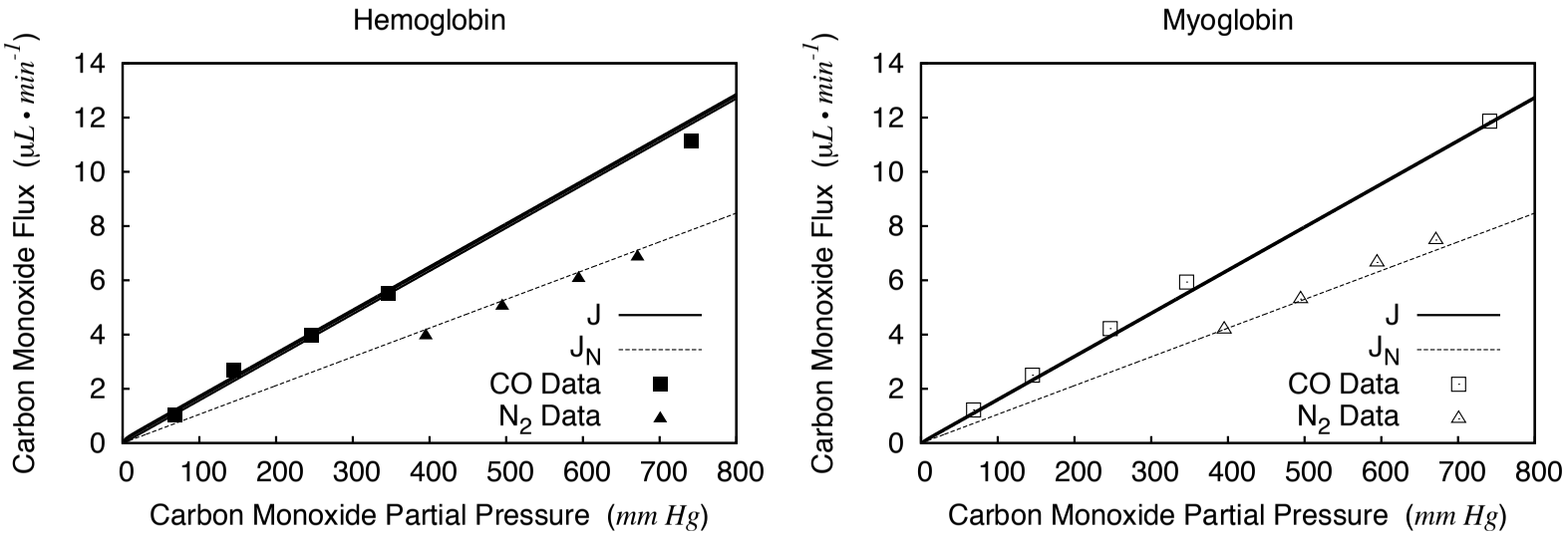

Figure 3.5: **Carbon Monoxide Flux *vs* Partial Pressure, with a Back Pressure of 1 mm Hg.**
These graphs were drawn in the same manner as those shown in Figure 3.4, with the only difference being that a small back pressure in the system of $PP_\ell = 1\ mm\ Hg$ is assumed. Note that in all cases the facilitation is nearly abolished, and each curve is in suitable agreement with the data.

3.4.4 Back Pressure Required to Abolish the Facilitation Effect as a Function of the Reaction Rate Constants

We can quantify the observation that increasing the back pressure in the system can abolish the facilitation effect by examining the form of J_{F_∞} from (3.25). First, note that the facilitated flux is largest when the down-stream free ligand concentration is zero, $p_0 = 0$, corresponding to the case with no back pressure:

$$\max_{p_0} J_{F_\infty} = J_{F_\infty}|_{p_0=0} = \frac{\gamma k_{+4} e_0^{tot}}{2\left(1 + \frac{k_{+4}}{k_{-2}}\right)}. \tag{3.28}$$

Define $p_{0_{1/2}}$ to be the down-stream concentration of the free ligand that decreases the facilitated flux to half of the maximum value:

$$p_{0_{1/2}} = \frac{1 + \frac{k_{+4}}{k_{-2}}}{K_2} = \frac{k_{-2} + k_{+4}}{k_{+2}}. \tag{3.29}$$

Note that as long as the transport rate is much slower than the association-dissociation rates, $k_{+4} \ll k_{+2}, k_{-2}$, then $p_{0_{1/2}} \approx \frac{k_{-2}}{k_{+2}}$. We can calculate the down-stream partial pressure, or back pressure, required to decrease the facilitated flux to half of the maximum value using Henry's law, $PP_{\ell_{1/2}} = \frac{p_{0_{1/2}}}{\sigma}$. For the hemoglobin-oxygen system shown in Figure 3.2, $PP_{\ell_{1/2}} \approx 7.4\ mm\ Hg$. For the hemoglobin- and myoglobin-carbon monoxide systems shown in Figure 3.4, $PP_{\ell_{1/2}} \approx 0.07\ mm\ Hg$ and $PP_{\ell_{1/2}} \approx 0.03\ mm\ Hg$ respectively. We can see that the back pressure required to abolish the facilitation of carbon monoxide by either carrier will be orders of magnitude smaller than the back pressure required to abolish the facilitation of oxygen by hemoglobin, making the facilitation effect harder to measure, as we expect from examining Figures 3.2 and 3.4.

We can see that a greater affinity for the ligand-carrier binding reaction requires a greater attention to keeping the down-stream free ligand concentration, or back pressure, small. Furthermore, we find that a small dissociation rate can have a two-fold effect on lowering the facilitation effect: if k_{-2} is small enough, the second term in the denominator of (3.24c) can become dominant, diminishing the facilitation, and if k_{-2} is very small, the down-stream ligand concentration, or back pressure, must be maintained at a very low level in order to measure the facilitation effect.

3.5 Conclusions

Our simple chemical kinetic model reproduces the main experimental and theoretical results and sheds new light on the mechanism behind facilitated transport. We see that the true cause of the enhanced diffusion is that the system is open with respect to the free ligand. The transport is driven by a fixed chemical potential gradient. In other words, every time a free oxygen binds to the carrier molecule at the up-stream end of the system, another free oxygen molecule can enter the cell. Likewise, every time an oxygen molecule dissociates at the down-stream end of the system, a free oxygen molecule must leave the cell. In this way, a facilitation effect is guaranteed given the presence of the carrier molecules in the system. The presence of the carrier molecules creates "parallel pathways" for transport. Furthermore, we find that slow dissociation rates correspond to an increased likelihood that even a small back pressure will abolish the facilitation effect. This conclusion is further supported by Wittenberg's experimental results that facilitation is not measurable for certain types of hemoglobin that have dissociation rates that are much slower than their association rates, such as *Ascaris* perienteric fluid hemoglobin [86]. In this case the oxygen that binds to the carrier protein cannot escape quickly enough compared to the diffusion time scale to produce a facilitation effect.

In summary, we have developed a simple biochemical kinetic model for facilitated transport phenomena. The model is quite general and conceptually simple. One of the advantages of the model is that it can be easily used by researchers. In addition to the formulae we have presented, the system of ordinary differential equations can be easily solved numerically using appropriate parameter values; a situation that may not be the case for the reaction-diffusion model developed earlier. Our model can also easily be extended to situations where more than one ligand is present in the system.

3.6 Facilitated Transport as an Energy-Driven Phenomenon

We would also like to study our model for facilitated transport of ligands mediated by carrier molecules from another perspective: that of energy-driven phenomena. We have already concluded that the transport is driven by the fixed chemical gradient in the ligand, and that the presence of the carrier molecules creates a "parallel pathway" for the ligand transport to follow,

resulting in the facilitation effect.

We can further quantify these statements using the concept of the *chemical potential*, μ. The reaction pathway for simple transport of the ligand from one end of the system to the other, without the presence of the carrier molecule, is:

$$S \underset{k_{-1}}{\overset{k_{+1}}{\rightleftharpoons}} P.$$

The change in the chemical potential for the reaction $S \to P$ via the direct pathway is:

$$\Delta\mu_1 = \mu_S - \mu_P = k_B T \ln \frac{k_{+1} s_0}{k_{-1} p_0}. \tag{3.30}$$

We can see that the fixed chemical gradient drives the ligand transport, as we expected. Furthermore, for the carrier-mediated pathway

$$E + S \underset{k_{-2}}{\overset{k_{+2}}{\rightleftharpoons}} ES \underset{k_{-4}}{\overset{k_{+4}}{\rightleftharpoons}} \widetilde{E} \underset{k_{+3}}{\overset{k_{-3}}{\rightleftharpoons}} \widetilde{E} + P,$$

$$E \underset{k_{-5}}{\overset{k_{+5}}{\rightleftharpoons}} \widetilde{E},$$

there is a change in chemical potential for the reaction $S \to P$ of

$$\Delta\mu_2 = k_B T \ln \frac{K_2 k_{+4} k_{-5} s_0}{K_3 k_{-4} k_{+5} p_0}, \tag{3.31}$$

where $K_2 = \frac{k_{+2}}{k_{-2}}$, $K_3 = \frac{k_{+3}}{k_{-3}}$, as in Section 3.2.

For the case of facilitated transport of oxygen or carbon monoxide via hemoglobin or myoglobin, our original systems of interest, recall that we assume that the transport due to diffusion is unbiased, so that the transport reaction rates are equal: $k_{+1} = k_{-1}$, $k_{+4} = k_{-4}$, $k_{+5} = k_{-5}$. We also assume that the association-dissociation processes are identical at each end of the system, so that $k_{+2} = k_{+3}$, $k_{-2} = k_{-3}$, $K_2 = K_3$. We can see that under these conditions,

$$\Delta\mu_1 = \Delta\mu_2 = \Delta\mu = k_B T \ln \frac{s_0}{p_0}, \tag{3.32}$$

and it is simply the fixed chemical gradient that drives the transport of the ligand through each of the pathways.

This framework will allow us to draw an interesting conclusion regarding the connection between the chemical gradient and the facilitation effect. We would like to study the ratio of

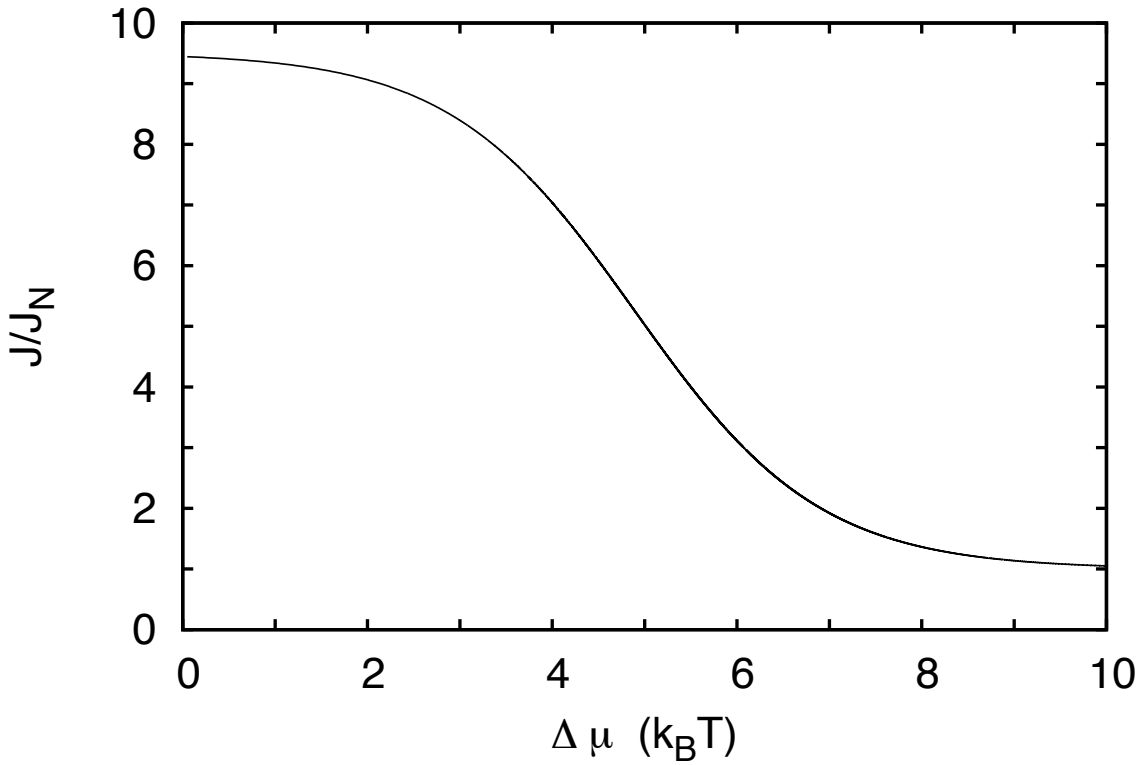

Figure 3.6: **Ratio of the Total Flux to the Non-Facilitated Flux as a Function of the Chemical Potential.**
Values for the rate constants and other parameters are the same as the lowest curve in Figure 3.2, with the exception of using a small, non-zero downstream concentration of the ligand of $p_0 = 1 \times 10^{-10}\ mol \cdot cm^{-3}$. Note that the units on the horizontal axis are $k_B T$.

the total flux to the non-facilitated flux,

$$\frac{J}{J_N} = 1 + \frac{J_F}{J_N}, \tag{3.33}$$

where J and J_N are as defined in (3.24).[4] In Figure 3.6, we plot this ratio as a function of the chemical potential. We can see that the facilitation effect dominates the simple non-facilitated flux for small concentration gradients, and that when the gradient becomes very large, the facilitation effect is relatively unimportant. This should come as no surprise, since

[4]Note that we expect that $\frac{J}{J_N} \geq 1$.

we already determined that the facilitation term rapidly reaches a maximum value, J_{F_∞}, as defined in (3.25), as the upstream concentration, s_0, approaches infinity. In other words, once the facilitation effect has "saturated," due to a large chemical gradient, the non-facilitated transport term will still continue to grow, and will begin to dominate the total transport of the ligand. This gives us the insight that facilitated transport is only important for systems with small gradients in the ligand concentration, where the transport rates due to the direct pathway are sufficiently slow. Once the gradient is large enough, even slow transport rates will result in large non-facilitated fluxes.

3.7 Facilitated Diffusion as Partially Reflected Brownian Motion

Facilitated transport of a ligand by a carrier molecule can also be studied in the context of partially reflected Brownian motion (PRBM). Consider a system including a ligand, `X`, and a carrier molecule, or protein, `P`, each undergoing Brownian motion in one spatial dimension. Let x and y represent the position of the ligand and the protein, respectively. The system can be in two qualitatively different states, depending on whether or not the ligand and protein are bound to each other. Let state 1 be `X+P`, or unbonded, and state 2 be `XP`, or bonded. In state 1, each molecule `X` and `P` has its own distinct position, however, in state 2, the molecules are bonded together, so they share the same position, say x. In state 1, the molecules diffuse freely independent of one another with diffusion constants D_1 and D_2. When the molecules collide they bond, or enter state 2, at a rate of q_1. In state 2, the molecules diffuse together with diffusion constant $D_3 = \dfrac{D_1 D_2}{D_1 + D_2}$. The bond between the molecules breaks, i.e. the molecules return to state 1, at a rate of q_2. The probability density functions for the two states can be modeled as:

$$\frac{\partial f_1(x,y,t)}{\partial t} = D_1 \frac{\partial^2 f_1(x,y,t)}{\partial x^2} + D_2 \frac{\partial^2 f_1(x,y,t)}{\partial y^2} - q_1 \delta(x-y) f_1(x,y,t) + q_2 f_2(x,t), \quad (3.34a)$$

$$\frac{\partial f_2(x,t)}{\partial t} = D_3 \frac{\partial^2 f_1(x,t)}{\partial x^2} + q_1 \delta(x-y) f_1(x,y,t) - q_2 f_2(x,t). \quad (3.34b)$$

A simulated trajectory of this system can be seen in Figure 3.7. The simulation algorithm is described in Appendix B.2.

Future work could include investigating facilitated diffusion as an exit problem using this mathematical framework.

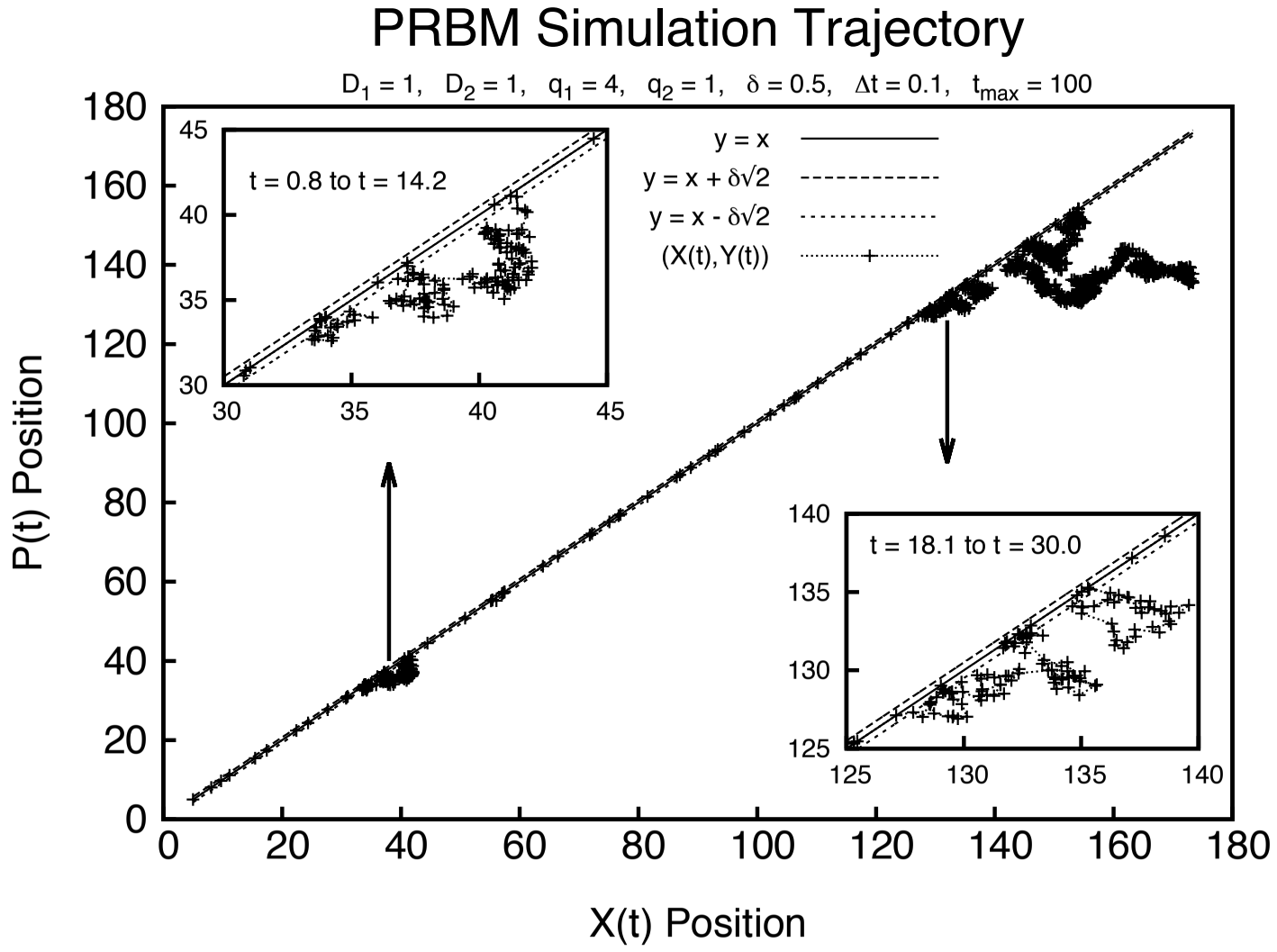

Figure 3.7: **Simulated Trajectory of Partially Reflected Brownian Motion.**

Chapter 4

FACILITATED TRANSPORT OF N LIGANDS

In Section 3.5 we stated that our simple chemical kinetic model for facilitated transitions could easily be extended to the case of N competing ligands. We now present the N-ligand model, and study the solution to the 2-ligand model, with special attention to the scenario of oxygen and carbon monoxide as competing ligands. This particular scenario is the system of interest for carbon monoxide poisoning in the human body.[1] As before, we will study a one-dimensional system where the distance between the up-stream and down-stream ends of the system is ℓ, as depicted in Figure 4.1. Again, E and $\widetilde{E}$ will represent the enzyme before and after the conformational change from the up- to down-stream end, respectively. Let S_i and P_i represent the i^{th} (free) ligand at either end of the system. Similarly, let ES_i and $\widetilde{E}P_i$ represent the ligand-enzyme complexes before and after the conformational change. For a system including N ligands, we will have $4N+2$ species that are governed by the following set of $4N+1$ reversible chemical reactions:

$$S_i \underset{k_{-i}}{\overset{k_{+i}}{\rightleftharpoons}} P_i, \quad E + S_i \underset{r_{-i}}{\overset{r_{+i}}{\rightleftharpoons}} ES_i, \quad \widetilde{E} + P_i \underset{r_{-i}}{\overset{r_{+i}}{\rightleftharpoons}} \widetilde{E}P_i, \quad ES_i \underset{k_{-(n+1)}}{\overset{k_{+(n+1)}}{\rightleftharpoons}} \widetilde{E}P_i, \quad E \underset{k_{-(n+1)}}{\overset{k_{+(n+1)}}{\rightleftharpoons}} \widetilde{E}. \tag{4.1}$$

Note that we have already assumed, for simplicity's sake that the association-dissociation kinetics are the same at both ends of the system, as we would expect in a facilitated diffusion situation. Let $c_{S_i}, c_{P_i}, c_E, c_{\widetilde{E}}, c_{ES_i}$ and $c_{\widetilde{E}P_i}$ denote the concentrations of the reactants. Then by the law of mass action, the system is governed by the set of $4N+2$ ordinary differential equations with initial conditions shown in (4.2). Notice that we have changed the notation from the previous chapter in order to make a distinction between the transport reaction rates, $k_{\pm i}$, and the association-dissociation rates, $r_{\pm i}$. The new conventions were adopted to make

[1] Note that other poisons, such as cyanide and azide, also act by saturating the hemoglobin or myoglobin in the blood. Our extended model can also be applied to these scenarios.

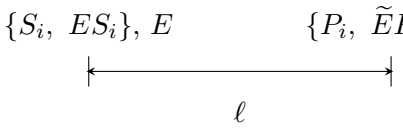

Figure 4.1: **N-Ligand Model Diagram.**
Schematic diagram for the one dimensional facilitated transition system with N Ligands. S_i and P_i represent the i^{th} free ligand at the left-hand "up-stream" end of the system and the right-hand "down-stream" end of the system respectively. Similarly, E and $\widetilde{E}$ represent the carrier molecules while ES_i and $\widetilde{E}P_i$ represent the ligand-carrier complexes.

the algebra less tedious.

$$\frac{dc_{S_i}}{dt} = k_{-i}c_{P_i} + r_{-i}c_{ES_i} - \left(k_{+i} + r_{+i}c_E\right)c_{S_i}, \qquad c_{S_i}(0) = s_i, \tag{4.2a}$$

$$\frac{dc_{P_i}}{dt} = k_{+i}c_{S_i} + r_{-i}c_{\widetilde{E}P_i} - \left(k_{-i} + r_{+i}c_{\widetilde{E}}\right)c_{P_i}, \qquad c_{P_i}(0) = p_i, \tag{4.2b}$$

$$\frac{dc_{ES_i}}{dt} = k_{-(n+1)}c_{\widetilde{E}P_i} + r_{+i}c_E c_{S_i} - \left(k_{+(n+1)} + r_{-i}\right)c_{ES_i}, \qquad c_{ES_i}(0) = 0, \tag{4.2c}$$

$$\frac{dc_{\widetilde{E}P_i}}{dt} = k_{+(n+1)}c_{ES_i} + r_{+i}c_{\widetilde{E}}c_{P_i} - \left(k_{-(n+1)} + r_{-i}\right)c_{\widetilde{E}P_i}, \qquad c_{\widetilde{E}P_i}(0) = 0, \tag{4.2d}$$

$$\frac{dc_E}{dt} = k_{-(n+1)}c_{\widetilde{E}} + \sum_{j=1}^{n} r_{-j}c_{ES_j} - \left(k_{+(n+1)} + \sum_{j=1}^{n} r_{+j}c_{S_j}\right)c_E, \qquad c_E(0) = e_0, \tag{4.2e}$$

$$\frac{dc_{\widetilde{E}}}{dt} = k_{+(n+1)}c_E + \sum_{j=1}^{n} r_{-j}c_{\widetilde{E}P_j} - \left(k_{-(n+1)} + \sum_{j=1}^{n} r_{+j}c_{P_j}\right)c_{\widetilde{E}}, \qquad c_{\widetilde{E}}(0) = \widetilde{e}_0. \tag{4.2f}$$

Note that the total enzyme concentration is conserved:

$$e_0^{tot} = e_0 + \widetilde{e}_0 = c_E + c_{\widetilde{E}} + \sum_{j=1}^{n}\left(c_{ES_j} + c_{\widetilde{E}P_j}\right). \tag{4.3}$$

We will also assume that our system is in the grand canonical scenario, so that

$$c_{S_i}(t) = s_i, \qquad c_{P_i}(t) = p_i. \tag{4.4}$$

In principal, the King-Altman-Hill (KAH) method can be used to solve for the steady-state concentrations of the enzymes, which can in turn be used to find an expression for the total reaction velocity, and eventually the total flux of each ligand, as in Chapter 3.

Next, we will show explicitly how this can be done in the $N = 2$ case, with special attention to possible implications for carbon monoxide poisoning.

4.1 Two Ligand Scenario: $N = 2$

First, we will fill in the details for the $N = 2$ case of our general model. In the two ligand scenario, we have a set of 10 differential equations with initial conditions of the form given in (4.2). We can use the KAH method to solve for the steady-state concentrations of each of the six enzyme states. Note that the graph for the KAH method can be seen in Figure A.3. Then in the standard notation, the steady-state concentrations of the enzyme states are given as

$$c_E = \frac{D_1 e_0^{tot}}{\mathcal{D}},\ c_{\widetilde{E}} = \frac{D_2 e_0^{tot}}{\mathcal{D}},\ c_{ES_1} = \frac{D_3 e_0^{tot}}{\mathcal{D}},\ c_{\widetilde{E}P_1} = \frac{D_4 e_0^{tot}}{\mathcal{D}},\ c_{ES_2} = \frac{D_5 e_0^{tot}}{\mathcal{D}},\ c_{\widetilde{E}P_2} = \frac{D_6 e_0^{tot}}{\mathcal{D}}, \tag{4.5}$$

where the expressions for the D_i can be found in (A.11) of Appendix A, and

$$\mathcal{D} = \sum_{j=1}^{6} D_i. \tag{4.6}$$

As in the previous chapter, we are interested in the steady-state reaction velocities,

$$v_i = \frac{dc_{P_i}}{dt} = (k_{+i} c_{S_i} - k_{-i} c_{P_i}) + \left(r_{-i} c_{\widetilde{E}P_i} - r_{+i} c_{\widetilde{E}} c_{P_i}\right) = v_{N_i} + v_{F_i}, \tag{4.7}$$

where, as before, the subscripts N and F refer to the non-facilitated and facilitated reaction velocities respectively. In the two ligand case, the steady-state facilitated reaction velocities are given by

$$v_{N_1} = k_{+1} s_1 - k_{-1} p_1, \quad v_{N_2} = k_{+2} s_2 - k_{-2} p_2, \tag{4.8a}$$

$$v_{F_1} = \frac{(r_{-1} D_4 - r_{+1} p_1 D_2)}{\mathcal{D}}, \quad v_{F_2} = \frac{(r_{-2} D_6 - r_{+2} p_1 D_2)}{\mathcal{D}}. \tag{4.8b}$$

After some algebra, we find that

$$v_{F_1} = \frac{k_{-3} k_{+3} r_{-1}^2 r_{-2}^2 \mathcal{R}_1 e_0^{tot} \left(\left(1 + \frac{k_{-3}+k_{+3}}{r_{-2}}\right)(s_1 - p_1) + \mathcal{R}_2 (s_1 p_2 - s_2 p_1)\right)}{\mathcal{D}}, \tag{4.9a}$$

$$v_{F_2} = \frac{k_{-3} k_{+3} r_{-1}^2 r_{-2}^2 \mathcal{R}_2 e_0^{tot} \left(\left(1 + \frac{k_{-3}+k_{+3}}{r_{-1}}\right)(s_2 - p_2) + \mathcal{R}_1 (s_2 p_1 - s_1 p_2)\right)}{\mathcal{D}}, \tag{4.9b}$$

where $\mathcal{D}$ simplifies to

$$\mathcal{D} = r_{-1}^2 r_{+1}^2 \left(k_{+3} + k_{-3}\right) \left[\begin{array}{l} \left(1 + \mathcal{R}_1 s_1 + \mathcal{R}_2 s_2\right)\left(1 + \mathcal{R}_1 p_1 + \mathcal{R}_2 p_2\right) \\ +\frac{1}{r_{-1}} \left(\begin{array}{l} k_{+3}\left(1 + \mathcal{R}_1 p_1 + \mathcal{R}_2 p_2\right)\left(1 + R_2 s_2\right) \\ +k_{-3}\left(1 + \mathcal{R}_1 s_1 + \mathcal{R}_2 s_2\right)\left(1 + \mathcal{R}_2 p_2\right) \end{array} \right) \\ +\frac{1}{r_{-2}} \left(\begin{array}{l} k_{+3}\left(1 + \mathcal{R}_1 p_1 + \mathcal{R}_2 p_2\right)\left(1 + R_1 s_1\right) \\ +k_{-3}\left(1 + \mathcal{R}_1 s_1 + \mathcal{R}_2 s_2\right)\left(1 + \mathcal{R}_1 p_1\right) \end{array} \right) \\ +\frac{1}{r_{-1} r_{-2}} \left(\begin{array}{l} k_{+3}^2\left(1 + \mathcal{R}_1 p_1 + \mathcal{R}_2 p_2\right) + k_{-3}^2\left(1 + \mathcal{R}_1 s_1 + \mathcal{R}_2 s_2\right) \\ +k_{+3} k_{-3}\left(2 + \mathcal{R}_1\left(s_1 + p_1\right) + \mathcal{R}_2\left(s_2 + p_2\right)\right) \end{array} \right) \end{array} \right]. \tag{4.10}$$

We can see that several terms cancel, so that

$$v_{F_1} = \frac{k_{-3} k_{+3} \mathcal{R}_1 e_0^{tot} \left(\left(1 + \frac{k_{-3} + k_{+3}}{r_{-2}}\right)\left(s_1 - p_1\right) + \mathcal{R}_2\left(s_1 p_2 - s_2 p_1\right)\right)}{\Sigma}, \tag{4.11a}$$

$$v_{F_2} = \frac{k_{-3} k_{+3} \mathcal{R}_2 e_0^{tot} \left(\left(1 + \frac{k_{-3} + k_{+3}}{r_{-1}}\right)\left(s_2 - p_2\right) + \mathcal{R}_1\left(s_2 p_1 - s_1 p_2\right)\right)}{\Sigma}, \tag{4.11b}$$

where

$$\Sigma = \left(k_{+3} + k_{-3}\right) \left[\begin{array}{l} \left(1 + \mathcal{R}_1 s_1 + \mathcal{R}_2 s_2\right)\left(1 + \mathcal{R}_1 p_1 + \mathcal{R}_2 p_2\right) \\ +\frac{1}{r_{-1}} \left(\begin{array}{l} k_{+3}\left(1 + \mathcal{R}_1 p_1 + \mathcal{R}_2 p_2\right)\left(1 + R_2 s_2\right) \\ +k_{-3}\left(1 + \mathcal{R}_1 s_1 + \mathcal{R}_2 s_2\right)\left(1 + \mathcal{R}_2 p_2\right) \end{array} \right) \\ +\frac{1}{r_{-2}} \left(\begin{array}{l} k_{+3}\left(1 + \mathcal{R}_1 p_1 + \mathcal{R}_2 p_2\right)\left(1 + R_1 s_1\right) \\ +k_{-3}\left(1 + \mathcal{R}_1 s_1 + \mathcal{R}_2 s_2\right)\left(1 + \mathcal{R}_1 p_1\right) \end{array} \right) \\ +\frac{1}{r_{-1} r_{-2}} \left(\begin{array}{l} k_{+3}^2\left(1 + \mathcal{R}_1 p_1 + \mathcal{R}_2 p_2\right) + k_{-3}^2\left(1 + \mathcal{R}_1 s_1 + \mathcal{R}_2 s_2\right) \\ +k_{+3} k_{-3}\left(2 + \mathcal{R}_1\left(s_1 + p_1\right) + \mathcal{R}_2\left(s_2 + p_2\right)\right) \end{array} \right) \end{array} \right]. \tag{4.12}$$

We can see that the addition of a second, competing ligand to the system adds some new terms to our facilitated flux equation. In order to better interpret the meaning of these additional terms, we will return to our system of interest, an unbiased transport system for facilitated diffusion, where the transport rates are given by $k_{-i} = k_{+i}$.

4.1.1 Unbiased Transport: $k_{-i} = k_{+i}$

If we assume that the transport is unbiased, as in the case of simple gradient-driven diffusion, i.e. $k_{-i} = k_{+i}$, then the steady-state reaction velocities of each ligand are given by

$$v_{N_1} = k_{+1}\left(s_1 - p_1\right), \tag{4.13a}$$

$$v_{N_2} = k_{+2}\left(s_2 - p_2\right), \tag{4.13b}$$

$$v_{F_1} = \frac{k_{+3}\mathcal{R}_1 e_0^{tot}\left(\left(1 + \frac{2k_{+3}}{r_{-2}}\right)\left(s_1 - p_1\right) + \mathcal{R}_2\left(s_1 p_2 - s_2 p_1\right)\right)}{\Omega}, \tag{4.13c}$$

$$v_{F_2} = \frac{k_{+3}\mathcal{R}_2 e_0^{tot}\left(\left(1 + \frac{2k_{+3}}{r_{-1}}\right)\left(s_2 - p_2\right) + \mathcal{R}_1\left(s_2 p_1 - s_1 p_2\right)\right)}{\Omega}, \tag{4.13d}$$

where

$$\Omega = 2\left[\begin{array}{l} \left(1 + \mathcal{R}_1 s_1 + \mathcal{R}_2 s_2\right)\left(1 + \mathcal{R}_1 p_1 + \mathcal{R}_2 p_2\right) \\ + \frac{k_{+3}}{r_{-1}}\left(\left(2 + \mathcal{R}_1 s_1 + 2\mathcal{R}_2 s_2\right)\left(1 + \mathcal{R}_2 p_2\right) + \mathcal{R}_1 p_1\left(1 + \mathcal{R}_2 s_2\right)\right) \\ + \frac{k_{+3}}{r_{-2}}\left(\left(2 + 2\mathcal{R}_1 s_1 + \mathcal{R}_2 s_2\right)\left(1 + \mathcal{R}_1 p_1\right) + \mathcal{R}_2 p_2\left(1 + \mathcal{R}_1 s_1\right)\right) \\ + \frac{2k_{+3}^2}{r_{-1}r_{-2}}\left(2 + \mathcal{R}_1\left(s_1 + p_1\right) + \mathcal{R}_2\left(s_2 + p_2\right)\right) \end{array}\right]. \tag{4.14}$$

Finally, we can see that the steady-state total reaction velocities can be expressed as

$$v_1 = k_{+1}\left(s_1 - p_1\right)\left(1 + \frac{k_{+3}\mathcal{R}_1 e_0^{tot}\left(1 + \frac{2k_{+3}}{r_{-2}}\right)}{k_{+1}\Omega}\right) + \theta, \tag{4.15a}$$

$$v_2 = k_{+2}\left(s_2 - p_2\right)\left(1 + \frac{k_{+3}\mathcal{R}_2 e_0^{tot}\left(1 + \frac{2k_{+3}}{r_{-1}}\right)}{k_{+2}\Omega}\right) - \theta, \tag{4.15b}$$

where

$$\theta = \frac{k_{+3}\mathcal{R}_1\mathcal{R}_2 e_0^{tot}\left(s_1 p_2 - s_2 p_1\right)}{\Omega}. \tag{4.16}$$

We can see that the formulae for the reaction velocities are reminiscent of the formula for the $N = 1$ case, (3.19c), where we expect an enhancement to each ligand, as long as the enzyme is present in the system. The major difference is that now there is an additional term directly representing an interaction between the ligands, θ.

No Second Ligand: $s_2 = p_2 = 0$

For a sanity check, we should examine the prediction of our extended model for the case where the second ligand is not present in the system initially. In this case, $s_2 = p_2 = 0$, so $\theta = 0$

and the total ligand flux for the first ligand simplifies to the formula for the $N = 1$ case, as we might expect:

$$\begin{aligned}
\Omega &= 2\left[\begin{array}{l}(1+R_1s_1)(1+R_1p_1)+\frac{k_{+3}}{r_{-1}}\left(2+R_1(s_1+p_1)\right)\\ +\frac{k_{+3}}{r_{-2}}\left(2+2R_1s_1\right)\left(1+R_1p_1\right)+\frac{2k_{+3}^2}{r_{-1}r_{-2}}\left(1+R_1(s_1+s_2)\right)\end{array}\right],\\
&= 2\left(1+\frac{2k_{+3}}{r_{-2}}\right)\left[(1+R_1s_1)(1+R_1p_1)+\frac{k_{+3}}{r_{-1}}\left(2+R_1(s_1+p_1)\right)\right],\\
v_1 &= \left(k_{+1}+\frac{k_{+3}R_1e_0^{tot}}{2\left[(1+R_1s_1)(1+R_1p_1)+\frac{k_{+3}}{r_{-1}}\left(2+R_1(s_1+p_1)\right)\right]}\right)(s_1-p_1),\\
v_2 &= 0.
\end{aligned}$$

No Back Pressure: $p_1 = p_2 = 0$

We would also like to know what the extended model predicts about the limiting case where there is no back pressure in the system. If the concentration of each free ligand is zero at the down-stream end of the system, i.e. $p_1 = p_2 = 0$, then $\theta = 0$. In this case, the ratio of the facilitated velocities will be:

$$\frac{v_{F_1}}{v_{F_2}} = \frac{\mathcal{R}_1\left(1+\frac{2k_{+3}}{r_{-2}}\right)s_1}{\mathcal{R}_2\left(1+\frac{2k_{+3}}{r_{-1}}\right)s_2} = \frac{r_{+1}r_{-2}\left(1+\frac{2k_{+3}}{r_{-2}}\right)s_1}{r_{+2}r_{-1}\left(1+\frac{2k_{+3}}{r_{-1}}\right)s_2} = \frac{r_{+1}\left(r_{-2}+2k_{+3}\right)s_1}{r_{+2}\left(r_{-1}+2k_{+3}\right)s_2}. \tag{4.17}$$

Furthermore, if $k_{+3} \ll r_{-1}, r_{-2}$, as we expect in the facilitated diffusion systems of interest, then the ratio is simply

$$\frac{v_{F_1}}{v_{F_2}} = \frac{r_{+1}r_{-2}s_1}{r_{+2}r_{-1}s_2}, \tag{4.18}$$

which is exactly the ratio of the ligand affinities multiplied by the ratio of the strengths of the free ligand gradients. However, since we know that in practice it is extremely difficult to completely remove the free ligands from the down-stream end of the system, the interaction between the ligands will not be as simple as in this idealized case.

Gradient-Free Second Ligand: $s_2 = p_2 = c_2 \neq 0$

Another case of possible interest is when the second ligand is present at the same concentration throughout the system, i.e. $s_2 = p_2 = c_2$. In the $N = 1$ case, if there is no gradient in the free

ligand concentration, then there will be no transport and the total flux will be zero. However, if we hold $s_2 = p_2 = c_2$:

$$
\begin{aligned}
v_1 &= k_{+1}\left(s_1 - p_1\right)\left(1 + \frac{k_{+3}R_1 e_0^{tot}\left(1 + \frac{2k_{+3}}{r_{-2}}\right)}{k_{+1}\Omega}\right) + \theta, && (4.19)\\
v_2 &= -\theta, && (4.20)\\
\theta &= \frac{k_{+3}R_1R_2e_0^{tot}c_2\left(s_1 - p_1\right)}{\Omega}, && (4.21)\\
\Omega &= 2\left[\begin{array}{l}
\left(1 + R_1s_1 + R_2c_2\right)\left(1 + R_1p_1 + R_2c_2\right)\\
+\frac{k_{+3}}{r_{-1}}\left(\left(2 + R_1s_1 + 2R_2c_2\right)\left(1 + R_2c_2\right) + R_1p_1\left(1 + R_2c_2\right)\right)\\
+\frac{k_{+3}}{r_{-2}}\left(\left(2 + 2R_1s_1 + R_2c_2\right)\left(1 + R_1p_1\right) + R_2c_2\left(1 + R_1s_1\right)\right)\\
+\frac{2k_{+3}^2}{r_{-1}r_{-2}}\left(2 + R_1\left(s_1 + p_1\right) + 2R_2c_2\right)
\end{array}\right], && (4.22)
\end{aligned}
$$

we can see that the gradient in the first ligand drives an up-stream (negative) flux in the second ligand where we would normally expect to see no flux at all! Furthermore, we find something else that is counter-intuitive: the presence of a second, gradient-free, ligand can actually increase the facilitated flux of the first ligand above the level of facilitation that would be seen if the second ligand was not present. This is exactly the phenomenon Ebel called "competitive acceleration" of the ligand transport [13]. It turns out that competitive acceleration can only occur in the gradient-free scenario when the down-stream ligand concentrations or partial pressures are non-zero. We would like to derive a condition that has to be satisfied to see competitive acceleration in our model. Using Ebel's key idea of showing that the partial derivative of the flux with respect to the concentration of the competing ligand is positive, we obtain the following relation. First, take the partial derivative of the total reaction velocity for the first ligand with respect to the concentration of the second ligand:

$$
\begin{aligned}
\frac{\partial v_1}{\partial c_2} &= \frac{\partial}{\partial c_2}\left(k_{+1}(s_1 - p_1)\right) + \frac{\partial}{\partial c_2}\left(\frac{k_{+3}R_1e_0^{tot}\left(\left(s_1 - p_1\right)\left(1 + \frac{2k_{+3}}{r_{-2}}\right) + R_2c_2\left(s_1 - p_1\right)\right)}{\Omega}\right),\\
&= \frac{k_{+3}R_1R_2e_0^{tot}\left(s_1 - p_1\right)\Omega - \left(k_{+3}R_1e_0^{tot}\left(\left(s_1 - p_1\right)\left(1 + \frac{2k_{+3}}{r_{-2}}\right) + R_2c_2\left(s_1 - p_1\right)\right)\right)\frac{\partial\Omega}{\partial c_2}}{\Omega^2},
\end{aligned}
$$

$$\frac{\partial\Omega}{\partial c_2} = 2R_2\left[\begin{array}{l} 2\left(1+R_2c_2\right)+R_1\left(s_1+p_1\right) \\ +\frac{k_{+3}}{r_{-1}}\left(4\left(1+R_2c_2\right)+R_1\left(s_1+p_1\right)\right) \\ +\frac{k_{+3}}{r_{-2}}\left(2+R_1\left(s_1+p_1\right)\right) \\ +\frac{4k_{+3}^2}{r_{-1}r_{-2}} \end{array}\right].$$

Then we can re-arrange some terms to find that

$$\frac{\partial v_1}{\partial c_2} = \frac{2k_{+3}R_1R_2e_0^{tot}\left(s_1-p_1\right)}{\Omega^2}\left(\frac{\Omega}{2}-\left(1+\frac{2k_{+3}}{r_{-2}}+R_2c_2\right)\frac{1}{2R_2}\frac{\partial\Omega}{\partial c_2}\right).$$

We know that the flux will be increasing with increasing c_2 if $\frac{\partial v_1}{\partial c_2} > 0$. We will assume that $s_1 > p_1$, so the condition is that the term in the parenthesis above must be positive, or

$$\frac{\Omega}{2} > \left(1+\frac{2k_{+3}}{r_{-2}}+R_2c_2\right)\frac{1}{2R_2}\frac{\partial\Omega}{\partial c_2}.$$

After some *extremely* tedious algebra, we find that the condition for competitive acceleration of ligand 1 by the presence of a gradient-free ligand 2 is

$$R_1^2s_1p_1-\frac{k_{+3}}{r_{-2}}R_1(s_1+p_1) > \left(1+\frac{2k_{+3}}{r_{-1}}\right)\left(1+\frac{2k_{+3}}{r_{-2}}\right)\left(1+\frac{R_2c_2}{\left(1+\frac{2k_{+3}}{r_{-2}}\right)}\right)^2. \tag{4.23}$$

Furthermore, the presence of a second competing ligand can cause the total ligand flux to be greater than it would be if the second ligand was not present at all. In other words the condition for competitive acceleration beyond the single-ligand flux level is given by $v_1|_{s_2=p_2=c_2} > v_1|_{s_2=p_2=0}$:

$$R_1^2s_1p_1-\frac{k_{+3}}{r_{-2}}R_1(s_1+p_1) > \left(1+\frac{2k_{+3}}{r_{-1}}\right)\left(1+\frac{2k_{+3}}{r_{-2}}\right)\left(1+\frac{R_2c_2}{\left(1+\frac{2k_{+3}}{r_{-2}}\right)}\right). \tag{4.24}$$

These conditions can be reformulated to answer the question, "Given a particular set of transport and reaction rates, and given a gradient in the first ligand, what must the level of the second ligand be in order to see an acceleration of the transport?" The conditions translate respectively to:

$$0 < c_2 < \frac{\left(1+\frac{2k_{+3}}{r_{-2}}\right)}{R_2}\left(\sqrt{\frac{R_1^2s_1p_1-\frac{k_{+3}}{r_{-2}}R_1(s_1+p_1)}{\left(1+\frac{2k_{+3}}{r_{-1}}\right)\left(1+\frac{2k_{+3}}{r_{-2}}\right)}}-1\right), \tag{4.25}$$

$$0 < c_2 < \frac{\left(1+\frac{2k_{+3}}{r_{-2}}\right)}{R_2}\left(\frac{R_1^2s_1p_1-\frac{k_{+3}}{r_{-2}}R_1(s_1+p_1)}{\left(1+\frac{2k_{+3}}{r_{-1}}\right)\left(1+\frac{2k_{+3}}{r_{-2}}\right)}-1\right). \tag{4.26}$$

Note that in order for the conditions (4.23) - (4.26) to yield results that make sense, we must have $R_1^2 s_1 p_1 - \frac{k_{+3}}{r_{-2}} R_1(s_1 + p_1) > 0$, which cannot be the case if $p_1 = 0$. In other words, observation of competitive acceleration requires non-zero down-stream ligand concentrations or partial pressures *for both ligands.*

4.2 Special Case: Carbon Monoxide and Oxygen

Now we would like to study the two ligand model in more detail in the context that relates to carbon monoxide poisoning. Without the presence of carbon monoxide (CO), oxygen (O_2) diffuses in the cell and the simple diffusive flux is augmented by the presence of hemoglobin or myoglobin. We will show that when carbon monoxide enters the system, the two ligands will compete for the facilitation by the carrier.

4.2.1 Comparison with Wittenberg's Experimental Results

We will now compare the results from our model to experiments carried out by Wittenberg in 1966 [86]. First Wittenberg measured the flux of oxygen and nitrogen through a milipore filter soaked with myoglobin. Nitrogen is not expected to bind to myoglobin, and was used by Wittenberg to infer the simple diffusional flux of the oxygen through the system in the absence of myoglobin. The experiment was repeated using a 22:1 mixture of oxygen to carbon monoxide. Wittenberg observed that the oxygen flux was still augmented when carbon monoxide was present, but that the facilitated component of the flux was smaller than when carbon monoxide was not present. Wittenberg did not observe an augmentation in the carbon monoxide flux. Note that Wittenberg's observations were complicated slightly by the oxidization of some of the myoglobin during the experiment. Let ligand 1 be oxygen and ligand 2 be carbon monoxide. As in the single ligand model, we can compare with Wittenberg's experimental ligand fluxes using the following relation,

$$J_i = \gamma \left(v_{N_i} + v_{F_i} \right) = J_{N_i} + J_{F_i}, \tag{4.27}$$

where γ is the scaling factor discussed in Section 3.4. As before, we can use the slope of a line fitting Wittenberg's experimental data points for non-facilitated nitrogen fluxes to determine values for k_{+1} and k_{+2} using the following method. Wittenberg states that the diffusive fluxes

of both oxygen and carbon monoxide can be approximated from the nitrogen flux using the coefficients for solubility in water and the molecular weights of the gases in the following way:

$$\frac{\text{Flux } O_2}{\text{Flux } N_2} = \frac{\alpha O_2}{\alpha N_2} \times \frac{\sqrt{28}}{\sqrt{32}} = 1.88, \qquad \frac{\text{Flux CO}}{\text{Flux } N_2} = \frac{\alpha CO}{\alpha N_2} \times \frac{\sqrt{28}}{\sqrt{28}} = 1.50. \tag{4.28}$$

In Figure 10 of Ref. [86], Wittenberg presents data sets for the two different experiments described above. Since both sets of experimental data are presented, we can use the oxygen-only data to fit k_{+3} as described below.

Recall that in the single ligand case, we have an expression for the maximum facilitated flux, J_{F_∞}, found in (3.25). If we fit the oxygen-only flux data, shown in Figure 4.2, using a straight line with slope γk_{+1}, then J_{F_∞} will be the "y"-intercept of that line. According to the notation for the N-ligand model, we have

$$J_{F_\infty} = \frac{\gamma k_{+3} e_0^{tot}}{2\left[(1 + R_1 p_1) + \frac{k_{+3}}{r_{-1}}\right]}, \qquad k_{+3} = \frac{2(1 + R_1 p_1) J_{F_\infty}}{\gamma e_0^{tot} - \frac{2J_{F_\infty}}{r_{-1}}}. \tag{4.29}$$

Now we can see whether our model predicts the right amount of reduction in the facilitated oxygen flux due to the presence of carbon monoxide. We assume that Wittenberg's experimental apparatus effects the down-stream ligand concentrations, or partial pressures, in the same way, i.e. $p_1 = p_2$ or $PP_{\ell_1} = PP_{\ell_2}$. In Figure 4.3, we see that if we assume that the downstream partial pressure is zero, then neither J_1 or J_2 fits the experimental data: J_1 is too small, and J_2 is too large. Based on the results of Section 3.4.4 this should not be surprising. Recall that we concluded that Wittenberg's experimental apparatus could not maintain a small enough back pressure to see a facilitation effect for carbon monoxide through either hemoglobin or myoglobin. We also calculated that the partial pressure necessary to reduce the facilitation of carbon monoxide through myoglobin to half of the maximum value was 0.03 $mm\ Hg$. If we assume that Wittenberg's experimental apparatus is capable of keeping the downstream partial pressures at half of that value, i.e. $PP_{\ell_1} = PP_{\ell_2} = 0.015\ mm\ Hg$, then we see suitable agreement between our model for both J_1 and J_2, as seen in the second panel of Figure 4.3. Recall that Wittenberg reported that some of the myoglobin oxidized during the course of the experiment, which may account for the mismatch between the slope of the calculated J_1 curve and the oxygen data in Figure 4.3.

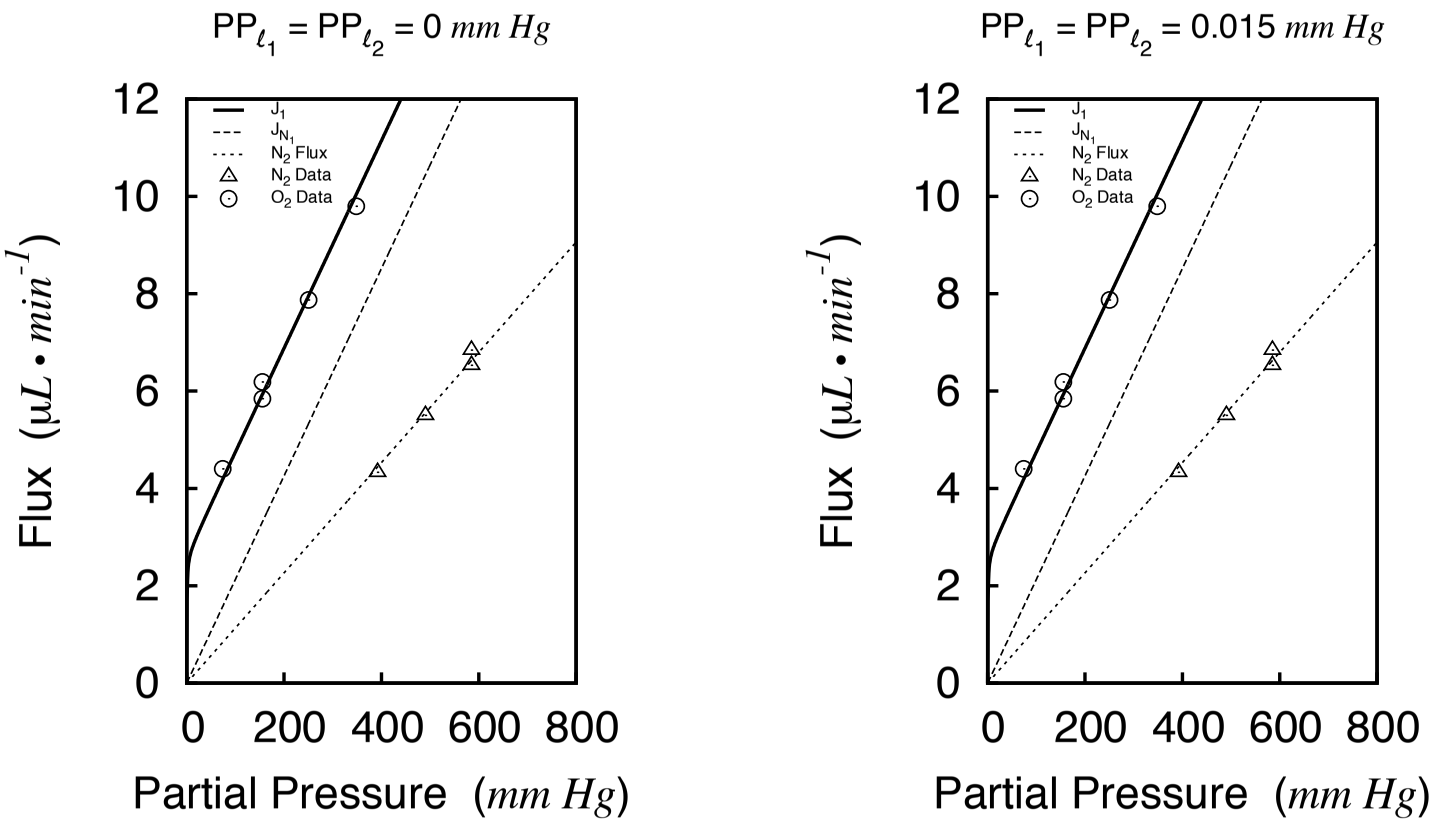

Figure 4.2: **2 Ligand Model Comparison with Wittenberg's Experimental Data - Oxygen Only.**
The value of $k_{+1} = 0.1514\ s^{-1}$ was fit using the slope of the nitrogen data, as described in the text. The values of $k_{+3} = 0.00935\ s^{-1}$ for $PP_{\ell_1} = PP_{\ell_2} = 0\ mm\ Hg$ and $k_{+3} = 0.00968\ s^{-1}$ for $PP_{\ell_1} = PP_{\ell_2} = 0.015\ mm\ Hg$ were fit using (4.29) as described in the text. The conversion factor $\alpha = 1.344 \times 10^9\ \mu L \cdot s \cdot min^{-1} \cdot mol^{-1}$ was determined using the ideal gas law and Wittenberg's experimental conditions, as in Section 3.4. The values of $\sigma_1 = 1.8 \times 10^{-9}\ mol \cdot cm^{-3} \cdot mm\ Hg^{-1}$ and $\sigma_2 = 1.08 \times 10^{-9}\ mol \cdot cm^{-3} \cdot mm\ Hg^{-1}$ are from Ref. [72] and Ref. [53] respectively. The other parameter values were, from Ref. [86], $e_0^{tot} = 7.2 \times 10^{-6}\ mol \cdot cm^{-3}$, $\rho = 0.79$, $A = 11.5\ cm^2$, $\ell = 0.64 \times 10^{-2}\ cm$, $r_{-1} = 11\ s^{-1}$, $r_{+1} = 14 \times 10^9\ cm^3 \cdot s^{-1} \cdot mol^{-1}$, $r_{-2} = 0.017\ s^{-1}$, $r_{+2} = 0.5 \times 10^9\ cm^3 \cdot s^{-1} \cdot mol^{-1}$.

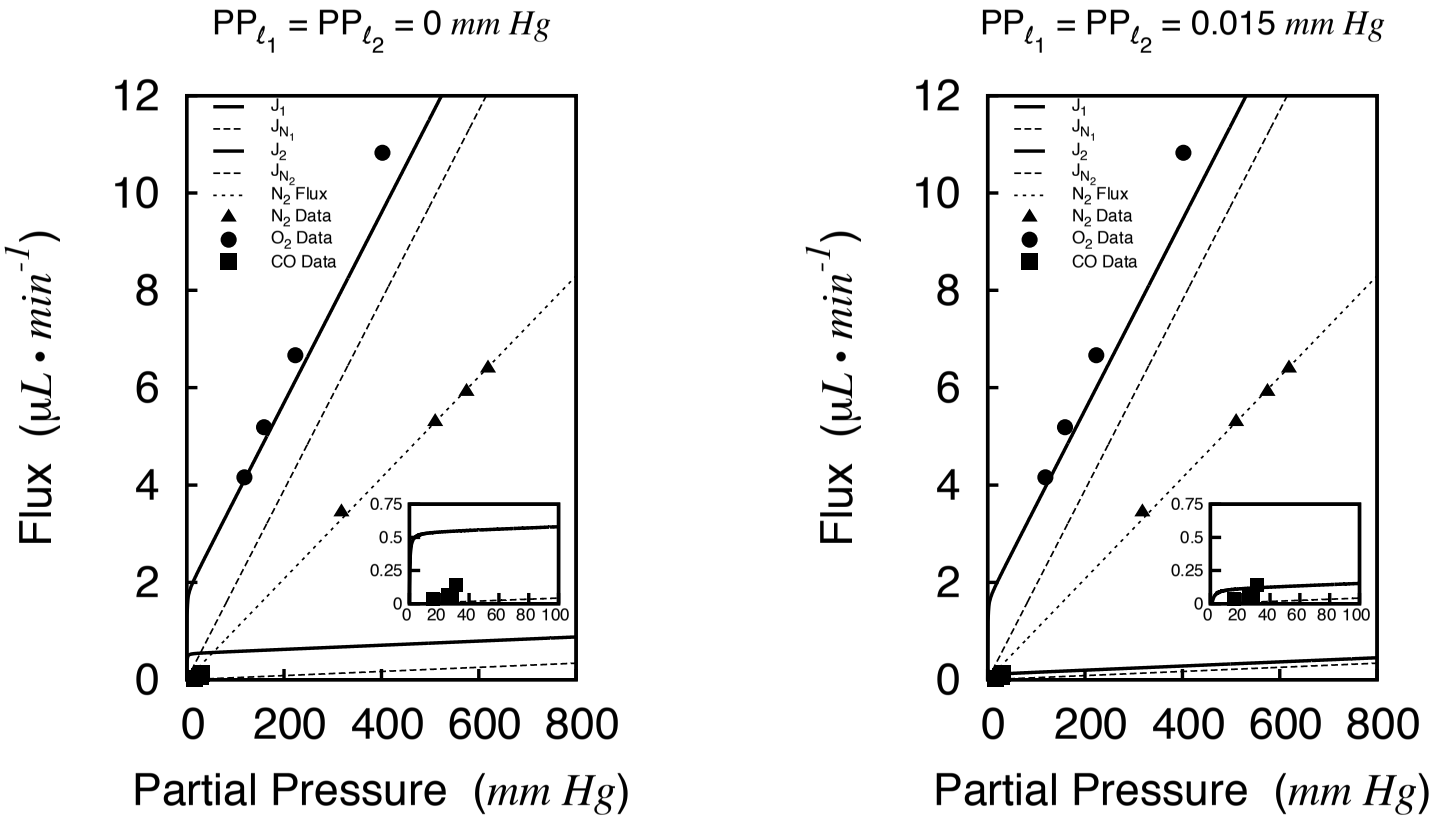

Figure 4.3: **2 Ligand Model Comparison with Wittenberg's Experimental Data - Oxygen and Carbon Monoxide.** The values of $k_{+1} = 0.1386\ s^{-1}$ and $k_{+2} = 0.1106\ s^{-1}$ were fit using the slope of the nitrogen data, as described in the text. The other parameters are as in Figure 4.2.

Limiting Values of the Facilitated Fluxes

As in Section 3.4, we can find the limiting values for the facilitated fluxes, analogous to (3.25). For the scenario where the ratio of ligand 1 to ligand 2 is held constant, i.e. $s_2 = \lambda s_1$, as in Wittenberg's experiment, we obtain the following expressions:

$$J_{F_{1_\infty}} = \lim_{\substack{s_2=\lambda s_1 \\ s_1\to\infty}} J_{F_1} = \frac{\gamma k_{+3} R_1 e_0^{tot}\left[\left(1+\frac{2k_{+3}}{r_{-2}}\right) - R_2\left(\lambda p_1 - p_2\right)\right]}{\Omega_\infty}, \tag{4.30a}$$

$$J_{F_{2_\infty}} = \lim_{\substack{s_2=\lambda s_1 \\ s_1\to\infty}} J_{F_2} = \frac{\gamma k_{+3} R_2 e_0^{tot}\left[\left(1+\frac{2k_{+3}}{r_{-1}}\right) + R_1\left(\lambda p_1 - p_2\right)\right]}{\Omega_\infty}, \tag{4.30b}$$

$$\Omega_\infty = 2\begin{bmatrix} (1+R_1p_1+R_2p_2)(R_1+\lambda R_2) \\ \frac{k_{+3}}{r_{-2}}\left(R_1(2+2R_1p_1+R_2p_2)+\lambda R_2(1+R_1p_1)\right) \\ \frac{k_{+3}}{r_{-1}}\left(R_1(1+R_2p_2)+\lambda R_2(2+R_1p_1+2R_2p_2)\right) \\ \frac{2k_{+3}^2}{r_{-1}r_{-2}}\left(R_1+\lambda R_2\right) \end{bmatrix}. \tag{4.30c}$$

We would like to use these expressions to compare the predictions of our model with Wittenberg's observation that the facilitated flux of oxygen without the presence of carbon monoxide was approximately twice that when carbon monoxide was present.[2] Our model predicts that if $PP_{\ell_1} = PP_{\ell_2} = 0\ mm\ Hg$, then the ratio is approximately 1.78, and if $PP_{\ell_1} = PP_{\ell_2} = 0.015\ mm\ Hg$, then the ratio is approximately 1.94.[3] We believe that the predictions of our model are consistent with the data in this case. Furthermore, our model predicts a limiting facilitated flux for carbon monoxide of $J_{F_{2_\infty}} \approx 0.74\ \mu L \cdot min^{-1}$ or $J_{F_{2_\infty}} \approx 0.32\ \mu L \cdot min^{-1}$, without and with back pressure respectively. Wittenberg reported that the carbon monoxide

[2]On page 110 of Ref. [86], Wittenberg states that the facilitated component of the oxygen flux without the presence of carbon monoxide was 2.95 $\mu L \cdot min^{-1}$ and 1.35 $\mu L \cdot min^{-1}$ with the presence of carbon monoxide, for the experimental data reproduced in Figures 4.2 and 4.3. This gives a ratio of $\frac{2.95\ \mu L \cdot min^{-1}}{1.35\ \mu L \cdot min^{-1}} = 2.18519$.

[3]These ratios are calculated as follows. Without the presence of carbon monoxide, the values $J_{F_\infty} = 2.62928\ \mu L \cdot min^{-1}$ and $J_{F_\infty} = 2.62948\ \mu L \cdot min^{-1}$ used to calculate k_{+3}, from the data in Figure 4.2 with $PP_{\ell_1} = 0\ mm\ Hg$, and $PP_{\ell_1} = 0.015\ mm\ Hg$ respectively. With carbon monoxide present in the system, using the parameters from Figure 4.3, along with (4.30), we calculate that $J_{F_{1_\infty}} = 1.48052\ \mu L \cdot min^{-1}$ and $J_{F_{1_\infty}} = 1.3575\ \mu L \cdot min^{-1}$ without and with back pressure, respectively. These calculations yield

$$\frac{J_{F_\infty}}{J_{F_{1_\infty}}} = \frac{2.62928\ \mu L \cdot min^{-1}}{1.48052\ \mu L \cdot min^{-1}} = 1.77591$$

$$\frac{J_{F_\infty}}{J_{F_{1_\infty}}} = \frac{2.62948\ \mu L \cdot min^{-1}}{1.3575\ \mu L \cdot min^{-1}} = 1.937$$

Table 4.1: **Parameter Values from Britton & Murray, Ref. [5].**

Our Notation	Value	([5] Notation)
D_{O_2}	$1.2 \times 10^{-5}\ cm^2 \cdot s^{-1}$	(D_1)
D_{CO}	$1.3 \times 10^{-5}\ cm^2 \cdot s^{-1}$	(D_2)
D_{Hb}	$2.45 \times 10^{-7}\ cm^2 \cdot s^{-1}$	(D)
ℓ	$2.2 \times 10^{-2}\ cm$	(ℓ)
e_0^{tot}	$1.2 \times 10^{-5}\ mol \cdot cm^{-3}$	(c_t)
r_{+1}	$2.85 \times 10^{9}\ cm^3 \cdot mol^{-1} \cdot s^{-1}$	(k_1)
r_{-1}	$40\ s^{-1}$	(k_{-1})
r_{+2}	$2 \times 10^{8}\ cm^3 \cdot mol^{-1} \cdot s^{-1}$	(k_2)
r_{-2}	$8 \times 10^{-3}\ s^{-1}$	(k_{-2})
s_1	$2 \times 10^{-7}\ mol \cdot cm^{-3}$	(γ_1)
p_1	$s_1 \times 10^{-2}$	$(c_1(\ell))$
s_2	λs_1	(γ_2)

flux reproduced in Figure 4.3 was "...just above the detectable level as would be expected from simple diffusion alone..." [86]. The above calculations from our model show that if a small back pressure was present, as we suspect, Wittenberg would have had trouble measuring the very small facilitation effect for carbon monoxide in this scenario.

These calculations also resolve the paradox that Wittenberg was unable to measure the facilitation of carbon monoxide, while Mochizuki and Forster were able to do so. Wittenberg's experimental set-up was probably both incapable of keeping the down-stream partial pressure low enough to easily measure the facilitation effect for carbon monoxide, and it is also likely that his instruments were not capable of resolving the small facilitation effect that was evident in the data (seen in the inset plots of Figure 4.3).

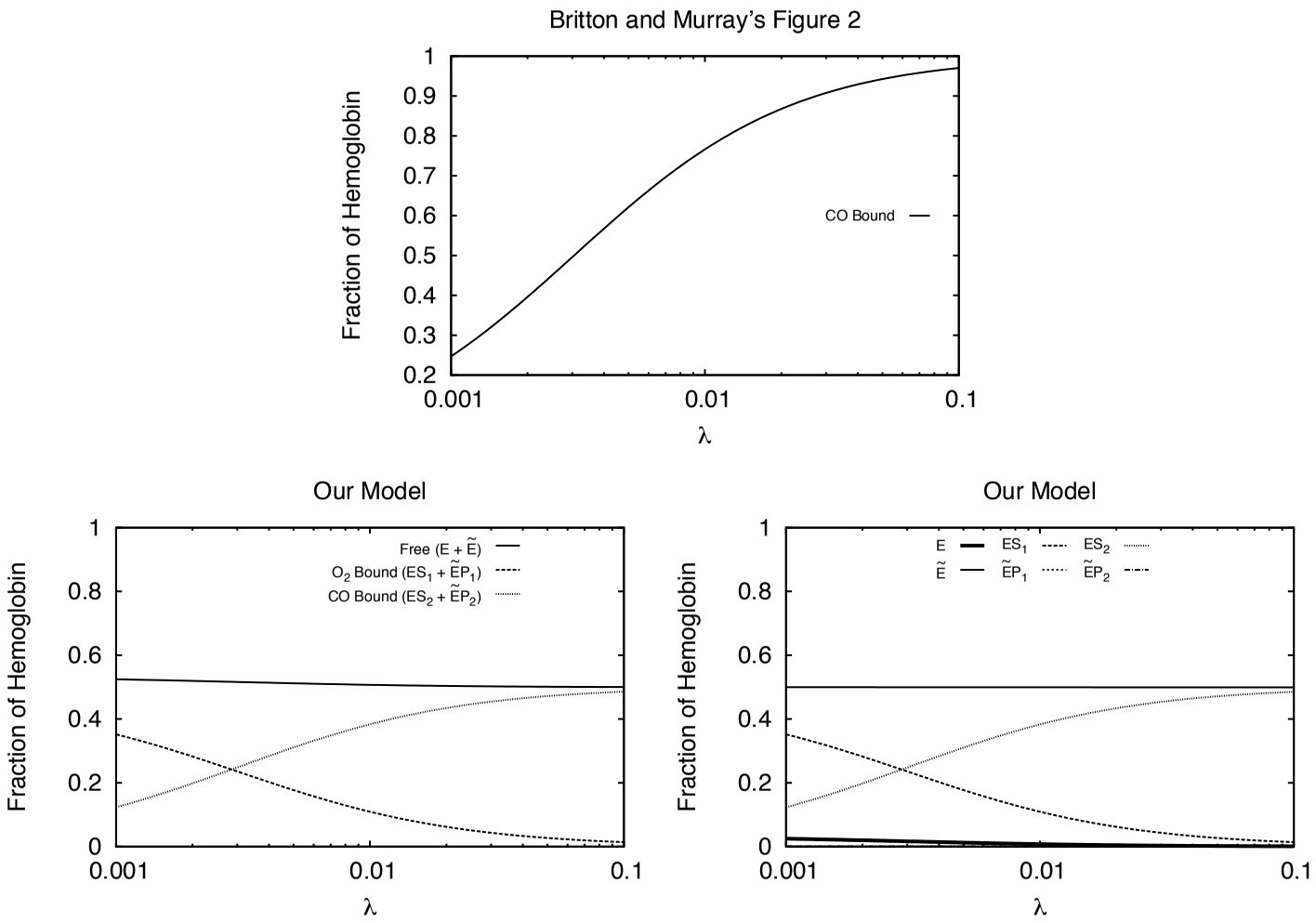

Figure 4.4: **Fraction of Hemoglobin Predictions for Britton & Murray's Model and our Extended Model.** The top panel shows Britton & Murray's Figure 2, reproduced from Figure 2.8. The bottom panels are plotted using (4.5) and (A.11), with the parameters from Table 4.1 and $k_{+1} = D_{O_2}/\ell$, $k_{+2} = D_{CO}/\ell$, $k_{+3} = D_{Hb}/\ell$, $p_1 = p_2 = 0$, with $s_1 = \gamma_1$ fixed, while varying λ.

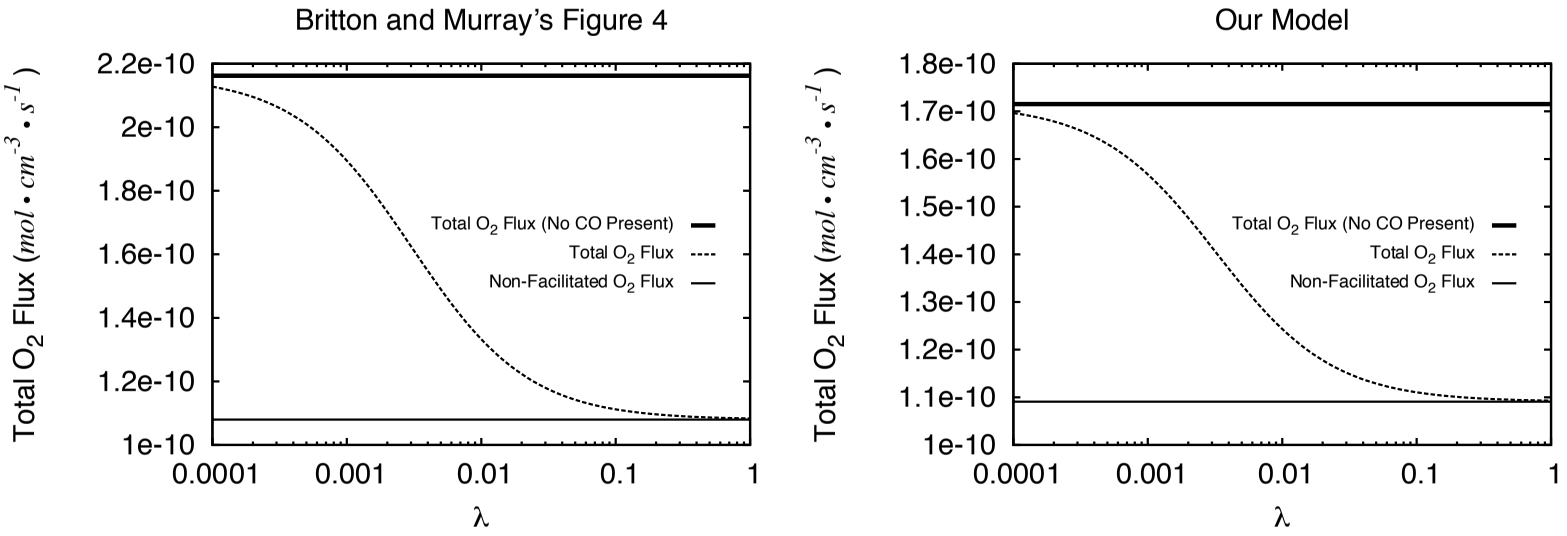

Figure 4.5: **Comparison with Britton & Murray's Figure 4 from Ref. [5].**
Britton and Murray's Figure 4 is reproduced from Figure 2.9. Our figures are plotted using (4.13) and (4.14) with ligand 1 as oxygen, ligand 2 as carbon monoxide. Parameters used are in Table 4.1, and we have taken $k_{+1} = D_{O_2}/\ell$, $k_{+2} = D_{CO}/\ell$, $k_{+3} = D_{Hb}/\ell$, $p_1 = p_2 = 0$, with $s_1 = \gamma_1$ fixed.

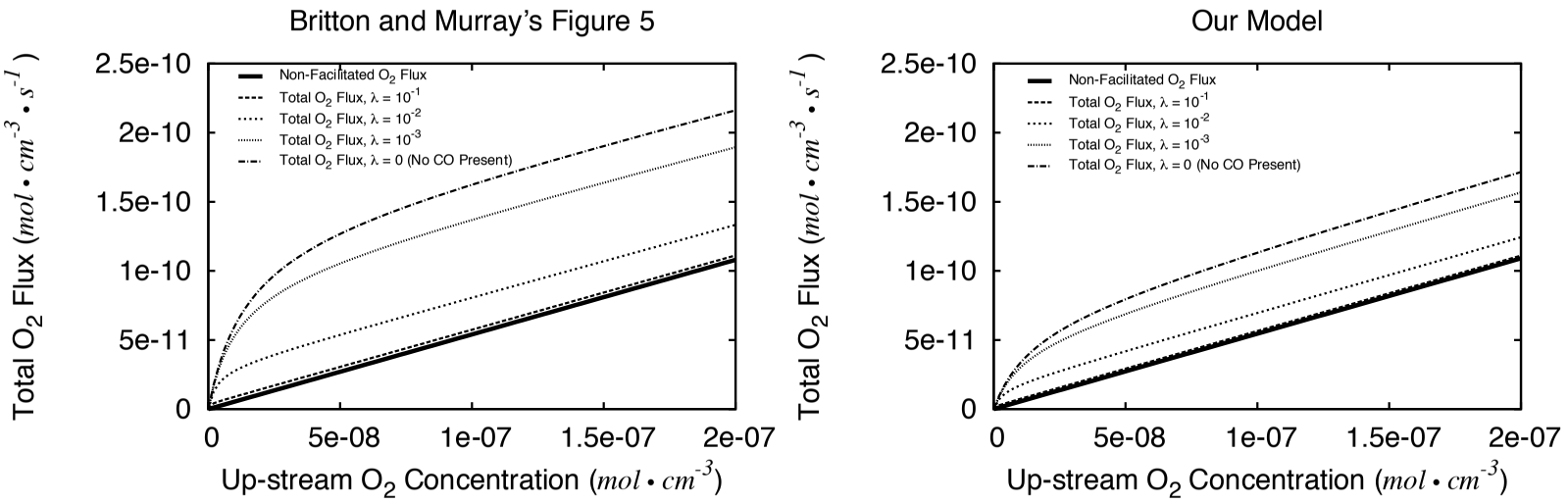

Figure 4.6: **Comparison with Britton & Murray's Figure 5 from Ref. [5].**
Britton and Murray's Figure 5 is reproduced from Figure 2.10. Our figures are plotted using (4.13) and (4.14) with ligand 1 as oxygen, ligand 2 as carbon monoxide. Parameters used are in Table 4.1, and we have taken $k_{+1} = D_{O_2}/\ell$, $k_{+2} = D_{CO}/\ell$, $k_{+3} = D_{Hb}/\ell$, $p_1 = p_2 = 0$.

4.2.2 Comparison with Britton & Murray's Model

A major difference between our model and Britton & Murray's model is that they predict that the fraction of carbon monoxide-bound hemoglobin will have the same value at both the up- and down-stream ends of the system, and furthermore, that as $\lambda \to \infty$, all of the hemoglobin will be bound by carbon monoxide. Our model makes a radically different prediction that much of the down-stream hemoglobin will remain free from either oxygen or carbon monoxide, as can be seen in Figure 4.4. In other words, our model predicts a gradient in *both* the oxygen- and carbon monoxide-bound hemoglobin, as well as the free hemoglobin, while Britton and Murray only allow for a gradient in the free and oxygen-bound hemoglobin. This difference can be ascribed to our different methods of dealing with the boundary conditions at the ends of the system. In our model, we fix both the up- and down-stream concentrations of both of the ligands, but Britton and Murray fix the up-stream concentrations of both ligands and assume that the ratio between the up- and down-stream oxygen concentrations is 10^{-2}, then solve for the down-stream carbon monoxide concentration using the (constant) value of the carbon monoxide-bound hemoglobin in terms of the up-stream ligand concentrations. This is probably the basis for the difference in magnitudes of the facilitation effects between the two models which can be seen in Figures 4.5 and 4.6. However, the models still agree qualitatively regarding the relative facilitation of the two ligands: even a small amount of carbon monoxide present in the system will significantly reduce the facilitation of the oxygen transport.

4.2.3 Comparison with Mochizuki & Forster's Experimental Results

Finally, we would like to compare the results from our two ligand model with the famous experimental results from Mochizuki & Forster (MF) in Ref. [46]. MF found that hemoglobin facilitated carbon monoxide transport with a low partial pressure gradient. They also found that the addition of gradient-free oxygen increased the facilitation effect on the carbon monoxide flux. Their experimental results are reproduced in the top panel of Figure 4.7.

Conversion to MF's Units

Note that we will assume for this section that ligand 1 is carbon monoxide and ligand 2 is oxygen, since oxygen is the gradient-free ligand in this system.

We can see that MF use a different system of units than Wittenberg, Murray, and others, so we must figure out how to relate these units to those we have been using in our model. Table 4.2 shows values for MF's experimental conditions, conversion rates, and the parameter values used in our model. First of all, we note that mm^3/min and $\mu L/min$ are equivalent units. Next, we can convert our ligand concentrations to partial pressures via Henry's law, as before,

$$s_1 = \sigma_{CO} \times PP_{0_1}, \qquad p_1 = \sigma_{CO} \times PP_{\ell_1}, \tag{4.31}$$

$$s_2 = \sigma_{O_2} \times PP_{0_2}, \qquad p_2 = \sigma_{O_2} \times PP_{\ell_2}, \tag{4.32}$$

where now the units on the partial pressures and solubilities are given in $\%\ atm$.

Before we can compare the results from our model with MF's experimental results, we must determine which value to use for one of the transition rates. We chose to fit k_{+1} using the slope of the "unfacilitated diffusion" line on Figure 2 of Ref. [46]. Based on the slope of their line and the scale on their graph, we calculate that the slope is $m \approx 3.4 \times 10^{-2}\ \frac{mm^3}{min\ \%\ atm}$. We know that this slope should match the slope of J_{N_1} from our model:

$$\begin{aligned} \alpha\rho A\ell k_{+1}\sigma_{CO}\left(PP_{0_1} - PP_{\ell_1}\right) &= 3.4 \times 10^{-2}\left(PP_{0_1} - PP_{\ell_1}\right), \\ \Rightarrow \quad k_{+1} &= \frac{3.4 \times 10^{-2}}{\alpha\rho A\ell\sigma_{CO}} \approx 3.75 \times 10^{-2} s^{-1}, \end{aligned} \tag{4.33}$$

where $\alpha = 1.295 \times 10^9\, \frac{\mu L}{min}\frac{s}{mol}$ is the conversion factor determined using the ideal gas law for MF's experimental conditions, ρA is the effective area of the surface of the milipore filter, and ℓ is the length of the milipore filter. Once we have fit the value for k_{+1}, we can calculate k_{+2} and k_{+3} using

$$\frac{k_{+2}}{k_{+1}} = \frac{D_{O_2}}{D_{CO}}, \qquad \frac{k_{+3}}{k_{+1}} = \frac{D_{Hb}}{D_{CO}}. \tag{4.34}$$

All of the other parameter values are known from the literature, and can be found in Table 4.2, so we should now be able to compare results from our model with MF's experimental data.

Table 4.2: **Parameter Values for Mochizuki & Forster's Experiments.**

Experimental Conditions [46]	
T	$37°C$
ℓ	$1.5 \times 10^{-2}\ cm$
A	$7\ cm^2$
ρ	0.79
e_0^{tot}	$4 \times \frac{10.8\ g}{100\ mL}$ $= 6.7 \times 10^{-6}\ \frac{mol}{cm^3}$
Conversion Factors	
$1\ mol$	$21.58\ L$ (ideal gas law)
$1\ \frac{mol}{s}$	$1.295 \times 10^9\ \frac{\mu L}{min}$
$\frac{mm^3}{min}$	$\frac{\mu L}{min}$
$1\ mm\ Hg$	$\frac{100}{760}\ \%\ atm$
Parameters From the Literature	
σ_{CO}	$1.11 \times 10^{-9}\ \frac{mol}{cm^3\ mm\ Hg}$ [38] $= 8.436 \times 10^{-9}\ \frac{mol}{cm^3\ \%\ atm}$
σ_{O_2}	$1.44 \times 10^{-9}\ \frac{mol}{cm^3\ mm\ Hg}$ [38] $= 1.0944 \times 10^{-8}\ \frac{mol}{cm^3\ \%\ atm}$
D_{CO}	$1.7 \times 10^{-5}\ \frac{cm^2}{s}$ [38]
D_{O_2}	$2.1 \times 10^{-5}\ \frac{cm^2}{s}$ [38]
D_{Hb}	$5.33 \times 10^{-7}\ \frac{cm^2}{s}$ [38]
r_{+CO}	$6.75 \times 10^8\ \frac{cm^3}{s\ mol}$ [53]
r_{-CO}	$0.05\ \frac{1}{s}$ [53]
r_{+O_2}	$2.85 \times 10^9\ \frac{cm^3}{s\ mol}$ [72]
r_{-O_2}	$40\ \frac{1}{s}$ [72]

Results

Before we can proceed with the comparison, one more problem still needs to be resolved. MF stated that there was initially no carbon monoxide at the down-stream end of their system, but that the level of down-stream carbon monoxide rose during the course of the experiment, and the average value over the 30- or 60-minute period of the experiment was used to calculate the equilibrated carboxyhemoglobin concentration. They claimed that although the down-stream carbon monoxide concentration changed, the carbon monoxide flux did not change after the first 30 minutes of the experiment, so they concluded that a steady state had been reached. Therefore, it is not at all clear what values to use in our model for the down-stream carbon monoxide partial pressures or concentrations. With these complications regarding the unreported down-stream ligand partial pressures, we cannot expect a perfect fit between our model and the data. However, we would still like to see if our model can recreate the qualitative behavior seen in the experimental data.

If we assume that the down-stream partial pressures are zero, as shown in the bottom left panel in Figure 4.7, we find that the curves from the model do not fit the data at all well. This is to be expected, since we know from Section 4.1 that the competitive acceleration of the carbon monoxide facilitation will only be seen if there are non-zero back pressures, or down-stream concentrations, for *both* ligands.

We explored using different values for the back pressure, and chose to report a graph with $PP_{\ell_1} = 0.04$ % atm in the lower right panel of Figure 4.7, since that value produced a plot with suitable agreement between MF's data and the model curves for the 0% O_2 and 21% O_2 data sets. While the curves are not a particularly good fit to the 7 % O_2 or 100 % O_2 data sets, we can at least see that our model shows the right qualitative behavior. Our model predicts that the facilitation effect increases with the increasing presence of the second, gradient-free, ligand, i.e. competitive acceleration occurs, which can also clearly be seen in the experimental data. Furthermore, as we mentioned in Section 2.2.2, Kreuzer & Hoofd's model was also unable to reproduce the behavior of the 7 % atm data set, which suggests that there may be an error in the experiment or graph [38].

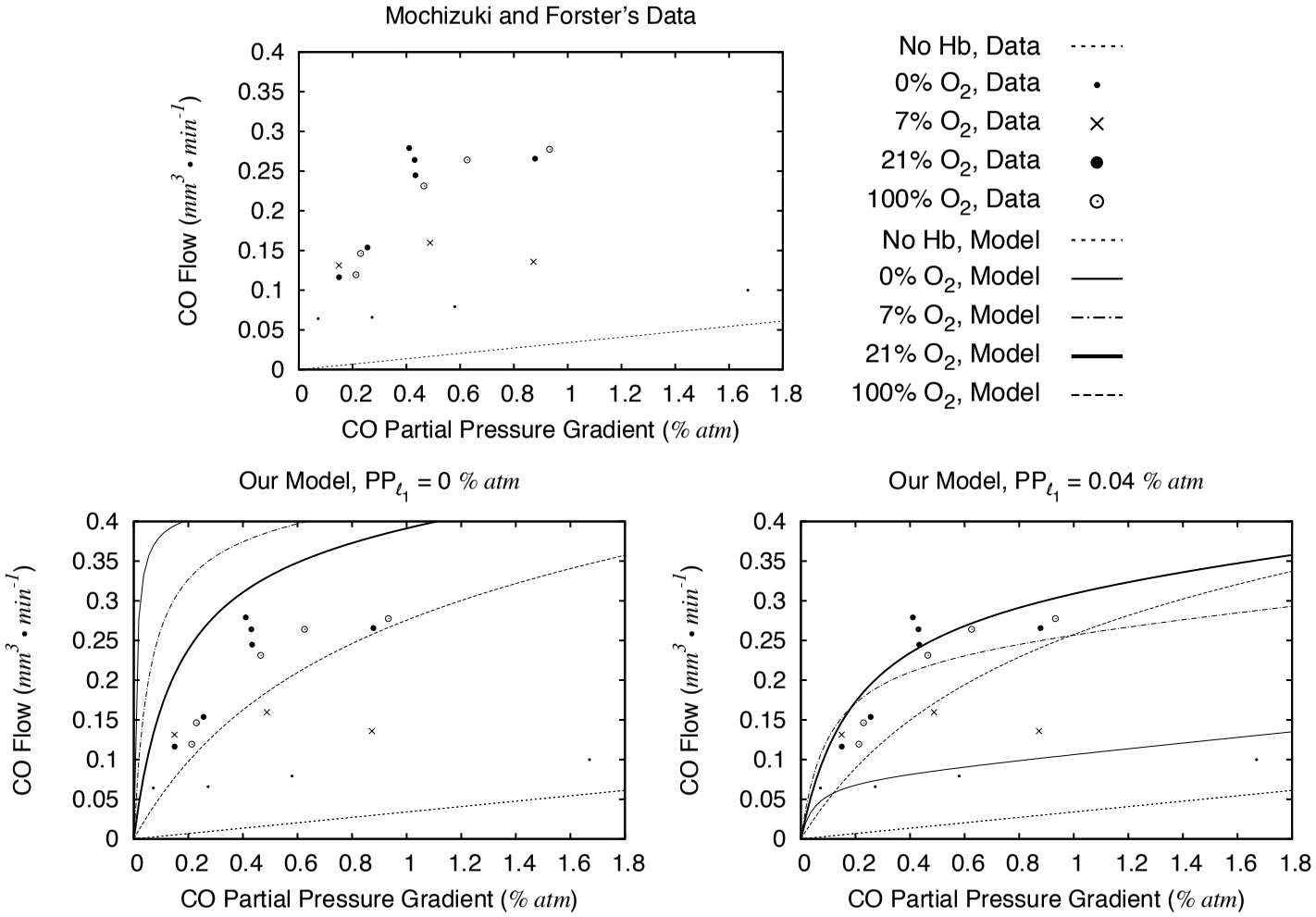

Figure 4.7: **Comparison with Mochizuki & Forster's Experimental Data.**
Mochizuki and Forster's data was reproduced from Figure 2 of Ref. [46]. Our curves were generated using (4.13) and (4.14) with carbon monoxide as ligand 1 and oxygen as ligand 2. The parameter values used appear in Table 4.2, and k_{+1}, k_{+2}, k_{+3} are as in (4.33) and (4.34). In the bottom left panel, we have set $PP_{L_1} = 0\%\ atm$, and in the bottom right panel, $PP_{L_1} = 0.04\ \%\ atm$, as described in the text.

4.3 Conclusions

Our N-ligand model captures all of the behaviors outlined in Ebel's work that were listed in Section 2.2.4: saturation of the carrier molecule, competitive inhibition, counter-transport, and competitive acceleration. Furthermore, we found that competitive acceleration requires non-zero downstream concentrations of *both* ligands. If the ratio of the up-stream ligand concentrations is held constant, while the down-stream concentrations are zero, we find that the presence of even a small amount of of carbon monoxide will significantly reduce the facilitation of oxygen, which is consistent with the predictions of Britton & Murray's model. We have also shown that our two ligand model can resolve the paradox of Wittenberg and Mochizuki & Forster's seemingly contradictory experimental results concerning the simultaneous diffusion of carbon monoxide and oxygen: both sets of experimental results can be reproduced with our model.

Part II

MATHEMATICAL MODELS FOR THE BROWNIAN RATCHET

Chapter 5

HISTORY OF THE BROWNIAN RATCHET AND MOLECULAR MOTORS

In this Chapter, we give a brief introduction to the most common molecular motor systems, introduce the concept of a "Brownian Ratchet" (BR), and give an overview of the history of the previous modeling efforts. We also discuss the connection between mathematical models for the BR and mathematical models for traditional molecular motors such as myosin and kinesin. Finally, we show that the measured stalling force for a molecular motor can be different for different types of applied measurement forces, i.e. the measured stalling force depends on the character of the measurement force itself, and there is indeed an uncertainty in the way that a molecular motor operates in the absence of an external force.

5.1 Review of Molecular Motors

At the most basic level, a molecular motor is a protein molecule in the cell that generates force and may cause transport of some material. A loose analogy can be made between conventional molecular motors, such as myosin and kinesin, and trains. Myosin and kinesin travel along actin filaments and tubulin microtubules respectively, similar to the way that trains travel on tracks. The chemical process of ATP hydrolysis acts as the fuel that myosin and kinesin motors burn in order to move along their tracks. However, unlike trains, molecular motors only move unidirectionally *on average* over time, and may occasionally take steps backwards. Another mode for generating motion or transport in the cell is via polymerization (or depolymerization) of microfilaments or microtubules themselves. Classic examples include the depolymerization of the spindle pulling apart sister chromatids during anaphase, and sickle hemoglobin polymerization creating deformed "sickle" red blood cells. If we represent the position of the end of the polymer as a mathematical point, the analysis of the growth or shrinking of a polymer and the motion of a conventional molecular motor become closely related. T. L. Hill developed a simple mathematical model that describes the process of polymerization or depolymerization

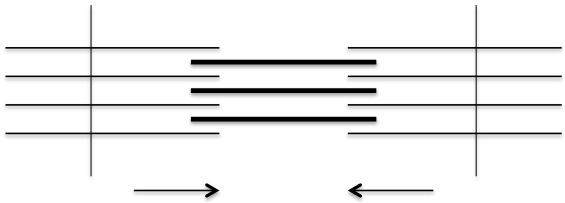

Figure 5.1: **Sarcomere Sketch.**
Schematic diagram of a sarcomere: the fundamental unit of striated muscle. The thick dark lines represent the thick filaments, the thin horizontal lines represent the thin filaments, and the vertical lines represent the Z lines, all of which are described in the text. The arrows represent the direction of motion during muscle contraction.

against a force, both as a purely mechanical process and including the chemical process of ATP or GTP hydrolysis [28]. We will now review what is known (or widely accepted) about several particular molecular motors as well as the basic mathematical models used to describe them.

5.1.1 The Actin-Myosin Muscle Motor

The interaction and relative motion between actin and myosin is what drives muscle contractions. Skeletal, or striated, muscles are attached to bones and are responsible for voluntary motions, such as the bending and straightening of an arm or leg. These muscles consist of thousands of cylindrical muscle fibers which are bundled by connective tissue containing blood vessels and nerves. The muscle fibers are made up of many cells called myoblasts. Muscle fiber is composed of a chain of myofibrils, as well as the usual cellular content such as mitochondria, nuclei, and endoplasmic reticulum. The fundamental unit of the myofibrils (and therefore, striated muscle) is the sarcomere.

Figure 5.1 shows a schematic diagram of a sarcomere. A sarcomere consists of horizontal alternating parallel thin and thick filaments. Thin filaments are made up of actin, troponin, and tropomyosin, and are approximately 5 nm in diameter. Thick filaments consist of hundreds of joined myosin molecules, and are roughly 15 nm in diameter. The vertical borders of the sarcomere are the Z lines, from which the thin filaments extend in both directions. In an electron micrograph, the parts of the thin filaments that do not overlap with the thick filaments appear

as a light region called the I band. The thick filaments appear as a dark region called the A band. The region where the thin and thick filaments do not overlap is called the H zone, the center of which is the M line.

If we zoom in even more, we can examine the interaction of one pair of myosin heads with an actin filament. The motion-producing process can be described as a cycle through four distinct stages, as seen in Figure 5.2. In the first stage pictured, we see that the myosin head nearest the actin filament points to the left. The myosin head in question has bound ADP and Pi, and has formed a weak bond with the particular shaded site on the actin filament. In stage two, the myosin head is strongly bonded, or docked, with the shaded actin site and ADP and Pi are still bound to the myosin head. The transition to the third stage comes when the Pi is released, initiating the *power stroke* in which the myosin head moves to point to the right, which in turn slides the actin filament in that direction by approximately 100 Å. After the power stroke, the ADP dissociates from the myosin head, a new ATP binds to the head, and the system returns to the weakly bound state seen in stage four. Then ATP hydrolysis occurs, moving the head back to the left-pointing state seen in stage one, and the process can repeat.[1] One can immediately see that this process lends itself to discrete-state stochastic/kinetic models, which will be discussed in Section 5.2.1.

5.1.2 The Kinesin Transportation Motor

Kinesin is involved in many important cellular processes including: membrane transport, mitosis, meiosis, mRNA and protein transport, ciliary and flagellar genesis, as well as microtubule polymer dynamics. Microtubules act as the tracks that kinesin motors travel along. Microtubules are hollow cylinders composed of 13 strands of linear polymers made out of tubulin dimers, called protofilaments. The tubulin dimer subunits are made up of one α- and one β-tubulin. While microtubules can grow and shrink at both ends via polymerization or depolymerization of the tubulin subunits, one end always grows or shrinks more rapidly. The more active end of the microtubule is known as the plus end, and the other end is the minus end, highlighting the polarity of the microtubule. Microtubule ends abruptly switch between

[1] A nice movie showing the motion of the actin-myosin molecular motor can be found at http://www.sci.sdsu.edu/movies/actin_myosin_gif.html.

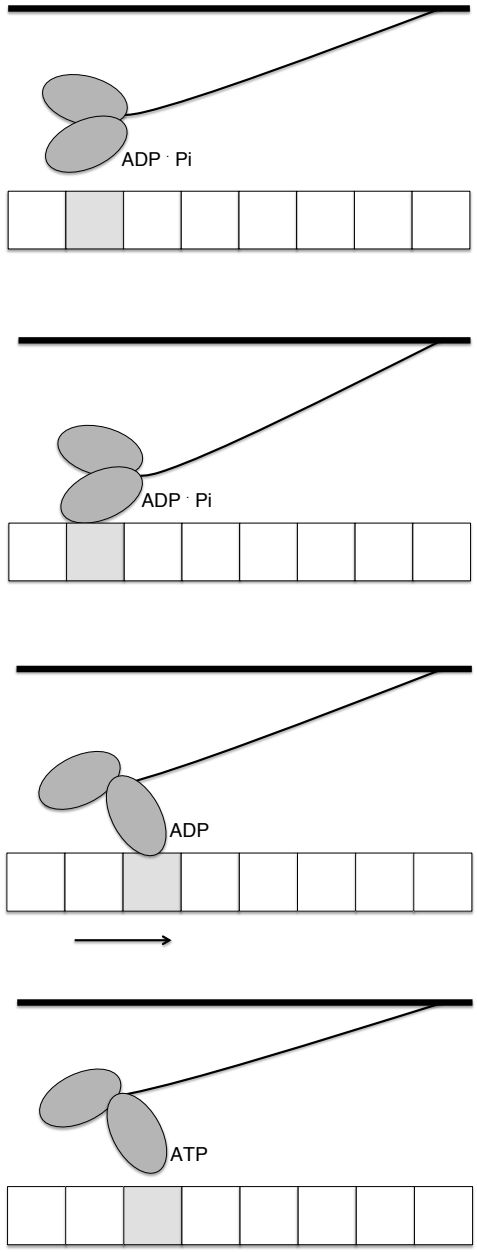

Figure 5.2: **Actin-Myosin Motor Process.** (After Ref. [82].)

growing and shrinking states via transitions known as catastrophe and rescue, a property that is often referred to as dynamic instability.

Most kinesin motors move towards the plus end of microtubules, although there are some that move towards the minus end. Like myosin, each kinesin motor consists of two heads, as can be seen in Figure 5.3. The heads are connected via long chain, or stalk, regions to the tails, where the load carried by the motor is attached. Unlike myosin, the two heads of the kinesin motor work together to transport the cargo, in a process that can also be broken into four stages. In the first stage, both heads are bound to β-tubulin sites on the microtubule. The leading head (on the right) has ATP bound, and the head on the left has already hydrolyzed the ATP and released the Pi. The binding of ATP to the leading head is what ultimately drives the motion of the trailing head to the front. In stage two, the trailing head has released from the microtubule and is swinging toward the front, where it will then re-bind to the microtubule. ATP hydrolysis takes place in the head that is now on the left and ADP is released from the head that is now bound on the right in stage 3. The binding of the newly forward head to the microtubule moves the cargo forward by approximately 80 Å. In stage 4 we see the binding of ATP to the empty site on the right-most head and the release of Pi on the left-most head, which will in turn be followed by the transition back to stage 1.

Although the details of the procedures used by myosin and kinesin to generate motion are different, we can see that they share many qualitative features. Both processes are driven by ATP hydrolysis, although the actual power stroke in myosin is initiated by the release of Pi while the binding of ATP initiates the forward motion in kinesin. Myosin heads release from the actin filament upon binding ATP, while the release of kinesin from the microtubule is driven by the release of Pi. Furthermore, myosin is only attached during the motion-generating phase of the motor, while kinesin can remain bound to the microtubule for many consecutive steps. These actions are consistent with the functions the motors carry out: many myosin motors work together in muscle contraction, so it may be more efficient for a single myosin head to briefly attach to the actin filament, produce motion, then get out of the way, while the continuous motion of kinesin may be more efficient for longer-range transport of cellular material using either a single motor protein or a small number of motor proteins. Therefore we can see that the same kinds of discrete-state models used to describe individual myosin motors could just

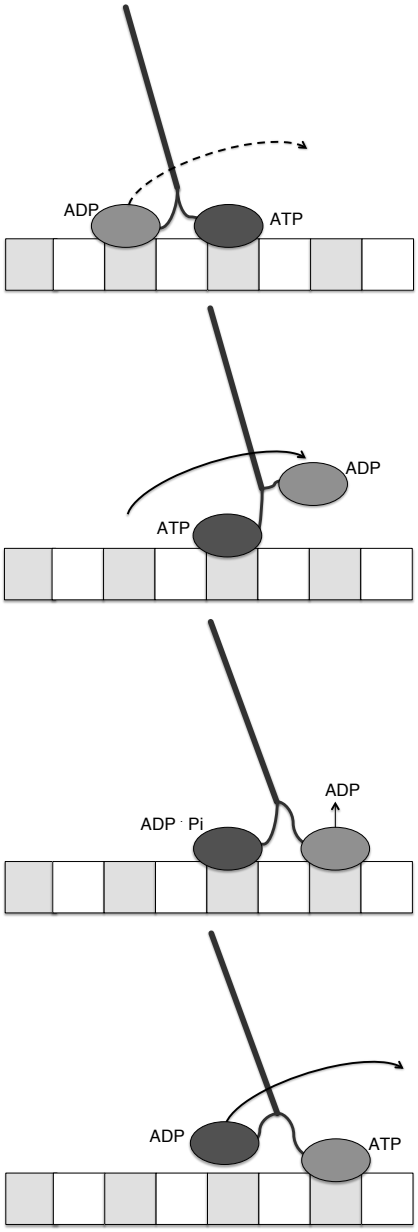

Figure 5.3: **Kinesin Motor Process.** (After Ref. [82].)

as easily describe a kinesin motor, although the theoretical mathematical states may represent different physical realities.

5.1.3 Polymerization as a Molecular Motor

Finally we can begin to explore the question of how polymerization can be considered to be a molecular motor. At the most basic level, depolymerization can cause the motion of an attached load similar to the way a fishing line reels in a fish. By making the fishing line shorter, or subtracting subunits from a polymer, the cargo is pulled in one direction. If the fishing line was stiff enough not to bend, one could imagine that making it longer, or adding subunits, could push the cargo in the opposite direction. Obviously the analogy is not perfect, since a fishing line cannot really push a fish farther out to sea, but it does suggest the basic idea that the change in length of one object can drive the motion of another object.

Polymerization is the process of adding subunits, or monomers, end-to-end to create a linear aggregate, or polymer. Depending on the type of polymer being built, polymerization may require hydrolysis of ATP or GTP, as in the cases of actin microfilaments or tubulin microtubules respectively, or it may be independent of an hydrolysis process, as in the case of sickle cell hemoglobin aggregation. Whether or not hydrolysis is required, the basic processes are similar, and models that describe one case can easily be adapted to describe the other. Hill has put forth a theoretical framework for describing polymerization or depolymerization against a force, which will be mentioned further in Section 5.2.3.

The classic example of depolymerization that causes transport is the separation of the sister chromatids during anaphase. The process of cell division, or mitosis, consists of five stages: prophase, prometaphase, metaphase, anaphase, and telophase. Before mitosis begins, during interphase, the cell increases in size and produces copies of the important nuclear material such as chromosomes and centrosomes. During prophase, the two centrosomes move to opposing sides, or poles, of the cell and the mitotic spindle begins to assemble. Spindles are composed of microtubules with the minus end at the poles and the plus end growing towards the center of the cell. Next, in prometaphase, the nuclear envelope disintegrates allowing the microtubules to attach to the kinetochore of the sister chromatids. The sister chromatids each become attached

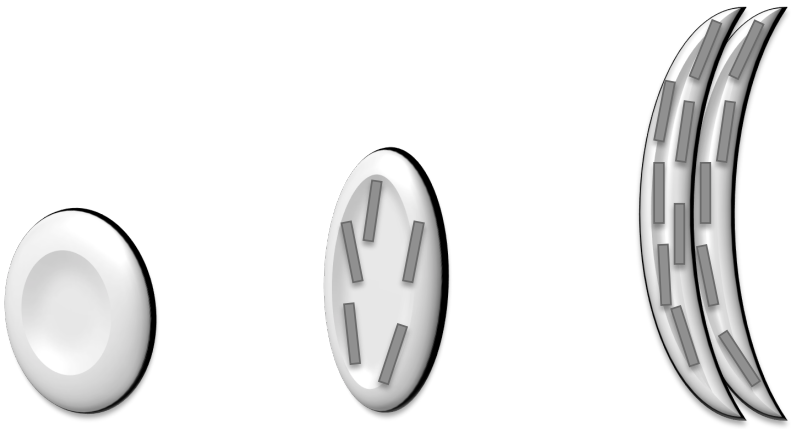

Figure 5.4: **Hemoglobin Polymerization Causing Sickle Cells.**
This sketch represents the polymerization of hemoglobin in red blood cells deforming the cell shape. In a normal red blood cell, shown on the far left, hemoglobin is present as isolated units. If the hemoglobin aggregates into rigid polymers, the polymers will eventually deform the red blood cell into the sickle shape represented on the far right.

to opposite poles. During metaphase, the sister chromatids are aligned down the center of the cell, waiting to divide during anaphase. When anaphase begins, the sister chromatids detach from each other and begin to move towards the poles. At this stage, the kinetochore microtubules are depolymerizing at both the plus and minus ends, acting to pull the newly separated chromosomes towards the poles. This process may also involve other molecular motors in concert with the depolymerization of the microtubules, but the exact mechanism is not yet well-known. Once the chromosomes are all separated, the nuclear envelopes re-form, one around each group of chromosomes, during telophase. After that, the cell undergoes cytokinesis to finally divide into two separate complete cells.

A classic biological example of polymerization against a force is the deformation of the cell membrane caused by the aggregation of sickle cell hemoglobin resulting in sickle red blood cells. Hemoglobin is a protein that is carried in red blood cells, which is composed of pairs of two subunits: the α subunit, which is normal in people with sickle cell disease, and the β subunit, which differs by one amino acid in people with sickle cell disease. Recall that in Part I of this

dissertation, we discussed the role of hemoglobin in oxygen or carbon monoxide transport in the blood stream. While normal hemoglobin is found as isolated units inside red blood cells, sickle hemoglobin tends to aggregate into rigid polymers that push against the cell membrane, eventually distorting the red blood cell into a sickle shape, as seen in the sketch shown in Figure 5.4. Not only are the sickled cells less robust than normal red blood cells, meaning that the life span of a sickled red blood cell may be less than half that of a normal red blood cell, but the rigid sickled shape can also lead to the clogging of capillaries, which decreases the blood flow to a particular area of tissue, and can cause pain as well as damage organs. The shortened life span of the red blood cells can also lead to anemia because the body cannot produce new red blood cells fast enough to replace those that have died. Note that while the polymerization of microtubules requires GTP hydrolysis, the aggregation of the sickle cell hemoglobin is an example of polymerization that does not require such a process.

5.1.4 Why Study Molecular Motors?

Now that we have described several examples of molecular motors, we can see that they perform many essential tasks in the cell and the human body. Understanding how molecular motors work is not only necessary to gain more insight into these important biophysical operations, but can also help to lay the groundwork necessary to build nano-scale robots. One important feature, apart from size, that makes molecular motors different from currently existing man-made motors is that they are able to convert chemical energy to mechanical energy directly, without first converting it to heat or electrical energy. Molecular motors can also operate much more efficiently than man-made motors. For example, a molecular motor can be up to 6 times more efficient than a car. While classical mechanics has been the foundation of engineering for the past 300 years, new models that are currently being studied will build the foundation for nano-scale engineering of the future. In particular, models for molecular motors will be the foundation upon which nano-mechano-chemical machines will be built. Many groups are already researching ways to build tiny robots that might ultimately perform tasks such as delivering drugs to particular sites in the body [85, 76]. One example of recent research in the area of fabricating nano-scale motors is the solar-powered motor designed by scientists in Italy

and fabricated at UCLA. The new motor, nicknamed "Sunny" can reportedly operate at speeds analogous to 60,000 rpm [2]. There is still a large amount of work to be done before molecular motors are thoroughly understood, and new mathematical models have the potential to give new insights into their inner workings.

5.2 Review of Mathematical Models for Molecular Motors

Now we will explore the major existing mathematical models for molecular motors. First we present the discrete-state kinetic models that are often used to describe the motion of individual myosin and kinesin motors. Then we discuss Brownian ratchet models for molecular motors. Finally, we mention Hill's mathematical model for polymerization against a force. These are the models that have been accepted to describe the motion of, and force exerted by, molecular motors that we will build upon in Chapters 6 and 7.

5.2.1 Discrete-State Kinetic Models

Discrete-state kinetic models allow us to calculate observable properties of molecular motors, such as the force-velocity relationship, without explicit inclusion of details concerning the biochemical and mechanical coupling of the system. Explicit details, such as whether ATP hydrolysis occurs when the motor is attached to the polymer track or when it is detached, can be incorporated implicitly into a simple model that could describe many biophysically different, but mathematically similar, systems. Particular systems can be split into several distinct kinetic states with the appropriate number of rate constants for transitions between the states. We will begin by studying the simplest such kinetic model, consisting of three states, following Qian's analysis from Ref. [59], and will then present the results from a more general N state model, due to Fisher and Kolomeisky from Refs. [35] and [20].

Simple Three-State Model

The simplest model that can describe the type of system we are interested in consists of only three states for a single enzyme molecule. As we mention above, many biophysical states can be lumped together into one mathematical kinetic state, and the explicit details of these states

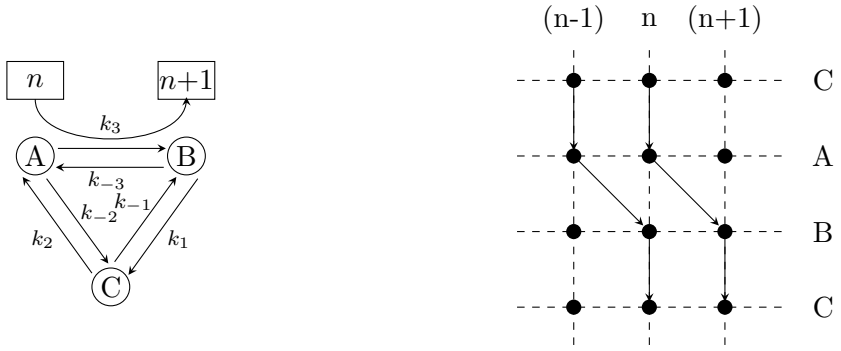

Figure 5.5: **Diagrams for a Simple Three-State Kinetic Model.**
The diagram on the left is the kinetic diagram for chemical cycle that the motor undergoes. The diagram on the right shows how the chemical cycle is coupled with the translocation of the motor along its track. The motor has three chemical states: A, B, C, and the translocation of the motor occurs when the motor transitions between states A and B. State C represents all intermediate biophysical states between A and B, as discussed in the text.

will only be included in the calculation of the rate constants for transitions between the three more abstract states. Figure 5.5 depicts a typical three-state kinetic cycle. State A represents the motor just before translocation along a polymer track, while state B represents the motor just after the translocation event has occurred. State C encompasses all of the intermediate biophysical kinetic states between states B and A required to get the motor back to the pre-translocation state. Some of the six rate constants are first-order, while others are pseudo-first-order, i.e. depending on the concentrations of ATP, ADP, or Pi present in the aqueous solution in which the motor protein and its track are immersed. We assume that the motor is operating in a stationary environment away from equilibrium, so that these concentrations remain at fixed levels.

Let $a(t)$, $b(t)$, and $c(t)$ represent the probability of the motor being in state A, B, or C,

respectively, at time t, without regard for the position of the motor along the track.[2] Then we can describe the dynamics of the system with the deterministic simultaneous rate equations below:

$$\frac{da}{dt} = -\left(k_3 + k_{-2}\right) a + k_{-3} b + k_2 c, \tag{5.1a}$$

$$\frac{db}{dt} = k_3 a - \left(k_1 + k_{-3}\right) b + k_{-1} c, \tag{5.1b}$$

$$\frac{dc}{dt} = k_{-2} a + k_1 b - \left(k_2 + k_{-1}\right) c. \tag{5.1c}$$

Note that the sum of the equations above is zero, representing the conservation of probability; the motor must be in one of the three states at all times. This allows us to eliminate c and reduce the system to:

$$\frac{da}{dt} = -\left(k_3 + k_{-2} + k_2\right) a + \left(k_{-3} - k_2\right) b + k_2, \tag{5.2a}$$

$$\frac{db}{dt} = \left(k_3 - k_{-1}\right) a - \left(k_1 + k_{-3} + k_{-1}\right) b + k_{-1}, \tag{5.2b}$$

$$c = 1 - a - b. \tag{5.2c}$$

To solve for the steady state, we simply set (5.2a) and (5.2b) equal to zero to solve for a and b, which can then in turn be used to solve for c using (5.2c). The steady-state solutions are

$$a = \frac{k_1 k_2 + k_{-1} k_{-3} + k_2 k_{-3}}{\Delta}, \tag{5.3a}$$

$$b = \frac{k_2 k_3 + k_{-1} k_3 + k_{-1} k_{-2}}{\Delta}, \tag{5.3b}$$

$$c = \frac{k_1 k_3 + k_{-2} k_{-3} + k_1 k_{-2}}{\Delta}, \tag{5.3c}$$

where the term in the denominators above is given by

$$\Delta = k_1 k_2 + k_2 k_3 + k_1 k_3 + k_{-1} k_{-2} + k_{-2} k_{-3} + k_{-1} k_{-3} + k_1 k_{-2} + k_2 k_{-3} + k_3 k_{-1}. \tag{5.4}$$

The steady-state net flux, or number of trips around the cycle per unit time, can be described by $J = J_+ - J_-$, where $J_\pm$ are the clockwise and counter-clockwise cycle fluxes respectively.

[2] Let $p_a(n,t)$, $p_b(n,t)$, and $p_c(n,t)$ be the joint probabilities that the motor is in chemical state A, B, or C, respectively, at position n along the track at time t. Then $a(t)$, $b(t)$, and $c(t)$ are given by:

$$a(t) = \sum_{n=-\infty}^{\infty} p_a(n,t), \qquad b(t) = \sum_{n=-\infty}^{\infty} p_b(n,t), \qquad c(t) = \sum_{n=-\infty}^{\infty} p_c(n,t).$$

Essentially, we are counting the number of forward steps taken by the motor, minus the number of backward steps taken by the motor, per unit time. We can obtain $J_\pm$ by simply looking at the steady-state rate of transition between states A and B, i.e. the pre- and post-translocation states:

$$J_+ = k_3 a, \qquad J_- = k_{-3} b. \tag{5.5}$$

Then the steady-state net flux is given by:

$$\begin{aligned} J &= \frac{k_3\left(k_1k_2 + k_{-1}k_{-3} + k_2k_{-3}\right) - k_{-3}\left(k_2k_3 + k_{-1}k_3 + k_{-1}k_{-2}\right)}{\Delta}, \\ &= \frac{k_1k_2k_3 - k_{-1}k_{-2}k_{-3}}{\Delta}. \end{aligned} \tag{5.6}$$

Note that since the system is not at equilibrium,[3] we do not expect the principle of detailed balance to hold, so in general we will *not* have

$$\frac{k_1k_2k_3}{k_{-1}k_{-2}k_{-3}} = 1, \tag{5.7}$$

and therefore we may have a non-trivial net flux. We define the translocation velocity, V, to be the product of the net cycle flux and the distance traveled over one cycle, $V = Jd$, where d is the length of a single step of the motor, i.e. the distance between sites n and $n+1$ in Figure 5.5.

The load carried by a molecular motor can be modeled as a constant external force. The only transitions in the kinetic cycle that effectively feel the external force are the transitions where translocation is taking place, namely between states A and B. Therefore, we can express the rate constants k_3 and k_{-3} in terms of the component of the external force parallel to the direction of motion, F. In thermodynamics, this is traditionally done by writing the ratio of the rate constants (the equilibrium constant) in the following way:

$$K_3 = \frac{k_3}{k_{-3}} = \frac{k_3^0}{k_{-3}^0} e^{-Fd/k_BT}, \tag{5.8}$$

where k_3^0, k_{-3}^0 are the rate constants when $F = 0$ (no load), k_B is Boltzmann's constant, T is temperature, and d is the length of one motor step.

---

[3]Recall that we have assumed that the concentrations of ATP, ADP, Pi are constant, which corresponds to "pumping" the system with a constant energy source.

We will assume that the transitions between states A and B are in rapid equilibrium with the other transitions, and then we can write down a simple force-velocity relationship for our system. Note that if this is not the case, a more complicated relationship between the force and the rates k_3 and k_{-3} must be determined, and what follows below does not apply. First, rewrite the expression for V by dividing the top and bottom of the velocity equation by k_{-3}:

$$V = \frac{(k_1 k_2 K_3 - k_{-1} k_{-2})\, d}{(k_2 + k_1 + k_{-1})\, K_3 + (k_{-2} + k_{-1} + k_2) + (k_1 k_2 + k_{-1} k_{-2} + k_1 k_{-2})\, \frac{1}{k_{-3}}}.$$

In making the rapid equilibrium assumption, we assume that $k_3, k_{-3} \gg k_{\pm 1}, k_{\pm 2}$. Therefore, we can neglect the last term in the denominator since k_{-3} is very large. Then the simple force-velocity relationship is:

$$V(F) = \frac{(k_1 k_2 K_3(F) - k_{-1} k_{-2})\, d}{(k_2 + k_1 + k_{-1})\, K_3(F) + (k_{-2} + k_{-1} + k_2)}. \tag{5.9}$$

Now we can find an expression for the *isometric stalling force*: the force required to stall the net motion of the motor. Define the stalling force, F^*, to be the applied force at which there is no net velocity of the motor in either the forward or backward direction, i.e. $V(F^*) = 0$. If $V(F^*) = 0$, then the terms inside the parentheses in the numerator above must be equal, so

$$\begin{aligned} k_1 k_2 K_3 &= k_{-1} k_{-2}, \\ e^{-\frac{F^* d}{k_B T}} &= \frac{k_{-2} k_{-2} k_{-3}^0}{k_1 k_2 k_3^0}, \\ F^* &= \frac{k_B T}{d} \ln\left(\frac{k_1 k_2 k_3^0}{k_{-1} k_{-2} k_{-3}^0}\right). \end{aligned} \tag{5.10}$$

Note that the "stalled" motor can still move forward or backward along the track, but it will do so with equal probabilities. We can say that the motor is now undergoing an unbiased random walk with mean-square-displacement (MSD) given by

$$MSD = d^2 \alpha t, \tag{5.11}$$

where α is the rate at which the motor moves forward (or backward). For this model,

$$\alpha = \frac{k_1 k_2 k_3(F^*)}{k_1 k_2 + k_{-1} k_{-2} + k_1 k_{-2}} = \frac{k_{-1} k_{-2} k_{-3}(F^*)}{k_1 k_2 + k_{-1} k_{-2} + k_1 k_{-2}}. \tag{5.12}$$

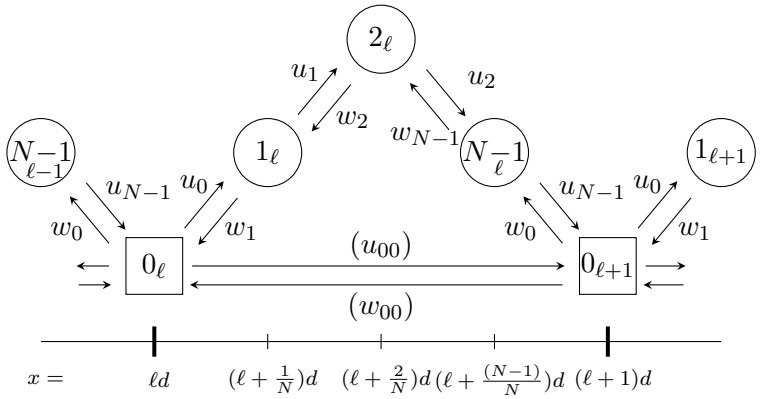

Figure 5.6: **N Discrete States Model Diagram.**
The schematic diagram for FK's N discrete states kinetic model. In their model, a complete cycle through the chemical states is from state $0 \to 1 \to 2 \to \ldots \to$ (N-1) $\to 0$. Rather than assigning the translocation of the motor to *one* chemical transition, it is split evenly between *all* of the intermediate states, i.e. when transitioning between states the motor moves a distance of d/N. Note that FK also account for the possibility that the motor can move between $x = \ell d$ and $(\ell+1)d$ without going through the cycle, corresponding to the motor drifting between sites on its track without undergoing an hydrolysis cycle.

General Model for N States

One can generalize the theory just presented to N discrete states. This has been thoroughly described by Fisher and Kolomeisky (FK) in Refs. [20, 35, 36], the results of which we summarize in this section. Label the sites on the motor's track with $\ell = 0, \pm1, \pm2, \ldots$ and let d be the spacing between the sites, or the step distance. Let j index the distinct kinetic states, where $j = 0$ is the free state of the motor, i.e. no energy source (ATP) is bound, and $j = 1, \ldots, N-1$ are the bound states. Let the forward rate constants be denoted by $u_j(\ell)$, and the backward rate constants be denoted by $w_j(\ell)$, where j refers to the state that the transition is *from*. FK use ℓ as a subscript on j to denote the site on the motor's track a particular transition is associated with. A transition through a full chemical cycle from state 0_ℓ to $0_{\ell+1}$ corresponds to the motor moving forward by one step, of size d. In their model, FK assume that the translocation of the motor is spread evenly across *all* of the transitions between the chemical states, as can be seen in Figure 5.6, rather than assuming that the translocation takes place in *one* of the transitions as we did in the previous section. Note that in Ref. [36], FK allow for the possibility that the

motor can move from state 0_ℓ to $0_{\ell+1}$ without going through the cycle, represented by the rates u_{00} and w_{00} in the diagram. They also extend the model to include the possibility that the motor "falls off" the track, and that it may undergo some other chemical process, rather than the hydrolysis cycle. Here, we will focus on the simple case where the motor must translocate by undergoing hydrolysis.

Based on the description of the model above, FK derive the simple kinetic scheme for the N-state model:

$$0_\ell \underset{w_1(\ell)}{\overset{u_0(\ell)}{\rightleftharpoons}} 1_\ell \underset{w_2(\ell)}{\overset{u_1(\ell)}{\rightleftharpoons}} \dots \underset{w_{N-1}(\ell)}{\overset{u_{N-2}(\ell)}{\rightleftharpoons}} (N-1)_\ell \underset{w_0(\ell+1)}{\overset{u_{N-1}(\ell)}{\rightleftharpoons}} 0_{(\ell+1)}. \tag{5.13}$$

Then the usual simultaneous rate equations for the probability that the motor is in state j between sites ℓ and $\ell+1$ at time t, $P_j(\ell;t)$, are given by

$$\frac{\partial}{\partial t}P_j(\ell;t) = u_{j-1}(\ell)P_{j-1} + w_{j+1}(\ell)P_{j+1}(\ell;t) - \left(u_j(\ell) + w_j(\ell)\right)P_j(\ell;t), \tag{5.14}$$

for $j = 0, 1, \dots, N-1$.

In order to solve for the steady state of the chemical cycle, the following identifications are made:

$$\begin{aligned} P_{-1}(\ell;t) &\equiv P_{N-1}(\ell-1;t), & u_{-1}(\ell) &= u_{N-1}(\ell-1), \\ P_N(\ell;t) &\equiv P_0(\ell+1;t), & w_N(\ell) &= w_0(\ell). \end{aligned} \tag{5.15}$$

Note that in the case where N=3, the above equations will simplify to exactly (5.1a)-(5.1c).

In Ref. [20], FK use Derrida's method to find the following relations for V_N and D_N, the

drift and diffusion coefficients that characterize the motion of the motor:

$$\Gamma = \prod_{j=0}^{N-1} \left(\frac{u_j}{w_j} \right) = e^{\epsilon}, \tag{5.16a}$$

$$V_N = \frac{d}{R_N} \left(1 - \prod_{j=0}^{N-1} \frac{w_j}{u_j} \right) = \frac{d}{R_N} \left(1 - \Gamma \right), \tag{5.16b}$$

$$D_N = \left(\frac{V_N S_N + d D_N}{R_N^2} - \frac{(N+2) V_N}{2} \right) \frac{d}{N}, \tag{5.16c}$$

$$R_N = \sum_{j=0}^{N-1} r_j, \tag{5.16d}$$

$$S_N = \sum_{j=0}^{N-1} s_j \sum_{k=0}^{N-1} (k+1)\, r_{k+j+1}, \tag{5.16e}$$

$$U_N = \sum_{j=0}^{N-1} u_j r_j s_j, \tag{5.16f}$$

$$s_j = \frac{1}{u_j} \left(1 + \sum_{k=1}^{N-1} \prod_{i=1}^{k} \frac{w_{j+1-i}}{u_{j-i}} \right), \tag{5.16g}$$

$$r_j = \frac{1}{u_j} \left(1 + \sum_{k=1}^{N-1} \prod_{i=1}^{k} \frac{w_{j+i}}{u_{j+i}} \right). \tag{5.16h}$$

Note that in order to apply these formulas, we must assume that all subscripts are $\mod N$.

It is useful to examine the ratio of the products of the forward and backward rate constants, Γ. If $\Gamma = 1$, then $V_N = 0$ and the system is in detailed balance, i.e. the motor is stalled and undergoing unbiased random fluctuations, like an unbiased random walk or unbiased Brownian motion. If $\Gamma > 1$, i.e. $\epsilon > 0$, then the $V_N > 0$ or if $\Gamma < 1$, i.e. $\epsilon < 0$, then the drift is in the negative direction. Note that on a biophysical basis, we would not expect the drift to be negative since most molecular motors under normal conditions exhibit a net forward motion, and in fact rarely step backwards.

5.2.2 Brownian Ratchet Models

The Brownian ratchet model for molecular motors is a generalization of the thermal ratchet proposed by Feynman to explain and explore the fact that there is a maximum amount of energy that can be produced by a heat engine. Feynman generated a paradox by proposing a simple

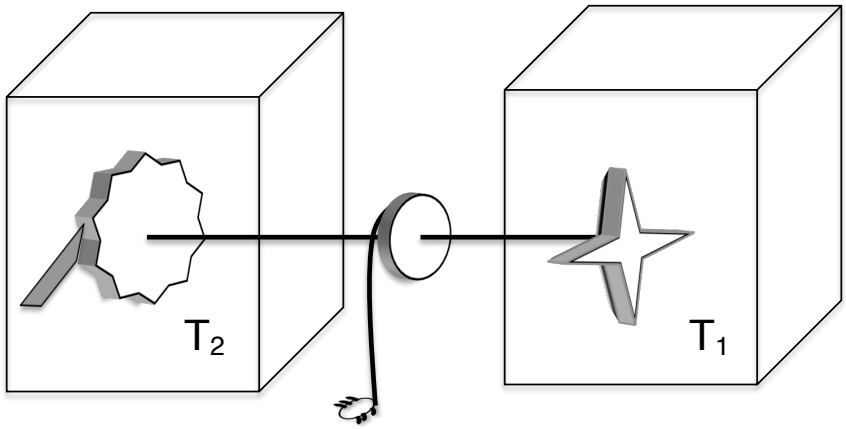

Figure 5.7: **Feynman's Thermal Ratchet System.**
Sketch of Feynman's thermal ratchet, after Ref. [19].

ratchet and pawl machine that might be able to violate the Second Law of Thermodynamics and produce perpetual motion through Brownian motion, seen in Figure 5.7 [19]. Assume that each box is filled with gas at $T_1 = T_2 = T$, so that gas molecules in the boxes will randomly bombard the pinwheel in one box as well as the ratchet and pawl in the other box. The pawl should block the "backward" motion of the wheel, only allowing forward motion thereby generating the force required to lift some small object, such as a bug. The paradox can be resolved by noting the fact that not only the pinwheel, but also the ratchet and pawl themselves are bombarded by gas molecules, which will sometimes cause the pawl to stay up long enough to allow the ratchet to "slip" backwards. Therefore, no net motion of the wheel will occur when $T_1 = T_2 = T$. In fact, net forward motion will occur if $T_2 < T_1$, and net backward motion will occur if $T_2 > T_1$. We can see that the thermal ratchet is not a perpetual motion machine, but the idea of the thermal ratchet itself can still be used as a powerful modeling tool.

There are three main approaches to modeling isothermal Brownian ratchets: fluctuating forces, fluctuating potentials, and fluctuating between states. The basic formulations of the models are quite similar, and in each case the stochasticity of the system drives the rectified motion of the so-called ratchet. An interested reader can find a thorough description of each

type of Brownian ratchet model in Ref. [33]. To introduce the basic idea of the Brownian ratchet molecular motor models, we will now present a fluctuating states model, after Ref. [60]. The theoretical foundation for the model is that a single molecular motor, such as kinesin or dynein, moves along a periodic polymer track, such as an actin filament or tubulin microtubule. As the center of mass of the protein moves along the track, the protein undergoes a cycle of conformational changes that are associated with hydrolysis of ATP or another energy source. The motion of the motor is stochastic, and the interaction between the protein and the track may be different for the different conformational states of the protein.

Single State Diffusion Model

It is instructive to begin the discussion of Brownian ratchet models with a derivation of a one state diffusion model from first principles, beginning from Fick's laws. We will then discuss a two state coupled diffusion model, which can easily be extended to more states if desired.

Let $P(x,t)$ be the probability density function (*pdf*) for the motor protein's center of mass being at position x, at time t:

$$P(x,t)dx = \Pr\{x < \text{center of mass} \leq x + dx, \text{time} = t\}. \tag{5.17}$$

Then the probability flux, according to Fick's first law, is given by:

$$J(x,t) = -D\frac{\partial P(x,t)}{\partial x} + \frac{F(x)}{\eta}P(x,t), \tag{5.18}$$

where D represents the diffusion coefficient of the motor protein, $F(x) = -\frac{dU(x)}{dx}$ represents the internal force between the motor protein and the track, which is governed by the potential function $U(x)$, and η is the viscous damping coefficient.[4] According to Fick's second law, the position of the motor changes over time according to

$$\frac{\partial P(x,t)}{\partial t} = -\frac{\partial}{\partial x}J(x,t) = \frac{\partial}{\partial x}\left(D\frac{\partial P(x,t)}{\partial x} - \frac{F(x)}{\eta}P(x,t)\right). \tag{5.19}$$

Note that we can use (5.18) and (5.19) to calculate the mean velocity of the motor as follows. Define the mean position of the motor to be the expected value of x:

$$\langle x \rangle = \int_{-\infty}^{\infty} xP(x,t)dx. \tag{5.20}$$

[4]Note that this is equivalent to saying that the "drift term" is due to overdamped Newtonian motion such that $\eta x'(t) + F(x) = 0$ [60].

Then the mean velocity is simply the derivative of the mean position with respect to time:

$$\begin{aligned}\frac{\partial}{\partial t}\langle x\rangle &= \int_{-\infty}^{\infty} x\frac{\partial P(x,t)}{\partial t}dx,\\ &= -\int_{-\infty}^{\infty} x\frac{\partial J(x,t)}{\partial x}dx,\\ &= -\left(xJ(x,t)\right))|_{x=-\infty}^{x=\infty} + \int_{-\infty}^{\infty} J(x,t)dx,\end{aligned}$$

where we can use (5.18) and the fact that $P(x,t)$ is a probability distribution function, i.e. $\int_{-\infty}^{\infty} P(x,t)dx = 1$, to argue that

$$\lim_{x\to\pm\infty} P(x,t) = \lim_{x\to\pm\infty} \frac{\partial P(x,t)}{\partial x} = 0, \tag{5.21}$$

so the first term in the expression for the mean velocity must vanish, and we are left with simply

$$\frac{\partial}{\partial t}\langle x\rangle = \int_{-\infty}^{\infty} J(x,t)dx. \tag{5.22}$$

Define a *steady-state solution* to (5.19) to be a solution such that the flux is constant, $J(x,t) = J$, and an *equilibrium solution* to be the solution where the flux is zero, $J(x,t) = J = 0$. We can see that if we are only interested in the steady-state solution and the mean velocity, we can simply solve (5.19) for the steady-state solution under the periodic boundary condition $P_{ss}(0) = P_{ss}(L)$, and the resulting steady-state velocity will simply be $v = JL$, where L is the period of the motor protein's track. The steady-state solution to (5.19) can be written as,

$$P_{ss}(x)\exp\left(\frac{U(x)}{D\eta}\right) - P_{ss}(0)\exp\left(\frac{U(0)}{D\eta}\right) = -\frac{J}{D}\int_0^x \exp\left(\frac{-U(s)}{D\eta}\right). \tag{5.23}$$

So far, this very general model could describe any particle that is diffusing with diffusion coefficient D and a drift term given by $F(x)/\eta$. Now we will make some assumptions regarding the form of $U(x)$ that pertain particularly to molecular motors. Since we know we are describing a particle that moves along a track that has a periodic structure, we will assume that the potential energy between the motor and the track is periodic, with period L,

$$U(x) = U(x+L), \tag{5.24}$$

and furthermore, $F(x)$ inherits the periodicity of the potential function. To apply the periodic boundary conditions, we simply evaluate (5.23) at $x = L$, and using (5.24), we obtain

$$P_{ss}(L)\exp\left(\frac{U(L)}{D\eta}\right) - P_{ss}(0)\exp\left(\frac{U(0)}{D\eta}\right) = -\frac{J}{D}\int_0^L \exp\left(\frac{-U(s)}{D\eta}\right) = 0. \tag{5.25}$$

Therefore, the flux, J, must be zero, since all of the other terms in the above equation are positive. In other words, for a single-state model, if the potential is periodic, or the average force over the period is zero,

$$\frac{1}{L}\int_0^L F(x)dx = -\frac{U(L)-U(0)}{L} = 0, \tag{5.26}$$

then there can be no net flux of the motor protein in either direction, i.e. there is no bias to the Brownian motion of the particle. Note that while the mean velocity is zero, the mean-square-displacement (MSD), $\langle x^2 \rangle$, actually grows in time.[5]

Two State Coupled Diffusion Model

Since we know that there *is* a bias to the motion of the motor protein, and the nature of the potential must be periodic, and since we can define discrete states for the motor protein undergoing translocation, the next step is to consider a two state coupled diffusion model. Assume that the particle can exist in two different conformational states, and that the transition between the states is triggered by the consumption of some type of fuel. We can easily see that this type of model could describe the actin-myosin motor, where the fuel consumed is ATP and the two states could be pre- and post-power stroke. The transitions between the two states can be described using chemical kinetics, and a one dimensional periodic position-dependent potential $U_i(x)$ can be defined for each state. Note that in practice, $U_i(x)$ could be found either by measuring the force required to move the particle away from position x, or by measuring the force required to keep it at position x. An example of what the $U_i(x)$ might look like can be seen in Figure 5.8. Note that, as in the one state model, there is no average force, or biased motion, in either state. Assume that the particle switches between the two states with rates given by $q_i(x)$, where i refers to the state the particle is leaving during the transition. Note that the $q_i(x)$ must be non-negative in order to make sense as rate constants, and will also inherit the periodicity from the motor track, so that $q_i(x) = q_i(x+L)$. The generic two state coupled

[5]For a particle undergoing unbiased Brownian motion with diffusion coefficient D, the mean position, $\mu(t) = 0$, and the variance, $\sigma^2(t) = 2Dt$.

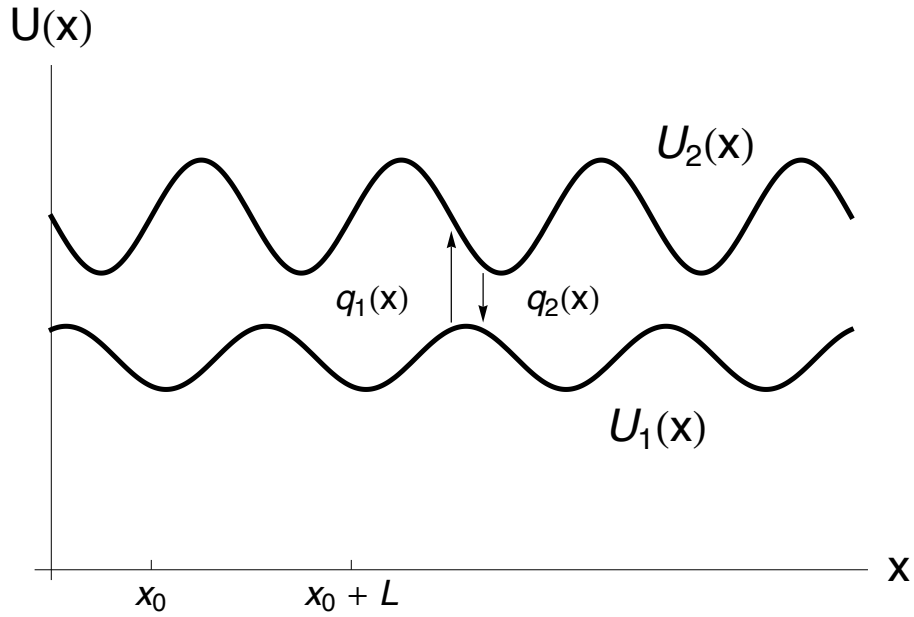

Figure 5.8: **Periodic Potentials for the Two State Coupled Diffusion Model.** $U_1(x)$ and $U_2(x)$ are the periodic potentials, with period L, for each conformational state of the motor protein. The protein transitions between states at rates $q_1(x)$ and $q_2(x)$, which are also periodic with period L. We somewhat arbitrarily used the following functions and parameter values to generate the plot: $D_1 = D_2 = \eta_1 = \eta_2 = 1$, $F_1(x) = \cos x - 2\sin x$, $F_2(x) = -4\cos x$, $q_1(x) = \exp(\cos x)$, and $q_2(x) = 1$.

diffusion model is given by

$$\frac{\partial f_1(x,t)}{\partial t} = \frac{\partial}{\partial x}\left(D_1\frac{\partial f_1(x,t)}{\partial x} - \frac{F_1(x)}{\eta_1}f_1(x,t)\right) - q_1(x)f_1(x,t) + q_2(x)f_2(x,t), \quad (5.27a)$$

$$\frac{\partial f_2(x,t)}{\partial t} = \frac{\partial}{\partial x}\left(D_2\frac{\partial f_2(x,t)}{\partial x} - \frac{F_2(x)}{\eta_2}f_2(x,t)\right) + q_1(x)f_1(x,t) - q_2(x)f_2(x,t), \quad (5.27b)$$

where the $f_i(x,t)$ represent the *pdfs* for the motor protein being in chemical state i, with the center of mass located at position x, at time t:

$$f_i(x,t)dx = \Pr\{x < \text{center of mass} \le x + dx, \text{chemical state} = i, \text{time} = t\}. \quad (5.28)$$

Rapid Biochemical Cycling Condition

We will assume that the motor is acting in a regime where the transitions between states of the motor are rapid compared to the diffusion along the track. In this situation, the *rapid*

biochemical cycling approximation can be made [60], so that a conditional equilibrium between the two states of the motor is established at any position along the track:

$$\frac{f_1(x,t)}{f_2(x,t)} = \frac{q_2(x)}{q_1(x)}, \qquad \forall x. \tag{5.29}$$

Under this condition, we immediately obtain

$$f_1(x,t) = \frac{q_2(x)}{q_1(x)+q_2(x)} f(x,t), \qquad f_2(x,t) = \frac{q_1(x)}{q_1(x)+q_2(x)} f(x,t), \tag{5.30}$$

where $f(x,t)$ is the *pdf* for the position of the motor, regardless of its chemical state. Note that $f(x,t)$ may be more easily compared to experimental data, since it is not necessary to keep track of the chemical state of the motor protein.

Now we can study the motion of the motor protein, without keeping track of the chemical state. When we combine (5.30) and (5.27), we obtain the following single partial differential equation for the motion of the center of mass of the motor:

$$\frac{\partial f(x,t)}{\partial t} = \frac{\partial^2}{\partial x^2}\left(\overline{D}(x) f(x,t)\right) - \frac{\partial}{\partial x}\left(\frac{\overline{F}(x)}{\overline{\eta}(x)} f(x,t)\right), \tag{5.31}$$

where

$$\overline{D}(x) = \frac{D_1 q_2(x) + D_2 q_1(x)}{q_1(x)+q_2(x)}, \tag{5.32a}$$

$$\overline{\eta}(x) = \frac{\eta_1 \eta_2 \left(q_1(x)+q_2(x)\right)}{\eta_1 q_1(x) + \eta_2 q_2(x)}, \tag{5.32b}$$

$$\overline{F}(x) = \frac{F_1(x)\eta_2 q_2(x) + F_2(x)\eta_1 q_1(x)}{\left(\eta_1 q_1(x) + \eta_2 q_2(x)\right)}, \tag{5.32c}$$

and $\overline{D}(x)$ and $\overline{\eta}(x)$ can be interpreted as the weighted average diffusion and viscous damping coefficients, respectively.[6] Note that each of $\overline{D}(x)$, $\overline{\eta}(x)$, and $\overline{F}(x)$ inherit L-periodicity from the $q_i(x)$ and the $F_i(x)$. The steady-state solution to (5.31) can be written as

$$\overline{D}(x)\exp\left(\overline{U}(x)\right) f_{ss}(x) - \overline{D}(0)\exp\left(\overline{U}(0)\right) f_{ss}(0) = -J\int_0^x \exp\left(\overline{U}(s)\right) ds, \tag{5.33}$$

---

[6] This interpretation for the viscous damping coefficient is more clear when it is written as

$$\frac{1}{\overline{\eta}(x)} = \frac{q_2(x)}{\eta_1\left(q_1(x)+q_2(x)\right)} + \frac{q_1(x)}{\eta_2\left(q_1(x)+q_2(x)\right)}.$$

where we define a generalized effective potential $\overline{U}(x)$, such that

$$\overline{U}(x) = -\int \frac{\overline{F}(x)}{\overline{D}(x)\overline{\eta}(x)}dx. \tag{5.34}$$

If we evaluate (5.33) at $x = L$, and apply the periodic boundary condition $f_{ss}(0) = f_{ss}(L)$, as well as the L-periodicity of $\overline{D}(x)$, we obtain

$$\overline{D}(0)\exp\left(\overline{U}(0)\right) f_{ss}(0)\left(1-\exp\left(\overline{U}(L)-\overline{U}(0)\right)\right) = J\int_0^L \exp\left(\overline{U}(s)\right) ds, \tag{5.35}$$

which we can solve for the steady-state flux, J:

$$J = \frac{\overline{D}(0)\exp\left(\overline{U}(0)\right) f_{ss}(0)\left(1-\exp\left(\overline{U}(L)-\overline{U}(0)\right)\right)}{\int_0^L \exp\left(\overline{U}(s)\right) ds}. \tag{5.36}$$

Note that, as in the single-state model, if the effective potential is periodic, i.e. $\overline{U}(0) = \overline{U}(L)$, then $J = 0$, and there is no steady-state net flux. If, however, the effective potential is not periodic, e.g. $\overline{U}(0) > \overline{U}(L)$, as can be seen in Figure 5.9, then $J > 0$ and there is a steady-state flux, or a bias to the Brownian motion. If we examine the form of $\overline{U}(x)$ in (5.34), then we see that the integrand is periodic, since $\overline{F}(x)$, $\overline{\eta}(x)$, and $\overline{D}(x)$ are each periodic. In general, it can be shown that the integral of a periodic function can be expressed as the sum of a periodic function with the same period as the integrand and a linear term with slope equal to the average value of the integrand over a period, up to a constant of integration.[7] Therefore, we can write

---

[7]This can be shown as follows. First, define the function $g(x)$ as,

$$g(x) = -\int_0^x \frac{\overline{F}(s)}{\overline{D}(s)\overline{\eta}(s)}ds + \alpha x,$$

where α is defined as in (5.37). Then, we can see that

$$\frac{d}{dx}\left(g(x) - \alpha x\right) = -\frac{\overline{F}(x)}{\overline{D}(x)\overline{\eta}(x)}.$$

Furthermore, we can show that $g(x)$ is periodic, with period L:

$$\begin{aligned} g(x+L) &= \alpha(x+L) - \int_0^{x+L} \frac{\overline{F}(s)}{\overline{D}(s)\overline{\eta}(s)}ds = \alpha(x+L) - \int_0^{x+L} \frac{\overline{F}(s)}{\overline{D}(s)\overline{\eta}(s)}ds - \int_x^{x+L} \frac{\overline{F}(s)}{\overline{D}(s)\overline{\eta}(s)}ds, \\ &= \alpha(x+L) - \int_0^{x+L} \frac{\overline{F}(s)}{\overline{D}(s)\overline{\eta}(s)}ds - \alpha L, \\ &= g(x). \end{aligned}$$

The reader can find an interesting discussion of the use of this fact to introduce the existence of periodic solutions to differential equations such as the simple harmonic oscillator to students at the elementary calculus level in Ref. [14].

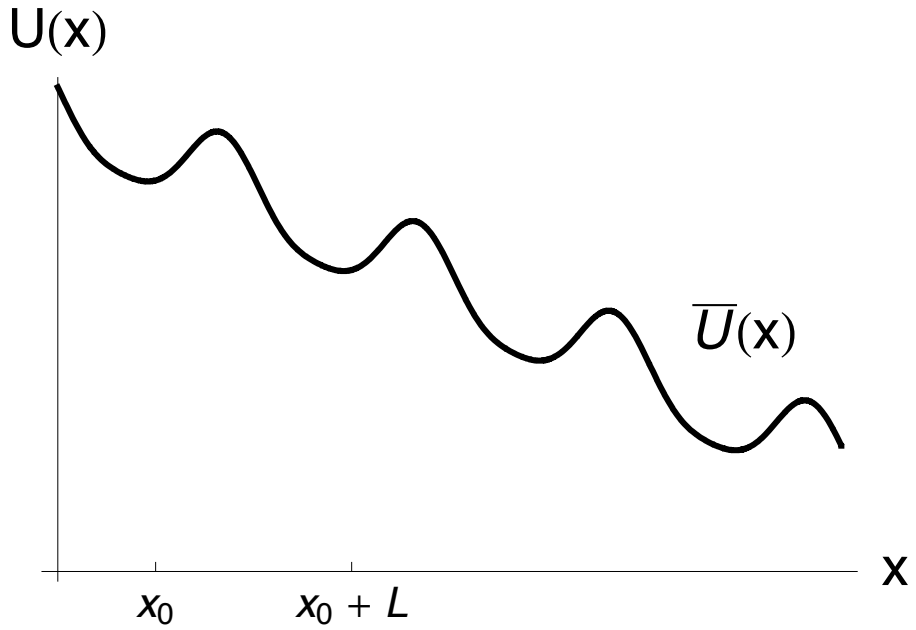

Figure 5.9: **Effective Potential for the Two State Coupled Diffusion Model.** The effective potential, $\overline{U}(x)$, for the $U_i(x)$ shown in Figure 5.8, calculated from (5.34).

$\overline{U}(x)$ as

$$\overline{U}(x) = -\int \frac{\overline{F}(x)}{\overline{D}(x)\overline{\eta}(x)}dx = g(x) - \alpha x + c, \qquad \alpha = \frac{1}{L}\int_x^{x+L} \frac{\overline{F}(s)}{\overline{D}(s)\overline{\eta}(s)}ds, \tag{5.37}$$

where $g(x)$ is a periodic function of period L, α is the average value of the integrand over one period as defined above, and c is a constant of integration such that $\overline{U}(0) = g(0) + c$. Then we can see that the only requirement on the $q_i(x)$, D_i, η_i and $F_i(x)$ in order to produce directed motion is that the integrand,

$$-\frac{(F_1(x)\eta_2 q_2(x) + F_2(x)\eta_1 q_1(x))}{(D_1 q_2(x) + D_2 q_1(x))\,\eta_1\eta_2}, \tag{5.38}$$

has a non-zero average value over a single period. Figures 5.8 and 5.9 show a particular example for periodic $U_i(x)$ and $q_i(x)$ that produce an effective potential that is not periodic, and can therefore produce directed motion.

5.2.3 Polymerization Against a Force

The growth of filamentous protein polymers, such as F-actin and microtubules, can do work against molecular or intracellular objects that resist movement. It has been suggested that these filaments are responsible for the shape of various cells, and their polymerization dynamics underlie the mechanics for the extension of lamellipodia of cells in motion [9, 17]. To understand the physical principles behind this important class of biochemical processes with cell-mechanical implications, T.L. Hill, following the work of Oosawa and Asakura [54], has developed an elegant thermodynamic theory for polymerization against force, both in equilibrium and more importantly in non-equilibrium steady-states [28, 29]. Later, Peskin, Odell and Oster proposed a more mechanistic kinetic model termed the *Brownian ratchet* (BR) [56]. A detailed mathematical analysis of the BR model has revealed the crucial roles played by both the thermal fluctuations in the filamentous lengthening and the Brownian motion of the driven object, or barrier; a molecular picture of the process with fluctuations emerged from these models. In the earlier studies, the interaction between the tip of the BR and the object was assumed to be ballistic.

Since then, protein polymerization has been an active area of biophysical research. See recent Refs. [1, 84, 90, 80, 74] for more details. In recent years, the actin-polymerization propelled *Listeria monocytogenes* movement has become a fertile model system for studying actin-based motility of non-muscle cells [83]. Kuo and McGrath measured the stochastic movement of the bacterium in cells using single-particle tracking (SPT) methodology with nanometer precision and analyzed their data statistically in terms of the mean-square-displacement (MSD) [39]. The Brownian motion of the driven bacteria shows a significantly reduced diffusivity compared to that expected from its geometric size. To explain this observation, Kuo and McGrath suggested that there is an association between the actin filaments and the bacterium. This binding explains the reduced Brownian motion of the bacterium; it also makes the formation of a "fluctuating gap" between actin filaments and a bacterium the rate-limiting process in the overall kinetics. This last point is significant, since it immediately leads to the conclusion that the bacteria will move stepwise with the step size of a single G-actin monomer, which was observed in Ref. [39].

The BR model developed by Peskin, Odell, and Oster (POO) is a theory for a single filament;

from their mathematical formalism it is not at all clear how to generalize the model to account for multiple filaments in a bundle, a situation which is biologically more realistic. Mogilner and Oster modified the BR model to consider thermal fluctuations of the filaments, rather than Brownian motion of the bacteria, as the mechanism of the "gap," which they call the "elastic Brownian ratchet," and subsequently modified that model to incorporate multiple filaments, called the "tethered ratchet" model [47, 48]. Their model incorporates a complicated branching cytoskeletal network of actin filaments, requiring a force-balance equation and assumed constitutive relations to describe the force and dissociation rates, while our model describes a simple bundle of parallel identical filaments. Growth of multiple filaments as a bundle has great relevance to cell biology in general and to the cytoskeleton and cell motility in particular. Note that in Refs. [78, 79, 77], Kolomeisky *et. al.* have proposed discrete chemical kinetic models for multiple filamentous bundle growth, but their models do not include an explicit interaction with a fluctuating barrier, and are not BR models *per se*.

In Chapter 6, we present an alternative diffusion formalism for the polymerization of a BR instead of the random walk approach originally employed by POO. In Ref. [62] it was shown that in several limiting cases the two mathematical frameworks give identical predictions; [8] however, the present formalism is conceptually simpler and analytically more tractable with elementary calculus. More importantly, the alternative formalism enables us to further develop the theory by incorporating an attractive interaction between the polymer and the barrier, and multiple filamentous bundle growth, as will be discussed in Chapter 7.

5.3 Coupled Diffusion Formulation for Molecular Motors: Measured Stalling Force Depends on Functional Form of the Applied Force

One of the important insights from theoretical studies on motor proteins and polymerization processes is that the kinetics of the force generation by single molecules depend on the the dynamic characteristics of the force apparatus by which the external (resistant, load) force is applied. This point has only become evident through the mechanical measurements on single macromolecules [16, 67, 75]. There is an uncertainty in how a single-molecule device indeed

[8] For other cases, there are certainly differences between the two approaches, and an exhaustive comparison is yet to be carried out.

works in the absence of the external force exerted by a mechanical measurement. In electrical engineering, this corresponds to the situation in which a battery has a large nonlinear internal resistance; different measurements can lead to very different readings of the current and voltage.

In Section 5.2.2, we introduced the standard coupled diffusion formalism for Brownian ratchet models for molecular motors. Now we will use that formalism to show that the measured stalling force for a molecular motor can be different depending on the type of measurement force applied. The motivation for this section is that there are at least two qualitatively different experimental techniques that are commonly used to measure the stalling force for molecular motors. One method for measuring the stalling force is to apply a viscous flow to the system, eventually causing the motor to stall, which corresponds to a constant applied external force. Another method is to use either a fiber-glass beam or an optical trap system to apply an elastic force that stalls the motor. We will show that the measured stalling force for the same molecular motor can be different depending on the type of measurement force applied.

We begin by building upon the two state coupled diffusion molecular motor model from (5.27). We will use a more general form of the standard model, allowing both the diffusion coefficient and the viscous damping coefficient to depend on position,

$$\frac{\partial f_1(x,t)}{\partial t} = \frac{\partial}{\partial x}\left(D_1(x)\frac{\partial f_1(x,t)}{\partial x} - \frac{F_1(x)}{\eta_1(x)}f_1(x,t)\right) - q_1(x)f_1(x,t) + q_2(x)f_2(x,t), \tag{5.39a}$$

$$\frac{\partial f_2(x,t)}{\partial t} = \frac{\partial}{\partial x}\left(D_2(x)\frac{\partial f_2(x,t)}{\partial x} - \frac{F_2(x)}{\eta_2(x)}f_2(x,t)\right) + q_1(x)f_1(x,t) - q_2(x)f_2(x,t), \tag{5.39b}$$

where the subscripts refer to the two different conformational states of the motor protein, the $D_i(x)$ represent the diffusion coefficient in each state, the $\eta_i(x)$ represent the viscous damping coefficient in each state, and the $f_i(x,t)$ represent the *pdfs* for the motor protein being in chemical state i, with center of mass located at position x, at time t:

$$f_i(x,t)dx = \Pr\{x < \text{center of mass} \leq x + dx, \text{chemical state} = i, \text{time} = t\}. \tag{5.40}$$

Note that in Ref. [60], the coupled diffusion model with constant coefficients was studied, where $D_1(x) = D_+$ and $D_2(x) = D_-$, which was summarized in Section 5.2.2. The key difference in the model in this section is that the $F_i(x)$ now include a term for the measurement force, in addition to the usual interaction force between the motor protein and the filament. In particular, we

now have

$$F_i(x) = -\frac{dU_i(x)}{dx} - F_{ext}(x), \tag{5.41}$$

where $U_i(x)$ is the periodic potential due to the interaction between the motor and the filament as before, and $F_{ext}(x)$ is the measurement force opposing the motor movement. We assume that the motor feels the same external force, regardless of its chemical state. It is very important to note that $F_i(x)$ is no longer necessarily a periodic function, due to the applied measurement force.

5.3.1 Rapid Biochemical Cycling Condition

Again, we will assume that the motor is acting in a regime where the transitions between states of the motor are rapid compared to the diffusion along the track, so the *rapid biochemical cycling* approximation can be made:

$$\frac{f_1(x,t)}{f_2(x,t)} = \frac{q_2(x)}{q_1(x)}, \qquad \forall x. \tag{5.42}$$

As before, we immediately obtain

$$f_1(x,t) = \frac{q_2(x)}{q_1(x)+q_2(x)} f(x,t), \qquad f_2(x,t) = \frac{q_1(x)}{q_1(x)+q_2(x)} f(x,t), \tag{5.43}$$

where $f(x,t)$ is the *pdf* for the position of the motor, regardless of its chemical state. As before, we can write down the partial differential equation governing the position of the motor:

$$\frac{\partial f(x,t)}{\partial t} = \frac{\partial}{\partial x}\left(\widehat{D}(x)\frac{\partial f(x,t)}{\partial x} - \frac{\widehat{F}(x)}{\widehat{\eta}(x)} f(x,t)\right), \tag{5.44}$$

where

$$\widehat{D}(x) = \frac{D_1(x)q_2(x) + D_2(x)q_1(x)}{q_1(x)+q_2(x)}, \tag{5.45a}$$

$$\widehat{\eta}(x) = \frac{\eta_1(x)\eta_2(x)\left(q_1(x)+q_2(x)\right)}{\eta_1(x)q_1(x) + \eta_2(x)q_2(x)}, \tag{5.45b}$$

$$\begin{aligned}\widehat{F}(x) = {} & \frac{F_1(x)\eta_2(x)q_2(x) + F_2(x)\eta_1(x)q_1(x)}{\left(\eta_1(x)q_1(x) + \eta_2(x)q_2(x)\right)} \\ & + \frac{\left(D_2(x) - D_1(x)\right)\left(q_1(x)q_2'(x) - q_2(x)q_1'(x)\right)\widehat{\eta}(x)}{\left(q_1(x)+q_2(x)\right)^2},\end{aligned} \tag{5.45c}$$

and $\widehat{D}(x)$ and $\widehat{\eta}(x)$ are analogous to the expressions for $\overline{D}$ and $\overline{\eta}$ from (5.32) in the previous section.[9] Note that $\widehat{F}(x)$ contains terms that depend only on the properties of the motor itself, as well as terms including the external measurement force. We can separate these terms so that we have

$$\widehat{F}(x) = \widehat{F}_{mot}(x) - F_{ext}(x), \tag{5.46a}$$

$$\begin{aligned}\widehat{F}_{mot}(x) = &-\frac{U_1'(x)\eta_2(x)q_2(x) + U_2'(x)\eta_1(x)q_1(x)}{(\eta_1(x)q_1(x) + \eta_2(x)q_2(x))} \\ &+ \frac{(D_2(x) - D_1(x))\,(q_1(x)q_2'(x) - q_2(x)q_1'(x))\,\widehat{\eta}(x)}{(q_1(x) + q_2(x))^2}.\end{aligned} \tag{5.46b}$$

It will also be useful to rewrite (5.44) in the following form:

$$\frac{\partial f(x,t)}{\partial t} = \frac{\partial}{\partial x}\left(\widehat{D}(x)\left(\frac{\partial f(x,t)}{\partial x} - \frac{\widehat{F}(x)}{\widehat{\eta}(x)\widehat{D}(x)}f(x,t)\right)\right). \tag{5.47}$$

Note that we can argue from a biophysical standpoint that we need not be concerned with the case where $\widehat{D}(x) = 0$.[10]

5.3.2 Isometric Stalling Force

Now we would like to investigate whether different types of measurement forces can result in different measured values of the isometric stalling force. Recall that a *stalled* motor is defined as a motor that has zero mean velocity, i.e.

$$\begin{aligned}0 = \frac{d}{dt}\langle x\rangle &= \int_{-\infty}^{\infty} J(x,t)dx, \\ J(x,t) &= -\left(\widehat{D}(x)\left(\frac{\partial f(x,t)}{\partial x} - \frac{\widehat{F}(x)}{\widehat{\eta}(x)\widehat{D}(x)}f(x,t)\right)\right).\end{aligned}$$

---

[9] Note that if the diffusion coefficients and the coefficients of viscous damping are constants, i.e. $D_1(x) = D_1$, $D_2(x) = D_2$, $\eta_1(x) = \eta_1$, and $\eta_2(x) = \eta_2$, then (5.44) agrees exactly with (5.31) from Section 5.2.2. In particular, we will have $\widehat{D}(x) = \overline{D}(x)$, $\widehat{\eta}(x) = \overline{\eta}(x)$, and $\widehat{F}(x) = \overline{F}(x) - \overline{D}'(x)$, where $\overline{D}(x)$, $\overline{\eta}(x)$, and $\overline{F}(x)$ come from (5.31), and $\widehat{D}(x)$, $\widehat{\eta}(x)$, and $\widehat{F}(x)$ come from (5.45).

[10] Recall that the $q_i(x)$ are rate constant for switching between the two motor states, so they must be non-negative. The $D_i(x)$ represent diffusion coefficients, so they must also be non-negative. We argue that we would not be using these equations to model the system if any of the $D_i(x)$ or $q_i(x)$ were zero for any values of x, so they, and $\widehat{D}(x)$, must be strictly positive in the systems of interest.

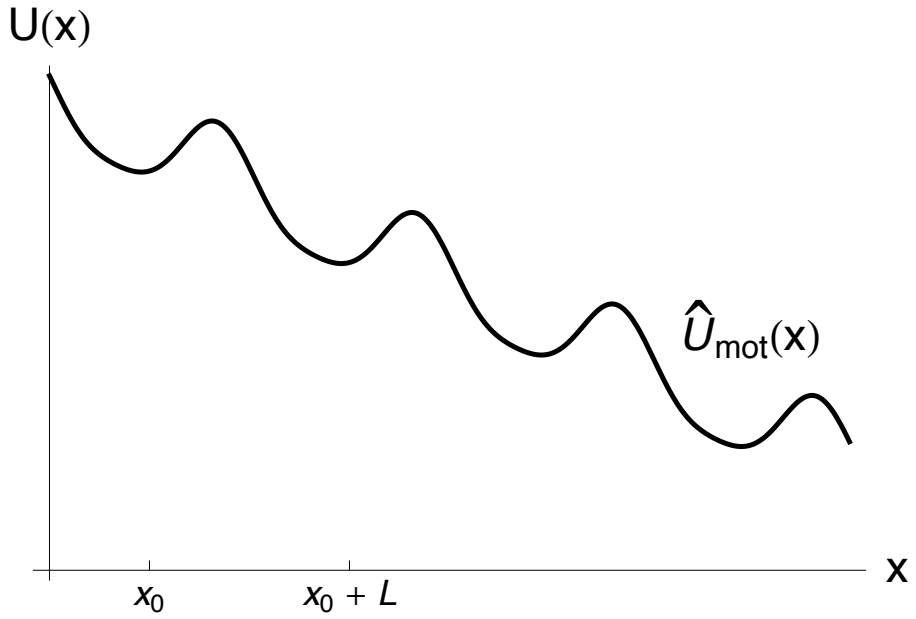

Figure 5.10: **Effective Potential in the Absence of an External Force.**
This figure shows an effective potential for a coupled motor system in which the motor moves in the positive direction on average over time. The potential can be expressed $\widehat{U}_{mot}(x) = g(x) - \alpha x$, where $g(x)$ is a function that is L-periodic in x, and α is the average motor force over one period, as in (5.48). As in Figure 5.8, we used the following functions to generate the plot: $D_1(x) = D_2(x) = \eta_1(x) = \eta_2(x) = 1$, $F_1(x) = \cos x - 2\sin x$, $F_2(x) = -4\cos x$, $q_1(x) = \exp(\cos x)$, and $q_2(x) = 1$.

Note that for our stalled isothermal ratchet, $D_1(x)\eta_1(x) = D_2(x)\eta_2(x) = k_BT$, and we can show via (5.45) that $\widehat{D}(x)\widehat{\eta}(x) = k_BT$, so the flux can be expressed as

$$J(x,t) = -\left(\widehat{D}(x)\left(\frac{\partial f(x,t)}{\partial x} - \frac{\widehat{F}(x)}{k_BT}f(x,t)\right)\right).$$

Define $\widehat{U}(x)$, the effective potential for the motor under the the external measurement force, as

$$\widehat{U}(x) = \widehat{U}_{mot}(x) - U_{ext}(x) = -\int\left(\widehat{F}_{mot}(x) - F_{ext}(x)\right)dx = g(x) - \alpha x - U_{ext}(x), \tag{5.48a}$$

$$\alpha = \frac{1}{L}\int_x^{x+L}\widehat{F}_{mot}(x)dx, \tag{5.48b}$$

where $g(x)$ is a periodic function that inherits the $L-$periodicity of $\widehat{F}_{mot}(x)$, ultimately due to the periodic nature of the motor-track interaction, and α is the average value of the effective motor force over one period. This is analogous to (5.37) from Section 5.2.2.

As we mentioned before, we will consider two particular applied measurement forces: a constant force $F_{ext_a}(x) = F_0$, which in real experiments is achieved by a flowing viscous drag, or an elastic force due to a fiber-glass beam or optical trap, $F_{ext_b}(x) = \kappa(x-d)$. We will see that a constant measurement force results in a system of a different character than an elastic measurement force.

Constant Measurement Force: $F_{ext_a}(x) = F_0$

For a constant measurement force, the measurement potential is $U_{ext_a}(x) = -F_0x$. Then the effective potential felt by the motor, $\widehat{U}_a(x)$ is given by

$$\widehat{U}_a(x) = \widehat{U}_{mot}(x) - U_{ext_a}(x) = g(x) - \alpha x + F_0x. \tag{5.49}$$

As we already know from Section 5.2.2, a periodic potential will result in a stalled motor. Therefore we can see that a constant force of $F_0 = \alpha$, exactly opposing the average force of the motor over one period, will restore the periodicity of the motor, thereby stalling the system. In other words, a constant measurement force will give exactly the value of the average motor force. This idea is illustrated in Figure 5.11. Note that a constant measurement force results in a motor with zero average velocity, but with the MSD increasing with time, as previously discussed.

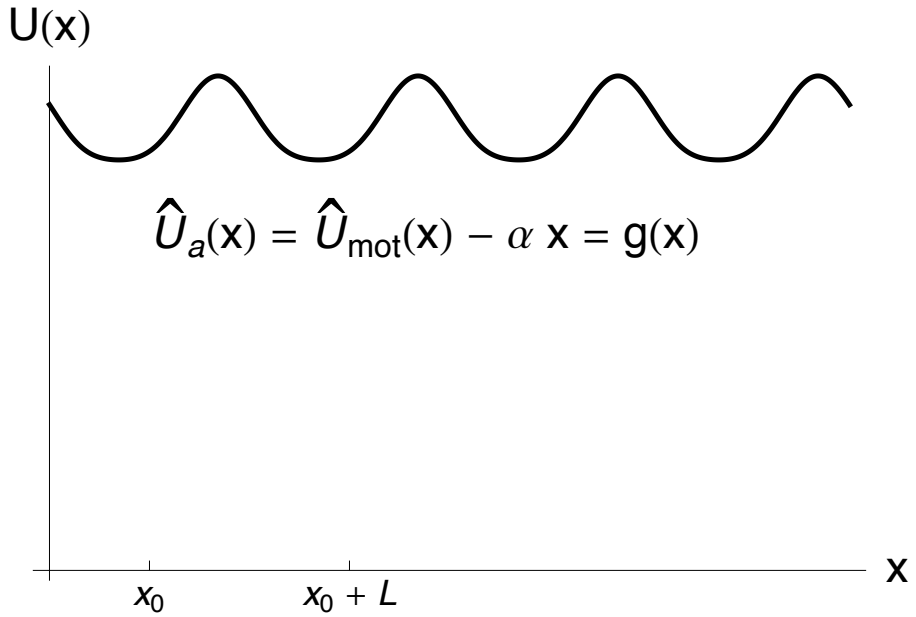

Figure 5.11: **Effective Potential with a Constant Stalling Force, $\mathbf{F_0} = \alpha$.**
A constant stalling force of F_0 will have potential $U_{ext}(x) = -F_0 x$, so $\widehat{U}_a(x) = \widehat{U}_{mot}(x) + F_0 x$. In order to stall the motor, the effective potential must be L-periodic, i.e. $\widehat{U}_a(x) = \widehat{U}_a(x + L)$, so the value of the constant force must be $F_0 = \alpha$, and $\widehat{U}_a(x) = g(x)$. This plot was generated using the same $\widehat{U}_{mot}(x)$ shown in Figure 5.10.

Elastic Measurement Force: $F_{ext_b}(x) = \kappa(x - d)$

On the other hand, if the measurement force is elastic, the stalled motor will satisfy an equilibrium solution for (5.47),

$$0 = \frac{df_{ss}(x)}{dx} - \frac{\widehat{F}(x)}{k_B T} f_{ss}(x). \tag{5.50}$$

The equilibrium solution to (5.50) is given by

$$f_{ss}(x) = A \exp\left(-\frac{\left(\widehat{U}_{mot}(x) + \kappa(x^2/2 - dx)\right)}{k_B T} \right), \tag{5.51}$$

where A is the normalization constant, and $\widehat{U}_{mot}(x)$ is as defined in (5.48). Note that we are guaranteed that the normalization constant can be found, due to the quadratic term in the exponential. In other words, *any* applied elastic force will completely stall the motor, and the mean-square-displacement will be independent of time, unlike the constant measurement force case.

Let μ denote the mean position of the stalled motor, and F^* denote the measured stalling force, i.e. the average value of the external measurement force:

$$\mu = \langle x \rangle = \int x f_{ss}(x) dx, \tag{5.52}$$

$$F^* = \langle F_{ext}(x) \rangle = \int F_{ext}(x) f_{ss}(x) dx. \tag{5.53}$$

Note that the immediate results are:

$$F_b^* = \langle \kappa(x - d) \rangle = \kappa \left(\langle x \rangle - \langle d \rangle \right) = \kappa \left(\mu - d \right). \tag{5.54}$$

For an elastic stalling force, the effective potential $\widehat{U}_b(x)$ can be written as a periodic function, plus a quadratic term:

$$\widehat{U}_b(x) = g(x) - \alpha x + \kappa \left(\frac{x^2}{2} - dx \right) = g(x) + \frac{\kappa}{2} \left(x - x_{min} \right)^2 - \frac{\kappa x_{min}^2}{2}, \qquad x_{min} = d + \frac{\alpha}{\kappa}. \tag{5.55}$$

An example for a particular $\widehat{U}_{mot}(x)$ can be seen in Figure 5.12. In this case, we see that the effective potential has the qualitative shape of a parabola with oscillations superimposed. Our intuition might tell us that if the oscillations are small, then $\mu \approx x_{min}$, i.e. if the effective potential was simply quadratic, then the mean would coincide with the x-value of the vertex

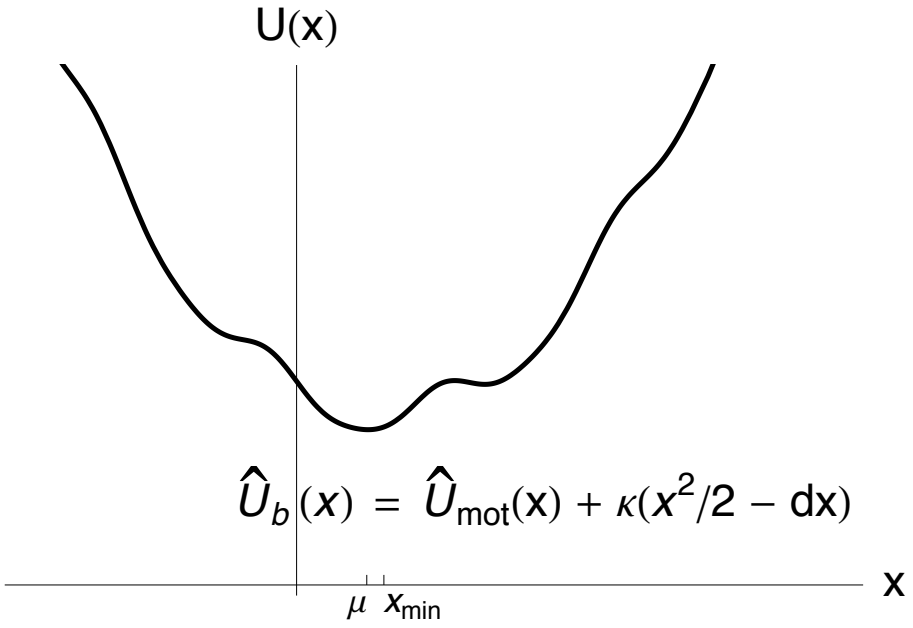

Figure 5.12: **Effective Potential with an Elastic Stalling Force, $\kappa(\mathbf{x}-\mathbf{d})$.**
An elastic stalling force of $F_{ext} = \kappa(x-d)$ will have potential $U_{ext}(x) = -\kappa\left(\frac{x^2}{2} - dx\right)$, so that $\widehat{U}_b(x) = \widehat{U}_{mot} - U_{ext} = g(x) + \frac{\kappa}{2}(x - x_{min})^2 - \frac{\kappa x_{min}^2}{2}$, where $x_{min} = \frac{(\kappa d+\alpha)}{\kappa}$, and $g(x)$ is a periodic function with period L, as in (5.48), and $\widehat{U}_{mot}(x)$ is as in Figure 5.10.

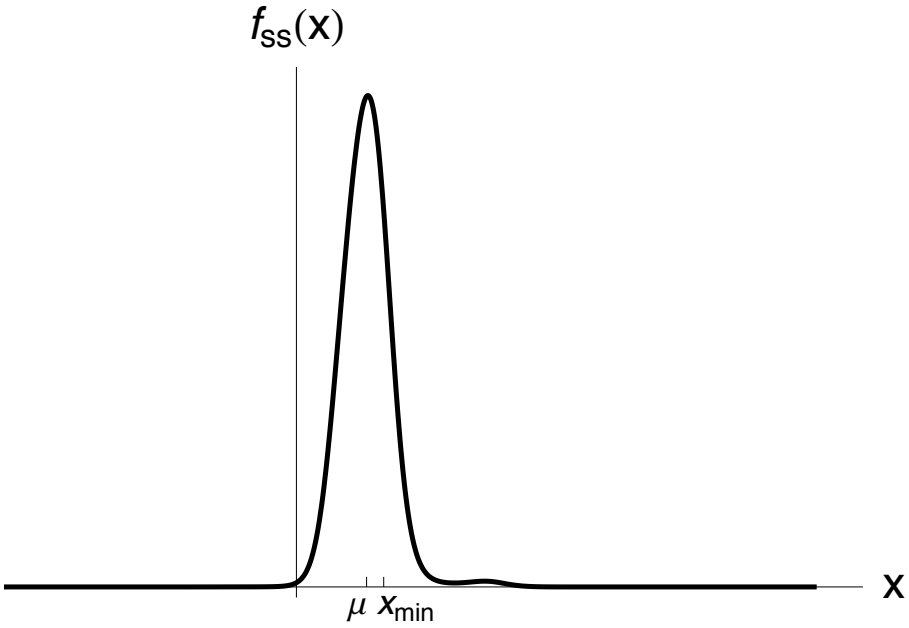

Figure 5.13: **Probability Distribution Function for Figure 5.12.**
$f_{ss}(x) = Ae^{-\frac{\widehat{U}_b(x)}{k_B T}}$, where $\widehat{U}_{mot}(x)$ is as in Figure 5.10, $\kappa = 0.5$, and $d = 2$.

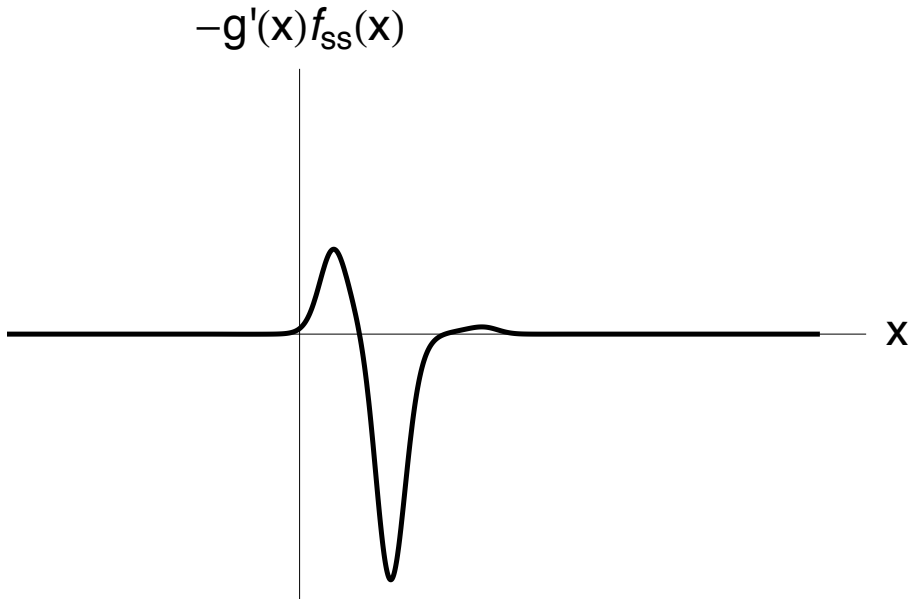

Figure 5.14: $\langle -\mathbf{g}'(\mathbf{x})\rangle$ **for Figure 5.12.**
$f_{ss}(x) = Ae^{-\frac{\widehat{U}_b(x)}{k_B T}}$, for the particular $\widehat{U}_{mot}(x)$ shown in Figure 5.10, and $\kappa = 0.5$, $d = 2$ as in Figure 5.12. Note that while $g'(x)$ has zero average over one period, it does not have a measured average value of zero relative to the distribution function. For the example shown above, we can calculate: $\alpha = 0.588929$, $x_{min} = 3.17786$, $\langle -g'(x)\rangle = -0.3116$, $\mu = x_{min} + \frac{\langle -g'(x)\rangle}{\kappa} = 2.55466$, and $\langle F_{ext}(x)\rangle = \langle -g'(x)\rangle + \alpha = 0.277328$.

of the parabola, and we would have $F_b^* \approx \alpha$. However, we will see that this is not necessarily the case. Rather than calculating the mean position of the motor, we will calculate the mean elastic force directly. We can see that by definition,

$$\langle F_{ext}(x) \rangle = \langle F_{mot}(x) \rangle , \tag{5.56}$$

$$= \left\langle -g'(x) - \alpha \right\rangle = \left\langle -g'(x) \right\rangle + \alpha. \tag{5.57}$$

Then in order for the measured elastic stalling force to be the same as the measured constant stalling force, i.e. $F_b^* = \alpha$, $\langle -g'(x) \rangle$ must be zero. While we know that $g'(x)$ is periodic with zero average value over the period, it is not necessarily the case that $\langle -g'(x) \rangle$ is zero. We can demonstrate that $\langle -g'(x) \rangle \neq 0$ *in general* by finding a counterexample. We present two such counterexamples in Figures 5.14 and 5.15.

In Figure 5.14, we show $\langle -g'(x) \rangle$ for the $g(x)$ shown in Figure 5.11, with the applied elastic stalling force shown in Figures 5.12 and 5.13. We can see that while $g'(x)$ has zero average value over the period, $\langle -g'(x) \rangle < 0$, resulting in a measured stalling force that is less than α. In Figure 5.15, we present graphs of the measured stalling force, F_b^* as a function of the strength of the applied elastic force, κ, for the motor potential $\widehat{U}_{mot}(x) = 30 + \sin(x) - 2x$. Note that in the large κ limit, the equilibrium solution effectively acts as a delta function located at d, so that F_b^* approaches $\alpha - g'(d)$. Therefore, we can see that the measured stalling force can also depend on the positioning of the optical trap, or fiber-glass beam, relative to the periodic structure of the motor potential. Thus, we have shown that different types of measurement forces can give different results for the measured stalling force of the coupled states motor system.

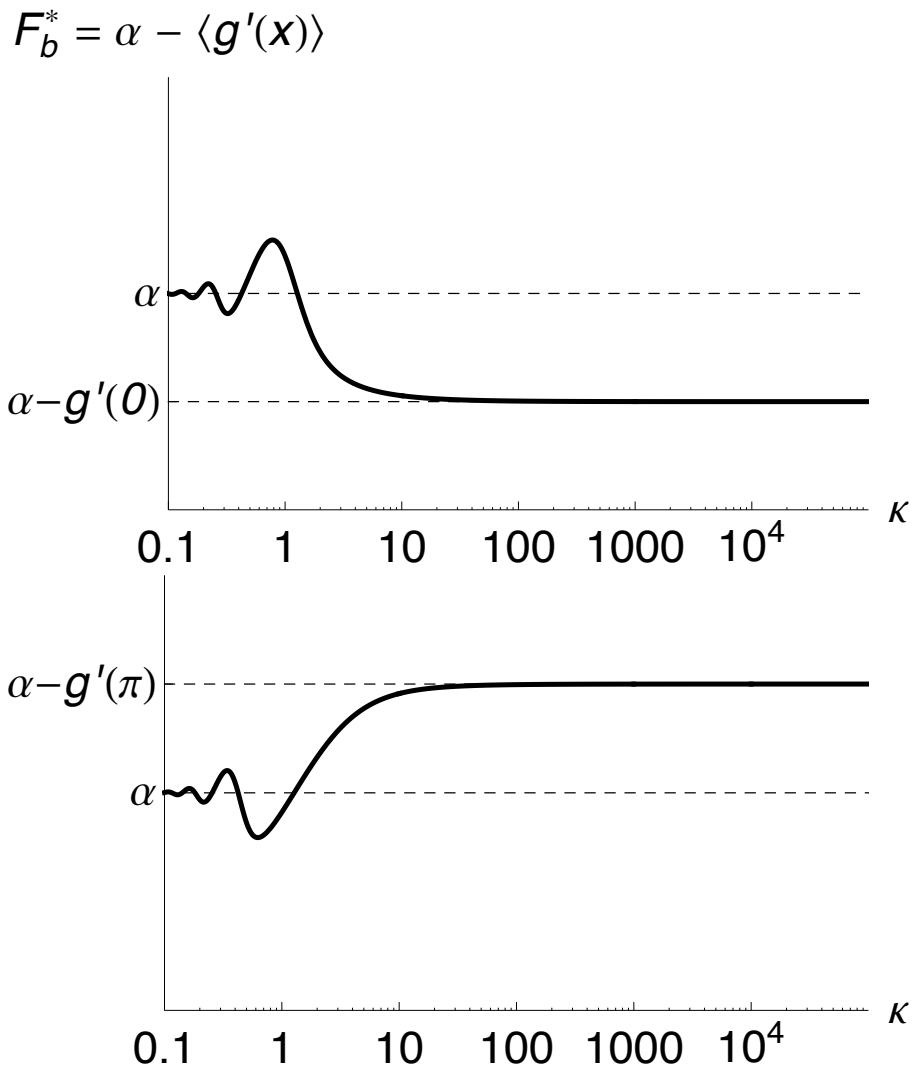

Figure 5.15: **Measured Stalling Force, $\mathbf{F_b^*}$, as a Function of Elastic Force Strength, κ.** Example plots drawn using (5.51) with $\alpha = 2$, $g(x) = 30 + \sin(x)$, $k_B T = 1$, top panel: $d = 0$, bottom panel: $d = \pi$. We see that in the limit as $\kappa \to \infty$, $F_b^* \to \alpha - g'(d)$. In other words, in the large κ limit, $f_{ss}(x)$ behaves like a delta function located at d: $\delta(x - d)$.

Chapter 6

POLYMERIZATION AS A BROWNIAN RATCHET: FROM DISCRETE TO CONTINUOUS FORMALISM

Traditionally, as mentioned in Chapter 5, polymerization as a Brownian ratchet (BR) has been studied in a spatially discrete setting, which is natural for the type of physical systems that it describes. In this chapter, we introduce the spatially continuous diffusion formalism for the polymerization ratchet. In Ref. [62] it was shown that in several limiting cases the two mathematical frameworks give identical predictions. However, the diffusion formalism is conceptually simpler and analytically tractable with elementary calculus. More importantly, the diffusion formalism enables us to further develop the theory by incorporating several features, which will be the focus of Chapter 7.

6.1 Random Walk to Diffusion: Toward a Continuous Formalism for the Polymerization Ratchet

In our alternative mathematical formalism for the Brownian ratchet, polymer growth is represented by a spatially continuous diffusion process, rather than a discrete-state, continuous-time random walk. This approximation has been used extensively in the earlier work of T.L. Hill. We will derive the diffusion and drift coefficients for the length of a single polymer, beginning with a continuous-time one-dimensional random walk model for the length of a polymer in the absence of a barrier. Note that we have assumed that the monomer pool stays constant in the present study. Therefore, our model for polymerization is a homogeneous process. For systems with rapid depletion of monomer pool, the latter effect can lead to a state-dependent transition. See Ref. [36] for more discussions.

6.1.1 Single Polymer in Free Space

We will begin with a continuous-time one-dimensional random walk model for the length of a single polymer in free space. Let x represent the position of the tip of the polymer, Δx represent

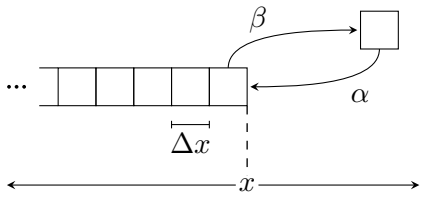

Figure 6.1: **Single Polymer in Free Space: Schematic Diagram.**
The position of the tip of the polymer is represented by x, α and β are the rates for adding and subtracting a monomer from the polymer, respectively, and Δx is the width of one monomer.

the width of one monomer, and α and β represent the rates of adding and subtracting a single monomer, respectively, as can be seen in Figure 6.1. Note that α and β are pseudo-first order rate constants. In principle, the polymerization rate should be the product of a second-order reaction rate and the concentration of the available monomers in the solution. However, as we mentioned above, we will be considering a system where the monomer pool is held constant, so we can assume that α is also constant. The position of the polymer tip can be modeled using a one-dimensional biased random walk where α and β, as described above, are the rates of moving forward or backward by one step of size Δx, as can be seen in Figure 6.2. If we define $p(x,t)$ to be the probability that the tip of the polymer is at position x at time t, then we can write

$$p_t(x,t) = \alpha\ p(x-\Delta x,t) + \beta\ p(x+\Delta x,t) - (\alpha+\beta)\ p(x,t), \tag{6.1}$$

where the first and second terms on the right hand side of the equation are rates of the particle moving to position x, and the third term is the rate of the particle leaving position x. Next, we can perform Taylor expansions on both terms on the right-hand-side to obtain:

$$\begin{aligned} p_t(x,t) &= \alpha\left(p(x,t) - \Delta x p_x(x,t) + \frac{\Delta x^2}{2}p_{xx}(x,t) + \ldots\right) \\ &\quad +\beta\left(p(x,t) + \Delta x p_x(x,t) + \frac{\Delta x^2}{2}p_{xx}(x,t) + \ldots\right) \\ &\quad -(\alpha+\beta)\ p(x,t), \end{aligned}$$

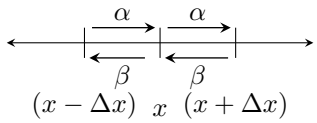

Figure 6.2: **1-D Biased Random Walk Diagram.**
The position of the tip of the single polymer shown in Figure 6.1 can be modeled as a one-dimensional random walk, with the schematic diagram shown above.

which simplifies to

$$p_t(x,t) = (\alpha+\beta)\frac{(\Delta x)^2}{2}p_{xx}(x,t) - (\alpha-\beta)\Delta x\ p_x(x,t) + O(\Delta x^3).$$

Then if the following limits hold,

$$\lim_{\Delta x\to 0}(\alpha+\beta)\frac{(\Delta x)^2}{2} = D, \qquad \lim_{\Delta x\to 0}(\alpha-\beta)\Delta x = V, \tag{6.2}$$

and all of the higher order terms vanish, our system becomes

$$p_t(x,t) = Dp_{xx}(x,t) - Vp_x(x,t), \tag{6.3}$$

which is exactly the diffusion equation with drift. Solutions to this equation describe Brownian motion, so the connection between the continuous-time random walk and diffusion formalism for Brownian motion is made. In other words, in the limit that the random walk becomes spatially continuous, the position of the particle can be described by Brownian motion.

6.1.2 Single Polymer System with a Fixed Barrier

The next step toward building a polymerization ratchet model is to include a fixed barrier for the polymer to interact with. A schematic diagram for this system can be seen in Figure 6.3. Instead of modeling the position of the tip of the polymer, we can consider the distance between the tip of the polymer and the fixed barrier, which we will call the gap distance. This gap distance can also be modeled using a random walk, with a special boundary condition to

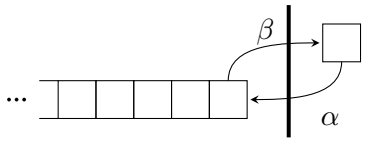

Figure 6.3: **Single Polymer Interacting with a Fixed Barrier: Schematic Diagram.** Schematic diagram for a single polymer interacting with a fixed barrier.

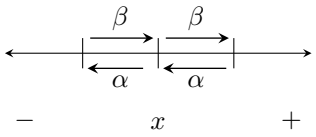

Figure 6.4: **Random Walk Diagram for the Gap Distance (Fixed Barrier).** The distance between a single polymer and a fixed barrier can be modeled using a one-dimensional random walk. Note that the only difference between this diagram and that shown in Figure 6.2 is that the forward and backward rates have been swapped.

account for what happens when the gap distance is zero. The slight difference is that in this case, the gap distance grows with rate β and shrinks with rate α, so our gap distance follows the random walk diagram shown in Figure 6.4.

Gap Distance Steady State Solution - Continuous Space

The only difference between the governing equation for the gap distance and equation (6.3), is the sign in front of the second term on the right hand side. The reason for the sign change will be clear if we write down the analogue of equation (6.1):

$$p_t(x,t) = \beta\ p(x-\Delta x,t) + \alpha\ p(x+\Delta x,t) - (\alpha+\beta)\ p(x,t). \tag{6.4}$$

We can see that after performing a Taylor expansion, this equation will become

$$p_t(x,t) = (\alpha+\beta)\frac{(\Delta x)^2}{2}p_{xx}(x,t) + (\alpha-\beta)\Delta x\ p_x(x,t) + O(\Delta x^3).$$

Therefore the governing equation for the gap distance is

$$p_t(x,t) = Dp_{xx}(x,t) + Vp_x(x,t). \tag{6.5}$$

Now we must concern ourselves with the appropriate boundary condition for $x = 0$. We know that the gap distance can never be negative, since the polymer must remain on the same side of the barrier at all times. What happens then, when the gap distance is zero?

We will assume that the polymer is rigid, meaning that a polymer cannot be added if the gap distance is less than the width of a monomer, i.e. the polymer will not slide, slip, or bend to allow addition of a monomer when the gap distance is too small. The appropriate boundary condition to describe this situation is called the no flux boundary condition. As discussed in Section 5.2.2, diffusive systems are governed by Fick's Laws, so we know that our governing equation can also be expressed as

$$p_t(x,t) = -\nabla \cdot J(x,t) = -\frac{\partial}{\partial x}J(x,t) = Dp_{xx}(x,t) + Vp_x(x,t),$$

where $J(x,t)$ is the flux, and we can see that

$$J(x,t) = -\left(Dp_x(x,t) + Vp(x,t)\right).$$

Then the no flux boundary condition at $x = 0$ is given by

$$0 = Dp_x(0,t) + Vp(0,t). \tag{6.6}$$

Furthermore, since $p(x,t)$ is a probability distribution, we also have a normalization condition,

$$1 = \int_0^\infty p(x,t)dx. \tag{6.7}$$

The two conditions given in (6.6) and (6.7) will allow us to solve for a steady state gap distribution.

In order to find the steady state solution, we may simply set the time derivative equal to zero:

$$p_t(x,t) = -\frac{\partial}{\partial x}J(x,t) = 0.$$

In the steady state, we can see that $J(x,t) = J$, i.e. the flux is constant for all values of x. The no flux boundary condition given by equation (6.6) fixes that constant to be zero, so we must

simply solve the first order ordinary differential equation

$$Dp_x(x) + Vp(x) = 0.$$

Using elementary calculus, we can see that $p(x) = Ae^{-\frac{V}{D}x}$, where A is a constant of integration. We can apply the normalization condition from (6.7) to solve for the constant.

$$\int_0^\infty Ae^{-\frac{V}{D}x}dx = A\,\frac{D}{V}e^{-\frac{V}{D}x}\Big|_0^\infty = 1.$$

Note that the improper integral only converges for $\dfrac{V}{D} > 0$. D is by definition a positive quantity, so this restriction simply requires V to be positive. In terms of the adding and subtracting rates for the polymer, this corresponds to the restriction $\alpha > \beta$, i.e. on average, the polymer is growing, rather than shrinking, which agrees well with our intuition. In other words, a steady state will only be reached if the polymer is growing toward the fixed barrier. Therefore the steady state solution to the spatially continuous problem is

$$p(x) = \frac{V}{D}e^{-\frac{V}{D}x}. \tag{6.8}$$

Note that the spatially discrete continuous-time random walk can be simulated exactly using the Gillespie algorithm [23].[1] A spatially discrete solution to the problem can be compared directly with simulation data, so we will also find the steady state solution for spatially discrete random walk model.

Gap Distance Steady State Solution - Discrete Space

Let $p_i(t)$ denote the probability that the gap distance is i monomers wide. Then from (6.4), we know that

$$\frac{d}{dt}p_i(t) = \beta p_{(i-1)}(t) - (\alpha+\beta)p_i(t) + \alpha p_{(i+1)}(t), \qquad i > 0, \tag{6.9a}$$

$$\frac{d}{dt}p_0(t) = -\beta p_0(t) + \alpha p_1(t). \tag{6.9b}$$

Note that the formula for the $i = 0$ case prevents the gap distance from ever becoming negative and is analogous to the no flux boundary condition at $x = 0$ in the spatially continuous model.

[1] More details on simulation algorithms can be found in Appendix B.

In order to solve for the steady state probability distribution, we set the left-hand-side of each equation from (6.9) equal to zero, which leads to

$$p_{(i+1)} = \frac{\alpha+\beta}{\alpha} p_i - \frac{\beta}{\alpha} p_{(i-1)}, \qquad i > 0, \tag{6.10a}$$

$$p_1 = \frac{\beta}{\alpha} p_0. \tag{6.10b}$$

Since p_i is a probability mass function, we also have a normalization condition:

$$1 = \sum_{i=0}^{\infty} p_i. \tag{6.11}$$

We could find the solution to (6.10a) using well-known techniques for finding solutions to linear constant-coefficient difference equations, or we could quickly prove by induction that $p_i = \left(\frac{\beta}{\alpha}\right)^i p_0$ for $i > 0$. Then we can use the normalization condition (6.11) to solve for p_0:

$$\begin{aligned} 1 &= p_0 \left(1 + \sum_{i=1}^{\infty} \left(\frac{\alpha}{\beta}\right)^i\right), \\ &= p_0 \left(1 + \left(\frac{1}{1-\frac{\beta}{\alpha}} - 1\right)\right), \end{aligned}$$

where the sum only converges if $\alpha > \beta$, just as in the spatially continuous model. We can see that $p_0 = \frac{\alpha-\beta}{\alpha}$, so the steady state gap distance is given by

$$p_i = \frac{\alpha-\beta}{\alpha}\left(\frac{\beta}{\alpha}\right)^i, \qquad i \geq 0. \tag{6.12}$$

Simulation results can be directly compared to the spatially discrete steady state solutions in order to verify that the theory and the simulation do indeed agree, as can be seen in Figure 6.7.

6.1.3 Single Polymer System with a Moving Barrier

In order to model a polymerization ratchet, we must be able to describe a polymer interacting with a *moving* barrier. If we modify our system so that the barrier also follows a biased random walk, we will see that we can make use of the results from the previous section for the gap distance in the steady state, with only minor modifications. First, let α_p and β_p be the adding and subtracting rates for the polymer and α_w and β_w be the rates at which the barrier moves toward and away from the polymer, in increments equal to the width of one monomer, as shown

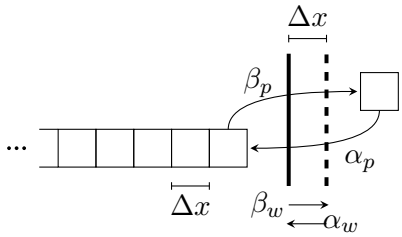

Figure 6.5: **Single Polymer Interacting with a Moving Barrier: Schematic Diagram.** α_p and β_p are the rates of adding and subtracting one monomer of width Δx, respectively. α_w and β_w are the rates of the barrier moving toward or away from the polymer by the width of Δx, respectively.

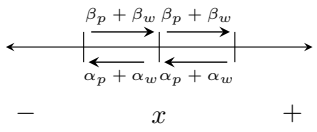

Figure 6.6: **Random Walk Diagram for the Gap Distance (Moving Barrier).**

in Figure 6.5. Note that the barrier can in principle move by any distance increment, but since Δx is the minimum distance that allows for the addition of a monomer, we will choose α_w and β_w appropriately for that distance increment.

Gap Distance

We can see that there are now two ways for the gap to change size: either by the motion of the barrier or by a change in length of the polymer. The gap distance shrinks at rate $\alpha_p + \alpha_w$ and grows at rate $\beta_p + \beta_w$, as shown in Figure 6.6. If we make the identifications

$$\alpha = \alpha_p + \alpha_w \qquad \beta = \beta_p + \beta_w, \tag{6.13}$$

then the governing equations for the gap distance steady state solutions from the previous section will hold.

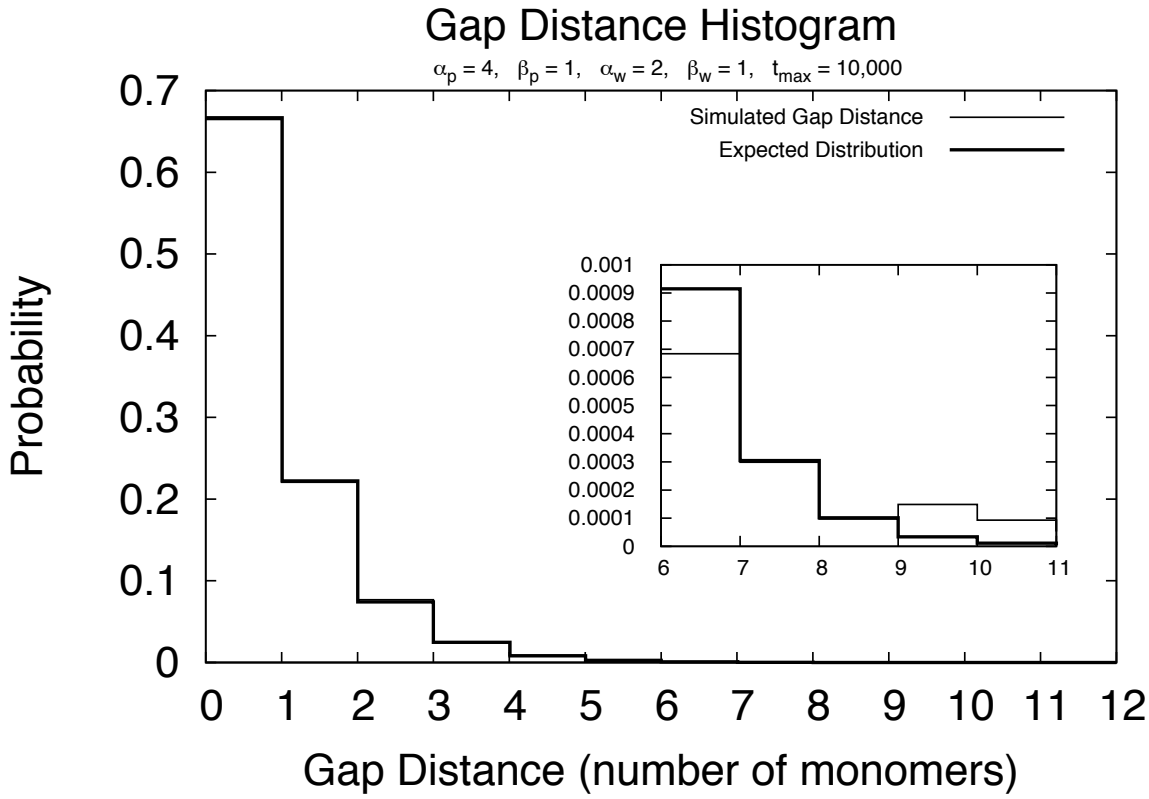

Figure 6.7: **Gap Distance Histogram.**
Histogram for the gap distance between a polymer and a moving barrier with the given parameters. The simulation was run for 10,000 time units, and the histogram for the gap distance is shown along with the predictions from the mathematical model. Note that the difference between the simulated gap distance distribution and the theoretical prediction can only be seen in the inset plot, indicating an excellent match between the theoretical results and the simulation data.

Table 6.1: **Average Motion of a Single Polymer Interacting with a Moving Barrier.** Summary of the conclusions about the net motion of the single polymer and moving barrier system, where $K_1 = \frac{\alpha_p \beta_w}{\beta_p \alpha_w}$, as defined in (6.14).

Physical Result	Average System Motion	Condition
polymer pushes barrier	Positive	$K_1 > 1$
barrier pushes polymer	Negative	$K_1 < 1$
balance, stalled system	None	$K_1 = 1$

Average Motion of the System

Furthermore, since the whole system now has the ability to move, we would also like to track the relative motion of the system. In particular, we want to be able to determine whether the polymer will push the barrier on average, or if the barrier will push the polymer on average, for a given set of parameter values. We can find a condition on the parameters for the relative motion of the system in the following way. Note that the entire system will advance by Δx if the polymer adds a subunit and the wall retreats by Δx. Similarly, the entire system will retreat by Δx if the polymer loses a subunit and the wall advances by Δx. Define K_1 to be the equilibrium constant for the system advancing, i.e. moving in the direction of polymer growth:

$$K_1 = \frac{\alpha_p}{\beta_p} \frac{\beta_w}{\alpha_w}. \tag{6.14}$$

We can see that if $K_1 > 1$, the system advances on average, i.e. the polymer pushes the barrier; if $K_1 = 1$, the system is stalled and there is no average motion; and if $K_1 < 1$, the system retreats on average, or the barrier pushes the polymer. These conditions are summarized in Table 6.1. For the simple single polymer system, this agrees exactly with our intuition: if the polymer grows faster than the barrier advances, on average, we would expect the polymer to push the barrier. We will build upon this idea in Section 6.3.1.

6.2 The Polymerization Ratchet: The Full Continuous Diffusion Formalism

In terms of the continuous diffusion formalism, a polymerization Brownian ratchet consists of the position of the polymer tip $\mathbf{X}(t)$ and a barrier $\mathbf{Y}(t)$, which both undergo one-dimensional

biased diffusion.[2] Based on the groundwork laid in the previous section, we will model the position of the polymer tip, $\mathbf{X}(t)$, as undergoing diffusion with a drift with D_a and V_a defined as

$$D_a = (\alpha + \beta)\delta^2/2, \qquad V_a = (\alpha - \beta)\delta, \tag{6.15}$$

where α, β, correspond to the polymerization and depolymerization rates, as in the previous section, and δ is the width of one monomer. The position of the barrier, $\mathbf{Y}(t)$, undergoes diffusion biased by a constant external resistant force, F_{ext}. The motion of the barrier is characterized by a diffusion coefficient, D_b, and drift $-F_{ext}/\eta_b$ where η_b is the frictional coefficient of the barrier.[3] We may define our coordinate system so that the polymer is on the left of the barrier and grows rightward, implying that $\mathbf{X}(t) \leq \mathbf{Y}(t)$. This relation introduces the simplest interaction possible between the polymer and the barrier: simple geometric exclusion.

The stochastic dynamics of this BR can be expressed in terms of a 2-dimensional diffusion equation,

$$\begin{aligned} \frac{\partial P_{\mathbf{XY}}(x,y,t)}{\partial t} &= D_a \frac{\partial^2 P_{\mathbf{XY}}(x,y,t)}{\partial x^2} + D_b \frac{\partial^2 P_{\mathbf{XY}}(x,y,t)}{\partial y^2} \\ &\quad -V_a \frac{\partial P_{\mathbf{XY}}(x,y,t)}{\partial x} + \frac{F_{ext}}{\eta_b} \frac{\partial P_{\mathbf{XY}}(x,y,t)}{\partial y}, \end{aligned} \tag{6.16}$$

where $P_{\mathbf{XY}}(x,y,t)dxdy = \Pr\{x < \mathbf{X}(t) \leq x + dx, y < \mathbf{Y}(t) \leq y + dy\}$ is the joint probability density function (*pdf*) for the position of the polymer tip being x and the position of the barrier being y at time t.

In the system with simple geometric exclusion, we can decouple (6.16) by using a simple coordinate transformation,

$$\mathbf{\Delta} = \mathbf{Y} - \mathbf{X}, \qquad \mathbf{Z} = \frac{D_b\mathbf{X} + D_a\mathbf{Y}}{D_b + D_a}, \tag{6.17}$$

where $\mathbf{\Delta}(t)$ is the distance between the tip of the polymer and the barrier, or the *gap distance*, and $\mathbf{Z}(t)$ is the average position, or *center of friction*, of the polymer-barrier system. Note that

[2]The reader should note that bold face symbols will be used to represent one-dimensional random variables throughout this discussion.

[3]From now on, we assume that the barrier truly fluctuates according to Brownian motion, rather than following a random walk, which follows our intuition for an object such as a bacterium in an aqueous solution.

after the coordinate transformation, the geometric constraint $\mathbf{X}(t) \leq \mathbf{Y}(t)$ becomes $\mathbf{\Delta}(t) \geq 0$. After the coordinate transformation we obtain the following system of decoupled equations:

$$\frac{\partial P_{\mathbf{\Delta}}(\Delta,t)}{\partial t} = (D_a + D_b)\frac{\partial^2 P_{\mathbf{\Delta}}(\Delta,t)}{\partial \Delta^2} + \left(V_a + \frac{F_{ext}}{\eta_b}\right)\frac{\partial P_{\mathbf{\Delta}}(\Delta,t)}{\partial \Delta}, \qquad (\Delta \geq 0), \tag{6.18a}$$

$$\frac{\partial P_{\mathbf{Z}}(z,t)}{\partial t} = D_z\frac{\partial^2 P_{\mathbf{Z}}(z,t)}{\partial z^2} - V_z\frac{\partial P_{\mathbf{Z}}(z,t)}{\partial z}, \qquad (-\infty < z < +\infty), \tag{6.18b}$$

where

$$D_z = \frac{D_a D_b}{D_a + D_b}, \qquad V_z = \frac{D_b V_a - D_a F_{ext}/\eta_b}{D_a + D_b}. \tag{6.19}$$

Note the continuous diffusion formalism for the BR was introduced in Ref. [62], which contained some typos, particularly in the Appendix which focused on the time-dependent solution to (6.18a).[4] We can see that as long as $V_a + \frac{F_{ext}}{\eta_b} > 0$, or the polymer and the barrier are drifting toward one another, then the gap approaches a stationary (exponential) distribution given by

$$P_{\mathbf{\Delta}}(\Delta) = \frac{V_a + F_{ext}/\eta_b}{D_a + D_b} e^{-\frac{V_a + F_{ext}/\eta_b}{D_a + D_b}\Delta}, \tag{6.20}$$

and the center of friction undergoes diffusion with effective diffusion and drift parameters given by (6.19), as expected from Ohm's law:

$$P_{\mathbf{Z}}(z,t) = \frac{1}{\sqrt{4\pi D_z t}} e^{-\frac{(z - V_z t)^2}{4 D_z t}}. \tag{6.21}$$

Note that the direction of the average drift, or average motion, of the center of friction can be summarized by looking at the sign of V_z, as shown in Table 6.2.[5]

---

[4] The first typo to be corrected is a missing "−" sign in the exponent of Ref. [62]'s (25). The formula should match our (6.20).

[5] We can see that the conditions in Table 6.2 on V_Z are consistent with the conditions on $K_1 = \frac{\alpha_p \beta_w}{\beta_p \alpha_w}$ in Table 6.1 if we make the identifications

$$\begin{aligned} V_a &= (\alpha_p - \beta_p)\Delta x, \qquad D_a = (\alpha_p + \beta_p)\frac{\Delta x^2}{2}, \\ \frac{F_{ext}}{\eta_b} &= (\alpha_w - \beta_w)\Delta x, \qquad D_b = (\alpha_w + \beta_w)\frac{\Delta x^2}{2}. \end{aligned}$$

Then, after some algebra, V_z can be written as

$$V_z = \frac{2\Delta x\,(\alpha_p \beta_w - \beta_p \alpha_w)}{(\alpha_p + \beta_p + \alpha_w + \beta_w)} = \frac{2\Delta x \beta_p \alpha_w\,(K_1 - 1)}{(\alpha_p + \beta_p + \alpha_w + \beta_w)},$$

and we can see that $V_z > 0$ if $K_1 > 1$, $V_z = 0$ if $K_1 = 1$, and $V_z < 0$ if $K_1 < 1$. Also note that the above expression for V_z is consistent with that derived for two random walkers in (D.6a) of Appendix D.

Table 6.2: **Average Motion of the Single Polymer Brownian Ratchet.**
Summary of the average direction of motion of the center of friction of the single polymer with a moving barrier system, where $V_z = \frac{D_b V_a - D_a F_{ext}/\eta_b}{D_a + D_b}$.

Direction of Motion	Physical Meaning	Condition
Right	polymer pushes barrier	$V_z > 0, \quad \frac{V_a}{D_a} > \frac{F_{ext}}{\eta_b D_b}$
Left	barrier pushes polymer	$V_z < 0, \quad \frac{V_a}{D_a} < \frac{F_{ext}}{\eta_b D_b}$
None	balance, stalled system	$V_z = 0, \quad \frac{V_a}{D_a} = \frac{F_{ext}}{\eta_b D_b}$

Also note that if the barrier is in thermal equilibrium, i.e. $\eta_b D_b = k_B T$, the critical stalling force, or the external resistant force at which $V_z = 0$, is given by $F^*_{ext} = k_B T V_a / D_a$.

6.2.1 Time Dependent Gap Distribution

For the interested reader we provide all of the details for finding the full time dependent gap distance solution in Appendix C, however, in this section, we simply state the results. Note that the time dependent solution was also presented in Appendix A of Ref. [62], without a derivation and with a few typos. We take this opportunity both to correct those typos, and to expand upon a few of the details that were left out.

In order to find the time dependent gap distribution, and for comparison with Ref. [62], it is useful to re-scale time. First, divide both sides of (6.18a) by $D_a + D_b$, and let $\omega = \frac{V_a + F_{ext}/\eta_b}{D_a + D_b}$:

$$\frac{1}{D_a + D_b} \frac{\partial P_{\mathbf{\Delta}}(\Delta, t)}{\partial t} = \frac{\partial^2 P_{\mathbf{\Delta}}(\Delta, t)}{\partial \Delta^2} + \omega \frac{\partial P_{\mathbf{\Delta}}(\Delta, t)}{\partial \Delta}.$$

Next, replace $t \to (D_a + D_b)t$, and let $u(x,t) = P_{\mathbf{\Delta}}(\Delta, t)$, where x represents the gap distance, and t is the re-scaled time. Then the initial boundary value problem describing the time-dependent gap distance distribution is given by

$$u_t(x,t) = u_{xx}(x,t) + \omega u_x(x,t), \qquad 0 \le x < \infty, t > 0, \tag{6.22a}$$

$$\delta(x) = u(x,0), \tag{6.22b}$$

$$0 = u_x(x,t) + \omega u(x,t), \qquad x = 0, x = \infty, t > 0, \tag{6.22c}$$

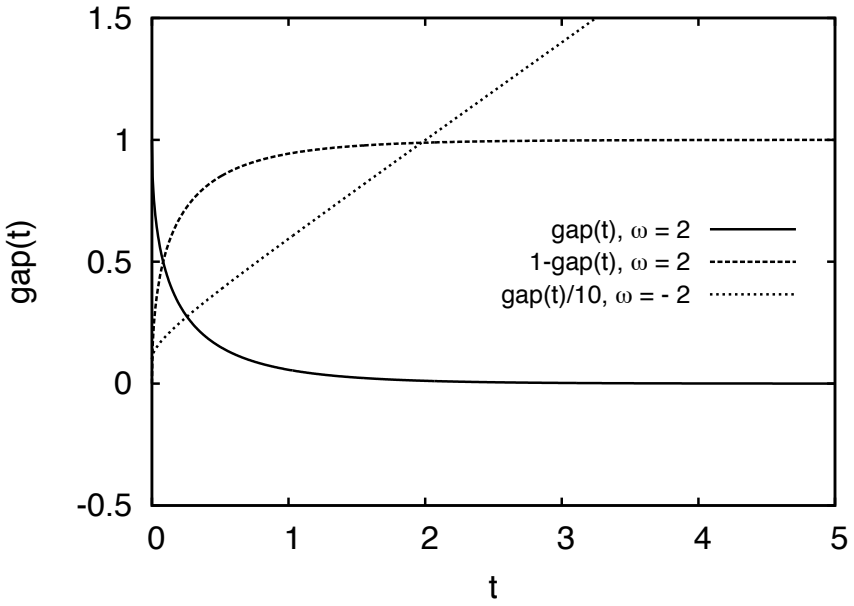

Figure 6.8: **Plots of gap(t) for $\omega = 2$ and $\omega = -2$.**
Corrected version of Figure 6 from Ref. [62].

where the $\delta(x)$ in (6.22b) has the physical interpretation that the gap distance is zero at $t = 0$. Note that this is a singular Sturm-Liouville problem due to the semi-infinite spatial interval. The solution to the initial boundary value problem, as well as its mean and second moment can be expressed as

$$u(x,t) = \omega e^{-\omega x} + e^{-\frac{\omega x}{2} - \frac{\omega^2 t}{4}} \int_0^\infty \frac{z e^{-\frac{z^2 t}{4}} \left[z \cos\left(\frac{\omega x}{2}\right) - \omega \sin\left(\frac{\omega x}{2}\right) \right] dz}{\pi \left(\omega^2 + z^2\right)}, \quad (6.23)$$

$$\begin{aligned} \int_0^\infty x u(x,t) dx &= \frac{1}{\omega} - e^{-\frac{\omega^2 t}{4}} \int_0^\infty \frac{4 z^2 e^{-\frac{z^2 t}{4}}}{\pi \left(\omega^2 + z^2\right)^2} dz, \\ &= \frac{1}{\omega} \left[(1 + 2\tau)\, erf\left(\sqrt{\tau}\right) - 2\tau + 2\sqrt{\frac{\tau}{\pi}} e^{-\tau} \right], \quad (6.24) \end{aligned}$$

$$\int_0^\infty x^2 u(x,t) = \frac{8}{\omega} \int_0^\tau gap(s) ds, \quad (6.25)$$

where $\mu(z) = -\frac{1}{4}\left(\omega^2 + z^2\right)$, $\tau = \frac{\omega^2 t}{4}$, $gap(\tau) = 1 - \omega\langle x \rangle$. Note that $\int_0^\infty u(x,t) dx = 1$, as we expect.

Corrections and Clarifications for Ref. [62]

The main error in the Appendix in Ref. [62] occurs in Figure 6. There are actually two errors in the original plot: the qualitative shape of the $gap(t)$ curves and a labeling error. In the original plot, the curves do not monotonically approach their limiting values, as they should. (It is not clear what caused this error.) Also in the original plot, the third curve, for $\omega < 0$ was labeled incorrectly as "$(1 - gap(t))/10$" when it should have been labeled "$gap(t)/10$."

In summary, the curve $gap(t)$ for $\omega > 0$ should monotonically approach zero, the curve $1 - gap(t)$ for $\omega > 0$ should monotonically approach one, and $gap(t)$ for $\omega < 0$ should grow monotonically without bound, as we would expect, and as can be seen in Figure 6.8.

$\langle \mathbf{x^2} \rangle$ Expression Clarification

The expression given in Ref. [62] for the expected value of x^2 is correct, but the method of derivation was not immediately obvious, which we will now clarify. Typically, since we have an analytic closed form solution for $u(x,t)$, we would perform the integration directly to obtain an expression similar to that shown in (6.24). However, it may be useful to express $\langle x^2 \rangle$ in terms of the function $gap(\tau)$. In order to do so, use integration by parts:

$$\begin{aligned} \langle x \rangle &= \int_0^\infty x u(x,t) dx, \\ &= \frac{x^2}{2} u(x,t)\Big|_{x=0}^{\infty} - \int_0^\infty \frac{x^2}{2} u_x(x,t) dx, \end{aligned}$$

where the first term on the second line vanishes since $u(x,t) \to 0$ dominates the growth of x^2 as $x \to \infty$. Then we can use (6.22a) to replace $u_x(x,t) = \frac{1}{\omega}\left(u_t(x,t) - u_{xx}(x,t)\right)$, and then integrate by parts again:

$$\begin{aligned} \langle x \rangle &= -\frac{1}{\omega}\int_0^\infty \frac{x^2}{2} u_t(x,t) dx + \frac{1}{\omega}\int_0^\infty \frac{x^2}{2} u_{xx}(x,t) dx, \\ &= -\frac{1}{\omega}\int_0^\infty \frac{x^2}{2} u_t(x,t) dx + \frac{1}{\omega}\left(\frac{x^2}{2} u_x(x,t)\Big|_{x=0}^{\infty} - \int_0^\infty x u_x dx \right), \\ &= -\frac{1}{\omega}\int_0^\infty \frac{x^2}{2} u_t(x,t) dx - \frac{1}{\omega}\left(x u(x,t)|_{x=0}^{\infty} - \int_0^\infty u(x,t) dx \right), \\ &= -\frac{1}{\omega}\int_0^\infty \frac{x^2}{2} u_t(x,t) dx + \frac{1}{\omega}, \end{aligned}$$

where again we make use of the fact that $u(x,t) \to 0$ and $u_x(x,t) \to 0$ as $x \to \infty$, as well as $\int_0^\infty u(x,t)dx = 1$. Finally, we can make use of (6.24) to write

$$\frac{1}{\omega}\left(1 - gap\left(\frac{\omega^2 t}{4}\right)\right) = \frac{1}{\omega}\left(1 - \int_0^\infty \frac{x^2}{2} u_t(x,t)dx\right),$$

or

$$\int_0^\infty x^2 u_t(x,t)dx = 2gap\left(\frac{\omega^2 t}{4}\right).$$

We can see that if we integrate both sides over *time*, we obtain

$$\begin{aligned}
\int_0^t \int_0^\infty x^2 u_r(x,r)dxdr &= 2\int_0^t gap\left(\frac{\omega^2 r}{4}\right)dr, \\
\int_0^\infty x^2 u(x,t)dx &= \frac{8}{\omega^2}\int_0^{\frac{\omega^2 t}{4}} gap(s)ds, \\
\langle x^2 \rangle &= \frac{8}{\omega^2}\int_0^\tau gap(s)ds.
\end{aligned}$$

Area Under gap(τ)

It is also interesting to note that the area under $gap(\tau)$ approaches the value of $\frac{1}{4}$ as $\tau \to \infty$. This can be seen by direct integration, using (6.24):

$$\begin{aligned}
\int_0^\tau gap(s)ds &= \int_0^\tau \left(1 - \left[(1+2s)\,erf\left(\sqrt{s}\right) - 2s + 2\sqrt{\frac{s}{\pi}}e^{-s}\right]\right)ds, \\
&= \tau(1+\tau)(1 - erf\sqrt{\tau}) - \frac{1}{2}\sqrt{\frac{\tau}{\pi}}(1+2\tau)e^{-\tau} + \frac{1}{4}erf\sqrt{\tau}.
\end{aligned}$$

Note that $\lim_{\tau\to\infty} erf\sqrt{\tau} = 1$, so that the only term remaining in the long time limit is $\frac{1}{4}$.

Variance Calculation

The result in the previous section allows us to show that the long time limiting behavior of the gap distance is truly exponential since

$$\begin{aligned}
\lim_{t\to\infty}\langle x \rangle &= \frac{1}{\omega}, \\
\lim_{t\to\infty}\langle \sigma^2 \rangle = \lim_{t\to\infty}\left(\langle x^2\rangle - \langle x\rangle^2\right) &= \lim_{t\to\infty}\left(\frac{8}{\omega^2}\int_0^\tau gap(s)ds - \frac{1}{\omega^2}\left(1 - gap(\tau)\right)^2\right) = \frac{2}{\omega^2} - \frac{1}{\omega^2}, \\
&= \frac{1}{\omega^2}.
\end{aligned}$$

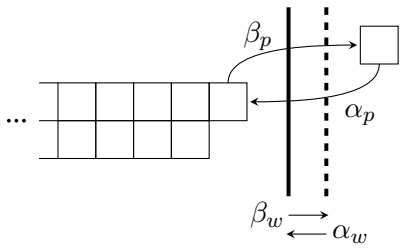

Figure 6.9: **Two Polymers Interacting with a Moving Barrier.**

6.3 Multiple Filament Preview: Insights from the Two Polymer System

As a preview of the model for N polymer filaments interacting with a moving barrier, we will first make some observations about the $N = 2$ case. One of our goals is to formulate a solution for the gap distances between multiple polymers interacting with a moving barrier. The polymers will be identical, but we will see that their interaction with the moving barrier will prevent them from being truly independent. We will use Monte Carlo simulations, as described in Appendix B, to illustrate this interesting phenomenon. Let both polymers have adding and subtracting rates α_p and β_p, and let the barrier move towards and away from the polymers at rates α_w and β_w, as in Figure 6.9. We have asserted that the interaction between the polymers and the moving barrier prevents the polymers from being independent. The easiest way to see that the polymers are not independent is to compare the steady state distribution of the gap distance between each polymer and the moving barrier to the solution for a single polymer interacting with the moving barrier. If the polymers were truly independent, as well as identical, then we would expect the steady state solution for each gap distance to be exactly the solution we saw before,

$$p_i = \frac{\alpha - \beta}{\alpha} \left(\frac{\beta}{\alpha} \right)^i, \tag{6.26}$$

where $\alpha = \alpha_p + \alpha_w$ and $\beta = \beta_p + \beta_w$. Figure 6.10 shows the gap distance distributions for two identical polymers interacting with a moving barrier with parameters $\alpha = 6$ and $\beta = 2$, for a simulation over 10,000 time units. We can see that the steady state distributions for the gap distances appear to be the same for each polymer, but they clearly differ from the

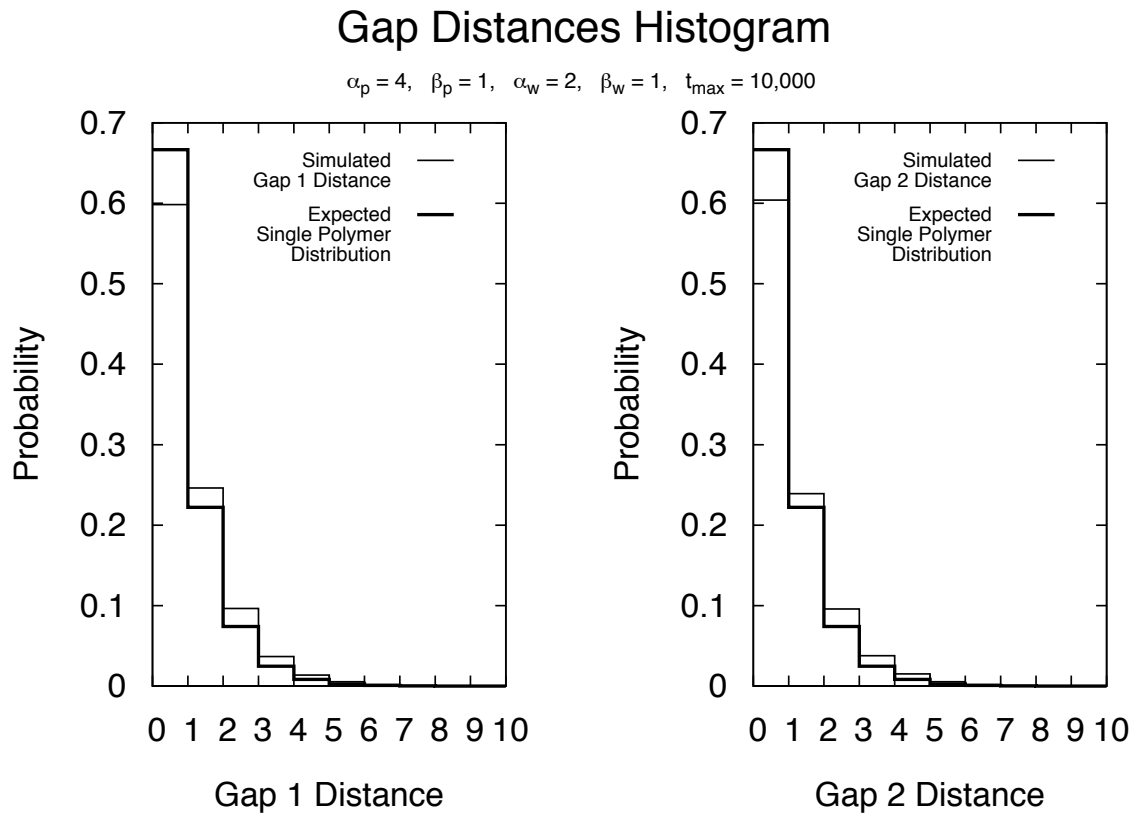

Figure 6.10: **Two Polymer System Gap Distributions.**
Histogram for the gap distances between two polymers and a moving barrier with the given parameters. The simulation was run for 10,000 time units, and the histogram for each gap distance is shown along with the prediction from the mathematical model for a single polymer system.

distribution predicted by equation (6.26). Now that we can see qualitatively that the polymers are not independent, we can start to quantify the cooperation between the polymers. Again, we will begin with a random walk analogy. In this case, we can view the gap distances as undergoing a two-dimensional random walk, from the point of view of the barrier, as shown in Figure 6.11. We can see that motion in the horizontal and vertical directions in Figure 6.11 is caused by adding and subtracting monomers from polymer 1 and 2 respectively, while motion in the diagonal direction is caused by the barrier moving toward or away from both polymers. We can use this diagram as a guide to derive a partial differential equation describing the gap

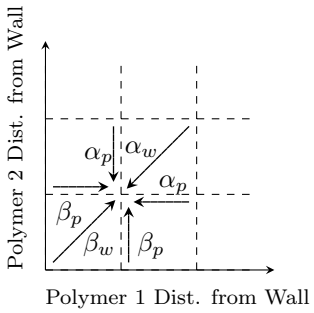

Figure 6.11: **2-D Random Walk Diagram for Gap Distances Between two Polymers and a Moving Barrier.**

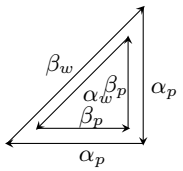

Figure 6.12: **The Smallest Cycle from Figure 6.11.**
Recall that horizontal motion corresponds to polymer 1 motion, vertical motion corresponds to polymer 2 motion, and movement along the diagonal corresponds to the motion of the barrier.

distances, as we did in the single polymer cases, as well as a guide to create a difference equation describing the gap distances.

6.3.1 Smallest Cycle Insight

We can gain further insight into the multiple polymer-moving barrier system by again examining Figure 6.11. If we were to draw all of the arrows on the grid, and then look at the smallest triangle made by the arrows, then we will see the cycle shown in Figure 6.12. One trip around the cycle in the clockwise direction corresponds to both polymers moving toward the barrier, and the barrier moving away from the polymers. Likewise, one trip around the cycle in the

Table 6.3: **Average Motion of Two Polymers Interacting with a Moving Barrier.** Summary of the conclusions about the net motion of the two polymers and a moving barrier system, where $K_2 = \frac{\alpha_p^2 \beta_w}{\beta_p^2 \alpha_w}$.

Net Cycle Direction	Physical Result	Net System Motion	Condition
Clockwise	polymer pushes barrier	Positive	$K_2 > 1$
Counterclockwise	barrier pushes polymer	Negative	$K_2 < 1$
None	balance, stalled system	None	$K_2 = 1$

counterclockwise direction corresponds to the barrier moving toward the polymers and both polymers moving away from the barrier. Therefore, we can use this cycle to determine a condition for the average motion of the system. If, on average, the system makes more clockwise cycles than counterclockwise cycles, then the polymers will push the barrier and the system will undergo net motion in the positive direction. On the other hand, if the system makes more counterclockwise cycles than clockwise cycles on average, then the barrier will push the polymers and the system will undergo net motion in the negative direction. Furthermore, if the system makes the same number of clockwise and counterclockwise cycles, on average, then a stalemate occurs and the system will undergo no net motion.

As in the single polymer case, we can define K_2 to be the equilibrium constant for positive average motion of the system, or moving around the cycle in the clockwise direction, as ratio of the product of the reaction rates in the forward, or clockwise, direction to the product of the reaction rates in the backward, or counterclockwise, direction:

$$K_2 = \frac{\alpha_p^2 \beta_w}{\beta_p^2 \alpha_w}. \tag{6.27}$$

Now we can use K_2 to determine the conditions on the net motion of the system. If $K_2 > 1$, then the system will undergo net positive motion, while if $K_2 < 1$, the system will undergo net negative motion. If $K_2 = 1$, then the system is balanced, and no net motion will occur. Table 6.3 summarizes these conclusions.

Recall that for a single polymer, the equilibrium constant for net positive motion of the system was $K_1 = \frac{\alpha_p \beta_w}{\beta_p \alpha w}$, so $K_2 = K_1 \frac{\alpha_p}{\beta_p}$; the addition of a second polymer simply causes the

equilibrium constant to be multiplied by an extra factor of $\frac{\alpha_p}{\beta_p}$. Furthermore, for N polymers, the equilibrium constant for net positive motion of the system will be given by

$$K_N = \frac{\beta_w}{\alpha_w}\left(\frac{\alpha_p}{\beta_p}\right)^N, \tag{6.28}$$

and the condition on the polymers pushing the barrier will be that $K_N > 1$. Likewise, the system will have no net motion, or be stalled, on average, if $K_N = 1$, and if $K_N < 1$ the barrier will push the polymers.

Under a constant external force F, the equilibrium constant for the system advancing by Δx will be given by

$$K_N(F) = K_N e^{-\frac{F\Delta x}{k_B T}}, \tag{6.29}$$

where T is the temperature and k_B is Boltzmann's constant, and K_N is defined as above. As before, if $K_N(F) > 1$ then the system will move in the direction of polymer growth, and if $K_N(F) < 1$ then the system will move in the opposite direction, on average. Define the stalling force, F^*, to be the external force at which $K_N(F^*) = 1$, so that the system undergoes no net motion. Then we can see that the stalling force scales with the number of polymers:

$$F^* = \frac{k_B T}{\Delta x}\left(N \log\left(\frac{\alpha_p}{\beta_p}\right) - \log\left(\frac{\alpha_w}{\beta_w}\right)\right). \tag{6.30}$$

We will reach an analogous conclusion using the diffusion formalism for a bundle of polymer filaments interacting with a moving barrier in Chapter 7.

Chapter 7

BROWNIAN RATCHET REVISITED: INTERNAL ATTRACTION AND MULTIPLE FILAMENTOUS BUNDLE GROWTH

We will now build upon the framework introduced in Chapter 6 in order to incorporate two new features: an interaction between the polymer filament and the barrier, and multiple filamentous bundle growth.[1]

To represent the interaction between a filament and a barrier, we use an internal interaction force, $F_{int}(\Delta)$, where Δ is the distance between the tip of the filament and the barrier, or "the gap." In the case of a chemical interaction, i.e. binding, $F_{int}(\Delta)$ is a statistical thermodynamic force averaged over the solvent molecules. Note that a similar idea is used in Ref. [3] to incorporate the interaction between helicase and strands of DNA. Dickinson *et. al.* have proposed "end-tracking" models to describe the interaction between polymer filaments and the objects they propel [12, 10, 11]. Based on our diffusion formalism for the BR, we shall show that the $F_{int}(\Delta)$ can be effectively treated as a *constant* resistant force. It is known that a resistant force can significantly reduce the apparent diffusion of a propelled bacterium [62]. Therefore, the data of Kuo and McGrath can be explained by the BR model without significant modification.

We would like to emphasize that the essence of the BR model is *not* a model for actin polymerization *per se*. It is actually a model for how a certain external load is exerted on a molecular force generator and alters its internal working. The BR model can be applied equally well to a motor protein, such as kinesin, moving against an intracellular organelle which is itself non-specifically bound to, and wandering randomly along, the same 1-dimensional microtubule [63, 66]. Another situation that can be considered is DNA polymerase pushing another non-

---

[1]This chapter is a postprint version of an article published as [DOI: 10.1142/S1793048011001269]:
The Brownian Ratchet Revisited: Diffusion Formalism, Polymer-Barrier Attractions, and Multiple Filamentous Bundle Growth, Christine Lind Cole and Hong Qian, *Biophysical Reviews and Letters*, Volume 6, Issues 1-2,

specifically bound DNA-binding protein along a strand of DNA. In each of these examples, there can be interactions between the individual molecular force generator and the microscopic object. If the interaction is only geometric exclusion, then this leads to the original BR. In general, however, the interaction can be mechanical or chemical, as discussed in this chapter (also see Ref. [15]). Different types of external resistant forces can also be applied. Constant or elastic forces, for example, have been applied in experiments on motor proteins, using viscous drag or fiber-glass beams respectively [32]. In principle, even the numerical values for the critical stalling (isometric) force can be different from measurements with different types of load and different ways of loading, as discussed in Section 5.3.

7.1 Internal Polymer-Barrier Interaction $U_{int}(y-x)$

If the interaction between the actin filament (or the motor protein) and the barrier is more complex than a simple geometric exclusion, then one can represent the interaction using a potential energy function, $U_{int}(y-x)$, and the corresponding force, $F_{int}(s) = -dU_{int}(s)/ds$. The potential, $U_{int}(y-x)$, can represent either an actual mechanical force between the polymer (or motor) and the barrier, or a chemical interaction in terms of the potential of mean force between the two molecular objects in an aqueous solution [75]. In the context of polymerization, a chemical potential allowing for interaction without physical attachment seems more appropriate, while in the case of a motor protein there could be a molecular tether. In either case, we modify the original equation, (6.16), to include the interaction term:

$$\begin{aligned}\frac{\partial P_{\mathbf{XY}}(x,y,t)}{\partial t} &= D_a\frac{\partial^2 P_{\mathbf{XY}}(x,y,t)}{\partial x^2} + D_b\frac{\partial^2 P_{\mathbf{XY}}(x,y,t)}{\partial y^2} \\ &\quad -\frac{\partial}{\partial x}\left(V_a + \frac{F_{int}(y-x)}{\eta_a}\right)P_{\mathbf{XY}}(x,y,t) \\ &\quad +\frac{\partial}{\partial y}\left(\frac{F_{ext}+F_{int}(y-x)}{\eta_b}\right)P_{\mathbf{XY}}(x,y,t). \end{aligned} \tag{7.1}$$

Using the coordinate transformation from (6.17) and some straightforward algebra, we obtain

$$\begin{aligned}\frac{\partial P_{\mathbf{\Delta Z}}(\Delta,z,t)}{\partial t} &= D_\delta\frac{\partial^2 P_{\mathbf{\Delta Z}}(\Delta,z,t)}{\partial \Delta^2} + D_z\frac{\partial^2 P_{\mathbf{\Delta Z}}(\Delta,z,t)}{\partial z^2} + \frac{\partial}{\partial \Delta}\left(V_1(\Delta)P_{\mathbf{\Delta Z}}(\Delta,z,t)\right) \\ &\quad -\frac{\partial}{\partial z}\left(V_2(\Delta)P_{\mathbf{\Delta Z}}(\Delta,z,t)\right), \qquad (0\le\Delta,\ -\infty<z<\infty), \end{aligned} \tag{7.2}$$

in which $D_\delta = (D_a + D_b)$, $D_z = D_a D_b/(D_a + D_b)$, as before, and

$$V_1(\Delta) = V_a + \frac{F_{ext}}{\eta_b} + \left(\frac{1}{\eta_a} + \frac{1}{\eta_b}\right) F_{int}(\Delta), \tag{7.3a}$$

$$V_2(\Delta) = \frac{D_b V_a - \frac{D_a F_{ext}}{\eta_b} + \left(\frac{D_b}{\eta_a} - \frac{D_a}{\eta_b}\right) F_{int}(\Delta)}{D_a + D_b}. \tag{7.3b}$$

If we assume that the gap reaches a steady state then we can separate the gap distance dependence from the center of friction and time dependence, $P_{\mathbf{\Delta Z}}(\Delta, z, t) = P_{\mathbf{\Delta}}(\Delta) P_{\mathbf{Z}}(z, t)$, and rewrite (7.2) after some algebra as a nearly-decoupled system,

$$0 = D_\delta \frac{d^2 P_{\mathbf{\Delta}}(\Delta)}{d\Delta^2} + \frac{d}{d\Delta}\left(V_1(\Delta) P_{\mathbf{\Delta}}(\Delta)\right), \qquad (\Delta \geq 0), \tag{7.4a}$$

$$P_{\mathbf{\Delta}}(\Delta) \frac{\partial P_{\mathbf{Z}}(z,t)}{dt} = P_{\mathbf{\Delta}}(\Delta) \left(D_z \frac{\partial^2 P_{\mathbf{Z}}(z,t)}{\partial z^2} - \frac{\partial}{\partial z}\left(V_2(\Delta) P_{\mathbf{Z}}(z,t)\right)\right), \quad (-\infty < z < +\infty). \tag{7.4b}$$

Note that by calling this a "nearly-decoupled" system, we are highlighting the fact that (7.4b) still includes explicit dependence on the gap distance, due the $V_2(\Delta)$ term.

By solving (7.4a) with a no flux boundary condition at both $\Delta = 0$ and $\Delta \to \infty$,[2] we obtain

$$P_{\mathbf{\Delta}}(\Delta) = \mathcal{N} \exp\left[-\frac{(V_a + F_{ext}/\eta_b)\Delta - (1/\eta_a + 1/\eta_b) U_{int}(\Delta)}{D_a + D_b}\right], \tag{7.5}$$

where $\mathcal{N}$ is a normalization factor. If we define $\overline{F}_{int}$ to be the mean force between the polymer and the barrier,

$$\overline{F}_{int} = \int_0^\infty F_{int}(s) P_{\mathbf{\Delta}}(s) ds, \tag{7.6}$$

then we can simply integrate by parts to find the relationship between the normalization constant and the other important system parameters:

$$\overline{F}_{int} = \frac{D_\delta}{1/\eta_a + 1/\eta_b} P_{\mathbf{\Delta}}(0) - \frac{V_a + F_{ext}/\eta_b}{1/\eta_a + 1/\eta_b}. \tag{7.7}$$

If $U_{int}(0) = 0$, then (7.7) simplifies to

$$\mathcal{N} = \frac{V_a + \overline{F}_{int}/\eta_a + (F_{ext} + \overline{F}_{int})/\eta_b}{D_a + D_b}, \tag{7.8}$$

---

[2] In this case, the no flux boundary condition is given by

$$\left[D_\delta \frac{dP_{\mathbf{\Delta}}(x)}{dx} + \left(V_a + \frac{F_{ext}}{\eta_b} + \left(\frac{1}{\eta_a} + \frac{1}{\eta_b}\right) F_{int}(x)\right) P_{\mathbf{\Delta}}(x)\right]\Big|_{x=0,\infty} = 0.$$

as we might expect from (6.20). We can also define the association (binding) constant, K_b, between the polymer and the barrier using the following Kirkwood-Buff integral [64]:

$$K_b = \int_0^\infty \left(e^{-U_{int}(s)/k_B T} - 1 \right) ds, \tag{7.9}$$

which will be used in Section 7.2.5.

Next, after we integrate (7.4b) over the gap distance $\mathbf{\Delta}$, the equation for the stochastic movement of $\mathbf{Z}(t)$, the "center of friction" of the BR reduces to

$$\frac{\partial P_{\mathbf{Z}}(z,t)}{\partial t} = D_z \frac{\partial^2 P_{\mathbf{Z}}(z,t)}{\partial z^2} - V_z \frac{\partial P_{\mathbf{Z}}(z,t)}{\partial z}, \quad (-\infty < z < +\infty), \tag{7.10}$$

in which D_z is defined as before, and

$$V_z = \frac{(D_b V_a - D_a F_{ext}/\eta_b) + (D_b/\eta_a - D_a/\eta_b)\overline{F}_{int}}{D_a + D_b}. \tag{7.11}$$

We note that if both diffusing particles are passive objects in thermal equilibrium, then $\eta_a D_a = \eta_b D_b = k_B T$ and the internal force will have no contribution to the motion of the center of friction. The D_z and V_z characterize the stochastic movement of the barrier under the propulsion of the polymerization, in terms of diffusivity and velocity [36].

In most experiments involving actin cytoskeletons, the polymer structure is large and $\frac{1}{\eta_a} \approx 0$. Then the net effect of the internal interaction is an effective resistant force $F_{eff} = F_{ext} + \overline{F}_{int}$, and (7.11) can be compared directly to (6.19). Therefore, in the rest of the chapter, the resistant force F is understood as the sum of both the external resistant force and the internal attractive force.

7.1.1 Force-Dependent Polymerization Rate $\alpha(F)$

The polymerization rate, α, is a pseudo-first order rate constant which is proportional to both the monomer concentration in the surrounding solution, c_0, and the probability of the gap being greater than the length of one monomer, $Pr\{\mathbf{\Delta}(t) \geq \delta\}$:

$$\alpha = \alpha_0 c_0 \int_\delta^\infty P_{\mathbf{\Delta}}(s) ds = \alpha_0 c_0 \exp\left[-\frac{V_a + F/\eta_b}{D_a + D_b} \delta \right], \tag{7.12}$$

where α_0 is the intrinsic, second-order rate constant for polymerization, and $P_{\mathbf{\Delta}}(\Delta)$ comes from (6.20). Recall that the parameters D_a and V_a are defined in terms of α, β, and δ in (6.15).

Since the gap distance fluctuates according to a distribution depending on the resistant force, α is itself a function of the effective resistant force, which can be described in a self-consistent manner by the following transcendental equation:

$$\alpha = \alpha_0 c_0 \exp\left[-\frac{(\alpha-\beta)\delta + F/\eta_b}{(\alpha+\beta)\delta^2/2 + D_b}\delta\right]. \tag{7.13}$$

Figure 7.1 shows α as a function of F for several different values of $\alpha_0 c_0$ when $\beta = 0$. Note that V_z in (7.11) is a linear function of resistant force F explicitly. However, a nonlinearity arises since D_a and V_a are implicit functions of F, via $\alpha(F)$. We can see that the resistant force F slows down the BR by two mechanisms: a linear Newtonian resistance and also an exponential decrease in the rate of polymerization due to a diminished gap. If $D_a \ll D_b$, then $D_z \approx D_a$, from (6.19). Furthermore, if $\alpha \gg \beta$, then $D_a \approx \alpha\delta^2/2$, from (6.15). Therefore, under these conditions, the resistant force F also reduces the diffusion coefficient D_z.

The depolymerization rate β can also be a function of the gap δ in general. However, since we are mainly interested in the rapid polymerization regime, i.e. $\alpha \gg \beta$ and $\beta \approx 0$, where the motion of the barrier is the rate-limiting process in the overall kinetics of the system, we shall neglect this effect in this study. However, in practice, the depolymerization process will become important in the high force regime.

7.2 Multiple Filamentous Bundle Growth

Now we will begin to work toward the goal of extending our model to describe a bundle of multiple filaments interacting with a moving barrier. We will begin with the basic model of a single filament in free space, without the presence of a barrier. The growth of a single filament is modeled by a continuous diffusion process $\mathbf{X}(t)$ with D_a and V_a given in (6.15). The position of the end of a single filament can be characterized by either $F_{\mathbf{X}}(x,t) = \Pr\{\mathbf{X}(t) \le x\}$, the cumulative probability distribution function (*cdf*), or $\partial F_{\mathbf{X}}(x,t)/\partial x = f_{\mathbf{X}}(x)$, the probability density function (*pdf*):

$$F_{\mathbf{X}}(x,t) = \frac{1}{2}\left[1 + \operatorname{erf}\left(\frac{x - V_a t}{\sqrt{4D_a t}}\right)\right], \tag{7.14a}$$

$$f_{\mathbf{X}}(x,t) = \frac{1}{\sqrt{4\pi D_a t}} e^{-\frac{(x-V_a t)^2}{4D_a t}}, \tag{7.14b}$$

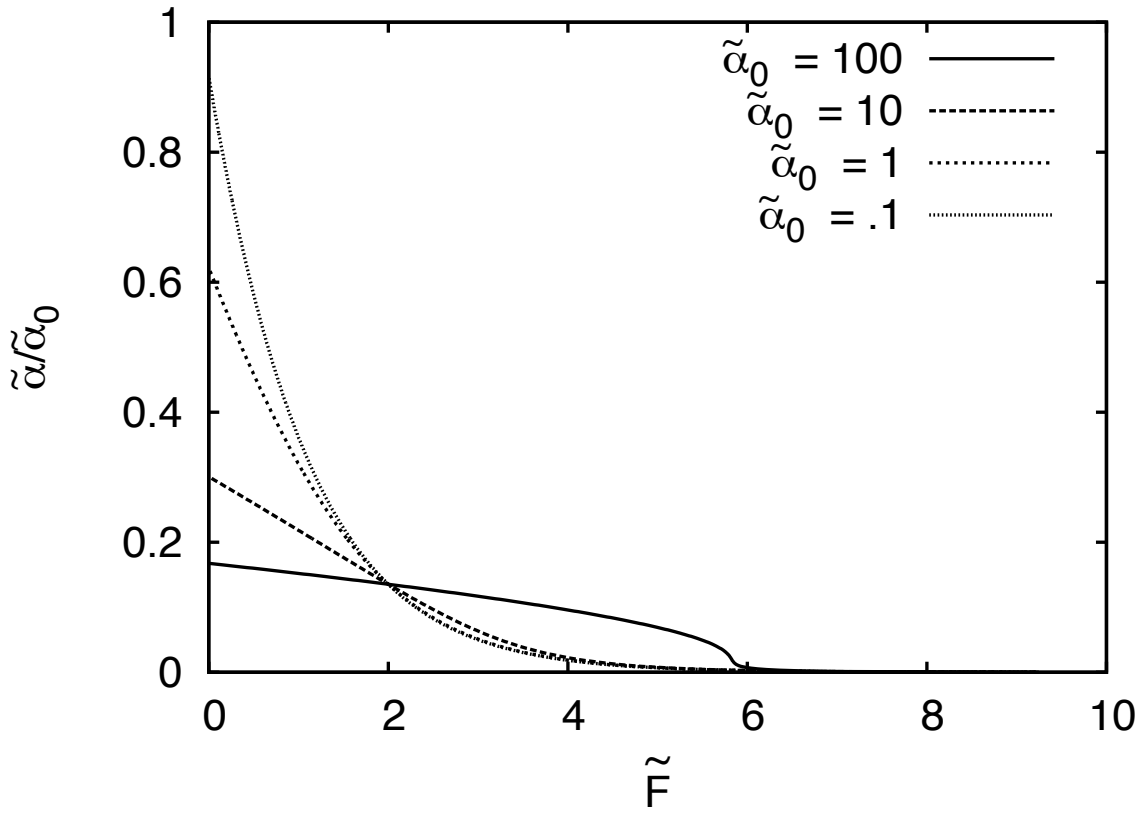

Figure 7.1: **Polymerization Rate as a Function of the Resistant Force.**
In nondimensionalized form, $\widetilde{\alpha} = \alpha\delta^2/D_b$, $\widetilde{\alpha}_0 = \alpha_0 c_0 \delta^2/D_b$, and $\widetilde{F} = F\delta/(D_b\eta_b)$. Using these nondimensionalized quantities, (7.13), with $\beta = 0$, can be rewritten as $\frac{\widetilde{\alpha}}{\widetilde{\alpha}_0} = \exp\left(-\frac{\widetilde{\alpha}+\widetilde{F}}{\widetilde{\alpha}/2+1}\right)$. Curves are shown for several different values of $\widetilde{\alpha}_0$, the ratio of the intrinsic polymerization rate to the barrier diffusion rate. Note that as $\widetilde{\alpha}_0 \to \infty$, $\frac{\widetilde{\alpha}}{\widetilde{\alpha}_0} \to \exp(-2)$.

where the error function erf(z) is defined as

$$\text{erf}(z) = \frac{2}{\sqrt{\pi}} \int_0^z e^{-t^2} dt. \tag{7.15}$$

Note for future reference that the *pdf* given in (7.14b) represents biased diffusion. The solution has a peak located at $x = V_a t$, traveling with velocity V_a, with increasing dispersion.

7.2.1 Growth of a Filamentous Bundle Without a Barrier

We now study the growth of a filamentous bundle in the absence of a resisting object and force. We represent the N filaments by their respective tips at $\mathbf{X}_i(t)$ $(i = 1, 2, ..., N)$ as N independent, identical diffusion processes. The mean position of the filaments, $\overline{\mathbf{X}}(t) = (1/N) \sum_{j=1}^{N} \mathbf{X}_j(t)$, is well understood: it moves with a drift rate V_a and a diffusion coefficient D_a/N [55]. However, since we wish to study the growth of the bundle, we will be more interested in the position of the longest filament, or the *tip* of the bundle, which will be mathematically defined as

$$\mathbf{X}^{(1)}(t) = \max\{\mathbf{X}_1(t), \mathbf{X}_2(t), ..., \mathbf{X}_N(t)\}. \tag{7.16}$$

We will define the position of the k^{th} longest filament using an alternate definition of the order statistics. Let $\mathbf{X}^{(k)}(t)$ be the position of the k^{th} longest filament, when the filament positions are ordered from longest to shortest:

$$\mathbf{X}^{(1)}(t) \geq \mathbf{X}^{(2)}(t) \geq \ldots \geq \mathbf{X}^{(k-1)}(t) \geq \mathbf{X}^{(k)}(t) \geq \mathbf{X}^{(k+1)}(t) \geq \ldots \geq \mathbf{X}^{(N-1)}(t) \geq \mathbf{X}^{(N)}(t).$$

The formulae for the *pdf* and *cdf* of the k^{th} longest filament can be obtained following essentially the standard derivation for the order statistics, which is for the k^{th} smallest among N identical, independent random variables [6, 25]. By definition, $F_{\mathbf{X}^{(k)}}(x,t) = \Pr\{\mathbf{X}^{(k)}(t) \leq x\}$ is the probability that there are at least $(N - k + 1)$ $\mathbf{X}_j(t)$ such that $\mathbf{X}_j(t) \leq x$. Then, by the standard argument using "successful" outcomes of Bernoulli trials, differentiation, and some algebra, we find the *cdf* and *pdf* for the position of the tip of the k^{th} longest filament:

$$F_{\mathbf{X}^{(k)}}(x,t) = \sum_{j=N-k+1}^{N} \begin{pmatrix} N \\ j \end{pmatrix} F_{\mathbf{X}}(x,t)^j \left[1 - F_{\mathbf{X}}(x,t)\right]^{N-j}, \tag{7.17a}$$

$$f_{\mathbf{X}^{(k)}}(x,t) = \frac{N!}{(k-1)!(N-k)!} F_{\mathbf{X}}(x,t)^{N-k} \left[1 - F_{\mathbf{X}}(x,t)\right]^{k-1} f_{\mathbf{X}}(x,t). \tag{7.17b}$$

Note that the physical interpretation of the sum in (7.17a) is the sum of all of the different possible ways that the tips of at least $(N-k+1)$ filaments in the bundle are at positions less than or equal to x. Recall that we are particularly interested in the position of the tip of the bundle, or the longest filament, which has *cdf* and *pdf*

$$F_{\mathbf{X}^{(1)}}(x,t) = 2^{-N}\left[1+\operatorname{erf}\left(\frac{x-V_a t}{\sqrt{4D_a t}}\right)\right]^N, \tag{7.18a}$$

$$f_{\mathbf{X}^{(1)}}(x,t) = \frac{N}{2^{N-1}}\left[1+\operatorname{erf}\left(\frac{x-V_a t}{\sqrt{4D_a t}}\right)\right]^{N-1}\frac{e^{-\frac{(x-V_a t)^2}{4D_a t}}}{\sqrt{4\pi D_a t}}. \tag{7.18b}$$

Note that in the theory of stochastic processes, $\mathbf{X}^{(1)}(t)$ is known as an extremal process [41].

Now the stochastic movement of $\mathbf{X}^{(1)}(t)$ can be understood. We note that (7.18b) describes a biased-diffusion-like behavior. By "biased-diffusion-like," we mean that the solution is unimodal, with a traveling peak but also increasing dispersion, qualitatively similar to the noted behavior of (7.14b). The location of the peak, $x^{(1)}(t)$, and the velocity of the peak movement, $v^{(1)}(t)$, are given by

$$x^{(1)}(t) = V_a t + \omega_1\sqrt{4D_a t}, \qquad v^{(1)}(t) = V_a + \omega_1\sqrt{D_a/t}, \tag{7.19}$$

where ω_1 is a constant that satisfies the transcendental algebraic equation

$$(N-1) = \sqrt{\pi}\ \omega_1\ [1+\operatorname{erf}(\omega_1)]\ e^{\omega_1^2}. \tag{7.20}$$

Note that when $N=1$, $\omega_1 = 0$ as expected. For very large N, $\omega_1 \sim \sqrt{\ln N}$. We can also find the location of the probability peak, and its velocity, for the k^{th} longest filament, $\mathbf{X}^{(k)}(t)$:

$$x^{(k)}(t) = V_a t + \omega_k\sqrt{4D_a t}, \qquad v^{(k)}(t) = V_a + \omega_k\sqrt{D_a/t}, \tag{7.21}$$

in which ω_k is a constant that satisfies the transcendental equation

$$k = 1 + \frac{1-\operatorname{erf}(\omega_k)}{2}\left[N-1-\sqrt{\pi}\omega_k[1+\operatorname{erf}(\omega_k)]e^{\omega_k^2}\right]. \tag{7.22}$$

Figure 7.2 shows how ω_k changes as function of k, with several different values for N. It is seen that the curve is monotonically decreasing with k/N, so for a fixed N, $\omega_k > \omega_{k+1}$. We can approximate the distance between the $\mathbf{X}^{(k)}(t)$ and $\mathbf{X}^{(k+1)}(t)$ using (7.21):

$$\mathbf{X}^{(k)}(t) - \mathbf{X}^{(k+1)}(t) \approx x^{(k)}(t) - x^{(k+1)}(t) = 2(\omega_k - \omega_{k+1})\sqrt{D_a t}. \tag{7.23}$$

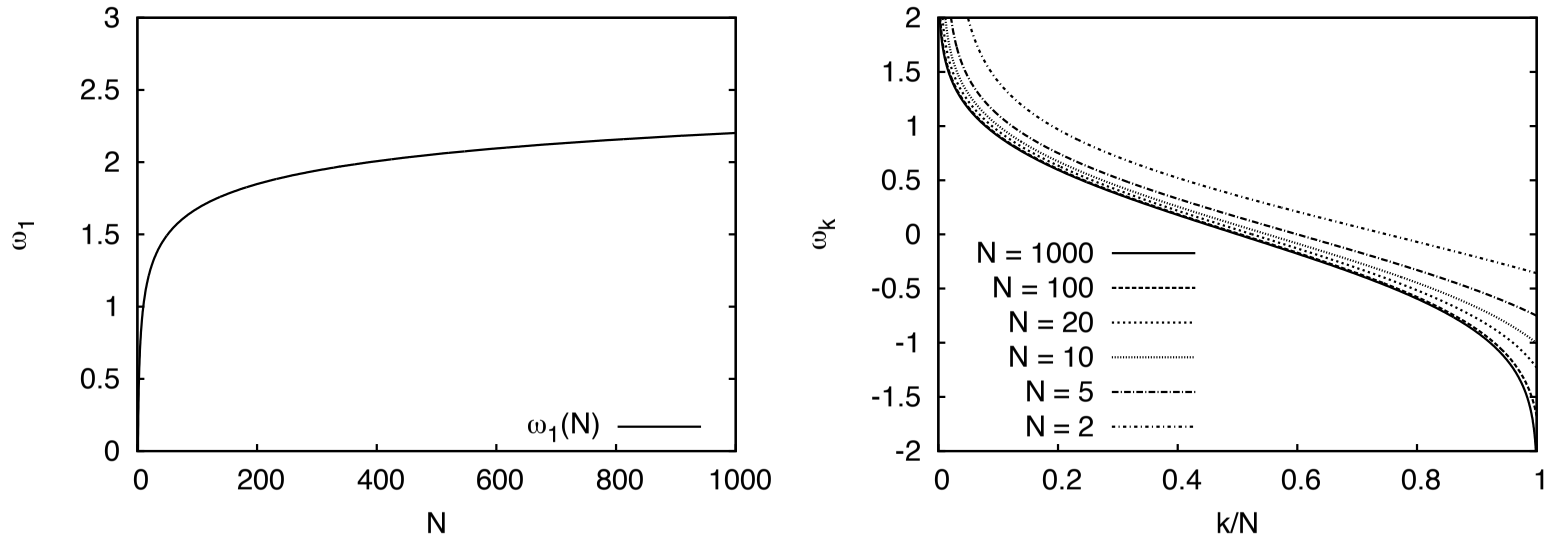

Figure 7.2: **The Roots of ω_k,** (7.22)**.**
On the left, the root of (7.20), ω_1, is plotted for increasing values of N. Note that for very large N, $\omega_1 \sim \sqrt{\ln N}$. On the right, the roots of (7.22), ω_k, are plotted as a function of k/N for different values of N. Note that although continuous curves are shown, we are only interested in discrete points along the curve at $k/N = 1/N, \ldots, 1$. The ω_k curve is monotonically decreasing with k/N, so for a fixed N, $\omega_k > \omega_{k+1}$.

Now we can describe the growth of a filamentous bundle in the absence of a barrier. From (7.19), we can see that the growth velocity of the tip of the bundle is non-uniform. It is largest when the tips of all the filaments are even at the beginning, and decreases with $\sqrt{1/t}$. Furthermore, although each filament grows with t, the distance between them grows with $\sqrt{t}$. Hence, in the long-time limit, the bundle grows as a single filament with all the other filaments lagging behind. Note that we derive the discrete counterpart of (7.19) below.

Finally, we can derive a nonlinear diffusion equation for the motion of the tip of the bundle, $\mathbf{X}^{(1)}(t)$, using (7.18a) and the fact that each $\mathbf{X}_i(t)$ satisfies a diffusion equation, as mentioned at the beginning of Section 7.2,

$$\frac{\partial F_{\mathbf{X}^{(1)}}(x,t)}{\partial t} = D_a \frac{\partial^2 F_{\mathbf{X}^{(1)}}(x,t)}{\partial x^2} - q(x,t)\frac{\partial F_{\mathbf{X}^{(1)}}(x,t)}{\partial x}, \tag{7.24}$$

where the drift rate, $q(x,t)$, is given by

$$q(x,t) = V_a + \frac{D_a(N-1)}{N F_{\mathbf{X}^{(1)}}(x,t)} \left(\frac{\partial F_{\mathbf{X}^{(1)}}(x,t)}{\partial x} \right). \tag{7.25}$$

We can see that the drift rate for the bundle is always greater than V_a, as expected from our intuition, because the *pdf* for the longest filament, $\partial F_{\mathbf{X}^{(1)}}(x,t)/\partial x$, is never negative, as can be seen from (7.18b).

Filamentous Growth: The Discrete Counterpart

In the spatially continuous diffusion formalism, described by (7.19), the displacement of the tip of the bundle due to drift is proportional to t, while the displacement due to diffusion is proportional to $\sqrt{t}$. Hence, the velocity due to diffusion is proportional to $t^{-1/2}$. We will now derive the spatially discrete counterpart of (7.19) for the random walk on a lattice. For a continuous-time random walk, we can model the number of events or steps that occur in time t as a Poisson process with rate $\lambda = (\alpha+\beta)t$. The probability that no events occur, corresponding to the probability that the filament neither grows nor shrinks is then $e^{-\lambda}$. If the time interval is short enough so that at most one event can occur, then the probability that the filament either grows or shrinks is $\left(1 - e^{-\lambda}\right)$. If an event occurs, the probability that it is an adding or subtracting event is given by $\frac{\alpha}{\alpha+\beta}$ or $\frac{\beta}{\alpha+\beta}$ respectively. We can define the probabilities that a

single filament will shrink by one monomer, remain the same length, or grow by one monomer as $P(-\delta,t)$, $P(0,t)$, and $P(+\delta,t)$, respectively:

$$P(-\delta,t) = \frac{\beta}{\alpha+\beta}\left(1-e^{-(\alpha+\beta)t}\right), \tag{7.26}$$

$$P(0,t) = e^{-(\alpha+\beta)t}, \tag{7.27}$$

$$P(+\delta,t) = \frac{\alpha}{\alpha+\beta}\left(1-e^{-(\alpha+\beta)t}\right). \tag{7.28}$$

Now we can find the probabilities for the displacement of the tip of a bundle composed of N identical, independent filaments. Assume that the bundle starts out with each of the filaments having the same length, i.e. the ends are even. The only way that the bundle can shrink is if *all* of the filaments shrink, so define the probability of the bundle displacement of $-\delta$ to be

$$P_B(-\delta,t) = P(-\delta,t)^N = \left[\frac{\beta}{\alpha+\beta}\left(1-e^{-(\alpha+\beta)t}\right)\right]^N. \tag{7.29}$$

The length of the bundle will remain the same if each filament either shrinks or stays the same length, but at least one filament must not shrink. Then the probability that the bundle will stay the same length is given by

$$P_B(0,t) = [P(0,t)+P(-\delta,t)]^N - P(-\delta,t)^N. \tag{7.30}$$

The only other possibility in time t is that the bundle will grow one unit, so

$$P_B(+\delta,t) = 1 - P_B(-\delta,t) - P_B(0,t) = 1 - [P(0,t)+P(-\delta,t)]^N. \tag{7.31}$$

Hence, we can calculate the initial rate of lengthening to be

$$\lim_{t\to 0}\frac{\delta P_B(+\delta,t) - \delta P_B(-\delta,t)}{t} = \begin{cases} (\alpha-\beta)\delta, & N=1 \\ N\alpha\delta, & N\geq 2 \end{cases}, \tag{7.32}$$

or, in terms of the diffusion formalism parameters from (6.15),

$$\lim_{t\to 0}\frac{\delta P_B(+\delta,t) - \delta P_B(-\delta,t)}{t} = \begin{cases} V_a, & N=1 \\ N\left(\frac{V_a}{2}+\frac{D_a}{\delta}\right), & N\geq 2 \end{cases}, \tag{7.33}$$

which is the discrete analogue of (7.19). We can see that in the single filament case, the initial lengthening rate is simply the drift rate, V_a, but for a bundle of filaments, the initial lengthening rate has both drift and diffusive components. For the bundle, the diffusive component diverges in the spatially continuous limit, as we would expect from (7.19).

7.2.2 Filamentous Bundle Growth Against a Rigid Wall

We now study the gap between the tip of a filamentous bundle and a rigid wall. Recall from Chapter 6 that for a single filament in the steady state, the gap is a positive exponentially distributed random variable $\mathbf{\Delta}$ with *pdf*

$$P_{\mathbf{\Delta}}(x) = \frac{V_a}{D_a} e^{-V_a/D_a x}. \tag{7.34}$$

Again, we consider N identical gaps. The smallest gap between a filament and the wall corresponds to the gap between the tip of the filamentous bundle and the wall:

$$\mathbf{\Delta}_{(1)} = \min\{\mathbf{\Delta}_1, \mathbf{\Delta}_2, ..., \mathbf{\Delta}_N\}. \tag{7.35}$$

It is easy to show, using the standard definition of order statistics, that the *pdf* for $\mathbf{\Delta}_{(1)}$ is

$$P_{\mathbf{\Delta}_{(1)}}(x) = \frac{NV_a}{D_a} e^{-NV_a/D_a x}. \tag{7.36}$$

In this case, the gap distribution is still exponential, but its expectation is N times smaller.

7.2.3 Growth of a Filamentous Bundle Against a Fluctuating Object with Resistant Force

We now extend our model to analyze the growth of the filamentous bundle in the presence of a diffusive barrier $\mathbf{Y}(t)$ with a resistant force $F = \overline{F}_{int} + F_{ext}$ and frictional coefficient η_b:

$$\frac{\partial P_{\mathbf{Y}}(y,t)}{\partial t} = D_b \frac{\partial^2 P_{\mathbf{Y}}(y,t)}{\partial y^2} + \left(\frac{F}{\eta_b}\right) \frac{\partial P_{\mathbf{Y}}(y,t)}{\partial y}. \tag{7.37}$$

The essential idea of a Brownian ratchet is that the motion of $\mathbf{X}^{(1)}(t)$ and $\mathbf{Y}(t)$ are interacting such that (7.24) and (7.37) are coupled with the geometric constraint that $\mathbf{X}^{(1)}(t) \leq \mathbf{Y}(t)$. Alternatively, we can write out a single equation for the joint *pdf* of all of the $\mathbf{X}_i(t)$ and $\mathbf{Y}(t)$, similar to (7.1), as the model for the filamentous bundle polymerization against a fluctuating barrier with resistant force,

$$\frac{\partial f(\{x_i\}, y, t)}{\partial t} = \sum_{k=1}^{N} \left(D_a \frac{\partial^2 f}{\partial x_k^2} - V_a \frac{\partial f}{\partial x_k} \right) + D_b \frac{\partial^2 f}{\partial^2 y} + \frac{F}{\eta_b} \frac{\partial f}{\partial y}, \tag{7.38}$$

which turns out to be more analytically tractable.

Next, we introduce a transformation of variables, as we did before in (6.17):

$$\xi_i = y - x_i, \;\; (i = 1, 2, ..., N); \qquad z = \frac{D_b \sum_{j=1}^{N} x_j + D_a y}{N D_b + D_a}, \tag{7.39}$$

where ξ_i represents the length of the gap between the i^{th} filament and the moving barrier, and z represents the center of friction of the filament-bundle-barrier system. After performing the transformation of variables, we obtain

$$\begin{aligned}\frac{\partial f(\{\xi_i\}, z, t)}{\partial t} &= \sum_{i,j}^{N} \left(D_a \delta_{ij} + D_b\right) \frac{\partial^2 f(\{\xi_i\}, z, t)}{\partial \xi_i \partial \xi_j} + \frac{D_b D_a}{N D_b + D_a} \frac{\partial^2 f(\{\xi_i\}, z, t)}{\partial z^2} \\ &+ \left(V_a + \frac{F}{\eta_b}\right) \sum_{i=1}^{N} \frac{\partial f(\{\xi_i\}, z, t)}{\partial \xi_i} - \left(\frac{N D_b V_a - D_a F/\eta_b}{N D_b + D_a}\right) \frac{\partial f(\{\xi_i\}, z, t)}{\partial z}. \end{aligned} \tag{7.40}$$

Note that the gap and center of friction dependence can be decoupled, so that $f(\{\xi_i\}, z, t) = \phi(\{\xi_i\}, t) P_{\mathbf{Z}}(z, t)$. The joint distribution for the N gaps between the N filaments and the barrier, $\phi(\{\xi_i\}, t)$, approaches a stationary distribution,

$$\phi(\{\xi_i\}) = \epsilon^N \exp\left(-\epsilon \sum_{i=1}^{N} \xi_i\right), \tag{7.41}$$

where

$$\epsilon = \frac{V_a + F/\eta_b}{N D_b + D_a}. \tag{7.42}$$

We can see from (7.41), that the gaps are identical, independent, exponentially distributed random variables with mean $1/\epsilon$. For the BR, we are interested in the steady-state distribution of $\mathbf{\Delta}_{(1)}$, the minimum gap between the bundle and the barrier. As in the stationary barrier case, the steady-state *pdf* for the minimum gap distance is also exponentially distributed,

$$P_{\mathbf{\Delta}_{(1)}}(x) = N \epsilon e^{-N \epsilon x}, \tag{7.43}$$

with mean $1/(N\epsilon)$. Note that when $D_b = 0$ and $\eta_b = \infty$, the barrier is a rigid wall, and the result in (7.43) agrees with (7.36).

While the N gaps reach stationarity, the filament bundle and the barrier, together, move steadily according to diffusion with a drift

$$\frac{\partial P_{\mathbf{Z}}(z, t)}{\partial t} = D_z \frac{\partial^2 P_{\mathbf{Z}}(z, t)}{\partial z^2} - V_z \frac{\partial P_{\mathbf{Z}}(z, t)}{\partial z}, \tag{7.44}$$

where the drift and diffusion coefficients are given by

$$D_z = \frac{D_b D_a}{N D_b + D_a}, \qquad V_z = \frac{N D_b V_a - D_a F/\eta_b}{N D_b + D_a}. \tag{7.45}$$

The critical stalling force at which $V_z = 0$ is $F^* = N k_B T V_a / D_a$ which is N times the critical stalling force of a single filament, as expected. We see that the interaction between the barrier and the individual filaments allows all N filaments in the bundle to move together, rather than separating by an increasing factor of $\sqrt{t}$ as seen in the previous section. Furthermore, by comparing (7.45) with (6.19), we can see that *the effect of N filaments is to reduce the effective diffusion coefficient of the bundle, $D_{a_{eff}} = D_a/N$, by a factor of N*, or to reduce the stochasticity of the (smallest) gap between the bundle and the barrier.

Now we can investigate the behavior of the system under various limiting scenarios, using (7.43) and (7.45). We have already verified that the limiting behavior for a rigid barrier agrees with the previous model. If the motion of the BR is limited by the slow fluctuation of the barrier, $D_b \ll D_a$, then a steady state with a decreased gap is reached, where the bundle is shrinking. However, if the filaments fluctuate slowly, $D_a \ll D_b$, then the BR behaves according to the growth of a single filament. On the other hand, if the barrier fluctuates rapidly, or $D_b \to \infty$, then the gap will not reach a steady state and the behavior of the center of friction will be dominated by the dynamics of the mean filament length, $D_z \to D_a/N$, $V_z \to V_a$, as noted at the beginning of Section 7.2.1. Likewise, if the filaments fluctuate rapidly, or $D_a \to \infty$, then the gap will not reach a steady state and the behavior of the center of friction will be dominated by the barrier, $D_z \to D_b$, $V_z \to -F/\eta_b$. Since we know that the diffusion and drift coefficients for the filaments are defined in terms of the polymerization and depolymerization rates, we can specifically investigate the scenario in which the BR is most relevant: rapid polymerization of the filaments.

7.2.4 Rapid Polymerization, or $\alpha \gg \beta$

As in the analysis for a single filament, the rate of growth of a filament in a bundle, α, is proportional to the monomer concentration c_0 and the probability of $\mathbf{\Delta} \geq \delta$ for the bundle:

$$\alpha = \alpha_0 c_0 e^{-\epsilon\delta}, \tag{7.46}$$

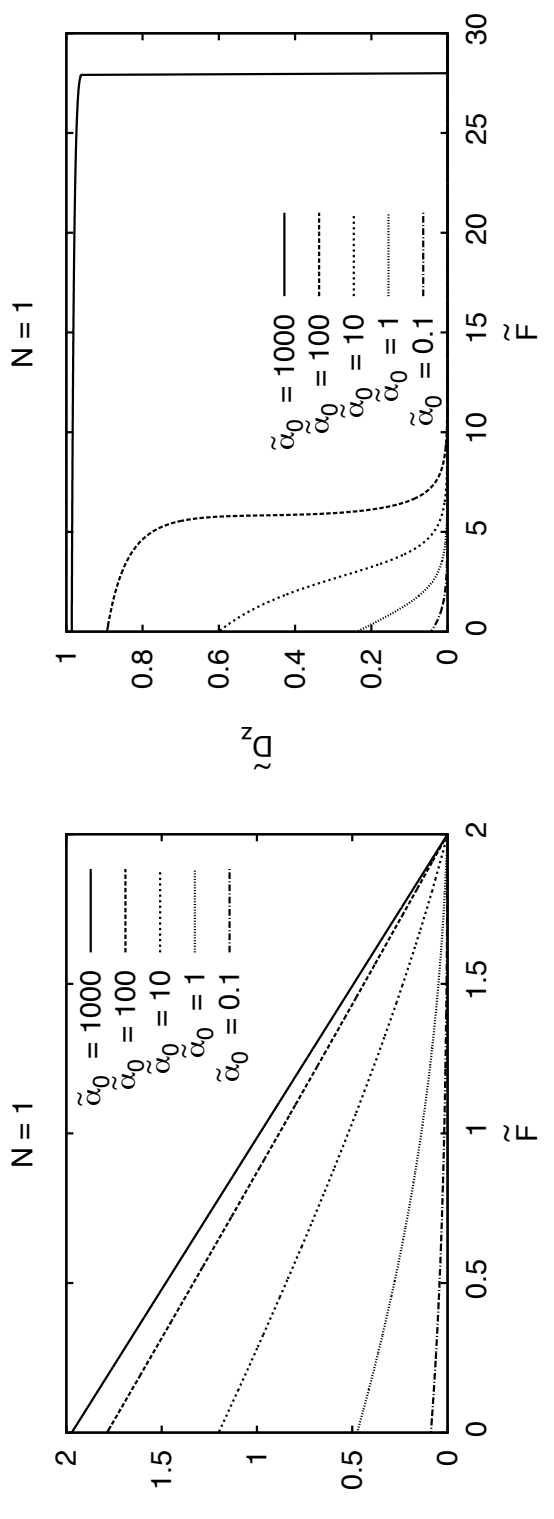

Figure 7.3: **Force-Velocity and Force-Fluctuation Relations for a Single Filament.** Nondimensionalized $\tilde{V}_z = V_z\delta/D_b$ and $\tilde{D}_z = D_z/D_b$ as functions of nondimensionalized resistant force $\widetilde{F} = F\delta/(D_b\eta_b)$, from (7.49). Curves are plotted for several different values of $\widetilde{\alpha}_0 = \alpha_0 c_0 \delta/D_b$, all with $N = 1$. Note that as $\alpha_0 c_0 \to \infty$, $\tilde{V}_z \to 2 - \widetilde{F}$ and $\tilde{D}_z \to 1$ as described below.

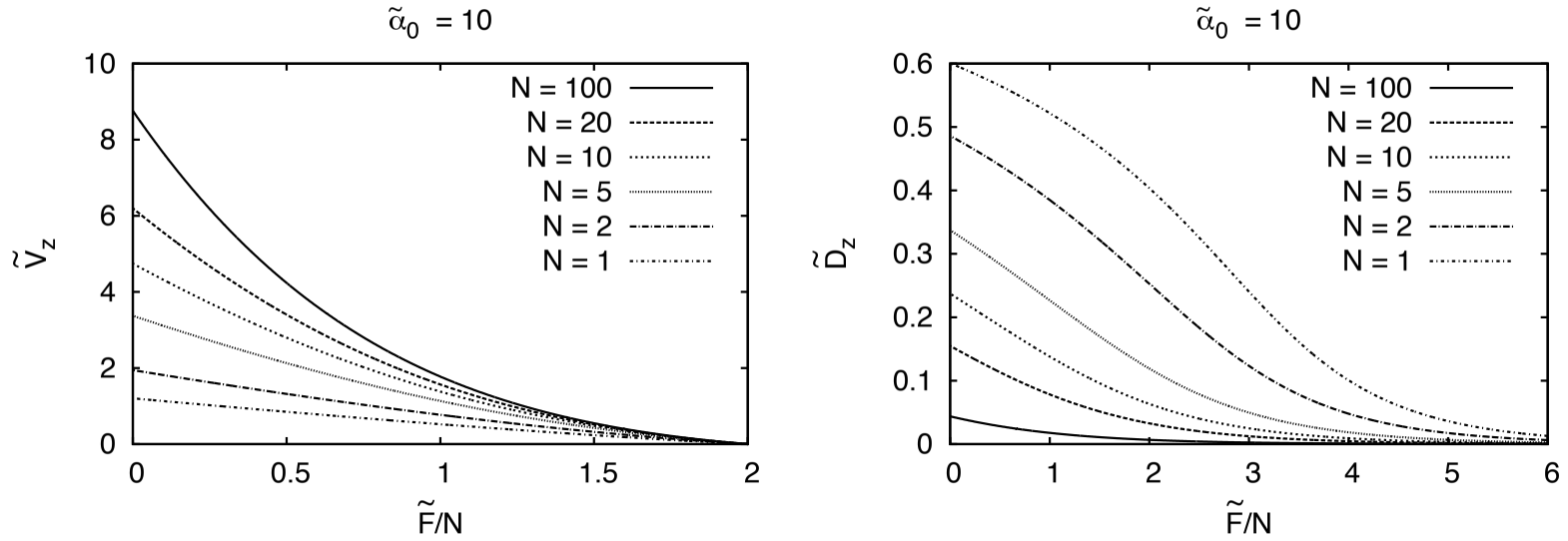

Figure 7.4: **Force-Velocity and Force-Fluctuation Relations for Filamentous Bundles.** Nondimensionalized $\widetilde{V}_z = V_z\delta/D_b$ and $\widetilde{D}_z = D_z/D_b$ as functions of nondimensionalized resistant force $\widetilde{F} = F\delta/(D_b\eta_b)$ from (7.49). Curves are plotted for filamentous bundles with different N, all with $\widetilde{\alpha}_0 = \alpha_0 c_0 \delta^2/D_b = 10$. Note that the abscissa is also scaled by $1/N$: $\widetilde{F}/N$.

in which

$$\epsilon(\alpha) = \frac{(\alpha - \beta)\delta + F/\eta_b}{ND_b + (\alpha + \beta)\delta^2/2}. \tag{7.47}$$

We can see that (7.46) gives a self-consistent definition of the polymerization rate $\alpha(F)$, as function of resistant force, for the filaments in a bundle.

We now consider the case of rapid polymerization, where $\frac{\beta}{\alpha} \approx 0$. Under this condition, (7.45) and (7.46) can be written as

$$\widetilde{V}_z = \widetilde{\alpha}\frac{N - \widetilde{F}/2}{N + \widetilde{\alpha}/2}, \qquad \widetilde{D}_z = \frac{\widetilde{\alpha}/2}{N + \widetilde{\alpha}/2}, \qquad \widetilde{\alpha} = \widetilde{\alpha}_0 e^{-\left(\frac{\widetilde{\alpha}+\widetilde{F}}{N+\widetilde{\alpha}/2}\right)}, \tag{7.48}$$

with the following nondimensionalized quantities defined as: $\widetilde{V}_z = V_z\delta/D_b$, $\widetilde{D}_z = D_z/D_b$, $\widetilde{\alpha} = \alpha\delta^2/D_b$, $\widetilde{\alpha}_0 = \alpha_0 c_0 \delta^2/D_b$, and $\widetilde{F} = F\delta/(\eta_b D_b)$. By eliminating $\widetilde{\alpha}$, we obtain implicit force-velocity and force-fluctuation relations:

$$\widetilde{F} = \frac{2N\widetilde{V}_z}{\widetilde{V}_z + \widetilde{F} - 2N} - \frac{2N^2 - N\widetilde{F}}{2N - \widetilde{V}_z - \widetilde{F}} \ln\left(\frac{2N\widetilde{V}_z/\widetilde{\alpha}_0}{2N - \widetilde{V}_z - \widetilde{F}}\right), \tag{7.49a}$$

$$\widetilde{F} = \frac{2N\widetilde{D}_z}{\widetilde{D}_z - 1} - \frac{N}{1 - \widetilde{D}_z} \ln\left(\frac{2N\widetilde{D}_z/\widetilde{\alpha}_0}{1 - \widetilde{D}_z}\right). \tag{7.49b}$$

Figures 7.3 and 7.4 show $\widetilde{V}_z$ and $\widetilde{D}_z$ as functions of the resistant force $\widetilde{F}$, the intrinsic polymerization rate $\widetilde{\alpha}_0$, and the number of filaments N.

For the single filament case, shown in Figure 7.3, we see that in the limit of extremely fast intrinsic polymerization rates compared to barrier fluctuations, or $\widetilde{\alpha}_0 \to \infty$, that $\frac{\widetilde{\alpha}}{\widetilde{\alpha}_0} \to \exp(-2)$, and the nondimensionalized center of friction drift and diffusion both increase, and in fact approach $\widetilde{V}_z = 2 - \widetilde{F}$ and $\widetilde{D}_z = 1$, which is in agreement with Ref. [62]. When $\widetilde{\alpha}_0$ is held constant, shown in Figure 7.4, we observe that increasing the number of filaments effectively increases the drift of the center of friction, but decreases the fluctuation, or diffusion coefficient. Note that in the "no load" scenario, i.e. $\widetilde{F} = 0$, $\widetilde{V}_z \to \widetilde{\alpha}_0$ as $N \to \infty$. In other words, when there is no load on the bundle, the effect of adding more filaments is to increase the center of friction drift toward an upper limit which is the drift of a single filament. Note that we can also observe that the nondimensionalized critical stalling force is equal to $2N$, as we expect from (7.48).

7.2.5 The Binding of the Barrier to the Bundle

The chemical interaction, i.e. binding, between the barrier and the bundle can be represented by the potential of the mean force, $U_{int}(\Delta)$. For strong affinity, $U_{int}(\Delta)$ has a dominant energy well which characterizes the bound state of the complex. The life-time of the complex, which is also the reciprocal of the dissociation rate constant, is directly related to the depth of the energy well. The association equilibrium constant can be computed from (7.9).

If we assume that the energy landscape for the binding of the bundle to the barrier has a dominant well with bound energy E^*, bond length ℓ^*, and that the dissociated state has zero energy,[3] then we can approximate the potential energy function by the harmonic potential

$$U_{int}(\Delta) = \begin{cases} -E^* + \kappa(\Delta - \ell^*)^2/2, & 0 < \Delta \leq \ell^* + \sqrt{\frac{2E^*}{\kappa}} \\ 0, & \Delta > \ell^* + \sqrt{\frac{2E^*}{\kappa}} \end{cases}. \tag{7.50}$$

By plugging (7.50) into (7.9), the association (binding) equilibrium constant is given by

$$K_b = e^{E^*/k_BT}\sqrt{\frac{\pi k_BT}{2\kappa}}\left(\operatorname{erf}\left(\sqrt{\frac{E^*}{k_BT}}\right) + \operatorname{erf}\left(\sqrt{\frac{\kappa\ell^{*2}}{2k_BT}}\right)\right) - \ell^* - \sqrt{\frac{2E^*}{\kappa}}, \tag{7.51}$$

and the dissociation rate constant is proportional to e^{-E^*/k_BT}. We can also see how the internal attraction force might affect the *pdf* for the minimum gap distance between the bundle and the barrier, given in (7.43). We can work backwards, assuming that the bundle structure is large, $1/\eta_a \approx 0$, so that the internal attraction force acts only on the barrier, as discussed in Section 7.1. Then we can modify (7.43) by assuming that $F = F_{ext} + \overline{F}_{int}$, where $\overline{F}_{int} = \int_0^\infty F_{int}(s)P_{\boldsymbol{\Delta}_{(1)}}(s)ds$, as before, so that

$$P_{\boldsymbol{\Delta}_{(1)}}(\Delta) = \mathcal{N}\exp\left(-N\left(\frac{(V_a + F_{ext}/\eta_b)\,\Delta - U_{int}(\Delta)/\eta_b}{ND_b + D_a}\right)\right), \tag{7.52}$$

where $\mathcal{N}$ is the normalization constant. For the potential function given in (7.50), the normalization constant is given by

$$\mathcal{N} = N\epsilon\exp\left(\gamma E^* - \frac{\gamma\kappa\ell^{*2}}{2}\right), \tag{7.53}$$

where ϵ is the reciprocal of the mean gap size, as in (7.42), and

$$\gamma = \frac{1}{\eta_b\left(D_b + \frac{D_a}{N}\right)}. \tag{7.54}$$

---

[3]Note that $\lim_{x\to\infty} U_{int}(x) = 0$ is required in order for the integral in (7.9) to converge.

7.3 Discussion

Molecular motor proteins and filament polymerizations are two main machineries by which biological cells convert chemical energy into mechanical work. The chemical energy, as always, is in the form of a chemical potential, such as a sustained concentration in the cellular ATP for motor proteins, or G-actin (tubulin) monomers for microfilament (microtubule) polymerization. While great attention has been paid to the former in connection with muscle contraction and organelle transport, it is only relatively recently that people have started to pay attention to the chemomechanical energy transduction in the latter [81].

While the molecular mechanisms for the two force generating systems are quite different, the physical principle behind them is in fact remarkably similar. This was first recognized in a series of pioneering but often neglected papers by Hill (starting in 1980 and culminating in a monograph in 1987) who has also made a fundamental contribution to the theory of muscle contraction [28, 29, 27, 31]. In the 1990's, Peskin and Oster also proposed the Brownian ratchet model for both polymerization and motor proteins [56]. The contribution of the latter work is to introduce a mathematically more cogent kinetics into the theory for single motor proteins and polymerizations against a force, recognizing the importance of the dynamic characteristic of the load. The role of the dynamics of the barrier is absent in Hill's theory, which corresponds to the case of $D_b = \infty$. We have shown that the BR model is in general agreement with the phenomenological kinetic analysis of Hill [62]. Combining the earlier thermodynamic and the later kinetic approaches, we now in fact have *a non-equilibrium stochastic theory of chemomechanical energy transduction by single macromolecules in an aqueous solution.* It has been shown that this theory is also consistent with the general principle of non-equilibrium statistical mechanics and thermodynamics [61].

In connection with polymerization against force, we would like to distinguish the polymerization mechanism from that of the treadmilling mechanism. In the former, the free energy source is the concentration of the monomer pool while in the latter, the concentration of monomer pool is unchanged while the filament of a constant length moves against force [31]. The BR converts chemical free energy, in the form of the monomer pool, into mechanical work [31], while treadmilling converts chemical free energy, in the form of nucleotide hydrolysis, into mechanical

work.

Experimental measurements on the movement of *Listeria monocytogenes* propelled by actin polymerization have revealed a discrete step with step size equal to the size of a G-actin. It is interesting to point out that after almost ten years, there is still no consensus, among the experimentalists, on the validity and significance of this observation. Theoretically, however, according to the BR model, we show this is expected *if* the bacterium moves sufficiently slowly. In this situation all of the filaments in the bundle have sufficient time to grow to an equal length before an additional step is taken, which occurs when the gap is finally large enough for a monomer to be added. A slow diffusion coefficient for the bacterium is indeed observed. Kuo and McGrath have suggested that the reduced Brownian motion is due to an association between the bacterium particle and the actin filaments, via the regulation of other important proteins such as ActA and Arp2/3 [39]. As long as the association is sufficiently dynamic, the actin filament can grow. The waiting time for incorporating the next monomer, thus, is related to the life-time of the association.

There are also experimental measurements on force-velocity curves for actin-based motility. McGrath *et. al.* find a bi-phasic curve for measurements of *Listeria* in tissue extracts, resembling that of muscle but with a significantly greater curvature [43]. Direct measurements on an actin-coated bead by Marcy *et. al.* yield a relation that decays weakly with increasing resistant forces that is qualitatively similar to our mathematical results, as can be seen in Figure 4c of Ref. [42]. More recently, Prass *et. al.* reported a force-velocity relationship for protruding lamellipodia which is qualitatively different than other curves, including a region where the velocity is insensitive to the load, as well as a concave decrease under larger loads [57]. A closer comparison between our theory and these data can provide further insights into these systems.

In this chapter, we have introduced two additional features into the original BR model. First, we augmented the BR model with an attractive interaction between the polymer and the barrier. We mathematically demonstrated that the net effect of such an interaction is an increased apparent resistant force for the barrier. A resistant force was included in the original formalism of the BR, and it is known that such a force will reduce the Brownian motion of the barrier [62]. With a resistant force acting on the barrier from one side, and the growing tip of the filament on the other side, the probability distribution for the gap between the filament and

the barrier is exponential, which accentuates the stepping behavior of the BR. Our quantitative model provides relationships between the reduction in the diffusion coefficient D_z and the resistant force, seen for example in the second panel of Figure 7.3, as well as for the mean size for the gap ϵ^{-1} and the resistant force. These relationships could be tested experimentally by applying an external force to the bacterium. The model also suggests other statistical methods for analyzing experimental data in addition to the mean-square-displacement analysis. For example, both the gap size distribution and the waiting time distribution can be estimated from "noisy" experimental data.

The second feature we introduced was to consider multiple filaments in a bundle. In this case, we have shown that the velocity of the propelled barrier increases, approaching the value of the lengthening rate for a single filament without barrier, as seen in the first panel of Figure 7.4. However, the bundle generates more force in the stalling scenario. The fluctuation in the motion of a barrier propelled by a bundle also decreases with the number of filaments, as seen in the second panel of Figure 7.4. Another interesting feature of the bundle growth is that the lengthening process is not uniform if there is no interaction with a barrier at all. In the long-time limit, the longest filament is moving ahead of the rest of the filaments which almost never catch up. Future work could include incorporating interactions between the filaments in the bundle, which are known to exist in filapodia or stress fibers.

Inside a cell, there are two different modes in which polymerization occurs against a resistant force. One scenario is an isometric situation in which the static shape of a cell is maintained by a balance between the external force on the cell wall and the polymerization of the cytoskeleton, while the tip of the filaments is at rest. On the other hand, in the extension of lamellipodia, the filaments undergo a stationary growth. Our results on filamentous bundle growth indicate that the former force is proportional the number of filaments, N, but the latter is relatively insensitive to the number of filaments.

In summary, our results show that, in general terms, (a) Both V_z and D_z decrease with an increasing resistant force $F = \overline{F}_{int} + F_{ext}$. (b) Both increase with $\alpha_0 c_0$. (c) The critical stalling force $F^* = 2N\eta_b D_b/\delta$ is scaled with N. (d) The free-load velocity V_z when $F = 0$ is scaled with $\alpha_0 c_0$ and N: $\widetilde{V}_z = \widetilde{\alpha}_0 e^{-\widetilde{V}_z/N}$. (e) After being normalized by the critical stalling force F/F^*, $V_z(F/F^*)$ increases with N while $D_z(F/F^*)$ decreases with it.

BIBLIOGRAPHY

[1] J. B. Alberts and G. M. Odell. In silico reconstitution of *Listeria* propulsion exhibits nano-saltation. *PLoS Biology*, 2(12):2054–2066, December 2010.

[2] V. Balzani, M. Clemente-León, A. Credi, B. Ferrer, M. Venturi, A. H. Flood, and J. F. Stoddart. Autonomous artificial nanomotor powered by sunlight. *PNAS*, 103(5):1178–1183, January 2006.

[3] M. D. Betterton and F. Jülicher. A motor that makes its own track: Helicase unwinding of DNA. *Phys. Rev. Lett.*, 91(25):258103, Dec 2003.

[4] N. F. Britton. A mathematical model for carbon monoxide poisoning in man. *Nonlinear Analysis*, 3(3):361 – 377, 1979.

[5] N. F. Britton and J. D. Murray. The effect of carbon monoxide on haem-facilitated oxygen diffusion. *Biophys. Chem.*, 7:159–167, Sep 1977.

[6] G. Casella and R. L. Berger. *Statistical Inference*. Duxbury Advanced Series, 2nd edition, 2002.

[7] C. L. Cole and H. Qian. Simple chemical model for facilitated transport with an application to Wyman-Murray facilitated diffusion. *Acta Phys. -Chim. Sin.*, 26(11):2857–2864, 2010.

[8] C. L. Cole and H. Qian. The Brownian ratchet revisited: Diffusion formalism, polymer-barrier attractions, and multiple filamentous bundle growth. *Biophysical Reviews and Letters*, 6(1-2):59–79, 2011.

[9] J. D. Cortese, B. Schwab, C. Frieden, and E. L. Elson. Actin polymerization induces a shape change in actin-containing vesicles. *Proc. Natl. Acad. Sci. USA*, 86:5773–5777, 1989.

[10] R. B. Dickinson, L. Caro, and D. L. Purich. Force generation by cytoskeletal filament end-tracking proteins. *Biophys. J.*, 87:2838–2854, October 2004.

[11] R. B. Dickinson and D. L. Purich. Diffusion rate limitations in actin-based propulsion of hard and deformable particles. *Biophys. J.*, 91:1548–1563, August 2006.

[12] R. B. Dickinson, F. S. Southwick, and D. L. Purich. A direct-transfer polymerization model explains how the multiple profilin-binding sites in the actoclampin motor promote rapid actin-based motility. *Archives of Biochemistry and Biophysics*, 406:296–301, 2002.

[13] W. Ebel. Carrier facilitated diffusion. *Journal of Mathematical Biology*, 21:243–271, 1985.

[14] S. F. Ellermeyer and D. G. Robinson. Integrals of periodic functions. *Mathematics Magazine*, 74(5):393–396, December 2001.

[15] T. Elston and C. S. Peskin. The role of protein flexibility in molecular motor function: coupled diffusion in a tilted periodic potential. *SIAM J. Appl. Math.*, 60:842–867, 2000.

[16] E. Evans and K. Ritchie. Dynamic strength of molecular adhesion bonds. *Biophys. J.*, 72:1544–1555, 1997.

[17] S. Felder and E. L. Elson. Mechanics of fibroblast locomotion: quantitative analysis of forces and motions at the leading lamellas of fibroblasts. *J. Cell. Biol.*, 111:2513–2526, 1990.

[18] A. Fersht. *Enzyme Structure and Mechanism*. W. H. Freeman and Company, New York, 2nd edition, 1985.

[19] R. P. Feynman, R. B. Leighton, and M. Sands. *The Feynman Lectures on Physics*, chapter 46. Addison-Wesley, Reading, MA, 1966.

[20] M. E. Fisher and A. B. Kolomeisky. Molecular motors and the forces they exert. *Physica A*, 274:241–266, 1999.

[21] J. E. Fletcher. On facilitated oxygen diffusion in muscle tissues. *Biophys. J.*, 29:437–458, Mar 1980.

[22] A. S. Fokas. A new transform method for evolution partial differential equations. *IMA Journal of Applied Mathematics*, 67:559–590, 2002.

[23] D. T. Gillespie. Stochastic simulation of chemical kinetics. *Annu Rev Phys Chem*, 58:35–55, 2007.

[24] R. Goodman. *Introduction to Stochastic Models*. Benjamin/Cummings Publishing Company, Inc., 1988.

[25] E. J. Gumbel. *Statistics of Extremes*. Columbia University Press, 1958.

[26] E. A. Hemmingsen. Enhancement of oxygen transport by myoglobin. *Comp. Biochem. Physiol.*, 10:239–244, Nov 1963.

[27] T. L. Hill. Bioengetic aspects and polymer length distribution in steady-state head-to-tail polymerization of actin or microtubules. *Proc. Natl. Acad. Sci. USA.*, 77(4803-4808), 1980.

[28] T. L. Hill. Microfilament or microtubule assembly or disassembly against a force. *Proc. Natl. Acad. Sci. USA.*, 78:5613–5617, 1981.

[29] T. L. Hill. *Linear Aggregation Theory in Cell Biology*. Springer-Verlag, New York, 1987.

[30] T. L. Hill. *Free Energy Transduction and Biochemical Cycle Kinetics*. Dover Publications, New York, 2004.

[31] T. L. Hill and M. W. Kirschner. Subunit treadmilling of microtubules or actin in the presence of cellular barriers: possible conversion of chemical free energy into mechanical work. *Proc. Natl. Acad. Sci. USA.*, 79:490–494, 1982.

[32] J. Howard. The movement of kinesin along microtubules. *Ann. Rev. Physiol.*, 58:703–729, 1996.

[33] F. Jülicher, A. Ajdari, and J. Prost. Modeling molecular motors. *Reviews of Modern Physics*, 69(4):1269–1281, October 1997.

[34] E. L. King and C. Altman. A schematic method of deriving the rate laws for enzyme-catalyzed ractions. *J. Phys. Chem.*, 60:1375–1378, October 1956.

[35] A. B. Kolomeisky and M. E. Fisher. Periodic sequential kinetic models with jumping, branching and deaths. *Physica A*, 279:1–20, 2000.

[36] A. B. Kolomeisky and M. E. Fisher. Molecular motors: A theorists's perspective. *Annu. Rev. Phys. Chem.*, 58:675–695, 2007.

[37] F. Kreuzer and L. J. Hoofd. Facilitated diffusion of oxygen in the presence of hemoglobin. *Respir Physiol*, 8:280–302, Mar 1970.

[38] F. Kreuzer and L. J. C. Hoofd. Facilitated diffusion of CO and Oxygen in the presence of hemoglobin or myoglobin. *Adv. Exper. Med. Biol*, 75:207–215, 1976.

[39] S. C. Kuo and J. L. McGrath. Steps and fluctuations of *Listeria monocytogenes* during actin-based motility. *Nature*, 407:1026–1029, 2000.

[40] R. C. La Force. Steady-state diffusion in the carbon monoxide + oxygen + haemoglobin system. *Trans. Faraday Soc.*, 62:1458–1468, 1966.

[41] M. R. Leadbetter, G. Lindgren, and H. Rootzén. *Extremes and Related Properties of Random Sequences and Processes*. Springer-Verlag, New York, 1980.

[42] Y. Marcy, J. Prost, M.-F. Carlier, and C. Sykes. Forces generated during actin-based propulsion: A direct measurement by micromanipulation. *Proc. Natl. Acad. Sci. USA*, 101(16):5992–5997, April 2004.

[43] J. L. McGrath, N. J. Eungdamrong, C. I. Fisher, F. Peng, L. Mahadevan, T. J. Mitchison, and S. C. Kuo. The force-velocity relationship for the actin-based motility of *Listeria monocytogenes*. *Current Biology*, 13:329–332, February 2003.

[44] R. A. Meyer, H. L. Sweeney, and M. J. Kushmerick. A simple analysis of the "phosphocreatine shuttle". *Am. J. Physiol.*, 246:C365–377, May 1984.

[45] P. J. Mitchell and J. D. Murray. Facilitated diffusion: the problem of boundary conditions. *Biophysik*, 9:177–190, May 1973.

[46] M. Mochizuki and R. E. Forster. Diffusion of Carbon Monoxide through Thin Layers of Hemoglobin Solution. *Science*, 138:897–898, Nov 1962.

[47] A. Mogilner and G. Oster. Cell motility driven by actin polymerization. *Biophys. J.*, 71:3030–3045, December 1996.

[48] A. Mogilner and G. Oster. Force generation by actin polymerization II: The elastic ratchet and tethered filaments. *Biophys. J.*, 84:1591–1605, March 2003.

[49] J. D. Murray. On the molecular mechanism of facilitated oxygen diffusion by haemoglobin and myoglobin. *Proc. R. Soc. Lond., B, Biol. Sci.*, 178:95–110, Jun 1971.

[50] J. D. Murray. On the role of myoglobin in muscle respiration. *J. Theoret. Biol.*, 47:115–126, 1974.

[51] J. D. Murray. *Mathematical Biology I: An Introduction*. Springer, New York, 3rd edition, 2007.

[52] J. D. Murray and J. Wyman. Facilitated diffusion. The case of carbon monoxide. *J. Biol. Chem.*, 246:5903–5906, Oct 1971.

[53] J. Nedelman and S. I. Rubinow. Facilitated diffusion of oyxgen and carbon monoxide in the large affinity regime. *J Math Biol*, 12(1):73–90, 1981.

[54] F. Oosawa and S. Asakura. *Thermodynamics of the Polymerization of Protein*. Academic Press, New York, 1975.

[55] A. Papoulis. *Probability, Random Variables, and Stochastic Processes*. McGraw-Hill, New York, 3rd edition edition, 1991.

[56] C. S. Peskin, G. M. Odell, and G. F. Oster. Cellular motions and thermal fluctuations: the Brownian ratchet. *Biophys. J.*, 65:316–324, 1993.

[57] M. Prass, K. Jacobson, A. Mogilner, and M. Radmacher. Direct measurement of the lamellipodial protrusive force in a migrating cell. *J. Cell. Biol.*, 174(6):767–772, September 2006.

[58] F. Qi, R. K. Dash, Y. Han, and D. A. Beard. Generating rate equations for complex enzyme systems by a computer-assisted systematic method. *BMC Bioinformatics*, 10:238, 2009.

[59] H. Qian. A simple theory of motor protein kinetics and energetics. *Biophysical Chemistry*, 67:263–267, 1997.

[60] H. Qian. The mathematical theory of molecular motor movement and chemomechanical energy transduction. *J. Math. Chem.*, 27:219–234, 2000.

[61] H. Qian. Mathematical formalism for isothermal linear irreversibility. *Proc. R. Soc. A.*, 457:1645–1655, 2001.

[62] H. Qian. A stochastic analysis of a Brownian ratchet model for actin-based motility and integrate-and-firing neurons. *MCB: Mol. & Cell. Biomech.*, 1:267–278, 2004.

[63] H. Qian. Cycle kinetics, steady-state thermodynamics and motors — a paradigm for living matter physics. *J. Phys: Cond. Matt.*, 17:S3783–S3794, 2005.

[64] H. Qian. An asymptotic comparative analysis of the thermodynamics of non-covalent association. *J. Math. Biol.*, 52:277–289, 2006.

[65] H. Qian. Phosphorylation energy hypothesis: open chemical systems and their biological functions. *Annu Rev Phys Chem*, 58:113–142, 2007.

[66] H. Qian. Viscoelasticity of living materials: Mechanics and chemistry of muscle as an active macromolecular system. *MCB: Mol. & Cell. Biomech.*, 5:107–117, 2008.

[67] H. Qian and B. E. Shapiro. A graphical method for force analysis: macromolecular mechanics with atomic force microscopy. *Prot. Struct. Funct. Genet.*, 37:576–581, 1999.

[68] V. Riveros-Moreno and J. B. Wittenberg. The self-diffusion coefficients of myoglobin and hemoglobin in concentrated solutions. *J. Biol. Chem.*, 247:895–901, Feb 1972.

[69] S. M. Ross. *Simulation.* Statistical Modeling and Decision Science. Academic Press, 2nd edition, 1997.

[70] F. J. W. Roughton. Diffusion and chemical reaction velocity as joint factors in determining the rate of uptake of oxygen and carbon monoxide by the red blood corpuscle. *Proc. R. Soc. Lond. Series B*, 111(769):1–36, 1932.

[71] S. I. Rubinow. *Introduction to Mathematical Biology.* John Wiley & Sons, 1975.

[72] S. I. Rubinow and M. Dembo. The facilitated diffusion of oxygen by hemoglobin and myoglobin. *Biophys. J.*, 18:29–42, Apr 1977.

[73] P. F. Scholander. Tension gradients accompanying accelerated oxygen transport in a membrane. *Science*, 149:876–877, Aug 1965.

[74] C. H. Schreiber, M. Stewart, and T. Duke. Simulation of cell motility that reproduces the force-velocity relationship. *Proc. Natl. Acad. Sci. USA*, 107(20):9141–9146, May 2010.

[75] B. E. Shapiro and H. Qian. A quantitative analysis of single protein-ligand complex separation with the atomic force microscope. *Biophys. Chem.*, 67:211–219, 1997.

[76] S. Silvi, M. Venturi, and A. Credi. Artificial molecular shuttles: from concepts to devices. *J. Mater. Chem*, 19:2279–2294, 2009.

[77] J. Son, G. Orkoulas, and A. B. Kolomeisky. Monte Carlo simulations of rigid biopolymer growth processes. *J Chem Phys*, 123:124902, 2005.

[78] E. B. Stukalin and A. B. Kolomeisky. Simple growth models of rigid multifilament biopolymers. *J Chem Phys*, 121(2):1097–1104, July 2004.

[79] E. B. Stukalin and A. B. Kolomeisky. Polymerization dynamics of double-stranded biopolymers: Chemical kinetic approach. *J Chem Phys*, 122:104903, 2005.

[80] E. B. Stukalin and A. B. Kolomeisky. ATP hydrolysis stimulates large length fluctuations in single actin filaments. *Biophys. J.*, 90:2673–2685, 2006.

[81] J. A. Theriot. The polymerization motor. *Traffic.*, 1:19–28, 2000.

[82] R. D. Vale and R. A. Milligan. The way things move: Looking under the hood of molecular motor proteins. *Science*, 288:88–95, April 2000.

[83] A. van Oudenaarden and J. A. Theriot. Cooperative symmetry-breaking by actin polymerization in a model for cell motility. *Nature Cell. Biol.*, 1:493–499, 1999.

[84] D. Vavylonis, Q. Yang, and B. O'Shaughnessy. Actin polymerization kinetics, cap structure, and fluctuation. *Proc. Natl. Acad. Sci. U.S.A.*, 102:8543–8548, 2005.

[85] M. von Delius, E. M. Geertsema, and D. A. Leigh. A synthetic small molecule that can walk down a track. *Nature Chemistry*, 2:96–101, 2010.

[86] J. B. Wittenberg. The molecular mechanism of hemoglobin-facilitated oxygen diffusion. *J. Biol. Chem.*, 241:104–114, Jan 1966.

[87] J. B. Wittenberg. Myoglobin-facilitated oxygen diffusion: role of myoglobin in oxygen entry into muscle. *Physiol. Rev.*, 50:559–636, Oct 1970.

[88] J. Wyman. Facilitated diffusion and the possible role of myoglobin as a transport mechanism. *J. Biol. Chem.*, 241:115–121, Jan 1966.

[89] D. B. Zilversmit. Oxygen-hemoglobin system: A model for facilitated membranous transport. *Science*, 149:874–876, Aug 1965.

[90] C. Zong, T. Lu, T. Shen, and P. G. Wolynes. Nonequilibrium self-assembly of linear fibers: Microscopic treatment of growth, decay, catastrophe and rescue. *Phys. Biol.*, 3:83–92, 2006.

APPENDICES

Appendix A

SUMMARY OF THE KING-ALTMAN-HILL METHOD

In this Appendix, we provide a brief summary of the King-Altman-Hill (KAH) method, which is described in Refs. [58, 34, 71], for example; our discussion will follow the latter reference. After introducing the method, we will show how it can be applied to the single ligand facilitated diffusion model of Chapter 3, and then state the results for the two ligand facilitated diffusion model of Chapter 4.

A.1 Introduction to the KAH Method

In general, the KAH method can be used for any enzyme kinetics problem where there are n states for the enzyme molecule, corresponding to different states of combination with ligands, substrates, inhibitors, effectors, and so on. If the reaction is in the quasi-steady-state, then the substrate is being converted to the product so slowly that we can treat the substrate concentrations as constants in the ODEs for the n enzyme states. The rate-equation ODEs for the n enzyme states can be expressed using the notation

$$\frac{dc}{dt} = Ac, \quad c = \begin{bmatrix} c_1 \\ c_2 \\ \vdots \\ c_n \end{bmatrix}, \quad A = \begin{bmatrix} A_{11} & A_{12} & \dots & A_{1n} \\ A_{21} & A_{22} & \dots & A_{2n} \\ \vdots & \vdots & \ddots & \vdots \\ A_{n1} & A_{2n} & \dots & A_{nn} \end{bmatrix}, \tag{A.1}$$

where c_i represents the concentration of complex i, and the A_{ij} are the coefficients from the law of mass action. If we make the quasi-steady-state assumption, all of the A_{ij} are constants since the ligand concentrations are assumed to be constant. Solving for the equilibrium values of the complexes corresponds to solving the equation

$$Ac = 0. \tag{A.2}$$

The diagonal entries of the matrix, A_{ii}, have the following special property:

$$A_{ii} = -\sum_{j=1}^{n}{}' A_{ji}, \tag{A.3}$$

where the prime denotes that the $j = i$ element is not included in the summation. As a consequence of this special property, we know that the c_i are not linearly independent and one of the equations can be eliminated using

$$e_0 = \sum_{i=1}^{n} c_i. \tag{A.4}$$

Note that this is equivalent to the statement that the total enzyme concentration is conserved. We will use some elements of graph theory to help us solve (A.2). In order to do so, we will construct a graph with n nodes corresponding to the n states of the enzyme. Then we will make use of the terminology from graph theory that is listed below:

- **branch:** a connection from one node to another, which has a direction and a value, given by A_{ij}
- **path:** a way to travel continuously along the branches of the graph from one node to the next without passing through any node more than once
- **path value, tree value:** product of the branch values of the path or tree
- **loop:** path that begins and ends at the same node
- **basic node, basic tree:** a particular node is selected, the basic node, and a basic tree associated with that particular node is a set of branches that touch all of the nodes in the graph without forming a loop, such that all of the branches are directed towards the basic node
- **basic determinant, D_i:** sum of all of the basic tree values for the basic node i

Given the set of definitions above, the quasi-steady-state solution to (A.2) and (A.4) can be expressed as

$$c_i = \frac{e_0 D_i}{\sum_{j=1}^{n} D_j}, \qquad i = 1, 2, \ldots, n. \tag{A.5}$$

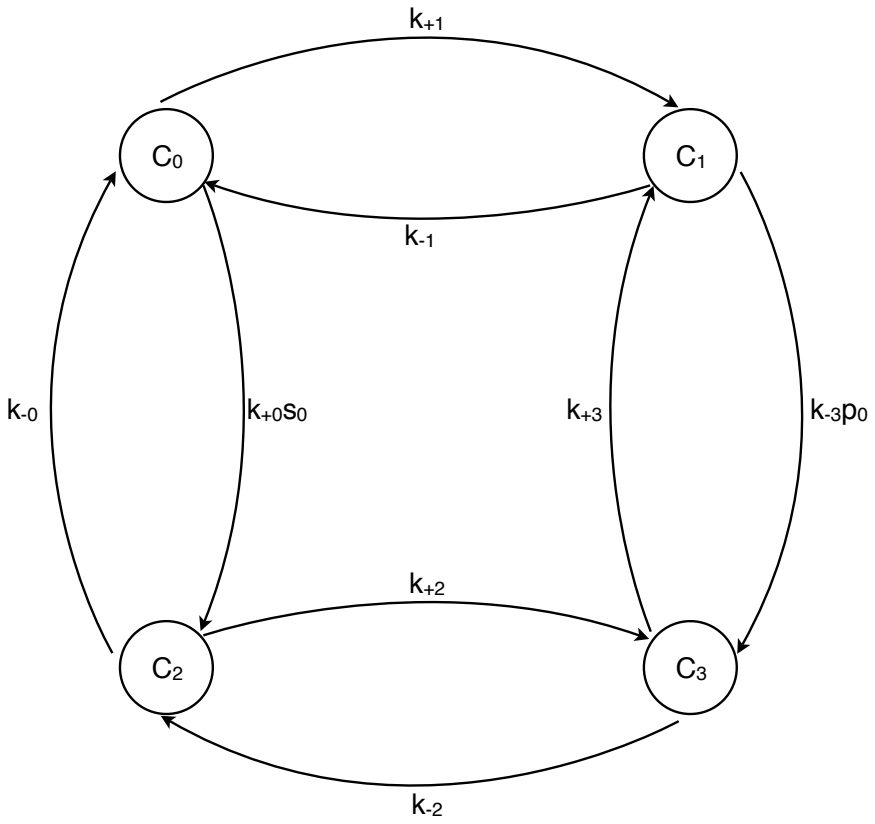

Figure A.1: **Graph for the Single Ligand Model.**
For the set of reactions shown in (A.6).

The equilibrium concentration values can then be used to calculate the velocity of the reaction, as required in Chapters 3 and 4.

A.2 KAH Method Applied to the Single Ligand Model of Chapter 3

In order to more easily follow the method, we will modify the notation for the simple one ligand case of our model from Chapter 3. The modifications can be summarized as follows:

- S, P: the substrate and the product, corresponding to the ligand at the up- and downstream ends of the system respectively

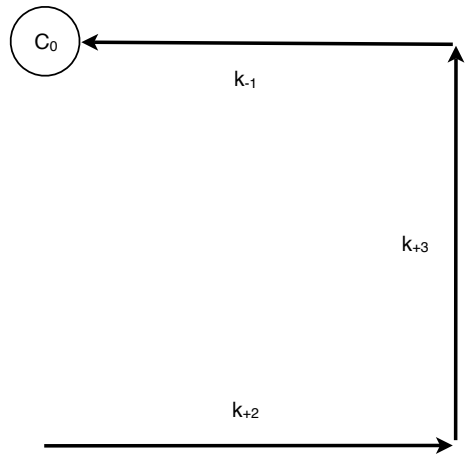

(a) Tree 1 Value: $k_{-1}k_{+2}k_{+3}$

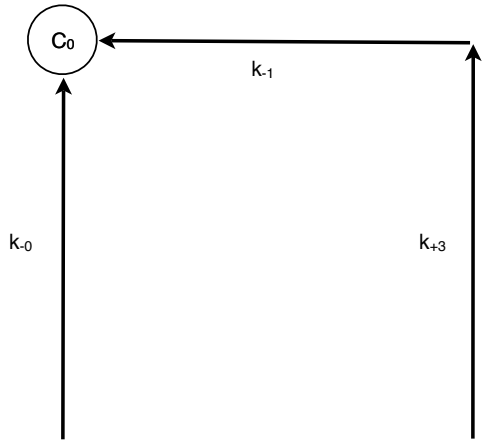

(b) Tree 2 Value: $k_{-0}k_{-1}k_{+3}$

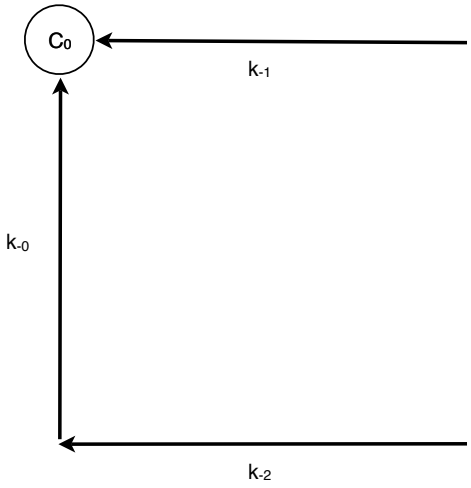

(c) Tree 3 Value: $k_{-0}k_{-1}k_{-2}$

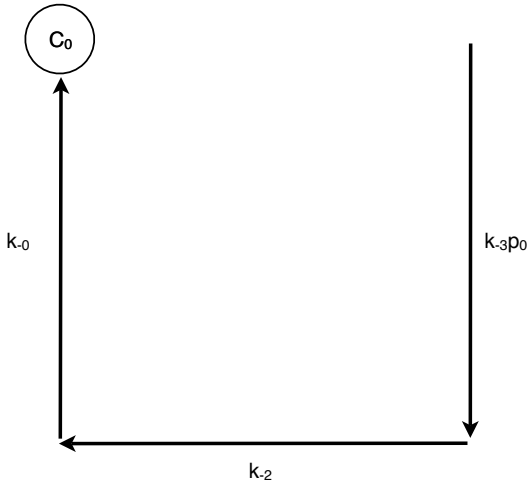

(d) Tree 4 Value: $k_{-0}k_{-2}k_{-3}p_0$

Figure A.2: **Basic Trees for the C_0 Node for the Single Ligand Model.**

- C_0, C_1: the free enzymes, corresponding to the carrier molecules at the up- and down-stream ends of the system

- C_2, C_3: the enzyme-substrate and enzyme-product complexes, corresponding to the carrier-ligand complexes at the up- and down-stream ends of the system

- $k_{\pm 0}, k_{\pm 3}$: association-dissociation rate constants at the up- and down-stream ends of the system

- $k_{\pm 1}, k_{\pm 2}, k_{\pm 4}$: transport rate constants for the free enzymes, enzyme-ligand complexes, and free ligands respectively

Then the set of reactions for our single ligand model from Chapter 3 can be written as:

$$\begin{aligned} S + C_0 \underset{k_{-0}}{\overset{k_{+0}}{\rightleftharpoons}} C_2 \quad & \underset{k_{-2}}{\overset{k_{+2}}{\rightleftharpoons}} \quad C_3 \underset{k_{-3}}{\overset{k_{+3}}{\rightleftharpoons}} C_1 + P, \\ C_0 \quad & \underset{k_{-1}}{\overset{k_{+1}}{\rightleftharpoons}} \quad C_1, \\ S \quad & \underset{k_{-4}}{\overset{k_{+4}}{\rightleftharpoons}} \quad P_1. \end{aligned} \tag{A.6}$$

Once we know the equilibrium values of the c_i from (A.5), we can calculate the velocity of the product formation for our model. Note that since our indexing begins with $i = 0$, the equation will be

$$\begin{aligned} v = \frac{dp}{dt} &= (k_{+4} s_0 - k_{-4} p_0) + (k_{+3} c_3 - k_{-3} p_0 c_1), \\ &= (k_{+4} s_0 - k_{-4} p_0) + \frac{e_0 (k_{+3} D_3 - k_{-3} p_0 D_1)}{D_0 + D_1 + D_2 + D_3}. \end{aligned} \tag{A.7}$$

Note that if we are studying the grand canonical scenario, S and P are always held constant, so the above equation will hold once the enzymes reach the steady state. Figure A.1 shows the graph for our problem. We can calculate D_0 by adding the basic tree values shown in Figure

A.2, while the other D_i can be found in the same manner:

$$D_0 = k_{-1}k_{+2}k_{+3} + k_{-0}k_{-1}k_{+3} + k_{-0}k_{-1}k_{-2} + k_{-0}k_{-2}k_{-3}p_0, \tag{A.8a}$$

$$D_1 = k_{-0}k_{+1}k_{-2} + k_{-0}k_{+1}k_{+3} + k_{+1}k_{+2}k_{+3} + k_{+0}k_{+2}k_{+3}s_0, \tag{A.8b}$$

$$D_2 = k_{+0}k_{-1}k_{+3}s_0 + k_{+0}k_{-1}k_{-2}s_0 + k_{+)}k_{-2}k_{-3}s_0p_0 + k_{+1}k_{-2}k_{-3}p_0, \tag{A.8c}$$

$$D_3 = k_{+0}k_{-1}k_{+2}s_0 + k_{+0}k_{+2}k_{-3}s_0p_0 + k_{+1}k_{+2}k_{-3}p_0 + k_{-0}k_{+1}k_{-3}p_0. \tag{A.8d}$$

In light of the facilitated transition situation that our model describes, we can make the following simplifying assumptions, which are discussed in depth in Chapter 3:

- $k_{+1} = k_{-1}, k_{+2} = k_{-2}, k_{+4} = k_{-4}$: The transport rates should be unbiased.
- $k_{\pm 0} = k_{\mp 3}$: The association-dissociation kinetics should be the same at both ends of the system.
- $k_{\pm 1} = k_{\pm 2}$: The ligand is so small compared to the enzyme that the transport rates for the ligand-enzyme complexes are the same as those for the enzyme.

Then our expressions for the D_i can be simplified to become:

$$D_1 = 2k_{-0}k_{+1}^2 + k_{-0}^2k_{+1} + k_{-0}k_{+0}k_{+1}p_0, \tag{A.9a}$$

$$D_2 = 2k_{-0}k_{+1}^2 + k_{-0}^2k_{+1} + k_{-0}k_{+0}k_{+1}s_0, \tag{A.9b}$$

$$D_3 = k_{-0}k_{+0}k_{+1}s_0 + k_{+0}k_{+1}^2(s_0 + p_0) + k_{+0}^2k_{+1}s_0p_0, \tag{A.9c}$$

$$D_4 = k_{+0}k_{+1}^2(s_0 + p_0) + k_{+0}^2k_{+1}s_0p_0 + k_{-0}k_{+0}k_{+1}p_0. \tag{A.9d}$$

Furthermore, we can see that the sum of the D_i simplifies to

$$\begin{aligned}\sum_{i=0}^{3} D_i &= 2k_{+1}\left[k_{-0}^2 + 2k_{-0}k_{+1} + k_{-0}k_{+0}(s_0 + p_0) + k_{+0}k_{+1}(s_0 + p_0) + k_{+0}^2s_0p_0\right], \\ &= \frac{2k_{+1}}{k_{-0}^2}\left[(1 + K_0s_0)(1 + K_0p_0) + \frac{k_{+1}}{k_{-0}}(2 + K_0(s_0 + p_0))\right],\end{aligned}$$

where we define $K_0 = \frac{k_{+0}}{k_{-0}}$ for notational convenience. Next, we can simplify the numerator of the second term in (A.7), or the enhancement term:

$$\begin{aligned} k_{+3}D_3 - k_{-3}p_0D_1 &= k_{-0}\left(k_{+0}k_{+1}^2(s_0+p_0) + k_{+0}^2k_{+1}s_0p_0 + k_{-0}k_{+0}k_{+1}p_0\right) \\ &\quad -k_{+0}p_0\left(2k_{-0}k_{+1}^2 + k_{-0}^2k_{+1} + k_{-0}k_{+0}k_{+1}s_0\right), \\ &= k_{+1}\left[k_{-0}k_{+0}k_{+1}(s_0+p_0) + k_{-0}k_{+0}^2s_0p_0 + k_{-0}^2k_{+0}p_0\right. \\ &\quad \left.-2k_{-0}k_{+0}k_{+1}p_0 - k_{-0}^2k_{+0}p_0 - k_{-0}k_{+0}^2s_0p_0\right], \\ &= \frac{k_{+1}^2}{k_{-0}^2}K_0(s_0-p_0). \end{aligned}$$

Finally, we can calculate the velocity of the conversion of the substrate to the product:

$$\begin{aligned} v &= (k_{+4}s_0 - k_{-4}p_0) + \frac{e_0\left(k_{+3}D_3 - k_{-3}p_0D_1\right)}{D_0+D_1+D_2+D_3}, \\ &= k_{+4}(s_0-p_0) + \frac{e_0\frac{k_{+1}^2}{k_{-0}^2}K_0(s_0-p_0)}{\frac{2k_{+1}}{k_{-0}^2}\left[\left(1+K_0s_0\right)\left(1+K_0p_0\right) + \frac{k_{+1}}{k_{-0}}\left(2+K_0(s_0+p_0)\right)\right]}, \end{aligned}$$

which we can rewrite as

$$v = \left(k_{+4} + \frac{k_{+1}K_0e_0}{2\left[\left(1+K_0s_0\right)\left(1+K_0p_0\right) + \frac{k_{+1}}{k_{-0}}\left(2+K_0(s_0+p_0)\right)\right]}\right)(s_0-p_0). \tag{A.10}$$

The enhancement term in the above equation is analogous to that in (3.21).

A.3 KAH Method Applied to the N = 2 *Case of the* N*-Ligand Model*

In this section, we simply state the resulting basic determinants for the two ligand system of Chapter 4. They were calculated for the graph shown in Figure A.3, using the automated script provided in the supplementary material of Ref. [58].

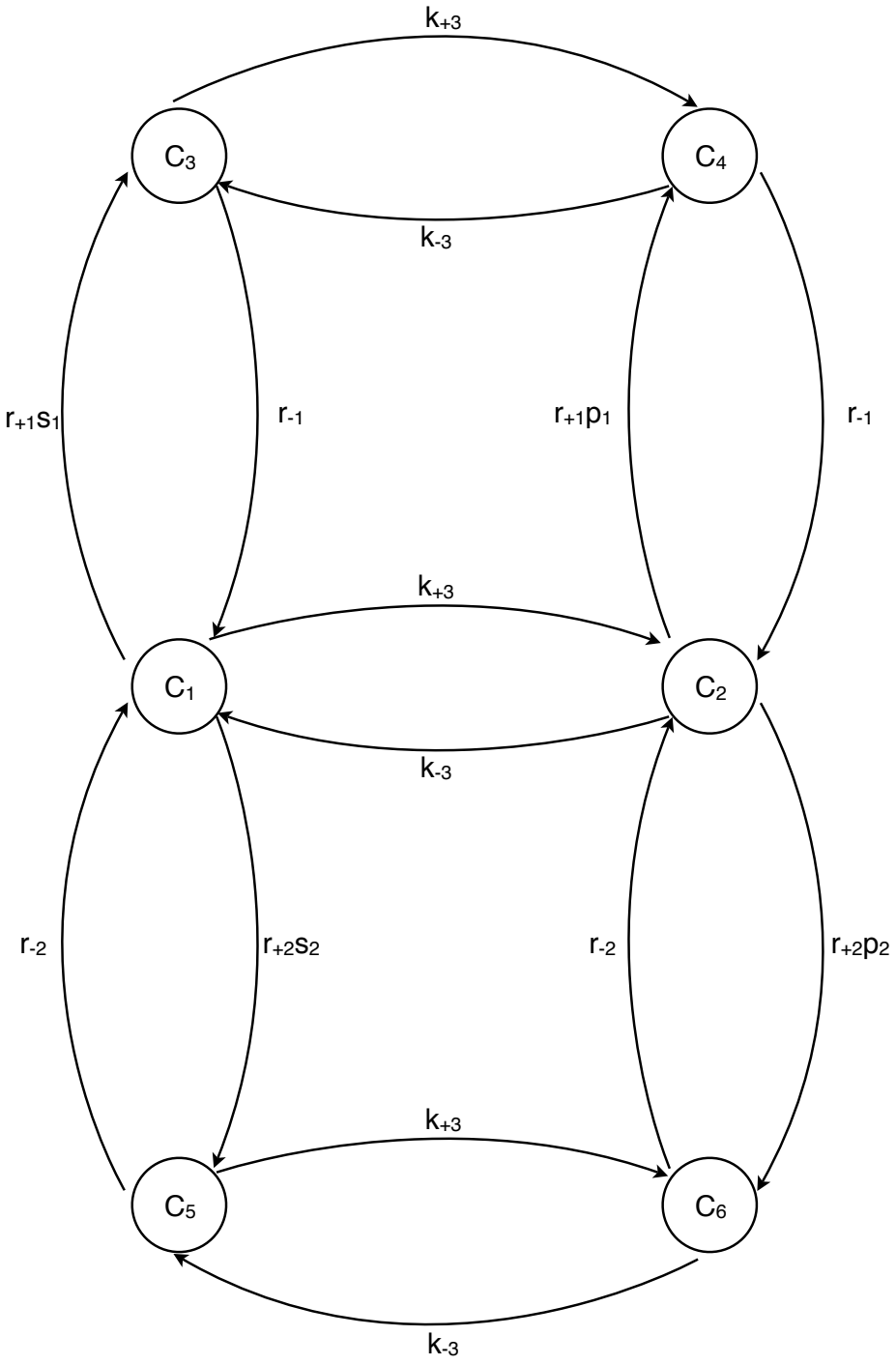

Figure A.3: **Graph for the N = 2 Model.**
The graph for the two ligand system studied in Chapter 4. Note that $C_1 = E$, $C_2 = \widetilde{E}$, $C_3 = ES_1$, $C_4 = \widetilde{E}P_1$, $C_5 = ES_2$, $C_6 = \widetilde{E}P_2$.

$$
\begin{aligned}
D_1 &= (k_{-3})^3 r_{-1} r_{-2} + 2(k_{-3})^2 k_{+3} r_{-1} r_{-2} + k_{-3}(k_{+3})^2 r_{-1} r_{-2} + (k_{-3})^2 (r_{-1})^2 r_{-2} \\
&\quad + k_{-3} k_{+3} (r_{-1})^2 r_{-2} + (k_{-3})^2 p_1 r_{-1} r_{+1} r_{-2} + k_{-3} k_{+3} p_1 r_{-1} r_{+1} r_{-2} + (k_{-3})^2 r_{-1} (r_{-2})^2 \\
&\quad + k_{-3} k_{+3} r_{-1} (r_{-2})^2 + k_{-3} (r_{-1})^2 (r_{-2})^2 + k_{-3} p_1 r_{-1} r_{+1} (r_{-2})^2 + (k_{-3})^2 p_2 r_{-1} r_{-2} r_{+2} \\
&\quad + k_{-3} k_{+3} p_2 r_{-1} r_{-2} r_{+2} + k_{-3} p_2 (r_{-1})^2 r_{-2} r_{+2}, \qquad \text{(A.11a)} \\
D_2 &= (k_{-3})^2 k_{+3} r_{-1} r_{-2} + 2 k_{-3} (k_{+3})^2 r_{-1} r_{-2} + (k_{+3})^3 r_{-1} r_{-2} + k_{-3} k_{+3} (r_{-1})^2 r_{-2} \\
&\quad + (k_{+3})^2 (r_{-1})^2 r_{-2} + k_{-3} k_{+3} r_{-1} (r_{-2})^2 + (k_{+3})^2 r_{-1} (r_{-2})^2 + k_{+3} (r_{-1})^2 (r_{-2})^2 \\
&\quad + k_{-3} k_{+3} r_{-1} r_{+1} r_{-2} s_1 + (k_{+3})^2 r_{-1} r_{+1} r_{-2} s_1 + k_{+3} r_{-1} r_{+1} (r_{-2})^2 s_1 + k_{-3} k_{+3} r_{-1} r_{-2} r_{+2} s_2 \\
&\quad + (k_{+3})^2 r_{-1} r_{-2} r_{+2} s_2 + k_{+3} (r_{-1})^2 r_{-2} r_{+2} s_2, \qquad \text{(A.11b)} \\
D_3 &= (k_{-3})^2 k_{+3} p_1 r_{+1} r_{-2} + k_{-3} (k_{+3})^2 p_1 r_{+1} r_{-2} + k_{-3} k_{+3} p_1 r_{+1} (r_{-2})^2 + (k_{-3})^3 r_{+1} r_{-2} s_1 \\
&\quad + (k_{-3})^2 k_{+3} r_{+1} r_{-2} s_1 + (k_{-3})^2 r_{-1} r_{+1} r_{-2} s_1 + k_{-3} k_{+3} r_{-1} r_{+1} r_{-2} s_1 + (k_{-3})^2 p_1 (r_{+1})^2 r_{-2} s_1 \\
&\quad + k_{-3} k_{+3} p_1 (r_{+1})^2 r_{-2} s_1 + (k_{-3})^2 r_{+1} (r_{-2})^2 s_1 + k_{-3} r_{-1} r_{+1} (r_{-2})^2 s_1 + k_{-3} p_1 (r_{+1})^2 (r_{-2})^2 s_1 \\
&\quad + (k_{-3})^2 p_2 r_{+1} r_{-2} r_{+2} s_1 + k_{-3} p_2 r_{-1} r_{+1} r_{-2} r_{+2} s_1 + k_{-3} k_{+3} p_1 r_{+1} r_{-2} r_{+2} s_2, \qquad \text{(A.11c)} \\
D_4 &= k_{-3} (k_{+3})^2 p_1 r_{+1} r_{-2} + (k_{+3})^3 p_1 r_{+1} r_{-2} + k_{-3} k_{+3} p_1 r_{-1} r_{+1} r_{-2} + (k_{+3})^2 p_1 r_{-1} r_{+1} r_{-2} \\
&\quad + (k_{+3})^2 p_1 r_{+1} (r_{-2})^2 + k_{+3} p_1 r_{-1} r_{+1} (r_{-2})^2 + (k_{-3})^2 k_{+3} r_{+1} r_{-2} s_1 + k_{-3} (k_{+3})^2 r_{+1} r_{-2} s_1 \\
&\quad + k_{-3} k_{+3} p_1 (r_{+1})^2 r_{-2} s_1 + (k_{+3})^2 p_1 (r_{+1})^2 r_{-2} s_1 + k_{-3} k_{+3} r_{+1} (r_{-2})^2 s_1 + k_{+3} p_1 (r_{+1})^2 (r_{-2})^2 s_1 \\
&\quad + k_{-3} k_{+3} p_2 r_{+1} r_{-2} r_{+2} s_1 + (k_{+3})^2 p_1 r_{+1} r_{-2} r_{+2} s_2 + k_{+3} p_1 r_{-1} r_{+1} r_{-2} r_{+2} s_2, \qquad \text{(A.11d)} \\
D_5 &= (k_{-3})^2 k_{+3} p_2 r_{-1} r_{+2} + k_{-3} (k_{+3})^2 p_2 r_{-1} r_{+2} + k_{-3} k_{+3} p_2 (r_{-1})^2 r_{+2} + k_{-3} k_{+3} p_2 r_{-1} r_{+1} r_{+2} s_1 \\
&\quad + (k_{-3})^3 r_{-1} r_{+2} s_2 + (k_{-3})^2 k_{+3} r_{-1} r_{+2} s_2 + (k_{-3})^2 (r_{-1})^2 r_{+2} s_2 + (k_{-3})^2 p_1 r_{-1} r_{+1} r_{+2} s_2 \\
&\quad + (k_{-3})^2 r_{-1} r_{-2} r_{+2} s_2 + k_{-3} k_{+3} r_{-1} r_{-2} r_{+2} s_2 + k_{-3} (r_{-1})^2 r_{-2} r_{+2} s_2 + k_{-3} p_1 r_{-1} r_{+1} r_{-2} r_{+2} s_2 \\
&\quad + (k_{-3})^2 p_2 r_{-1} (r_{+2})^2 s_2 + k_{-3} k_{+3} p_2 r_{-1} (r_{+2})^2 s_2 + k_{-3} p_2 (r_{-1})^2 (r_{+2})^2 s_2, \qquad \text{(A.11e)} \\
D_6 &= k_{-3} (k_{+3})^2 p_2 r_{-1} r_{+2} + (k_{+3})^3 p_2 r_{-1} r_{+2} + (k_{+3})^2 p_2 (r_{-1})^2 r_{+2} + k_{-3} k_{+3} p_2 r_{-1} r_{-2} r_{+2} \\
&\quad + (k_{+3})^2 p_2 r_{-1} r_{-2} r_{+2} + k_{+3} p_2 (r_{-1})^2 r_{-2} r_{+2} + (k_{+3})^2 p_2 r_{-1} r_{+1} r_{+2} s_1 + k_{+3} p_2 r_{-1} r_{+1} r_{-2} r_{+2} s_1 \\
&\quad + (k_{-3})^2 k_{+3} r_{-1} r_{+2} s_2 + k_{-3} (k_{+3})^2 r_{-1} r_{+2} s_2 + k_{-3} k_{+3} (r_{-1})^2 r_{+2} s_2 + k_{-3} k_{+3} p_1 r_{-1} r_{+1} r_{+2} s_2 \\
&\quad + k_{-3} k_{+3} p_2 r_{-1} (r_{+2})^2 s_2 + (k_{+3})^2 p_2 r_{-1} (r_{+2})^2 s_2 + k_{+3} p_2 (r_{-1})^2 (r_{+2})^2 s_2. \qquad \text{(A.11f)}
\end{aligned}
$$

Appendix B

SIMULATION TECHNIQUES

B.1 Polymer Growth System

We would like to explore a system of many polymers interacting with a moving barrier. A system of this type could easily represent a polymer of some kind pushing against a cell wall, or propelling a bacterium, as discussed in Chapter 7. We will start by exploring simpler systems, such as a single polymer without a barrier, before working our way up to the full system. The preliminary simulations model the growth of a single polymer in an aqueous solution containing monomers. We will focus on the growth and shrinkage of only one end of the polymer, and will neglect whatever process may be happening at the other end. Denote the concentration of monomers in the surrounding solution by c, the second order "on" rate constant by k_+, and the first order "off" rate constant by k_-, as can be seen in Figure B.1. We can model the position of the tip of the polymer using a random walk. First we will set up a discrete time model, then we will model the growth of the polymer in continuous time, using random time steps, as a Poisson process. After creating the basic polymerization simulations, we will add a barrier for the polymer to interact with. At first, the barrier will remain at a fixed position, then the barrier will also move according to a Poisson process. The results of these simulations will be compared to the analytical results for the same systems.

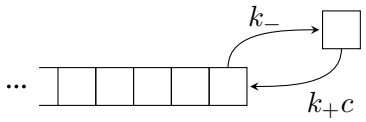

Figure B.1: **Simple Polymer System for Simulations.**

Table B.1: **Discrete Time Simulation Algorithm for Polymerization.**

Condition	Action
$0 \leq u < num_-$	subtract a monomer
$num_- \leq u < num_+$	do nothing
$num_+ \leq u \leq 1$	add a monomer

B.1.1 Discrete Time Simulation

For the discrete time simulation, the user can input the "on" rate k_+, concentration c, "off" rate k_-, time step size dt, and the maximum number of time steps to run the simulation. Let $\widehat{k}_+ = ck_+$ denote the first order rate of adding monomers, for the sake of simplicity. We will assume that the concentration of the monomers in the solution remains constant.

In order to ensure that exactly one event (either adding or subtracting) will happen in one time step, we require that

$$\left(k_- + \widehat{k}_+\right) dt = 1. \tag{B.1}$$

If $\left(k_- + \widehat{k}_+\right) dt > 1$, then we require the user to input a smaller value for dt. If $\left(k_- + \widehat{k}_+\right) dt < 1$, then we create a third "nothing" rate constant, k_0, to take into account the possibility that neither adding nor subtracting occurs during the time interval dt. We set k_0 so that

$$\begin{aligned} \left(k_- + k_0 + \widehat{k}_+\right) dt &= 1, \\ k_0 &= \frac{1 - \left(k_- + \widehat{k}_+\right) dt}{dt}. \end{aligned} \tag{B.2}$$

Now we can be certain that exactly one event (adding, subtracting, or doing nothing) occurs during each time step.

We will use a random number generator to generate a *uniform(0,1)* random number at each time step to determine whether to add a monomer, subtract a monomer, or do nothing. Note that the following discussion describes the process as though doing nothing during the time step is a possibility, but we can see that if $k_0 = 0$, the case where the time step is exactly the right size, and either addition or subtraction of a monomer will occur during each time step, is

included. Create constants

$$num_- = k_- dt, \tag{B.3}$$

$$num_+ = 1 - \widehat{k}_+ dt = (k_- + k_0)\, dt. \tag{B.4}$$

Note that if $k_0 = 0$, then $num_- = num_+$. Let u denote the random *uniform(0,1)* number generated at each time step. Then perform the actions listed in Table B.1. Continue this process until either the maximum number of time steps is reached, or the length of the polymer reaches zero. If the polymer length falls to zero, then logically the polymer can no longer either grow or shrink, so we end the simulation for that trial.

B.1.2 Continuous Time Simulation

For a continuous time simulation, we model the events of adding or subtracting monomers as a Poisson process of rate $\lambda = k_- + \widehat{k}_+$. We no longer need to account for the possibility of doing nothing in a time step, since the lengths of the time steps themselves are now random. It is well-known that the inter-arrival times between events in a Poisson process are exponentially distributed with the same rate as the Poisson process. Our continuous time simulation will randomly assign both the time when the event (adding or subtracting of a monomer) occurs, and which type of event occurs. We will use the same random number generator that returns *uniform(0,1)* random numbers both to assign the inter-arrival times and to decide which event occurs. Therefore, we must find a way to generate an *exponential(rate=λ)* random variable from a *uniform(0,1)* random variable. We can use the result of the following theorem to generate an exponential random variable [24].

Theorem 1. *Let U be a uniform(0,1) random variable, and let $\frac{1}{\lambda} > 0$. Then the random variable*

$$X = -\frac{1}{\lambda} \log U$$

is exponentially distributed with rate λ.

Proof. First, solve for the random variable U:

$$\log U = -\lambda X$$

$$U = e^{-\lambda X}.$$

Table B.2: **Continuous Time Simulation Algorithm for Polymerization.**

1. Generate two *uniform(0,1)* random numbers, u_1, u_2.
2. Use u_1 to generate the interarrival time, τ, for the event using (B.9).
3. Use u_2 to decide whether the event will be addition or subtraction:
   - If $0 \leq u_2 < num_-$ then subtract a monomer.
   - If $num_- \leq u_2 \leq 1$ then add a monomer.
4. Record the i^{th} event time $t_i = t_{i-1} + \tau$ and the location of the end of the polymer $x_i = x_{i-1} \pm$ *(width of monomer)*, where $\pm$ is determined by Step 3.

Then we know that $X > \tau$ is equivalent to $U < e^{-\lambda\tau}$. Therefore $u = e^{-\lambda x}$ maps x-values (τ, ∞) to u-values $(0, e^{-\lambda\tau})$, and the two events $\{X > \tau\}$ and $\left\{U < e^{-\lambda\tau}\right\}$ are the same. Furthermore

$$P\left(X > \tau\right) = P\left(U < e^{-\lambda\tau}\right) = e^{-\lambda\tau}, \tag{B.5}$$

as long as $\tau \geq 0$, or else $P(X > \tau) = 1$ since $e^{-\lambda\tau} > 1$ for $\tau < 0$. Define the *cumulative distribution function* (*cdf*) to be

$$F_X(x) = P(X \leq x),$$

and the *probability density function* (*pdf*) to be the function that satisfies

$$F_X(x) = \int_{-\infty}^{x} f_X(y)dy.$$

We know that the *pdf* for an exponential random variable with rate λ is given by

$$f_X(x) = \lambda e^{\lambda x}, \qquad 0 \leq x \leq \infty, \tag{B.6}$$

so we can see that the *cdf* must be given by

$$F_X(x) = \int_{-\infty}^{x} \lambda e^{\lambda y} dy = 1 - e^{\lambda x}. \tag{B.7}$$

Then it is easy to see that (B.5) describes the *cdf* of an exponential random variable, since

$$P(X > \tau) = 1 - P(X \leq \tau) = 1 - F_X(\tau) = 1 - \left(1 - e^{\lambda\tau}\right) = e^{\lambda\tau}. \tag{B.8}$$

□

Therefore, we see that if u is a uniformly distributed random number, then we can obtain an exponentially distributed random number, τ, by simply setting

$$\tau = -\frac{1}{\lambda}\log u. \tag{B.9}$$

Now that we know how to generate the inter-arrival times, all that remains is to define how to decide whether to add or subtract a monomer at each event time. Again we define num_- to make this process easier, but the definition must be adapted now that we do not have a fixed time step, dt. First we define the probabilities p_- and p_+, for subtracting and adding monomers, as:

$$p_- = \frac{k_-}{\lambda}, \qquad p_+ = \frac{\widehat{k}_+}{\lambda}, \tag{B.10}$$

where we can ensure that $p_- + p_+ = 1$ by recalling that $\lambda = k_- + \widehat{k}_+$:

$$p_- + p_+ = \frac{k_- + \widehat{k}_+}{\lambda} = \frac{k_- + \widehat{k}_+}{k_- + \widehat{k}_+} = 1. \tag{B.11}$$

Then in order to simulate the addition or subtraction of monomers at one end of a polymer as a Poisson process of rate λ, we can simply follow the procedure outlined in Table B.2, where num_- is given by

$$num_- = p_- = \frac{k_-}{\lambda}. \tag{B.12}$$

We simply repeat the process in Table B.2 until either the polymer disappears completely, or the maximum time limit is reached.

Table B.3: **Simulation Algorithm for Polymerization with a Fixed Barrier.**

1. Generate two *uniform(0,1)* random numbers, u_1, u_2.
2. Use u_1 to generate the interarrival time, τ, for the event using (B.9).
3. Use u_2 to decide whether the event will be addition or subtraction:
   - If $0 \leq u_2 < num_-$ then subtract a monomer ($\delta = -1$).
   - If $num_- \leq u_2 \leq 1$
     * and if $x_{barrier} - x_{i-1} \geq$ *(width of a monomer)* then add a monomer ($\delta = 1$).
     * and if $x_{barrier} - x_{i-1} <$ *(width of a monomer)* then do nothing ($\delta = 0$).
4. Record the i^{th} event time $t_i = t_{i-1} + \tau$ and the location of the end of the polymer $x_i = x_{i-1} + \delta \times$ *(width of monomer)*, where δ is determined as in Step 3.

B.1.3 Polymer System Including a Fixed Barrier

As a first step towards including a realistic boundary, such as a cell membrane, for the polymer to interact with, we can simply include a barrier at a fixed position in space. We build upon the continuous time simulation where the event of adding or subtracting a monomer is modeled as a Poisson process, as detailed above. Now we must keep track of how much distance is between the end of the polymer and the fixed barrier to ensure that they interact appropriately. The added complication is the geometric constraint that the polymer and the barrier cannot pass through one another. If we refer to Figure B.2, this condition is simply that the polymer must always remain to the left of the fixed barrier. Note that the interaction with the barrier will not prevent the subtraction of monomers, so we only need to check whether an interaction occurs in time steps that end in a decision to add a monomer. The modified simulation algorithm can be seen in Table B.3.

Simulation results can be directly compared to the spatially discrete steady state solutions in order to verify that the theory and the simulation do indeed agree, as can be seen in Figure B.3.

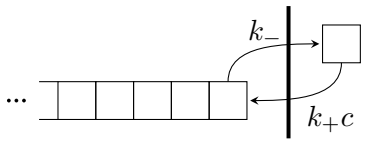

Figure B.2: **Polymer Interacting with a Fixed Barrier.**

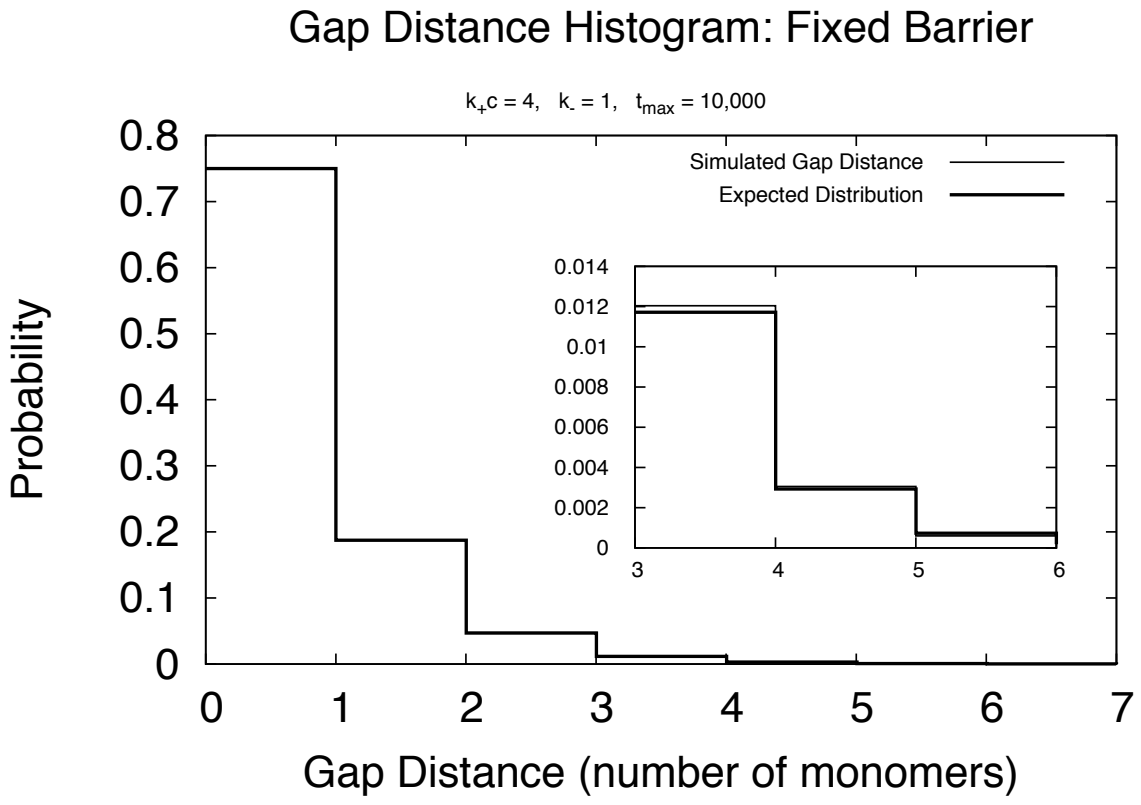

Figure B.3: **Gap Distance Histogram: Fixed Barrier.**
Histogram for the gap distance between a polymer and a fixed barrier with the given parameters. The simulation was run for 10,000 time units, and the histogram for the gap distance is shown, along with the predictions from (6.12).

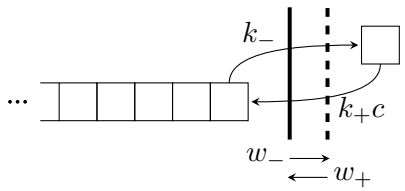

Figure B.4: **Polymer Interacting with a Moving Barrier.**

B.1.4 Polymer System Including a Moving Barrier

Finally, we can include a barrier that also moves according to a Poisson process. Define the rates of the barrier moving toward and away from the polymer to be w_+ and w_- respectively. In order to distinguish the rate of the Poisson process for the polymer from that of the barrier, let λ_p denote the rate for the polymer, and λ_w denote the rate for the barrier:

$$\lambda_p = k_- + \widehat{k}_+, \qquad \lambda_w = w_- + w_+. \tag{B.13}$$

Note that the positive direction for the motion of the barrier is opposite to that of the tip of the polymer. We must also create a new constant

$$num_{w-} = \frac{w_-}{\lambda_w} \tag{B.14}$$

to help determine how the barrier will move. Since the polymer and the barrier move at different random times, we must introduce a new flow for our algorithm, shown in Table B.4. A sample trajectory from this simulation can be seen in Figure B.5.

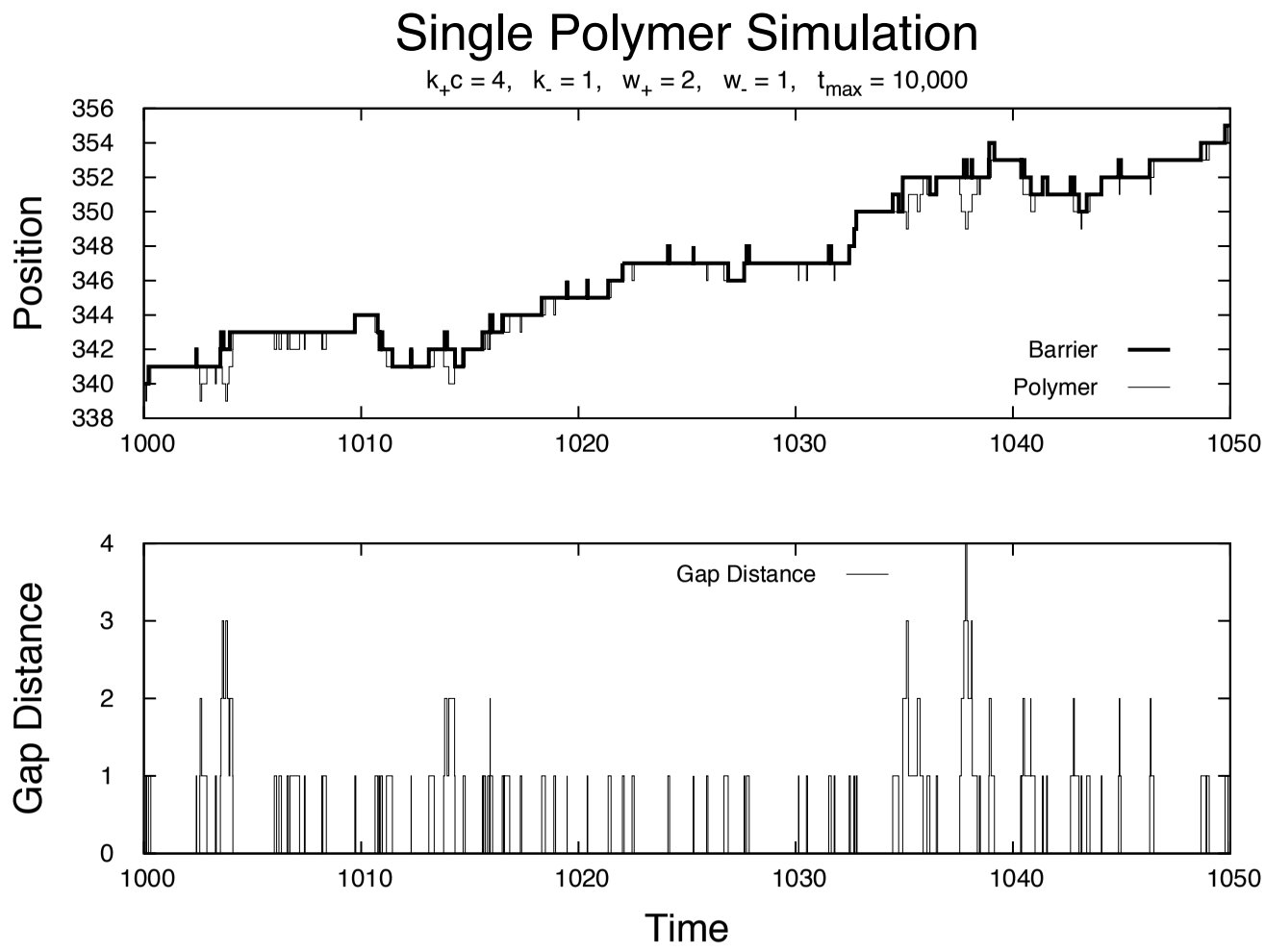

Figure B.5: **Single Polymer Simulation Trajectory.**
Continuous time simulation trajectory for a single polymer interacting with a moving barrier for the given parameter values. Note that the simulation was run for 10,000 time units, but we have only plotted part of the trajectory.

Table B.4: **Simulation Algorithm for Polymerization with a Moving Barrier.**

0. Set x_{p_0} = *initial polymer position* , x_{w_0} = *initial barrier position*, and $t_{p_0} = t_{w_0} = 0$.

1. Generate two *uniform(0,1)* random numbers, u_1, u_2.

2. Use u_1 and u_2 to generate the first interarrival times, τ_p and τ_w, for the event using:
$$\tau_p = -\frac{1}{\lambda_p}\log u \qquad\qquad \tau_w = -\frac{1}{\lambda_w}\log u$$

3. Set $t_{p_i} = t_{p_{(i-1)}} + \tau_p$ and $t_{w_j} = t_{w_{(j-1)}} + \tau_w$.

4. If $t_{p_i} < t_{w_j}$ then move the polymer. Generate two *uniform(0,1)* random numbers, u_3, u_4 and use u_3 to decide whether the event will be addition or subtraction:

   - If $0 \le u_3 < num_-$ then subtract a monomer ($\delta = -1$).
   - If $num_- \le u_3 \le 1$
     * and if $x_{w_{(j-1)}} - x_{p_{(i-1)}} \ge$ *(width of a monomer)* then add a monomer ($\delta = 1$).
     * and if $x_{w_{(j-1)}} - x_{p_{(i-1)}} <$ *(width of a monomer)* then do nothing ($\delta = 0$).
   - Record the i^{th} polymer event time t_{p_i} and the location of the end of the polymer $x_{p_i} = x_{p_{(i-1)}} + \delta \times$ *(width of monomer).*
   - Use the equation given in Step 2 and u_4 to generate a new τ_p and set $t_{p_{(i+1)}} = t_{p_i} + \tau_p$.

Table B.4: (continued)

5. If $t_{p_i} > t_{w_j}$ then move the barrier. Generate two *uniform(0,1)* random numbers, u_3, u_4 and use u_3 to decide whether the event will be addition or subtraction:

   - If $0 \leq u_3 < num_{w-}$ then move the barrier away from the polymer ($\delta = +1$).
   - If $num_{w-} \leq u_3 \leq 1$
     * and if $x_{w_{(j-1)}} - x_{p_{(i-1)}} \geq$ *(barrier increment)* then move the barrier towards the polymer ($\delta = -1$).
     * and if $x_{w_{(j-1)}} - x_{p_{(i-1)}} <$ *(barrier increment)* then do nothing ($\delta = 0$).
   - Record the j^{th} barrier event time t_{w_j} and location $x_{w_j} = x_{w_{(j-1)}} + \delta \times$ *(barrier increment)*.
   - Use the equation given in Step 2 and u_4 to generate a new τ_w and set $t_{w_{(j+1)}} = t_{w_j} + \tau_w$.

6. If $t_{p_i} = t_{w_j}$ then keep the polymer and the barrier at the same positions. (Note that this is extremely unlikely) Generate two *uniform(0,1)* random numbers, u_3, u_4 to create new interarrival times.

   - Record the i^{th} polymer event time t_{p_i} and the position of the end of the polymer $x_{p_i} = x_{p_{(i-1)}}$, and the j^{th} barrier event time t_{w_j} and location $x_{w_j} = x_{w_{(j-1)}}$.
   - Use the equations given in Step 2 and $u_3,\ u_4$ to generate new $\tau_p,\ \tau_w$ and set $t_{p_{(i+1)}} = t_{p_i} + \tau_p,\ t_{w_{9j+1)}} = t_{w_j} + \tau_w$.

7. Go back to Step 4 and loop through until the maximum time is reached, or the length of the polymer shrinks to zero.

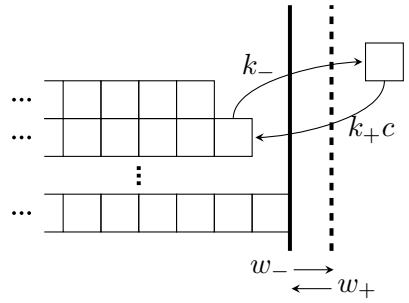

Figure B.6: **Multiple Polymers Interacting with a Moving Barrier.**

B.1.5 Polymer System Including Multiple Polymers and a Moving Barrier

Finally, we can continue to build upon our earlier simulations in order to include more than one polymer interacting with a moving barrier. The polymers share common adding and subtracting rates, as well as the concentration of free monomers in the solution. The new complication for our simulation algorithm is that the longest polymer is the one that mediates the interaction with the moving barrier. As before, each time a polymer adds a monomer, we must check that the barrier is not in the way. Now, however, when the barrier moves toward the polymers, we may simply check the position of the longest polymer to determine whether or not the move can be made. In order to keep the algorithm as simple as possible, let $t_{p_{min}}$ be the next event time for the polymers, and x_{pm} be the position of the polymer that adds or subtracts at $t_{p_{min}}$. Then the algorithm follows the procedure shown in Table B.5. It is important to note that the polymers are *identical* because they share adding and subtracting rates, as well as starting lengths, but the important question will be whether or not they are *independent*. A sample simulation trajectory can be seen in Figure B.7.

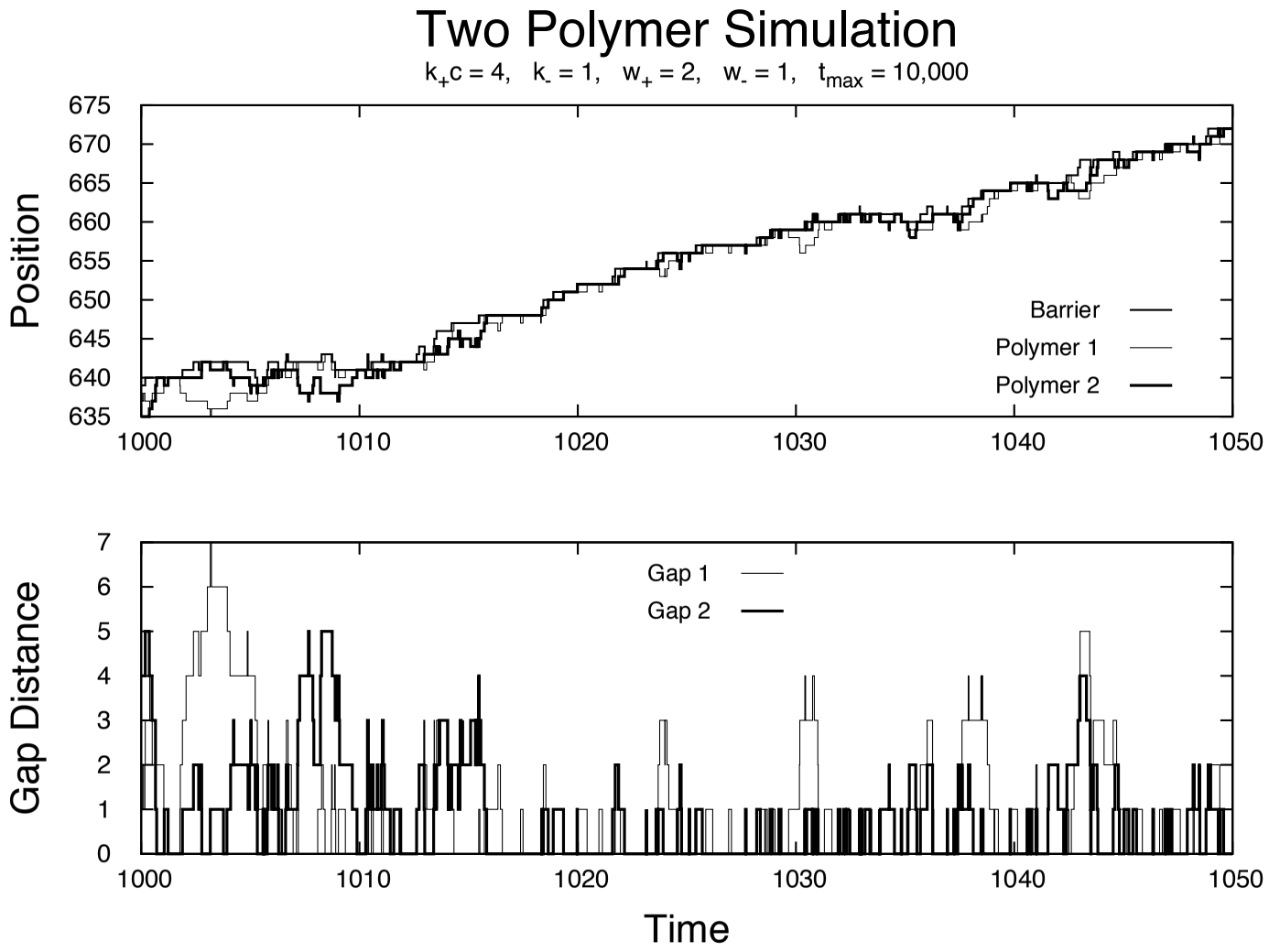

Figure B.7: **Two Polymer Simulation Trajectory.**
Continuous time simulation trajectory for two polymers interacting with a moving barrier for the given parameter values. Note that the simulation was run for 10,000 time units, but we have only plotted part of the trajectory.

Table B.5: **Simulation Algorithm for a Polymer Bundle with a Moving Barrier.**

0. Set x_{pk_0} = *initial position*, x_{w_0} = *initial barrier position*, and $t_{pk_0} = t_{w_0} = 0$ for $1 \leq k \leq n$.

1. Generate *n+1 uniform(0,1)* random numbers, $\{u_k\}, u_w$.

2. Use $\{u_k\}$ and u_w to generate the first interarrival times, $\{\tau_{pk}\}$ and τ_w, for the event using:

$$\tau_{pk} = -\frac{1}{\lambda_p} \log u_k \qquad\qquad \tau_w = -\frac{1}{\lambda_w} \log u_w$$

3. Set $t_{pk_i} = t_{pk_{(i-1)}} + \tau_{pk}$ and $t_{w_j} = t_{w_{(j-1)}} + \tau_w$.

4. Let $t_{p_{min}} = \min\{t_{pk}\}$, $x_{p_{max}} = \max\{x_{pk}\}$.

5. If $t_{p_{min}} < t_{w_j}$ then move the polymer. Generate two *uniform(0,1)* random numbers, u_1, u_2.

   - If $0 \leq u_1 < num_-$ then subtract a monomer ($\delta = -1$).
   - If $num_- \leq u_1 \leq 1$
     * and if $x_{w_{(j-1)}} - x_{pm_{(i-1)}} >$ *(width of a monomer)* then add a monomer ($\delta = +1$).
     * and if $x_{w_{(j-1)}} - x_{pm_{(i-1)}} \leq$ *(width of a monomer)* then do nothing ($\delta = 0$).
   - Record the i^{th} polymer event time $t_{pk_i} = t_{p_{min}}$ and the location of the end of the polymer $x_{pk_i} = x_{pk_{(i-1)}} + \delta \times$ *(width of monomer)*.
   - Use the equation given in Step 2 and u_2 to generate a new τ_{pk} and set $t_{pk_{(i+1)}} = t_{pk_i} + \tau_{pk}$.
   - Set $t_{p_{min}} = \min\{t_{pk}\}$, $x_{p_{max}} = \max\{x_{pk}\}$.

Table B.5: (continued)

6. If $t_{p_{min}} > t_{w_j}$ then move the barrier. Generate two *uniform(0,1)* random numbers, u_1, u_2.

   - If $0 \leq u_1 < num_{w-}$ then move the barrier away from the polymer ($\delta = +1$).
   - If $num_{w-} \leq u_1 \leq 1$
     * and if $x_{w_{(j-1)}} - x_{p_{max}} >$ *(barrier increment)* then move the barrier towards the polymer ($\delta = -1$).
     * and if $x_{w_{(j-1)}} - x_{p_{max}} \leq$ *(barrier increment)* then do nothing ($\delta = 0$).
   - Record the j^{th} barrier event time t_{w_j} and location $x_{w_j} = x_{w_{(j-1)}} + \delta \times$ *(barrier increment)*.
   - Use the equation given in Step 2 and u_2 to generate a new τ_w and set $t_{w_{(j+1)}} = t_{w_j} + \tau_w$.

7. If $t_{p_{min}} = t_{w_j}$ then keep the polymer and the barrier at the same positions. (Note that this is extremely unlikely.) Generate two *uniform(0,1)* random numbers, u_1, u_2.

   - Record the i^{th} polymer event time $t_{p_{min}}$ and the position of the end of the polymer $x_{pk_i} = x_{pk_{(i-1)}}$, and the j^{th} barrier event time t_{w_j} and location $x_{w_j} = x_{w_{(j-1)}}$.
   - Use the equations given in Step 2 and $u_1,\ u_2$ to generate new $\tau_{pk},\ \tau_w$ and set $t_{pk_{(i+1)}} = t_{pk_i} + \tau_{pk},\ t_{w_{(j+1)}} = t_{w_j} + \tau_w$.

8. Go back to Step 5 and loop through until the maximum time is reached, or the length of any polymer shrinks to zero.

B.2 Partially Reflected Brownian Motion

In order to simulate the Partially Reflected Brownian Motion (PRBM) system mentioned at the end of Chapter 3, we will follow the procedure outlined below. When the system is in State 1, we allow the molecules to diffuse freely in a 2-dimensional box. When the system is in State 2, the molecules will diffuse along the line $y = x$. When the molecules in State 1 cross the line $y = x$, we must find a method to determine whether or not they will bond and enter State 2. Similarly, in State 2, we must find a method to determine when the bond will break and the molecules will return to State 1. First, we will discuss the simulation of the free diffusion that occurs in both States 1 and 2. Then we will describe the methods for switching between the states. Note that the diffusion of the molecules in both states is assumed to be *unbiased*.

B.2.1 Simulation Techniques for Normal Random Variables

We know that diffusion can be modeled as Brownian motion, so we can create a discrete time, continuous space simulation as follows. Let x and y represent the positions of the `X` and `P` molecules, respectively. For each time step of length Δt, we know that

$$x(t + \Delta t) = x(t) + \Delta x, \qquad y(t + \Delta t) = y(t) + \Delta y, \tag{B.15}$$

where Δx and Δy are normal random variables with zero mean, since the motion is unbiased. In State 1, the variance for Δx and Δy is given by $2D_1\Delta t$ and $2D_2\Delta t$ respectively. However, in State 2, recall that $y = x$, so $y(t + \Delta t) = x(t + \Delta t) = x(t) + \Delta x$, and Δx is a normal random variable with zero mean and variance $2D_3\Delta t$. For simulating the two different states, we will use two different methods for simulating the Brownian motion.

State 1 (Two Normals at the Same Time): Box-Mueller and Polar Methods

To generate the two independent normal random variables for State 1, as described above, we will use the Box-Mueller Transformations. Let $\Delta X \sim normal(0, 2D_1\Delta t)$ and $\Delta Y \sim normal(0, 2D_1\Delta t)$. Then the joint probability density function (*pdf*) for ΔX and ΔY is given

by:

$$\begin{aligned} f(x,y) &= \frac{1}{\sqrt{4\pi D_1 \Delta t}} e^{-x^2/4D_1\Delta t} \frac{1}{\sqrt{4\pi D_2 \Delta t}} e^{-x^2/4D_2\Delta t}, \\ &= \frac{1}{4\pi\Delta t\sqrt{D_1 D_2}} e^{-\dfrac{(D_2x^2 + D_1y^2)}{4D_1D_2\Delta t}}. \end{aligned} \tag{B.16}$$

Perform a transformation of variables with $r^2 = D_2x^2 + D_1y^2$ and $\theta = \arctan\left(\frac{y\sqrt{D_1}}{x\sqrt{D_2}}\right)$. Then the Jacobian is given by

$$J = \begin{vmatrix} 2D_2x & 2D_1y \\ -\frac{\sqrt{D_1D_2}y}{D_2x^2+D_1y^2} & -\frac{\sqrt{D_1D_2}}{D_2x^2+D_1y^2} \end{vmatrix} = 2\sqrt{D_1D_2}, \tag{B.17}$$

and the joint *pdf* can be rewritten as

$$\begin{aligned} f(R^2,\Theta) &= \left(\frac{1}{2\sqrt{D_1D_2}}\right)\left(\frac{1}{4\pi\Delta t\sqrt{D_1D_2}} e^{-\dfrac{r}{4D_1D_2\Delta t}}\right), \\ &= \left(\frac{1}{2\pi}\right)\left(\frac{1}{4D_1D_2\Delta t} e^{-\dfrac{r}{4D_1D_2\Delta t}}\right) = f(R^2)g(\Theta). \end{aligned} \tag{B.18}$$

Now we can see that $R \sim$ *uniform(0,2π)* and $R^2 \sim$ *exponential(mean=*$4D_1D_2$*)*. Therefore, we can simply generate a pair of uniform and exponential random variables with the appropriate parameters, and then transform back to find Δx and Δy:

$$\Delta x = \frac{r\cos\theta}{\sqrt{D_2}}, \tag{B.19a}$$

$$\Delta y = \frac{r\sin\theta}{\sqrt{D_1}}. \tag{B.19b}$$

Given *uniform(0,1)* random variables U_1 and U_2, we can generate random variables r^2 and θ using the following formulas:

$$r^2 = -4D_1D_2\Delta t \log U_1, \qquad \theta = 2\pi U_2. \tag{B.20}$$

Finally, we arrive at the Box-Mueller Transformations:

$$\Delta x = \frac{\sqrt{-4D_1D_2\Delta t\log U_1}\cos(2\pi U_2)}{\sqrt{D_2}} = \sqrt{-4D_1\Delta t\log U_1}\cos(2\pi U_2), \tag{B.21a}$$

$$\Delta y = \frac{\sqrt{-4D_1D_2\Delta t\log U_1}\sin(2\pi U_2)}{\sqrt{D_1}} = \sqrt{-4D_2\Delta t\log U_1}\sin(2\pi U_2). \tag{B.21b}$$

Note that if the Box-Mueller Transformations prove to be too computationally expensive, one can instead use the Polar Method to indirectly compute the sine and cosine of the random angles [69]. If we generate a pair of random variables

$$V_1 = 2U_1 - 1, \qquad V_2 = 2U_2 - 1, \tag{B.22}$$

and let $S = V_1^2 + V_2^2$, we can indirectly calculate the sine and cosine in the following way. As long as $S = V_1^2 + V_2^2 \leq 1$, then the pair (V_1, V_2) is uniformly distributed in the unit circle. Therefore it follows that the polar coordinates for the pair, r and θ are independent and $R^2 = S \sim$ *uniform(0,1)* and $\Theta \sim$ *uniform(0,2π)*. Furthermore, we can calculate

$$\cos\theta = \frac{V_1}{S} = \frac{V_1}{\sqrt{V_1^2 + V_2^2}} = \frac{V_1}{\sqrt{S}}, \tag{B.23a}$$

$$\sin\theta = \frac{V_2}{S} = \frac{V_2}{\sqrt{V_1^2 + V_2^2}} = \frac{V_2}{\sqrt{S}}. \tag{B.23b}$$

Note that since $S \sim$ *uniform(0,1)*, we can use it in place of U_1 in our simulation scheme. The new simulation scheme would be to generate two *uniform(0,1)* random variables U_1 and U_2. Then set $V_1 = 2U_1 - 1$, $V_2 = 2U_2 - 1$, and $S = V_1^2 + V_2^2$. If $S > 1$, start over and generate a new pair of variables. If $S \leq 1$, then we obtain

$$\Delta x = \sqrt{\frac{-4D_1\Delta t \log S}{S}} V_1, \tag{B.24a}$$

$$\Delta y = \sqrt{\frac{-4D_2\Delta t \log S}{S}} V_2. \tag{B.24b}$$

State 2 (One Normal at a Time): Rejection Method

If the system is in State 2, only one normal random variable, $\Delta X \sim$ *normal(0,2D₃Δt)* is needed at each time step. Therefore we can use a rejection method to generate Δx for State 2. The algorithm for the rejection method can be seen in Table B.6.

B.2.2 Switching between States

Now we must provide a procedure for deciding what happens when the system switches between states. We assume that the probabilities for switching between the two states should be proportional to the reaction rates for transitioning between the two states. Therefore, if the

Table B.6: **Simulation Algorithm for the Rejection Method.**

1. Generate U_1, U_2 (uniform(0,1) random variables).
2. Set $Y_1 = -\log U_1$, $Y_2 = -\log U_2$ (exponential(mean=1) random variables).
3. If $Y_2 - (Y_1 - 1)^2/2 \leq 0$, return to Step 1. Otherwise:
4. Generate U_3 and set

$$\Delta x = \begin{cases} \frac{1}{\sqrt{2D_3\Delta t}} Y_1 & if\ U_3 \leq 1/2 \\ -\frac{1}{\sqrt{2D_3\Delta t}} Y_1 & if\ U_3 > 1/2 \end{cases}$$

molecules collide, they should bond with probability $\frac{q_1}{q_1+q_2}$. When the molecules are in State 2, the bound state, the bond should dissolve with probability $\frac{q_2}{q_1+q_2}$. Now we need to determine what happens when the molecules collide.

Transition from State 1 to State 2

When the molecules cross the line $y = x$, they will collide, and there is a chance that they will bond and diffuse together along the line. In order to check, we can generate a *uniform(0,1)* random variable U. If $U \leq \frac{q_1}{q_1+q_2}$, then the reaction occurs and the molecules diffuse along the line $y = x$ in State 2. Otherwise, we will return each molecule to a point on its previous path that lies on the line $y = x \pm \delta\sqrt{2}$, where the sign is determined by the previous placement of the molecules in the system, and δ is some small distance. This is meant to represent the molecules bouncing away from one another after the collision.

Transition from State 2 to State 1

When the system is in State 2, at each time step there is a chance that the molecular bond will dissolve and the system will transition to State 1. Therefore, at each time step, we should check whether or not to transition to State 1. In order to do this, generate a *uniform(0,1)* random variable U. If $U \leq \frac{q_2}{q_1+q_2}$, then transition to state 2, and begin to allow both molecules to diffuse freely. Otherwise, continue to run the simulation for diffusing along the line $y = x$.

Table B.7: **Simulation Algorithm for Partially Reflected Brownian Motion**.

0. Set $x_0 =$ initial `X` position, $y_0 =$ initial `P` position, $t_0 = 0$.

1. If $x_i \neq y_i$ (The system is in State 1):

   - Generate two *uniform(0,1)* random numbers, u_1, u_2.
   - Use u_1 and u_1 with the Box-Mueller method (B.21) to generate the position increments for `X` and `P`:

$$\Delta x = \sqrt{-4D_1\Delta t \log u_1}\cos(2\pi u_2)$$

$$\Delta y = \sqrt{-4D_2\Delta t \log u_1}\sin(2\pi u_2).$$

   - Set $x_{i+1} = x_i + \Delta x$, $y_{i+1} = y_i + \Delta y$.
   - If ($y_i < x_i$ and $y_{i+1} \geq x_{i+1}$) or ($y_i > x_i$ and $y_{i+1} \leq x_{i+1}$) i.e. the trajectory crosses the line $y = x$, check to see whether a transition to State 2 occurs.
     * Generate a *uniform(0,1)* random number, u_3 and set

$$m = \frac{y_{i+1} - y_i}{x_{i+1} - x_i}.$$

     * If $u_3 \leq \frac{q_1}{q_1+q_2}$ transition to State 2:
       – Set the positions of `X` and `P` to be where they trajectory would have crossed the line $y = x$:

$$y_{i+1} = x_{i+1} = \frac{y_i - mx_i}{1-m}.$$

     * Otherwise, remain in State 1 with `X` and `P` bouncing to the line $y = x \pm \delta\sqrt{2}$:
       – If $y_i > x_i$ and $y_{i+1} \leq x_{i+1}$, set

$$x_{i+1} = \frac{y_i - mx_i - \delta\sqrt{2}}{1-m}, \qquad y_{i+1} = x_{i+1} + \delta\sqrt{2}.$$

       – Otherwise, set

$$x_{i+1} = \frac{y_i - mx_i + \delta\sqrt{2}}{1-m}, \qquad y_{i+1} = x_{i+1} - \delta\sqrt{2}.$$

Table B.7: (continued)

2. If $x_i = y_i$ (The system is in State 2):

   - Generate a *uniform(0,1)* random number, u_3.
   - If $u_3 \leq \frac{q_1}{q_1+q_2}$, transition to State 1:
     * Generate two *uniform(0,1)* random numbers, u_1, u_2.
     * Use u_1 and u_1 with the Box-Mueller method (B.21) to generate the position increments for `X` and `P`:

$$\Delta x = \sqrt{-4D_1\Delta t \log u_1}\cos(2\pi u_2),$$

$$\Delta y = \sqrt{-4D_2\Delta t \log u_1}\sin(2\pi u_2).$$

     * Set $x_{i+1} = x_i + \Delta x$, $y_{i+1} = y_i + \Delta y$.
   - Otherwise, remain in State 2:
     * Use the Rejection Method from Table B.6 to set Δx.
     * Set $y_{i+1} = x_{i+1} = x_i + \Delta x$.

3. Set $t_i + 1 = t_i + \Delta t$.

4. Go back to Step 1 and loop through the algorithm until the maximum time has been reached.

B.2.3 Sample Simulation Trajectory

The complete algorithm for generating simulated trajectories can be found in Table B.7. A sample trajectory of the system can be seen in Figure B.8. Now we can see why we have called this the "Partially Reflected" Brownian motion system. If we plot the positions of the molecules as an ordered pair, (`X`,`P`), we see that the trajectory follows Brownian motion that is sometimes reflected across the line $y = x$, when the molecules collide and remain in State 1, but sometimes if the molecules collide, they will transition to State 2 and diffuse along the line $y = x$.

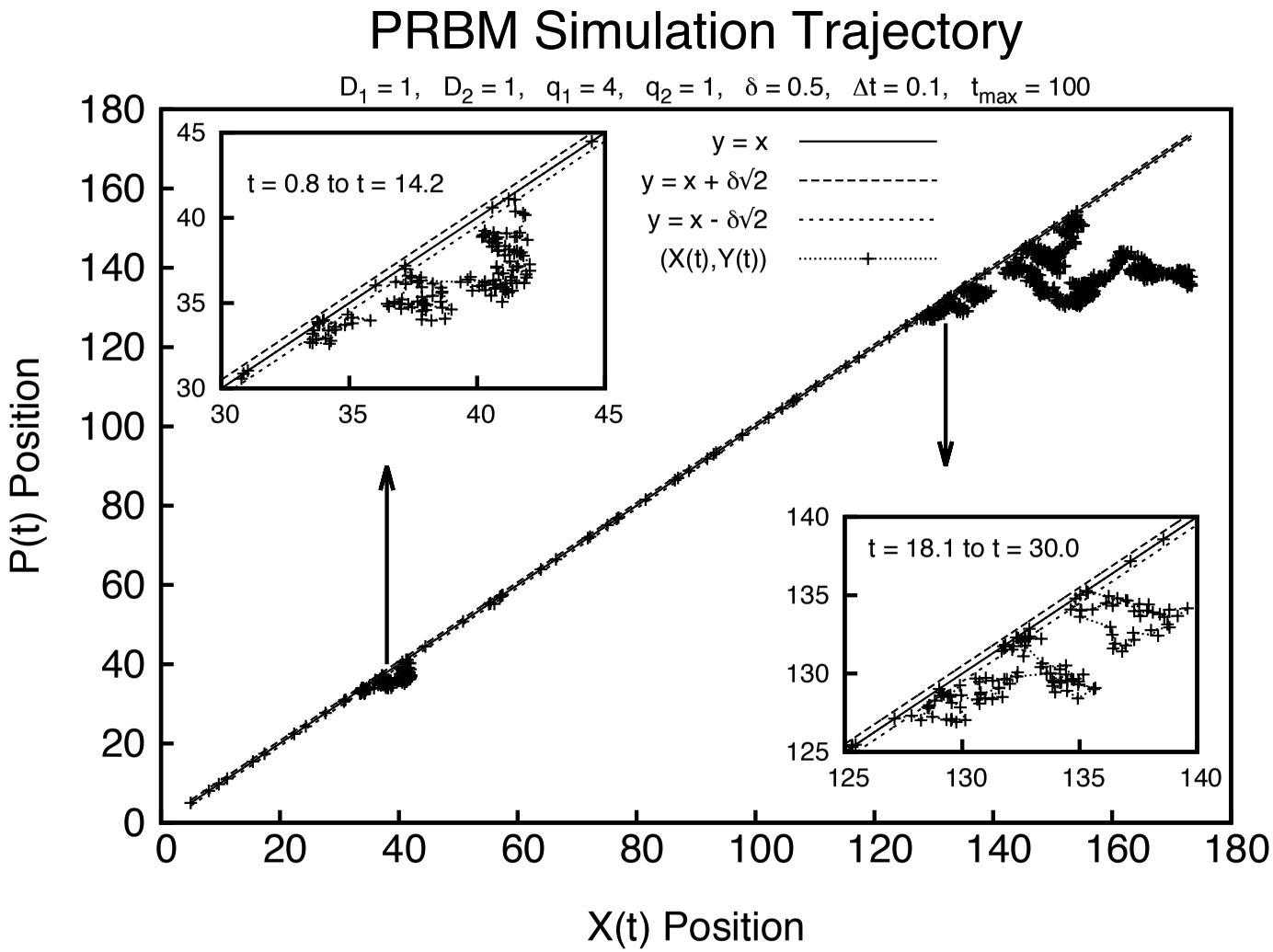

Figure B.8: **Partially Reflected Brownian Motion Simulation Trajectory from Figure 3.7.**
Note that this is the trajectory shown in Figure 3.7, reproduced here for convenience. Parameters as listed above. Also, the initial positions of the particles were $x = y = 5$.

Appendix C

TIME DEPENDENT SINGLE FILAMENT GAP DISTANCE SOLUTION

In this Appendix, we provide the details for the calculation of the full time dependent solution for the gap distance distribution for a single polymer filament interacting with a moving barrier from Chapter 6. First, we present the solution via the traditional Sturm-Liouville method, where we make some assumptions that would require more rigorous justification. Rather than go through all of those details, we present an alternative, more elegant, derivation using Fokas' New Transform Method [22].

C.1 Sturm-Liouville Solution to the Time-Dependent Gap Distance Problem

We would like to solve the initial boundary value problem below,

$$u_t(x,t) = u_{xx}(x,t) + \alpha u_x(x,t), \qquad 0 < x < \infty, t > 0, \tag{C.1a}$$

$$0 = u_x(0,t) + \alpha u(0,t), \qquad t > 0, \tag{C.1b}$$

$$0 = \lim_{x\to\infty} e^{\alpha x} u_x(x,t) = \lim_{x\to\infty} e^{\alpha x} u(x,t), \qquad t > 0, \tag{C.1c}$$

$$u(x,0) = u_0(x) = \delta(x), 0 < x < \infty, \tag{C.1d}$$

where $\alpha > 0$ and $\delta(x)$ is defined to be the function having the following properties over the semi-infinite interval:

$$1 = \int_0^\infty \delta(x)dx, \tag{C.2a}$$

$$f(0) = \int_0^\infty f(x)\delta(x)dx. \tag{C.2b}$$

First, we will show that the differential operator $\mathcal{L} = \frac{\partial^2}{\partial x^2} + \alpha\frac{\partial}{\partial x}$ is self-adjoint. Define the inner product with weight function $e^{\alpha x}$ such that

$$\langle u, v\rangle = \int_0^\infty e^{\alpha x} uv dx. \tag{C.3}$$

Then in order to demonstrate the $\mathcal{L}$ is self-adjoint, we must simply show that $\langle \mathcal{L}u, v\rangle = \langle u, \mathcal{L}v\rangle$, for u, v that satisfy (C.1). This is done in the usual manner, using integration by parts.

$$\begin{aligned}
\langle \mathcal{L}u, v\rangle &= \int_0^\infty e^{\alpha x}\left(u_{xx} + \alpha u_x\right) v dx, \\
&= e^{\alpha x} v\left(u_x + \alpha u_x\right)\big|_0^\infty - \int_0^\infty e^{\alpha x}\left(u_x + \alpha u\right)\left(v_x + \alpha v\right) dx, \\
&= \langle u, \mathcal{L}v\rangle,
\end{aligned}$$

where the boundary and vanishing conditions given in (C.1b) and (C.1c) guarantee that the terms from the integration by parts that are evaluated at $x = 0$ and $x = \infty$ vanish, and we can see that the second term on the second line is symmetric in u and v. Therefore, since the differential operator is self-adjoint subject to the weight function $\rho(x) = e^{\alpha x}$, we know that the eigenvalue problem $\mathcal{L}u = \mu u$ has an infinite number of eigenvalues, μ, which are real, and that the associated eigenfunctions can be chosen to be real-valued and orthonormal subject to the weight function $e^{\alpha x}$. Furthermore, since we expect the solution $u(x,t)$ to approach the steady-state solution over time, we can also assert that $\mu > 0$. Then we can perform separation of variables in the usual way, by assuming that $u(x,t) = X(x)T(t)$:

$$\begin{aligned}
X(x)T'(t) &= X''(x)T(t) + \alpha X'(x)T(t), \\
\frac{T'(t)}{T(t)} &= \frac{X''(x) + \alpha X'(x)}{X(x)} = -\lambda^2.
\end{aligned}$$

Then we can see that $T(t) = e^{-\lambda^2 t}$, where we have chosen to write the eigenvalue as $-\lambda^2$ since we know that it is both real-valued and positive. Now we must find the eigenvalues and the set of orthonormal eigenfunctions for the eigenvalue problem $X''(x) + \alpha X(x) + \lambda^2 X(x) = 0$. Note that since this is a linear, constant coefficient, second order ordinary differential equation, the eigenfunctions will be of the form $X(x) \sim e^{\eta x}$. By plugging in the Ansatz, we obtain

$$\begin{aligned}
e^{\eta x}\left(\eta^2 + \alpha\eta + \lambda^2\right) = 0, \\
\eta_\pm = \frac{-\alpha \pm \sqrt{\alpha^2 - 4\lambda^2}}{2}.
\end{aligned}$$

Note that there are two qualitatively different regimes for $\eta_\pm$. If $\lambda^2/4 < \alpha^2$, the $\eta_\pm$ will be real valued, and if $\lambda^2/4 > \alpha^2$, the $\eta_\pm$ will be a complex conjugate pair. In order to simplify our

notation, define

$$z = \begin{cases} \sqrt{\alpha^2 - 4\lambda^2}, & 0 < \frac{\lambda^2}{4} < \alpha^2, 0 < z < \alpha \\ \sqrt{4\lambda - \alpha^2}, & \frac{\lambda^2}{4} > \alpha^2, z > 0 \end{cases}. \tag{C.4}$$

Then we can see that

$$\eta_{\pm} = \begin{cases} -\frac{\alpha}{2} \pm \frac{z}{2}, & 0 < \frac{\lambda^2}{4} < \alpha^2 \\ -\frac{\alpha}{2} \pm i\frac{z}{2}, & \frac{\lambda^2}{4} > \alpha^2 \end{cases}. \tag{C.5}$$

The associated eigenfunctions will be

$$X(x,z) = \begin{cases} Ae^{-(\alpha+z)x/2} + Be^{-(\alpha-z)x/2}, & 0 < \frac{\lambda^2}{4} < \alpha^2, 0 < z < \alpha \\ Ce^{-\alpha x/2}\cos(zx/2) + De^{-\alpha x}\sin(zx/2), & \frac{\lambda^2}{4} > \alpha^2, z > 0 \end{cases}. \tag{C.6}$$

We can apply the boundary condition from (C.1b) to determine that

$$\begin{aligned} 0 &= X'(0,z) + \alpha X(0,z) = A\left(-\frac{\alpha+z}{2} + \alpha\right) + B\left(-\frac{\alpha-z}{2} + \alpha\right), \\ B &= A\frac{z-\alpha}{z+\alpha}, \\ 0 &= X'(0,z) + \alpha X(0,z) = C\left(-\frac{\alpha}{2} + \alpha\right) + D\left(\frac{z}{2}\right), \\ D &= -\frac{\alpha}{z}. \end{aligned}$$

So in summary, we have

$$X(x,z) = \begin{cases} \frac{A}{z+\alpha}\left((z+\alpha)e^{-(\alpha+z)x/2} + (z-\alpha)e^{-(\alpha-z)x/2}\right), & 0 < \frac{\lambda^2}{4} < \alpha^2, 0 < z < \alpha \\ \frac{C}{z}e^{-\alpha x/2}\left(z\cos(zx/2) - \alpha\sin(zx/2)\right), & \frac{\lambda^2}{4} > \alpha^2, z > 0 \end{cases}. \tag{C.7}$$

Then we must simply choose $A(z)$ and $C(z)$ so that the eigenfunctions are orthonormal subject to the weight function. We begin the process by checking the normality conditions:

$$\begin{aligned} 1 &= \int_0^\infty e^{\alpha x}\frac{A^2}{(z+\alpha)^2}\left((z+\alpha)^2e^{-(\alpha+z)x} + 2(z+\alpha)(z-\alpha)e^{-\alpha x} + (z-\alpha)^2e^{-(\alpha-z)x}\right)dx, \\ &= A^2\int_0^\infty \frac{\left((z+\alpha)^2e^{-zx} + 2(z+\alpha)(z-\alpha) + (z-\alpha)^2e^{zx}\right)dx}{(z+\alpha)^2}. \end{aligned}$$

Since this integral cannot be considered to converge, in any sense, we cannot find a value of A so that the orthonormality condition is satisfied.[1] We must still find $C(z)$:

$$\begin{aligned} 1 &= \int_0^\infty e^{\alpha x}\frac{C^2}{z^2}e^{-\alpha x}\left(z^2\cos^2(zx/2) - 2\alpha z\cos(zx/2)\sin(zx/2) + \alpha^2\sin^2(zx/2)\right)dx, \\ &= \frac{C^2}{z}\int_0^\infty \left(z^2\cos^2(zx/2) - 2\alpha z\cos(zx/2)\sin(zx/2) + \alpha^2\sin^2(zx/2)\right)dx. \end{aligned}$$

[1] We can also see that we cannot choose $A(z)$ so that the vanishing conditions in (C.1c) are satisfied, therefore solutions of this type can be thrown out!

If our interval of interest was finite, then we would be finished since we know that sine and cosine are orthogonal functions. We can interpret the integral above using that intuition. Therefore, we interpret the solution of the above integral to be:[2]

$$\begin{aligned} 1 &= \frac{C^2}{z^2}\left(z^2\pi + \alpha^2\pi\right), \\ C &= \frac{z}{\sqrt{\pi\left(z^2+\alpha^2\right)}}. \end{aligned}$$

Note that this requires more rigorous justification than we have given here, which is the main reason for including the alternate analysis in the following section. Then our eigenfunctions are given by

$$X(x,z) = \frac{e^{-\alpha x/2}}{\sqrt{\pi\left(z^2+\alpha^2\right)}}\left(z\cos(zx/2) - \alpha\sin(zx/2)\right). \tag{C.8}$$

Note that these eigenfunctions are orthonormal, as long as we interpret the integral over the semi-infinite domain so that the sine and cosine terms are orthonormal. There is an additional solution, which comes out of the case $\lambda^2 = 0$, i.e. the steady-state solution:

$$\begin{aligned} 0 &= X''_{ss}(x) + \alpha X'_{ss}(x), \\ &= \left(X'_{ss}(x) + \alpha X_{ss}\right)', \\ K &= X'_{ss}(x) + \alpha X_{ss}(x), \\ 0 &= X'_{ss}(0) + \alpha X_{ss}(0), \\ &\Rightarrow K = 0. \end{aligned}$$

We can see that the boundary condition at $x = 0$ fixes the constant of integration, and we must have

$$X_{ss}(x) = Fe^{-\alpha x}, \tag{C.9}$$

where F is a constant of integration to be determined using the orthonormality condition:

$$\begin{aligned} 1 &= \int_0^\infty e^{\alpha x}F^2e^{-2\alpha x}dx, \\ &= -\frac{F^2}{\alpha}e^{-\alpha x}\Big|_0^\infty, \\ &= \frac{F^2}{\alpha}, \end{aligned}$$

[2]If intuition is not enough, we could also evaluate the integral by taking the limit of the solution to the regular Sturm-Liouville problem over the finite domain $0 < x < L$ as $L \to \infty$.

so we can see that $F = \sqrt{\alpha}$. Note that $X_{ss}(x)$ is orthogonal to the rest of the eigenfunctions,

$$0 = \int_0^\infty e^{\alpha x} \left(\sqrt{\alpha} e^{-\alpha x}\right) \frac{e^{-\alpha x/2}}{\sqrt{\pi\left(z^2+\alpha^2\right)}} \left(z\cos(zx/2) - \alpha\sin(zx/2)\right) dx.$$

Therefore, we can express the full, time-dependent solution to (C.1) as

$$u(x,t) = a\sqrt{\alpha}e^{-\alpha x} + \int_0^\infty \frac{f(z)e^{-(\alpha^2+z^2)t/4}e^{-\alpha x/2}}{\sqrt{\pi\left(z^2+\alpha^2\right)}} \left(z\cos(zx/2) - \alpha\sin(zx/2)\right) dz, \qquad \text{(C.10)}$$

where a and $f(z)$ must be determined using the initial condition. This is done as follows. First, we may determine the value of a by evaluating the expression in (C.10) at $t = 0$ and integrating over x:

$$\begin{aligned}
\int_0^\infty u(x,0)dx &= \int_0^\infty a\sqrt{\alpha}e^{-\alpha x}dx + \int_0^\infty\int_0^\infty \frac{f(z)e^{-\alpha x/2}}{\sqrt{\pi\left(z^2+\alpha^2\right)}} \left(z\cos(zx/2) - \alpha\sin(zx/2)\right) dzdx, \\
\int_0^\infty \delta(x)dx &= a\sqrt{\alpha}\frac{1}{\alpha} + \int_0^\infty \frac{f(z)\int_0^\infty e^{-\alpha x/2}}{\sqrt{\pi\left(z^2+\alpha^2\right)}} \left(z\cos(zx/2) - \alpha\sin(zx/2)\right) dxdz, \\
1 &= \frac{a}{\sqrt{\alpha}},
\end{aligned}$$

so we find that $a = \sqrt{\alpha}$. Next, we will exploit the orthonormality of the eigenfunctions to determine $f(z)$. First, multiply both sides of (C.10) by $e^{\alpha x}X(x,z')$ and integrate over x. On the left-hand-side we have:

$$\begin{aligned}
&\int_0^\infty u(x,0)e^{\alpha x}\frac{e^{-\alpha x/2}}{\sqrt{\pi\left(z'^2+\alpha^2\right)}} \left(z'\cos(z'x/2) - \alpha\sin(z'x/2)\right) dx, \\
= &\int_0^\infty \delta(x)e^{\alpha x}\frac{e^{-\alpha x/2}}{\sqrt{\pi\left(z'^2+\alpha^2\right)}} \left(z'\cos(z'x/2) - \alpha\sin(z'x/2)\right) dx, \\
= &\frac{z'}{\sqrt{\pi\left(z'^2+\alpha^2\right)}}.
\end{aligned}$$

On the right-hand-side, we have:

$$\begin{aligned}
&\int_0^\infty \alpha\frac{e^{-\alpha x/2}}{\sqrt{\pi\left(z'^2+\alpha^2\right)}} \left(z'\cos(z'x/2) - \alpha\sin(z'x/2)\right) dx \\
&+\int_0^\infty\int_0^\infty \frac{f(z)\left(z\cos(zx/2) - \alpha\sin(zx/2)\right)dz}{\sqrt{\pi\left(z^2+\alpha^2\right)}} \frac{\left(z'\cos(z'x/2) - \alpha\sin(z'x/2)\right)}{\sqrt{\pi\left(z'^2+\alpha^2\right)}}dx, \\
= &\ 0 \\
&+\int_0^\infty f(z)\int_0^\infty \frac{\left(z\cos(zx/2) - \alpha\sin(zx/2)\right)\left(z'\cos(z'x/2) - \alpha\sin(z'x/2)\right)dx}{\sqrt{\pi\left(z^2+\alpha^2\right)}\sqrt{\pi\left(z'^2+\alpha^2\right)}}dz, \\
= &\ f(z').
\end{aligned}$$

Then we have shown that $f(z) = \frac{z}{\sqrt{\pi(z^2+\alpha^2)}}$, and the solution to the initial boundary value problem stated in (C.1) is given by

$$u(x,t) = \alpha e^{-\alpha x} + \int_0^\infty \frac{z e^{-(\alpha^2+z^2)t/4} e^{-\alpha x/2}}{\pi\left(z^2+\alpha^2\right)} \left(z\cos(zx/2) - \alpha\sin(zx/2)\right) dz. \tag{C.11}$$

We can see that we have obtained the solution given in the Appendix of [62], and stated in Chapter 6, but we have made several assumptions, including the interpretation of the improper integral as well as the assumption that the set of eigenfunctions that we have found is complete, that may leave a reader with a taste for mathematical rigor unsatisfied. Therefore, we will now show that the same solution arises in a much more natural way via the "New Method" of Fokas, without making these potentially troubling assumptions.

C.2 Time Dependent Gap Distance Solution: New Method of Fokas

We would like to solve the following initial boundary value problem, which arises as the probability distribution for the gap distance between a single polymer and a moving barrier, as discussed in Chapter 6:

$$u_t(x,t) = u_{xx}(x,t) + \alpha u_x(x,t), \qquad 0 < x < \infty, t > 0, \tag{C.12a}$$

$$u_x(0,t) + \alpha u(0,t) = 0, \tag{C.12b}$$

$$\lim_{x\to\infty} u(x,t) = \lim_{x\to\infty} u(x,t) = 0, \tag{C.12c}$$

$$u(x,0) = u_0(x) = \delta(x), \tag{C.12d}$$

where we again define the delta function according to (C.2).

In order to solve (C.12), we will apply the "New Transform Method" of Fokas [22]. We begin by expressing the partial differential equation in the form

$$\left(e^{-ikx+\omega t}u\right)_t = \left(e^{-ikx+\omega t}X\left(u, u_x, u_{xx}, \ldots\right)\right)_x, \tag{C.13}$$

which will allow us to solve for the dispersion relation, $\omega(k)$. For our problem, we can see that

$$X(x) = u_x(x,t) + (\alpha + ik)u(x,t), \tag{C.14}$$

$$\omega(k) = k^2 - i\alpha k, \tag{C.15}$$

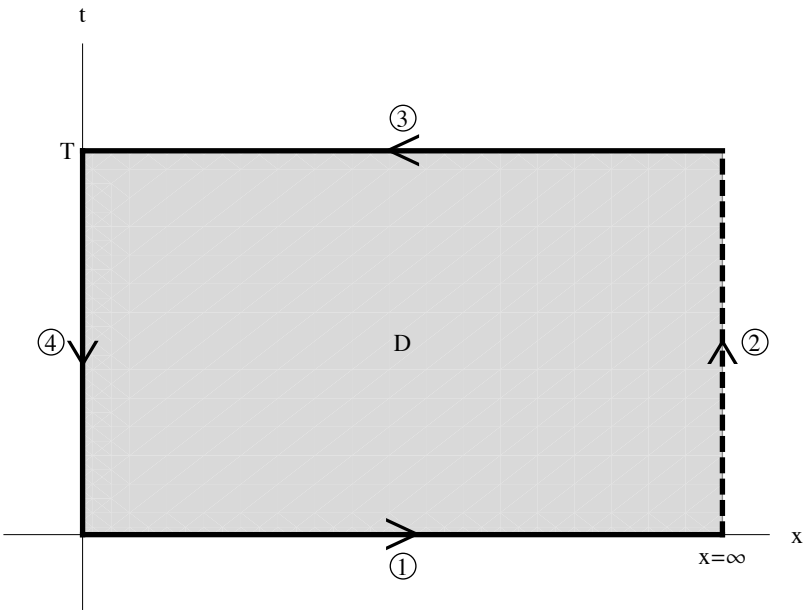

Figure C.1: **Physical Domain.**
The physical domain for the problem given in (C.12).

where k lies in the complex plane. Note that the dispersion relation is invariant under the transformation

$$k \to i\alpha - k. \tag{C.16}$$

The domain, D, over which we wish to obtain a solution for $u(x,t)$ is shown in Figure C.1. Inside D, we have

$$\int\int_D \left[\left(e^{-ikx+\omega t}u\right)_t - \left(e^{-ikx+\omega t}u_x(x,t) + (\alpha+ik)u(x,t)\right)_x\right] dxdt = 0, \tag{C.17}$$

so by Green's Theorem,

$$\oint_{\partial D} \left[e^{-ikx+\omega t}\left(u_x(x,t) + (\alpha+ik)u(x,t)\right)dt + e^{-ikx+\omega t}udx\right] = 0, \tag{C.18}$$

where ∂D refers to the boundary of D, as shown in Figure C.1.

Now we will investigate the contributions along each of the four paths along the boundary ∂D. Along the first path, $t = 0$, so we have

$$\int_0^\infty e^{-ikx}u_0(x)dx. \tag{C.19}$$

Along the second path, $x = \infty$, and since we know from (C.12c) that $u(x,t)$ and $u_x(x,t)$ vanish at infinity, there is no contribution along this path. Along the third path, $t = T$, so we have

$$-\int_0^\infty e^{-ikx+\omega T} u(x,T)dx. \tag{C.20}$$

Finally, along the fourth path, $x = 0$, so we have

$$-\int_0^T e^{\omega t}\left(u_x(0,t) + (\alpha + ik)\, u(0,t)\right) dt = -\int_0^T e^{\omega t} iku(0,t)dt, \tag{C.21}$$

where we have already applied the boundary condition from (C.12b). Since the sum of the integrals along the four paths vanishes, we have

$$\int_0^\infty e^{-ikx+\omega T} u(x,T)dx = -\int_0^T e^{\omega t} iku(0,t)dt + \int_0^\infty e^{-ikx} u_0(x)dx. \tag{C.22}$$

Define the following quantities for notational convenience:

$$\hat{u}_0(k) = \int_0^\infty e^{-ikx} u_0(x)dx, \tag{C.23a}$$

$$\hat{u}(k,T) = \int_0^\infty e^{-ikx} u(x,T)dx, \tag{C.23b}$$

$$g_0(\omega,T) = \int_0^T e^{\omega t} u(0,t)dt, \tag{C.23c}$$

$$g_1(\omega,T) = \int_0^T e^{\omega t} u_x(0,t)dt. \tag{C.23d}$$

Note that we were able to eliminate the term involving $g_1(\omega,T)$ using the boundary condition, but we have included its definition for completeness.

Now we can use our notation to rewrite (C.22) to obtain the *global relation*:

$$\hat{u}(k,T)e^{\omega t} = \hat{u}_0(k) - ikg_0(\omega,T). \tag{C.24}$$

We would like to determine the region of the complex $k-$plane in which the global relation is valid. In order for the global relation to be valid, we must have decaying exponential terms in the improper integrals. We can see that $g_0(\omega,T)$ and $g_1(\omega,T)$ do not contain improper integrals, and are therefore valid for all k, however $\hat{u}_0(k)$ and $\hat{u}(k,T)$ are only valid for $Im(k) < 0$, or the lower half plane (LHP). Later on, we will exploit the invariance of the dispersion relation, (C.16), to "flip" the global relation into a domain in the upper half plane (UHP). The domains

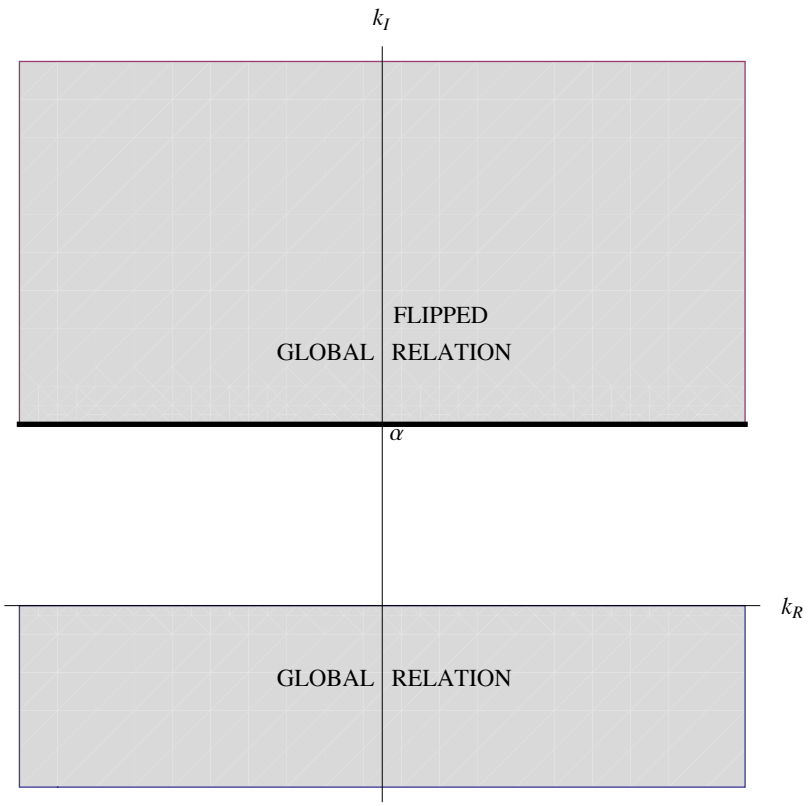

Figure C.2: **Global Relation Domains.**
Domains in the complex $k-$plane in which the global relation and the "flipped" global relation are valid.

in the complex $k-$plane in which the global relation and the "flipped" global relation are valid are shown in Figure C.2.

In order to find the solution, $u(x,T)$, we will simply invert the transform:

$$u(x,T) = \frac{1}{2\pi}\int_{-\infty}^{\infty} e^{ikx-\omega T}\left[\hat{u}_0(k) - ikg_0(\omega,T)\right]dk. \tag{C.25}$$

Before we can completely solve the problem, we must eliminate the unknown quantity $g_0(\omega,t)$. First, we will investigate the second term of (C.25) in more detail:

$$I_2 = -\frac{1}{2\pi}\int_0^{\infty} ike^{ikx-\omega t}\int_0^t e^{\omega\tau}u(0,\tau)d\tau dk = -\frac{1}{2\pi}\int_0^{\infty}\int_0^t ike^{ikx-\omega(t-\tau)}u(0,\tau)d\tau dk. \tag{C.26}$$

I_2 will be valid when the exponential terms are decaying. This yields two conditions: $Re(ik) < 0$ and $Re(\omega) > 0$, since the quantity $t-\tau$ will always be positive. For our problem, the region in which I_2 is both defined and analytic is shown in Figure C.3. Since the integrand is analytic in the shaded region, and and also goes to zero uniformly for $0 < \theta < \frac{\pi}{4}$ and $\frac{3\pi}{4} < \theta < \pi$, we can use Jordan's Lemma and Cauchy's Residue Theorem to deform the line integral to be along the path C where $k_I = |k_R|$ in the UHP, as shown in Figure C.3:

$$I_2 = -\frac{1}{2\pi}\int_C e^{ikx-\omega t}ikg_0(\omega,t)dk. \tag{C.27}$$

We hope to eliminate the dependence on $g_0(\omega,t)$ using the invariance properties of the dispersion relation, $\omega(k)$, along with the global relation. First, apply the transformation of variables under which the dispersion relation is invariant, (C.16), to the global relation:

$$\hat{u}(i\alpha-k,T)e^{\omega T} = \hat{u}_0(i\alpha-k) + (\alpha+ik)g_0(\omega,T). \tag{C.28}$$

Note that this "flipped" global relation is valid for $Im(k) > \alpha$, as shown in Figure C.2. Now solve the flipped global relation for $g_0(\omega,T)$:

$$g_0(\omega,T) = \frac{1}{\alpha+ik}\left(\hat{u}(i\alpha-k,T)e^{\omega T} - \hat{u}_0(i\alpha-k)\right). \tag{C.29}$$

We can replace the $g_0(\omega,T)$ term in I_2 to obtain

$$I_2 = -\frac{1}{2\pi}\int_C e^{ikx-\omega T}\frac{ik}{\alpha+ik}\left(\hat{u}(i\alpha-k,t)e^{\omega T} - \hat{u}_0(i\alpha-k)\right)dk. \tag{C.30}$$

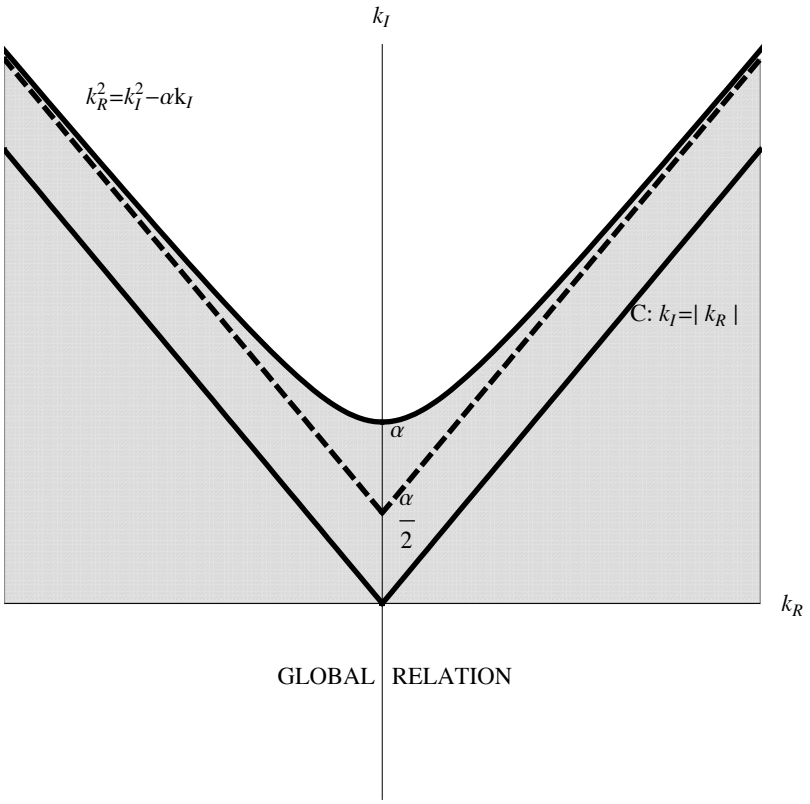

Figure C.3: **Integration Paths in the Upper Half Plane.**
The shaded region is the region of the complex $k-$plane where I_2, from (C.26), is both defined and analytic. Using Cauchy's Residue Theorem and Jordan's Lemma, we will deform the integral to be along the path C, rather than along the real axis. Note that the thick dashed curve is the asymptote for the hyperbola that bounds the shaded region. The asymptotes are: $k_I = \frac{\alpha}{2} \pm k_R$.

Returning to (C.25), we now see that the solution can be written as

$$\begin{aligned} u(x,T) &= \frac{1}{2\pi}\int_{-\infty}^{\infty} e^{ikx-\omega T}\hat{u}_0(k)dk + \frac{1}{2\pi}\int_C e^{ikx-\omega T}\frac{ik}{\alpha+ik}\hat{u}_0(i\alpha-k)dk \\ &\quad -\frac{1}{2\pi}\int_C e^{ikx}\frac{ik}{\alpha+ik}\hat{u}(i\alpha-k,T)dk. \end{aligned} \tag{C.31}$$

Note that by the same reasoning as before, the first integral term can also be deformed to the curve C. Furthermore, since $u_0(x) = \delta(x)$, we have

$$\hat{u}_0(k) = \int_0^{\infty} e^{-ikx}\delta(x)dx = 1, \qquad \hat{u}_0(i\alpha-k) = \int_0^{\infty} e^{-i(i\alpha-k)x}\delta(x)dx = 1, \tag{C.32}$$

and the first two integral terms from (C.31) can be combined and written as:

$$I_1 = \frac{1}{2\pi}\int_C e^{ikx-\omega T}\left(1+\frac{ik}{\alpha+ik}\right)dk, \tag{C.33}$$

which can be interpreted in a physical sense as the propagation of the initial condition over time. Next, we will focus on the third term from (C.31), I_3. We can see that

$$\begin{aligned} I_3 &= -\frac{1}{2\pi}\int_C e^{ikx}\frac{ik}{\alpha+ik}\hat{u}(i\alpha-k,T)dk, \\ &= -\frac{1}{2\pi}\int_C e^{ikx}\frac{ik}{\alpha+ik}\left(\int_0^{\infty} e^{-ikx}u(x,T)dx\right)dk. \end{aligned} \tag{C.34}$$

Note that I_3 does not contain any $e^{\omega T}$ terms, so the integral will converge for all k in the UHP. Furthermore, the integrand is analytic for all k in the UHP, except for a simple pole at $k = i\alpha$. Therefore, we can use Cauchy's Residue Theorem, along with Jordan's Lemma to determine that

$$\begin{aligned} I_3 &= -\frac{1}{2\pi}2\pi i\text{Res}\left(e^{-ikx}\frac{ik}{\alpha+ik}\hat{u}(i\alpha-k,T);i\alpha\right), \\ &= -i\lim_{k\to i\alpha}\left(\frac{ike^{-ikx}}{\alpha+ik}\hat{u}(i\alpha-k,T)(k-i\alpha)\right), \\ &= \alpha e^{-\alpha x}\hat{u}(0,T). \end{aligned}$$

Now we simply need to find $\hat{u}(0,T)$. First, note that $\hat{u}(0,T) = \int_0^{\infty} u(x,t)dx$. We can show that the integral of $u(x,t)$ is conserved over time, using the boundary and vanishing conditions from

(C.12b) and (C.12c):

$$\begin{aligned}\frac{\partial}{\partial t}\int_0^\infty u(x,t)dx &= \int_0^\infty u_t(x,t)dx,\\ &= \int_0^\infty \left(u_{xx}(x,t)+\alpha u_x(x,t)\right)dx,\\ &= \left(u_x(x,t)+\alpha u(x,t)\right)\big|_0^\infty,\\ &= 0,\end{aligned}$$

so we know that

$$\hat{u}(0,T)=\int_0^\infty u(x,T)dx=\int_0^\infty u(x,0)dx=\int_0^\infty \delta(x)dx=1. \tag{C.35}$$

Therefore, we can see that I_3 is equal to the steady-state solution,

$$I_3=\alpha e^{-\alpha x}. \tag{C.36}$$

Finally, we find that the solution to the initial boundary value problem given in (C.12) is given by

$$u(x,t)=\alpha e^{-\alpha x}+\frac{1}{2\pi}\int_C e^{ikx-(k^2-i\alpha k)t}\left(1+\frac{ik}{\alpha+ik}\right)dk. \tag{C.37}$$

We now show that if we deform the integral from the path C to the line $k_I=\alpha/2$, we will obtain the solution in the same form that was found via the singular Sturm-Liouville analysis, but with much less difficulty. We must split the path C into three pieces to justify the deformation to the line, which can be seen in Figure C.4:

$$C: k_I=\begin{cases} -k_R, & -\infty<k_R<-\alpha/2\\ |k_R|, & -\alpha/2\le k_R\le \alpha/2\\ k_R, & \alpha/2<\infty\end{cases}.$$

We can see that the integrand is analytic and bounded in the shaded region, with the exception of the point $k=i\alpha$. Therefore, we can easily justify deforming the path from C to $k_I=\alpha/2$ in the region from $-\alpha/2\le k_R\le\alpha/2$. As before, when we deformed the integrals from the real line to C, we can use Cauchy's Residue Theorem and Jordan's Lemma to deform from C to $k_I=\alpha/2$ in the regions where $\alpha/2<|k_R|<\infty$.

We can parametrize the curve $k_I=\alpha/2$ as $k(z)=z+i\alpha/2$, so $k'(z)=1$, and I_1 becomes

$$I_1=\frac{1}{2\pi}\int_{-\infty}^\infty e^{izx-\alpha x/2-\left(\alpha^2/4+z^2\right)t}\frac{2z^2+i\alpha z}{\frac{\alpha^2}{4}+z^2}dz.$$

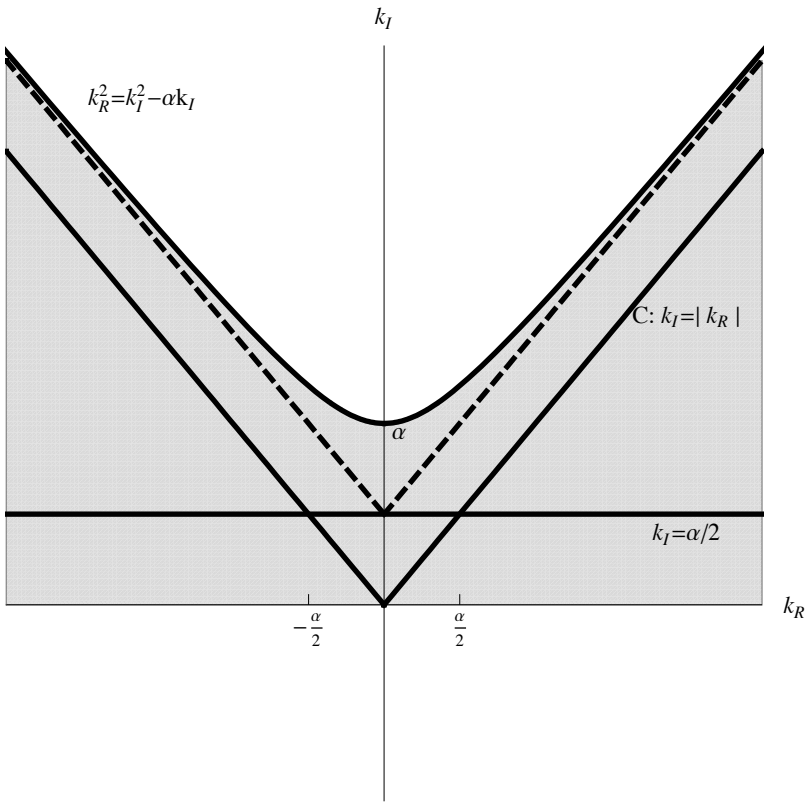

Figure C.4: **More Integration Paths in the UHP.**
We deform the integral I_1 from the path C to the line $k_I = \alpha/2$. The shaded region is the region in which the integral converges.

We can simplify the algebra by making the substitution $z \to z/2$, $dz \to dz/2$:

$$\begin{aligned} I_1 &= \frac{1}{2\pi}\int_{-\infty}^{\infty} e^{izx/2-\alpha x/2-(\alpha^2+z^2)t/4}\frac{z^2+i\alpha z}{\alpha^2+z^2}dz, \\ &= \frac{e^{-\alpha x/2}e^{-\alpha^2 t/4}}{2\pi}\int_0^{\infty}\frac{e^{-z^2t/4}\left(e^{izx/2}(z^2+i\alpha z)+e^{-izx/2}(z^2-i\alpha z)\right)dz}{\alpha^2+z^2}, \\ &= e^{-\alpha x/2}e^{-\alpha^2 t/4}\int_0^{\infty}\frac{ze^{-z^2t/4}\left(z\cos(zx/2)-\alpha\sin(zx/2)\right)dz}{\pi(\alpha^2+z^2)}. \end{aligned}$$

Finally, we have shown that the solution can be written as

$$u(x,t) = \alpha e^{-\alpha x} + e^{-\alpha x/2}e^{-\alpha^2 t/4}\int_0^{\infty}\frac{ze^{-z^2t/4}\left(z\cos(zx/2)-\alpha\sin(zx/2)\right)dz}{\pi(\alpha^2+z^2)}, \qquad \text{(C.38)}$$

which is in agreement with the solution published in Ref. [62] and in the previous section.

Appendix D

CENTER OF FRICTION OF TWO RANDOM WALKERS

Figure D.1: **Two Random Walkers Schematic Diagram.**

We have spent a great deal of time considering the picture of a polymer filament interacting with a moving barrier from the point of view of the gap distance between them. Now, we will consider the system from the point of view of the average position, or the *center of friction*. For this discussion, we will consider two random walkers that move to the left at rates α_1, α_2 and to the right at rates β_1, β_2, and take steps of size δ, as shown in Figure D.1. Let x represent the position of walker 1, and y represent the position of walker 2. We can also define another set of variables

$$\Delta = y - x, \quad \text{and} \quad z = \frac{(\alpha_2 + \beta_2)\, x + (\alpha_1 + \beta_1)\, y}{(\alpha_1 + \beta_1 + \alpha_2 + \beta_2)}, \tag{D.1}$$

where Δ represents the gap, or distance between the two walkers, and z represents the weighted average position, or "center of friction" of the two walkers. Note that the average is weighted by the jump rates of the walkers.

From Chapter 6, we know that each walker has effective diffusion and drift coefficients given by

$$D_1 = (\alpha_1 + \beta_1)\,\frac{\delta^2}{2}, \qquad D_2 = (\alpha_2 + \beta_2)\,\frac{\delta^2}{2}, \tag{D.2a}$$

$$V_1 = (\beta_1 - \alpha_1)\,\delta, \qquad V_2 = (\beta_1 - \alpha_1)\,\delta. \tag{D.2b}$$

We also know that the gap between them has effective diffusion and drift coefficients given by

$$D_\Delta = (\alpha_1 + \beta_1 + \alpha_2 + \beta_2)\,\frac{\delta^2}{2} = D_1 + D_2, \tag{D.3a}$$

$$V_\Delta = -\,(\beta_1 + \beta_2 - \alpha_1 - \alpha_2)\,\delta = -\,(V_1 + V_2)\,. \tag{D.3b}$$

However, we have not considered the same type of argument when deriving the effective diffusion and drift coefficients for the center of friction.

When one of the walkers moves either left $(-\delta)$ or right $(+\delta)$, the center of friction moves according to:

$$\frac{(\alpha_2 + \beta_2)\,(x \pm \delta) + (\alpha_1 + \beta_1)\,y}{(\alpha_1 + \beta_1 + \alpha_2 + \beta_2)} = \frac{(\alpha_2 + \beta_2)\,x + (\alpha_1 + \beta_1)\,y}{(\alpha_1 + \beta_1 + \alpha_2 + \beta_2)} \pm \frac{(\alpha_2 + \beta_2)}{(\alpha_1 + \beta_1 + \alpha_2 + \beta_2)}\delta, \tag{D.4a}$$

$$\frac{(\alpha_2 + \beta_2)\,x + (\alpha_1 + \beta_1)\,(y \pm \delta)}{(\alpha_1 + \beta_1 + \alpha_2 + \beta_2)} = \frac{(\alpha_2 + \beta_2)\,x + (\alpha_1 + \beta_1)\,y}{(\alpha_1 + \beta_1 + \alpha_2 + \beta_2)} \pm \frac{(\alpha_1 + \beta_1)}{(\alpha_1 + \beta_1 + \alpha_2 + \beta_2)}\delta. \tag{D.4b}$$

So we can see that the effective step sizes for the center of friction are either $\dfrac{(\alpha_2 + \beta_2)}{(\alpha_1 + \beta_1 + \alpha_2 + \beta_2)}\delta$, if walker 1 moves, or $\dfrac{(\alpha_1 + \beta_1)}{(\alpha_1 + \beta_1 + \alpha_2 + \beta_2)}\delta$, if walker 2 moves. Therefore, the effective diffusion coefficient for the center of friction is given by

$$\begin{aligned} D_z &= (\alpha_1 + \beta_1)\left(\frac{(\alpha_2 + \beta_2)}{(\alpha_1 + \beta_1 + \alpha_2 + \beta_2)}\right)^2 \frac{\delta^2}{2} + (\alpha_2 + \beta_2)\left(\frac{(\alpha_1 + \beta_1)}{(\alpha_1 + \beta_1 + \alpha_2 + \beta_2)}\right)^2 \frac{\delta^2}{2}, \\ &= \frac{(\alpha_1 + \beta_1)\,(\alpha_2 + \beta_2)}{(\alpha_1 + \beta_1 + \alpha_2 + \beta_2)^2}\,((\alpha_1 + \beta_1) + (\alpha_2 + \beta_2))\,\frac{\delta^2}{2}, \\ &= \frac{(\alpha_1 + \beta_1)\,(\alpha_2 + \beta_2)}{(\alpha_1 + \beta_1 + \alpha_2 + \beta_2)}\,\frac{\delta^2}{2}, \end{aligned}$$

which can also be expressed in terms of the diffusion coefficients for each walker:

$$D_z = \frac{D_1 D_2}{D_1 + D_2}. \tag{D.5}$$

Therefore, we can see that the effective diffusion coefficient for the center of friction, D_z, is reduced due to the reduced effective step size of the center of friction compared to the step size of a single random walker.[1]

On the other hand, the effective drift for the center of friction of the two walkers will be

[1]To illustrate that this diffusion coefficient is "reduced," examine the special case where the two random walkers are identical. In this case, we would have $D_1 = D_2 = D$, so $D_z = \frac{D^2}{2D} = \frac{D}{2}$.

given by

$$V_z = (\beta_1 - \alpha_1)\left(\frac{(\alpha_2 + \beta_2)}{(\alpha_1 + \beta_1 + \alpha_2 + \beta_2)}\right)\delta + (\beta_2 - \alpha_2)\left(\frac{(\alpha_1 + \beta_1)}{(\alpha_1 + \beta_1 + \alpha_2 + \beta_2)}\right)\delta, \tag{D.6a}$$

$$= \frac{2\left(\beta_1\beta_2 - \alpha_1\alpha_2\right)\delta}{(\alpha_1 + \beta_1 + \alpha_2 + \beta_2)}, \tag{D.6b}$$

which we can see is equivalent to the weighted average of the drift coefficients for each walker:

$$V_z = \frac{D_2V_1 + D_1V_2}{D_1 + D_2}. \tag{D.7}$$

So we see that for the center of friction of the two random walkers, the diffusion coefficient will be reduced, while the drift coefficient will be the weighted average of the drift coefficients.[2]

[2]In the special case where the random walkers are identical, i.e. $D_1 = D_2 = D$ and $V_1 = V_2 = V$, the center of friction drift coefficient will be $V_z = \frac{2DV}{2D} = V$.

VITA

Christine Louise Lind Cole was born on October 2, 1979, in Tacoma, Washington, where the groundwork for her later academic success was firmly laid by the education she received at Charles Wright Academy. In the fall of 1998, Christine traveled to St. Paul, Minnesota, to attend Macalester College. After graduating with a Bachelor of Arts in Mathematics and Physics in 2002, she returned to the Northwest, settling in Seattle, Washington. In the fall of 2003, she entered the Applied Mathematics graduate program at the University of Washington, where she earned a Master of Science in 2004, and a Doctor of Philosophy in 2011.